SWANSEA UNIVERSITY

Swansea University
Prifysgol Abertawe

DOCTORAL THESIS

First-order deconfining phase transitions in Yang-Mills theories

by:
David Mason

A thesis submitted in fulfillment of the requirements
for the Doctor of Philosophy

of the

Department of Physics,
Faculty of Science and Engineering,
Swansea University

Declaration of Authorship

I, David Mason, declare that this thesis titled, "First-order deconfining phase transitions in Yang-Mills theories" and the work presented in it are my own. I confirm that:

- This work has not previously been accepted in substance for any degree and is not being concurrently submitted in candidature for any degree.
- This thesis is the result of my own investigations, except where otherwise stated. Other sources are acknowledged by footnotes giving explicit references. A bibliography is appended.
- I hereby give consent for my thesis, if accepted, to be available for photocopying and for inter-library loan, and for the title and summary to be made available to outside organisations.
- The University's ethical procedures have been followed and, where appropriate, that ethical approval has been granted.

Signed: D. Mason

Date: November 7, 2024

Acknowledgements

I would like to thank my collaborators Biagio Lucini, Davide Vadacchino, Ed Bennet, Enrico Rinaldi, Fabian Zierler and Maurizio Piai, without your contributions this work would not have been possible. Biagio and Maurizio for being amazing, supportive supervisors and driving me to do this work. Davide and Ed for helping for helping me to learn HiRep and get things running. Enrico for starting the discussion on gravitational waves and organising time on Fugaku. Fabian for agreeing to continue with this project, its in good hands. Thanks to Fugaku and DiRAC for the computer time.

Thanks to everyone at the AIMLAC and DI CDTs for giving me great opportunities for development outside of Physics and funding my research. Particularly Alin-Marin Elena for giving me the opportunity to carry out the interesting research placement.

Thanks to the people in office 606 past and present, all of my friends, everyone at the Sandy BBQs, the cool kids and anyone who came to Talking Research, for making my time in Swansea amazing. Sid for the private correspondence.

Courtlyn thanks for being amazing.

I also want to thank my family for supporting me through this. Mum and Dad without you I would not exist. Marianne for all of the goat pictures. Robert, lattice is better than perturbative.

Finally to Aida, Tilda, Princess, Cashew the Dog, Dwayne, Bobby, Babbette, Kiwi, and Eddie, who cannot read but thanks for being the best dogs and cats.

Diolch i chi, Abertawe a Chymru.

Research Data Access Statement– Analysis and simulation code for research papers on related work, Ref. [1] and Ref. [2], can be found at Ref. [3], Ref. [4], Ref. [5] and Ref. [6].

Abstract

Finite temperature first-order deconfinement phase transitions of non-Abelian gauge theory systems can lead to rich phenomenological implications to the cosmological evolution of the early universe, resulting in potentially observable imprints on the current universe such as the matter anti-matter asymmetry and a background of gravitational waves. It is generally accepted that deconfinement in standard model of particle physics arises through a cross-over and therefore the system transitions from one regime to the other without producing non-equilibrium effects. However, it is also widely acknowledged that the standard model is not the full picture in particle physics, since, for instance, to explain problems such as the existence of dark matter, we require new physics. A large array of extensions of the standard model are based on the addition of a new strongly interacting sector, with a new set of non-Abelian gauge fields. This new sector might undergo a first order deconfinement phase transition whose observable effects can in principle be detectable. This thesis develops a methodology for precision studies of these phase transitions considering the beyond the standard model theory – and in particular its gauge sector - in isolation. As the confining properties of the model are inherently non-perturbative we choose to analyse it numerically using lattice field theory. However, the meta-stable dynamics characteristic of a first-order phase transition can lead to intractable problems with standard importance sampling methods. We resolve this issue through the use of the Logarithmic Linear Relaxation (LLR) method, which samples a flat energy distribution to accurately compute the density of states. Through the density of states, we can reconstruct observables, compute the energy distribution and determine thermodynamic properties, such as the free-energy, that are out of reach with importance sampling methods. This work develops a density of state approach based on the LLR method and tests in $SU(3)$ and $Sp(4)$ gauge theories, for which a highly accurate set of results for thermodynamic observables is obtained.

Contents

Chapter 1

Introduction

> "Studying finite temperature first order deconfinement phase transitions in pure Yang-Mills theories using lattice methods is intriguing for understanding QCD's confinement-deconfinement dynamics, advancing non-perturbative techniques, interpreting heavy-ion collision experiments, tackling computational challenges, and shedding light on early universe conditions. This research deepens our grasp of fundamental physics."
> ChatGPT.

Phase transitions, abrupt changes in the macroscopic behaviour of a system, are prevalent throughout physics. Although they occur in a wide range of systems, from the boiling of water to the most dramatic moments in the cosmological evolution of the universe, the classification and description of their dynamics are strikingly similar.

Phase transitions in physics can be described by the breaking, or restoration of a symmetry of the system. For example, this happens in the paramagnetic ferromagnetic phase transition, in which a material gains an overall magnetic field in a given direction. In the paramagnetic phase the magnetic moment of the molecules in the material are equally likely to point in any direction, giving a vanishing overall magnetisation. In the ferromagnetic phase the magnetic moments of the molecules in the material will align and pick out a preferred direction, generating an overall magnetic field for the material. Therefore in moving from the paramagnetic to the ferromagnetic phase a symmetry of the system has been spontaneously broken as a direction has become picked out. Associated with the symmetry breaking, and therefore the phase transition is an order parameter, which allows us to determine the phase of the system. In the disordered phase, paramagnetic, the order parameter will vanish, whereas in the ordered phase, ferromagnetic, the order parameter will have a finite value. In this example, the order parameter is the overall magnetisation of the material.

One of the most important properties of a phase transition is the order. In Ehrenfest's classification, an *nth* order phase transition will have a discontinuity or a divergence in the

nth derivative of the free energy with respect to a thermodynamic potential. In this work, we focus on phase transitions driven by the temperature. This distinction characterises much of the physics of the phase transition, and how we can study it. For example, in a second order phase transition the system gains a scale invariance becoming conformal at criticality, due to a diverging correlation length. Therefore, fluctuations at all length scales become important and the thermodynamic observables gain a power law behaviour as they approach the critical point, allowing them to be described by a finite set of critical exponents. This property allows these transitions to be further characterised by their university class, in which the asymptotic behaviour as we approach the critical point is identical to other transitions in the same class. Another important type of transition is a cross-over, in which there is no sudden change in the macroscopic characteristic of the system and it smoothly transitions from one regime to the other.

First order phase transitions, which will be the focus of this thesis, are characterised by a sudden change in the gradient of the free-energy, and a discrete jump in the internal energy. This occurs due to the co-existence of different phases. If the phase transition is driven by the change in temperature, for a range of temperatures around the critical point there is a finite probability for the system to be in either the high or low temperature phases. To move from one phase to the other, the system will have to overcome a potential barrier; for a quantum systems, this can be due to quantum fluctuations or tunnelling. The behaviour of the system around the phase co-existence and finite probability of tunneling between vacua gives rise to meta-stable dynamics and is the basis for the interesting phenomenological implications of first-order transitions and leads to the technical challenges that is at the heart of the work presented in this thesis.

If the system begins in the high temperature phase and cools, rather than an immediate global change in the phase of the system, bubbles in the lower temperature phase will nucleate. At the critical temperature, T_c, each phase is equally likely and therefore the difference in free-energy between the phases vanishes. At a temperature, T, around the critical temperature we can approximate difference in free-energy of the system by $\Delta F = L_h V(1 - T/T_c)$, where L_h is the latent heat per unit spatial volume, V, i.e. the difference in internal energy density between the phases. To create a bubble of radius r, an interface between the phases is created raising the free-energy by $\sim 4\pi r^2\sigma$, where σ is the surface tension of the transition. Once the system is below the critical temperature, and the lower temperature phase is more favourable, the reduction in free-energy due to the bulk of the bubble will be given by $\sim \frac{4}{3}\pi r^3 L_h(1 - T/T_c)$. Below a critical radius, r_c, the surface term will dominate leading to the bubble evaporating, thus the system remains in the high temperature phase. While bubbles larger than the critical radius will expand outwards. Therefore, in order for the system to

transition into the new phase, we require a bubble larger than this critical size to be nucleated. As the temperature decreases further, the free-energy difference between the phases will increase, reducing the critical radius. The properties of the nucleation and expansion of the bubbles can in principle be determined through from the thermodynamic properties of the transition, see for example Ref. [7] and Ref. [8].

Bubble nucleation in phase transitions in the early universe has an interesting implication for observations in our current universe. In his seminal work Ref. [9], Sakharov set out three requirements for baryogenesis: out of equilibrium dynamics, the breaking of C and CP symmetries and baryon number violation. Bubble nucleation from first order transitions has the required out of equilibrium dynamics to generate some of the matter antimatter asymmetry. See for example Ref. [10] for a review on electroweak baryogenesis, Ref. [11] for a discussion on darkbaryogenesis and Ref. [12] for a general overview on baryogenesis.

The nucleation and expansion of the bubble will not happen in isolation, many bubbles will independently nucleate and expand. Eventually, separate nucleated bubbles in the low temperature phase will collide and coalesce forming a new bubble. This is a violent process, that can lead to the generation of gravitational waves, which may continue to propagate through the cosmological evolution of the universe, expanding with the expansion of the universe, to now. Since the first detection of gravitational waves [13], gravitational wave astronomy has been seen as an exciting prospect to detect and constrain possible new physics. The first order phase transitions have the ability to generate a stochastic gravitational wave background. Waves of this type may have been detected in the NANOGrav experiment [14], and there is the possibility that they will become accessible to future experiments, see for example Ref. [15] and Ref. [16]. Using the thermodynamic properties of the transition, one can compute a set of parameters describing the strength of the transition, α, the dimensionless inverse duration, β/H_*[1], the bubble wall velocity, v_w, the number of degrees of freedom and the critical, T_c, and percolation, T_* temperatures. This can then be used to predict the gravitational wave power-spectrum using existing python packages such as PTPlot [15]. For more details on stochastic gravitational waves from first order transitions see Refs. [8, 17–24]

The cosmological history of the standard model of particle physics contains two cross-overs. The first is the electroweak transition, at a temperature of $\sim 159GeV$ [25], where the combined gauge symmetry of electroweak sector, $SU(2)_L \times U(1)_Y$, breaks to the quantum electrodynamics, as the Higgs field gains a potential. A combination of perturbative and lattice methods find that for a Higgs boson mass greater than around $72GeV$ this transition is a cross-over [25–31]. The measurement of the Higgs mass as $m_H \approx 125GeV$ [32, 33], has

[1] β is the inverse duration of the phase transition, note this differs from the β, used in the rest of the work, which denotes the inverse coupling. H_* is the Hubble parameter, H_*^{-1} gives an intrinsic timescale to compare against.

excluded the existence of an electro-weak phase transition in the standard model. However, extensions and modifications to the standard model can alter the critical endpoint and lead to the possibility of first order electro-weak transitions at larger Higgs masses, for a recent update on developments in this field find Ref. [34].

The second cross-over is the chiral symmetry breaking of the quantum chromodynamics (QCD), at a temperature of $\sim 150MeV$ [35]. In the chrial symmetric phase the left and right handed fermions transform independently under the chiral group, in the broken phase a mass term links them. The order parameter associated with this symmetry is the chiral condensate, $\langle \bar{q}q \rangle$. Associated with this transition is confinement where the strong sector of the standard model, described by QCD, changes from a pseudo free theory, with non-vanishing expectation for free quarks and gluons, to a system of confined hadrons and mesons. In pure gauge systems, the confinement transition is associated with the spontaneous breaking of the centre symmetry, with the Polyakov loop as the order parameter, more details on this will be given in Chap. 2. We can approximate the potential between quarks by the static quark potential,

$$V(r) = A + \frac{B}{r} + \sigma r, \tag{1.0.1}$$

for high temperatures, due to asymptotic freedom of QCD, the linear term disappears, and we have forces that behave like $1/r^2$. Whereas in the low temperature phase, the σ term dominates, leading to a constant force between static quarks, confining the quarks. Note this is a cartoon description for pedagogical purposes, and ignores important properties such as string breaking, see Ref. [36] for a comprehensive overview. Using lattice simulations, in Ref. [37] chiral symmetry breaking for physical quark masses was determined to be a smooth cross-over. The phase structure of the theory can be changed by altering the properties of the theory, this can be described by the Columbia plot, first introduced in Ref. [38], which demonstrates that for very light and very heavy quark masses the phase transition becomes first order. For a review on the exploration of phase space of the QCD phase transition find the review Ref. [39].

The standard model of particle physics is one of the best tested theories in science. However, we know that it is not complete. One well known problem is dark matter. Astronomical and cosmological evidence point to majority of the matter content of the universe not being described by the standard model, its existence has only been demonstrated through its gravitational interaction. It's interaction with the standard model is very weak, this is demonstrated by the lack of direct detection through collider experiments, see Ref. [40] for a recent update. For a recent review on the dark matter find Ref. [41].

A particularly interesting possibility for the research presented here, is dark matter models created by adding an additional strongly interacting sector to the standard model, see for

example Refs. [42–49]. This will generically contain new matter and gauge fields with different properties. The new gauge sector will be confining and it will contain composite particles that are stable on cosmological time scales. These will be the dark matter candidates. The models will contain a mechanisms that could lead to the observed dark matter distribution, for example strongly interacting massive particle (SIMP) models contain self-interactions that lead to a reduction in the number of particles, for example a $3 \to 2$ process, this leads to the dark sector decoupling from the standard model and a freeze out into a given distribution, see for example Ref. [50–57] and Refs. [58–64] for lattice studies of $Sp(4)$ SIMP dark matter models. The strongly interacting nature of the system, also makes direct interaction with these particles difficult, reducing the cross-section with standard model particles, explaining the lack of direct observation evidence.

Another popular extension to the standard model are composite Higgs models, in which the scalar Higgs particle is replaced with a composite particle in a new strongly interacting sector. These theories are created to resolve some naturalness problems with the measured value of the Higgs mass. For a review on these theories find Ref. [65].

The confining nature of strongly interacting theories are inherently non-perturbative. Therefore, the standard perturbative methods used for QED and electro-weak physics break down. To study these non-perturbative systems the only first principles method is to use lattice field theory, first introduced in Ref. [66]. In this method, the continuum Minkowski spacetime of the standard model is discretised onto a finite sized lattice in Euclidean spacetime. The lattice setup allows for the continuum theory to be approximated by a statistical mechanics system that can be analysed with numerical computer simulations. More details on lattice filed theory are given in Chap. 2.

In this work, we focus on analysing the finite temperature deconfinement phase transition in $Sp(4)$ pure gauge theory using numerical lattice methods. The context of this research is to analyse extensions to the standard model, for dark matter or composite Higgs, that have a first order deconfinement phase transition. Initially we are focusing on the pure gauge sector in isolation, without considering the effects of fermionic matter, to simplify the problem. This work is part of an extended research programme that aims is to compute the thermodynamic properties, like the latent heat and surface tension, of the first order deconfinement transition using lattice methods. The eventual goal of this work is to use the thermodynamic properties to analyse the possible gravitational wave background power-spectrums, and hopefully constrain new physics. The work presented here is also linked to a larger ongoing effort to study $Sp(N_c)$ gauge theories, Theoretical Exploration on the Lattice with Orthogonal and Symplectic groups (TELOS), see Refs. [67–84] and Ref. [85] for a comprehensive review on this project.

Although there is great interest and progress in the symplectic gauge theories at zero

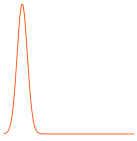

temperature from the lattice community, the literature on these systems at finite temperature is limited. The classic work on this subject, Ref. [86], demonstrated the first order nature of the deconfinement transition in $Sp(4)$ and $Sp(6)$ pure gauge theories. Prior to this paper, this subject was debated due to the Z_2 centre symmetry of $Sp(2N)$ gauge theories, making a second order transition in the Z_2 universality class a possibility for the transition from symmetry arguments. For similar reasons the deconfinement transition in a pure gauge theory based on the $G(2)$ exceptional group was studied. This system has a trivial centre symmetry, therefore there is no symmetry reason for a phase transition in this system. However, in Ref. [87–91] a first order phase transition was identified. This has lead to the conclusion that, rather than symmetry, the difference in degrees of freedom between the phases leads to its first order nature. The remaining literature on lattice studies of the finite temperature phase transition in $Sp(4)$ gauge theories are from a masters thesis Ref. [92], and upcoming work Ref. [93]. To this work we have added a proceedings, Ref. [94], an upcoming research paper, Ref. [2], and an upcoming proceedings, Ref. [95].

The best studied pure gauge system with a first order deconfinement transitions is $SU(3)$, see for example Refs. [96–104]. This is due to its relation to the heavy quark limit of QCD. Numerical studies on this transition began very soon after the lattice formalism itself was created, see Ref. [96]. Using modern state of the art methods, many of the thermodynamic properties of the transition have been determined for the continuum theory. Using anisotropic lattices Ref. [103] determined the latent heat in the continuum and verified that at the critical temperature the pressure gap, the pressure difference between the hot and cold phases, vanishes. The state of the art calculation is presented in Ref. [104], lattice simulations employing parallel tempering were used to determine the latent heat and the critical temperature.

For general $SU(N_c)$ gauge theories, many techniques for calculating the thermodynamic properties of the deconfinement phase transition are presented in Ref. [105]. The paper set out a method to compute the latent heat, and the interface tension, using numerical lattice methods. It then computed them for $SU(3)$, $SU(4)$, $SU(6)$ and $SU(8)$ and discussed the expected scaling with the number of colour charges N_c. It is expected that the strength of the transition grows as the number of colours increases, i.e. the surface tension and the latent heat increase with increasing N_c. For other work on deconfinement in $SU(N_c)$ pure gauge theories see Refs. [105–110]. An alternative non-perturbative technique for studying the behaviour of the deconfinement transition in $SU(N_c)$ gauge theories is through gauge gravity dualities and the large N_c limit, see for example Ref. [111]. There is also some work in lattice studies of $SU(4)$ gauge theory, with infinite mass quarks and very heavy quark theories, for stealth dark matter models, with the context of computing the expected gravitational wave power-spectrum, this is presented in Ref. [112].

A common technique for studying these transitions, in the context of BSM physics, is to build an effective theory using the lattice results as an input. Using Polyakov loop models, deconfinement has been studied in various $SU(N_c)$ gauge theories, with the aim of computing the thermodynamic quantities and study the expected gravitational wave spectrum. See for example Ref. [16], and an update containing fermionic matter Ref. [113]. Ref. [114] uses similar methods to analyse the transition in $Sp(N_c)$ pure gauge theories.

The meta-stable dynamics, that lead to the phenomenological implications that make these theories attractive for BSM physics, also lead to intractable problems when using standard importance sampling lattice methods. Importance sampling methods involve calculating expectation values by measuring observables from a set of configurations generated from the equilibrium distribution. It does this using a Markov chain, where each configuration is generated by considering a small change to the previous configuration in the chain, based on the probability of moving into the new configuration. To measure accurate results we must fully explore the equilibrium distribution, therefore, it must explore both phases, and all possible vacua. This is usually ensured a priori by checking the system has tunnelled between the phases a large number of times. For the system to move between phases it must move into the region with configurations with probabilities that are exponentially suppressed. As the volume of the lattice system increases, the potential barrier grows leading to an increased suppression of these intermediate configurations, making tunnelling between phases less likely. Therefore, as the volume grows an increasing number of configurations are required to ensure accurate results. This is the basis of the metastability problem.

There are many methods to resolve this issue. For example parallel tempering, also known as replica exchange see Ref. [115], used in Ref. [104], runs multiple lattices simultaneously with different temperatures, the temperature of the lattices are swapped between them allowing the lattice to move between the high and low temperature phases, and away from the critical region reducing the autocorrelation time. The multi-canonical approach, see Refs. [116–118], aims to solve the meta-stability problem by changing the probability distribution in the suppressed region of phase space, allowing the system to move between phases, the results are then reweighted to regain the canonical expectation values. Density of states methods are a general class of algorithms, see for example Refs. [119–121], that aim to alleviate the meta-stability problems by measuring observables with a flat energy distribution and reconstructing the density of states to compute observables. These methods will be discussed further in Chap. 3.

In this work we use the Logarithmic Linear Relaxation (LLR) method, introduced in Ref. [120]. This is a density of states method based on Wang-Landau method, see Ref. [119], but specialised to systems with continuous energy. It has been shown to be effective at mitigating the metastability problems in the bulk phase transition in $U(1)$ gauge theory,

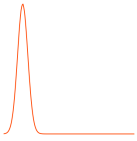

Ref. [122]. The method has also been used to study the bulk phase transition in $SU(N_c)$ gauge theories in the large N limit for dark matter models, with the aim of studying deconfinement and the possible generation of a gravitational wave background from these systems [123–125]. It has been applied to other problems in the lattice literature such the sign problem, for example see Ref. [126] and the thesis Ref. [127], and in the study of the freezing of topological charge, see Ref. [128]. A modification has been used to study the density of states for the Polyakov loop, the order parameter for the deconfinement phase transition, in $SU(3)$ pure gauge theory. The physical interpretation of the results in this case is of QCD with three heavy fermion flavours [129].

In this work, we set out a rigorous methodology for using the LLR method to study lattice systems in pure non-Abelian gauge theories. This methodology, presented previously in Ref. [1], was used in a detailed study of the deconfinement transition in $SU(3)$ pure gauge theory on a single lattice size, 4×20^3. In it we study the systematic errors associated with the LLR method. These results were also previously presented in the proceedings Ref. [130] and Ref. [131]. $SU(3)$ pure gauge theory was chosen for this study as a test bed for the algorithm and our methodology, due to the previously mentioned vast existing literature. Using the density of states, we were able to compute the critical coupling, various observables, such as the plaquette jump, and calculate thermodynamic potentials of the micro-states, such as the free-energy, demonstrating the first order nature of the system. This work is the basis for Chap. 4.

Using this methodology, we then studied the deconfinement transition in $Sp(4)$ pure gauge theory, focusing specifically on the thermodynamic limit for a lattice with $N_t = 4$. In this we again compute the critical coupling and the plaquette jump, and we also compute the surface tension for this lattice spacing. An initial exploration of lattices with reduced lattice spacing has been considered, with preliminary results presented for $N_t = 5$ and 6. This work is discussed in Chap. 5.

In the next chapter we introduce the basic concepts and numerical techniques of Lattice Field Theory. We also discuss the thermodynamics on the lattice and how we study the deconfinement phase transition in pure gauge theories. In Chap. 3, we focus on the density of states method, in particular the logarithmic linear relaxation method, and give full algorithmic details on the use for the deconfinement phase transition. In Chap. 4 and Chap. 5, we use these methods to analyse deconfinement in $SU(3)$ and $Sp(4)$ pure gauge theories, respectively. Finally, Chap. 6 summarises the results and discusses possible future work. Further technical detail on the analysis is given in the appendices.

Chapter 2

Lattice Field Theory

> "There's lots of gaps in this theory... get it, because it's a lattice."
> S. Pandey private correspondence

In this chapter we will introduce some of the background of non-Abelian gauge theories and how to study them using the lattice formalism. We will discuss thermodynamic details of the the finite temperature deconfinement phase transition in these lattice systems. The numerical methods used for simulating the system are discussed, and the inherent problems of simulating around first order phase transitions are introduced.

2.1 Continuum Yang-Mills theory

We want to study a quantum field theory invariant under the action of a local non-Abelian gauge symmetry, of group $\mathcal{G}$. We focus on the pure gauge sector of the theory, solely containing gauge fields $A_\mu(x)$, where $\mu = 0,1,2,3$ is the spacetime index, and x is the spacetime position. In this work we use Euclidean spacetime. The gauge fields are built of combination of components, $A_\mu(x) = A_\mu^{(a)}(x)T_a$, where we implicitly sum over the colour indices, for $SU(N)$ $a = 1,2,...,N_c^2-1$, where N_c^2-1 is the number of generators, T_a, of the gauge group. The generators obey the condition $[T_a, T_b] = if_{abc}T_c$, where f_{abc} are structure constants of the symmetry group. The theory is described by the Yang-Mills action,

$$S_{YM}(A) = \int d^4x \, \mathrm{Tr}\left(\frac{1}{2}F^{\mu\nu}(x)F_{\mu\nu}(x)\right), \tag{2.1.1}$$

$F_{\mu\nu}(x)$ is the field strength tensor, it is given by $F_{\mu\nu}(x) = \partial_\mu A_\nu(x) - \partial_\nu A_\mu(x) - i[A_\mu(x), A_\nu(x)]$.

The field strength tensor describes the dynamics of the gauge field, the equations of motion are given by $D_\mu F^{\mu\nu}(x) = \partial_\mu F^{\mu\nu}(x) - i[A_\mu(x), F^{\mu\nu}(x)] = 0$, and D_μ is the covariant derivative, the commutator term describes how the gauge field changes due to infinitesimal spacetime translations. To study how the field changes along a finite path, γ, we use the

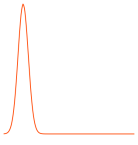

Wilson line,

$$W_L(x;y) = P\exp\left(i\int_\gamma ds^\mu A_\mu(s)\right), \tag{2.1.2}$$

where the operator P orders the gauge fields by the path γ, which starts at x and ends at y.

Under local gauge transformations, $\Omega(x) \in \mathcal{G}$, the gauge field, the field strength tensor and the Wilson line transform as

$$A_\mu(x) \to \Omega(x)A_\mu(x)\Omega^{-1}(x) + i\Omega(x)\partial_\mu\Omega^{-1}(x), \tag{2.1.3}$$

$$F_{\mu\nu}(x) \to \Omega(x)F_{\mu\nu}(x)\Omega^{-1}(x) \tag{2.1.4}$$

$$W_L(x;y) \to \Omega(x)W_L(x;y)\Omega^{-1}(y). \tag{2.1.5}$$

Physical observables in this theory must be gauge invariant, transform trivially under gauge transformations, therefore these are not observables of the theory. However, the trace of the field strength tensor, or the trace of any power of the field strength tensor, i.e. the Yang-Mills action, is gauge invariant. The trace over the colour indices of the Wilson loop is also gauge invariant, where the Wilson loop is a Wilson line over a closed loop, Γ, that starts and finishes at the same point, x, defined by,

$$W_o(x) = P\exp\left(i\oint_\Gamma ds^\mu A_\mu(s)\right). \tag{2.1.6}$$

In the next subsection we will show how the Yang-Mills action can be related to the sum of infinitesimal Wilson loops. In pure gauge theory observables are generally built from the trace of Wilson loops. The path is chosen such that its symmetries match the those of the physical state we wish to study.

To compare with real world experiments we calculate the vacuum expectation value (VEV). This can be computed through the path integral which integrates over all physical configurations using the Haar measure $\mathcal{D}A$. The VEV of an observable $O(A)$, for an inverse coupling β, $\langle O\rangle_\beta$, is given by,

$$\langle O\rangle_\beta = \frac{1}{Z(\beta)}\int \mathcal{D}A O(A)\exp(-\beta S_{YM}(A)). \tag{2.1.7}$$

The inverse coupling is given by , $\beta = 2N_c/g_0^2$, where g_0 is the bare coupling strength of the gluon field. We define the partition function of the system, $Z(\beta)$, as

$$Z(\beta) = \int \mathcal{D}A\exp(-\beta S_{YM}(A)). \tag{2.1.8}$$

The contribution of each contribution to the path integral is weighted by the action, states

with the minimal action contribute the most. The path integral will be discussed more concretely when we introduce the lattice formalism.

Since the inception of quantum chromodynamics and the study of non-Abelian gauge theories of this form, the peculiar behaviour of the beta function has caused technical problems with standard perturbative methods. To lowest order in perturbation theory the beta function for $SU(N)$ pure gauge theory is given by [132],

$$\mu \frac{dg}{d\mu} = -\frac{1}{(4\pi)^2}\left(\frac{11N}{3}\right) g^3 + \mathcal{O}(g^5), \tag{2.1.9}$$

where μ is the renormalisation scale, i.e. energy scales above this are filtered out. The negative sign in this expression leads to the coupling g, reducing as we increase the renormalisation scale. As μ approaches ∞, the coupling will vanish, therefore becoming a free theory and allowing perturbative methods to be used, this is asymptotic freedom. However, as we decrease the energy scale, the coupling grows, therefore in the infrared limit, the coupling becomes larger, leading to the breakdown of perturbative methods. In his seminal work, Ref. [66], Wilson introduced the lattice formulation to study confining properties of this theory. The next subsection will cover the background of this formulation.

2.2 Yang-Mills Theory on the Lattice

We rewrite our continuum theory as a lattice system in Euclidean spacetime. Spacetime is discretised onto a hypercubic lattice, with neighbouring sites separated by lattice spacing a. We denote the sites of the lattice by $n = (n_t, \vec{n}_s)$, where $n_t = 0, .., N_t - 1$ and $n_s = (n_1, n_2, n_3)$, $n_i = 0, .., N_s - 1$ for $i = 1, 2, 3$, are the temporal and spatial spatial labels respectively. The label n relates to the location in the continuum theory, x, through $x = an$. We denote the volume of the systems as $\tilde{V} = a^4(N_t \times N_s^3)$, for later convenience we define the spatial volume as $V = a^3 N_s^3$. We choose periodic boundary conditions in all directions.

Lattice discretisation explicitly breaks the $SO(4)$ symmetry of our continuum Euclidean spacetime down to the discrete subgroups of discrete translations by the lattice spacing, T_d, and the octahedral group O_h, of rotations about the lattice axes. These symmetries should be restored in the thermodynamic, $V \to \infty$, and continuum, $a \to 0$, limits. Lattice discretisation also corresponds to an ultraviolet cutoff, by cutting off the small distance and therefore high energy and momentum modes. As the continuous translation symmetry is broken, the momentum of the system is restricted to the Brillouin zone of the lattice, $|k| \leq \pi/a$. Lattice discretisation is therefore a regularisation scheme and must be renormalised, through the continuum limit, to compare with real world physics.

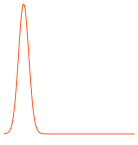

In the lattice formalism the theory is rewritten in terms of link variables, $U_\mu(n)$, the Wilson loop connecting the lattice site n, with the neighbouring site in the μ direction,

$$U_\mu(n) = \exp\left(i \int_{an}^{a(n+\hat{\mu})} dx^\mu A_\mu(x)\right), \tag{2.2.1}$$

where $\hat{\mu}$ labels the unitary link variable in the μ direction. The link variables are group valued, $U_\mu(n) \in \mathcal{G}$.

In our work we will focus on $SU(N)$ and $Sp(2N) = Sp(N_c)$ gauge theories, in particular $SU(3)$ and $Sp(4)$. We represent the link variables in $SU(N)$ gauge theory, $M = U_\mu(n) \in SU(N)$, as $N \times N$ matrices, obeying the conditions $M^\dagger M = \mathbb{1}$ and $\det(M) = 1$. We define $Sp(2N)$ as a subset of $SU(2N)$, $M \in Sp(2N) \subset SU(2N)$, obeying the additional condition $M^T \Omega M = \Omega$, where the symplectic matrix, Ω, is given by,

$$\Omega = \begin{pmatrix} 0 & \mathbb{1}_{N\times N} \\ -\mathbb{1}_{N\times N} & 0 \end{pmatrix}. \tag{2.2.2}$$

This condition restricts the group to the subset of $SU(2N)$ with the block structure,

$$M = \begin{pmatrix} A & B^* \\ -B & A^* \end{pmatrix}, \tag{2.2.3}$$

where A and B are $N \times N$ matrices, related through $A^\dagger A + B^\dagger B = \mathbb{1}$ and $A^T B = B^T A$.

Once again we build observables out of the trace of Wilson loops. On the lattice the Wilson loop is the ordered products of link variables in a path Γ,

$$W_o[U] = \prod_{(n,\mu)\in\Gamma} U_\mu(n). \tag{2.2.4}$$

The action of the system is built out of plaquettes, the trace of the Wilson loop around the elementary square on the lattice, $U_{\mu\nu}(n)$,

$$U_{\mu\nu}(n) = \frac{1}{N_c} Tr\left[U_\mu(n) U_\nu(n+\hat{\mu}) U_\mu^\dagger(n+\hat{\nu}) U_\nu^\dagger(n)\right], \tag{2.2.5}$$

in this expression we have used $U_\mu^\dagger(n) = U_{-\mu}(n+\hat{\mu})$. We denote the average plaquette of a configuration, $U = \{U_\mu(n), \forall n, \forall \mu\}$, by

$$u_p[U] = \frac{a^4}{6\tilde{V}} \sum_{n,\mu,\nu} \left(U_{\mu\nu}(n) + U_{\mu\nu}^\dagger(n)\right), \tag{2.2.6}$$

the factor of $a^4/6\tilde{V}$ in this expression comes from the number of plaquettes. In this work we use the Wilson action, defined as

$$S[U] = \sum_{n,\mu,\nu} \left(1 - \frac{1}{2N_c}\left(U_{\mu\nu}(n) + U^{\dagger}_{\mu\nu}(n)\right)\right) \tag{2.2.7}$$

$$= \frac{6\tilde{V}}{a^4}\left(1 - u_p\right). \tag{2.2.8}$$

In the limit of vanishing lattice spacing, $a \to 0$, the Yang-Mills action is recovered. For a small lattice spacing, the link variable, defined in Eq. 2.2.1, can be written as, $U_\mu(n = x/a) \approx \exp\left(iaA_\mu(x)\right)$. If we substitute this into the definition for the plaquette, we find,

$$U_{\mu\nu}(n = x/a) = \exp\left(\frac{ia^2 g}{2}F_{\mu\nu}(x) + \mathcal{O}(a^3)\right)) = 1 + \frac{ia^2 g}{2}F_{\mu\nu}(x) - \frac{g^2 a^4}{8}(F_{\mu\nu}(x))^2. \tag{2.2.9}$$

In the first equality we have used the Baker–Campbell–Hausdorff formula to combine the exponential and combined the gauge fields into field strength tensors. The second equality we have Taylor expanded the exponential. The sum over the link variables, multiplied by a volume factor a^4, becomes the integral over spacetime, $a^4 \sum_n \to \int dx$. Combining this with the expression for the plaquette it should be clear that if we take recover the Yang-Mills action from the Wilson action, up to a correction of order a.

We note other actions also recover the Yang-Mills action, and are created to improve convergence in the continuum limit. For example in Ref. [133] an improved gluon action containing terms with larger Wilson loops, such as rectangles, are included. In this work we focus on the unimproved Wilson action.

Now we have defined the action for the link variables, we can define the VEV of observables and the path integral. Taking the expression for the continuum path integral, Eq. 2.1.7, we replace the Haar measure for the gauge fields as the product of integrals over all links, $\mathcal{D}A \to \prod_{n,\mu} dU_\mu(n) = [DU]$, where the integral on each link is over all possible elements of the group. The VEV of an observable, $O[U]$, that depends on the configuration of the lattice, U, at inverse coupling β, is given by

$$\langle O \rangle_\beta = \frac{1}{Z(\beta)} \int \left(\prod_{n,\mu} dU_\mu(n)\right) O[U] \exp(-\beta S[U]). \tag{2.2.10}$$

Where $Z(\beta)$ is the partition function,

$$Z(\beta) = \int \left(\prod_{n,\mu} dU_\mu(n)\right) \exp(-\beta S[U]). \tag{2.2.11}$$

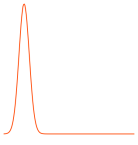

As the integral is now over a compact group element rather than the algebra, the integral is now over a finite space. This allows us to ignore the problem of gauge fixing and integrating over gauge redundancies in many cases as this will contribute the same factor to the top and bottom of the expression for the VEV, and thus will not affect the results.

For a statistical mechanics system with states $|n\rangle$, at temperature T, the partition function is given by

$$Z(T) = \sum_n e^{-\frac{E_n}{T}} = \sum_n \langle n|e^{-\frac{\hat{H}}{T}}|n\rangle, \tag{2.2.12}$$

where E_n is the energy of state and $\hat{H}$ is the corresponding Hamiltonian, $E_n|n\rangle = \hat{H}|n\rangle$. This is equivalent to the time evolution operator in Minkowski spacetime,

$$\langle n|e^{-i\hat{H}t}|m\rangle, \tag{2.2.13}$$

where $|n\rangle$ is the initial state and $|m\rangle$ is the final state, when we make the identification $t = -i\frac{1}{T}$. This is the imaginary time formalism, and leads to the Minkowski spacetime becoming Euclidean. We break the operator $\exp\left(-\hat{H}/T\right)$, into N_t parts, each of size $a_T = 1/N_t T$, and insert a complete set of states between each,

$$Z(T) = \sum_n \langle n|(e^{-\hat{H}a_T})^{N_t}|n\rangle = \sum_n \sum_{|n_1\rangle,..,|n_{N_t}\rangle} \langle n|e^{-\hat{H}a_T}|n_1\rangle\langle n_1|...e^{-\hat{H}a_T}|n_{N_t}\rangle\langle n_{N_t}|n\rangle, \tag{2.2.14}$$

if the states $|n\rangle$ are for our lattice system, this equation is equivalent to the path integral,

$$Z(T) = \int \left(\prod_{n,\mu} dU_\mu(n)\right) \exp\left(-\int_0^{N_t a_T} dt \int dx \mathcal{L}_E[U]\right), \tag{2.2.15}$$

where $\mathcal{L}_E[U]$ is the Lagrangian in Euclidean spacetime, with $\int_0^{N_t a_T} dt \int dx \mathcal{L}_E[U] = S[U]$. From the trace over the states, $\sum_n \langle n|...|n\rangle$, we have $\langle n_{N_t}|n\rangle$ and $\langle n|n_1\rangle$, this gives the requirement that the initial state is equal to the final state. For our lattice gauge system this leads to the requirement that we have periodic boundary conditions in the temporal direction $U_\mu(0, n_s) = U_\mu(N_t, n_s)$. In addition, when using the imaginary time formalism, the inverse temporal extent can be interpreted as the temperature of the lattice system, $T = 1/a_T N_t = 1/aN_t$. Using Euclidean spacetime, the action becomes real and allows us to the treat $e^{-\beta S[U]}$ as a Boltzmann weight, for the state U. As the inverse coupling, $\beta(a)$, depends through renormalisation on the energy scale and therefore the lattice spacing, to change the temperature on a fixed lattice size we will manually vary inverse coupling thus changing the temporal extent and the temperature of the system.

At finite temperature, the temporal extent is selected to be much smaller than the spatial extent, $N_t \ll N_s$. This differs from the case for zero temperature at which they are chosen

to be approximately the same size, $N_t \simeq N_s$. In both cases, at fixed lattice spacing the thermodynamic limit should be considered by taking $N_s \to \infty$ to account for errors due to finite spatial size, which will be related to the spatial extent aN_s. For zero temperature this implies that the N_t should also diverge along with N_s. However, for non-zero lattice spacing and finite temperature we require aN_t a remains fixed finite value, set the temperature of interest, therefore making N_t finite. In continuum limit $a \to 0$, there is also the requirement that the N_t also diverges, therefore keeping the temperature constant.

For pure gauge theory on a lattice with periodic boundary conditions in the temporal direction, the order parameter for deconfinement is the average Polyakov loop, l_p, the minimal Wilson loop wrapping the temporal direction,

$$l_p \equiv \frac{1}{N_s^3}\sum_{\vec{n}_s} l_p(\vec{n}_s), \quad l_p(\vec{n}_s) = \frac{1}{N_c}\mathrm{Tr}\left(\prod_{n_t=0}^{N_t-1} U_0(n_t,\vec{n}_s)\right), \tag{2.2.16}$$

where $l_p(\vec{n}_s)$ is the Polyakov loop for the spatial lattice site $\vec{n}_s$. The value of the Polyakov loop will depend on phase of the system, in the deconfined state this is non-zero, whereas for the confined state it vanishes. Across the phase transition the value of the Polyakov loop will vary with the temperature of the system.

Ref. [134] discussed the physical interpretation of the behaviour of the Polyakov loop, by demonstrating the link between correlation function between Polyakov loops and the free energy of a static quark anti-quark pair, $F_{q\bar{q}}(r)$. For two Polyakov loops, one at the origin and one at $\vec{n}_s = (0,0,n_3)$, a distance $r = an_3$ away, the correlation function between them relates to the free energy through,

$$e^{-\frac{F_{q\bar{q}}(r)}{T}} = \langle l_p^\dagger(\vec{n}_s) l_p(0)\rangle, \tag{2.2.17}$$

where T is the temperature of the system. Taking the limit of $r \to \infty$, we can relate the VEV of the Polyakov loop and the free energy of a static colour source, F_q,

$$\lim_{r\to\infty}\langle l_p^\dagger(\vec{n}_s) l_p(0)\rangle = |\langle l_p\rangle|^2 = e^{-\frac{2F_q}{T}}. \tag{2.2.18}$$

In the confined phase, we expect that free energy, F_q, will diverge, thus making the VEV of the Polyakov loop vanish. While in the deconfined state, it will have a finite value, reflecting the non-zero probability to observe a free quark.

This order parameter is related to the spontaneous breaking of the centre symmetry. The centre symmetry is a subgroup of the full gauge group, that commutes with all elements of the group, i.e. $U \in \mathcal{G}$, $zUz^\dagger = U$, where z is an element of the centre. For $SU(N)$ the centre symmetry is the cyclic group, $Z_N = \{e^{\frac{2\pi m}{N}i}, m = 0,...,N-1\}$, and for $Sp(2N)$ it is Z_2 for all N. The action and all topologically trivial observables of the lattice system are invariant under

a global transformations in the centre. However, as the Polyakov loop wraps the lattice, if it has an non-zero expectation value the centre symmetry can have a non-trivial affect on it, $l_p \to l'_p = z l_p \neq l_p$. Therefore in the deconfined state the Polyakov loop can have N (2) values, for $SU(N)$ ($Sp(2N)$) pure gauge theory, with $l_p = z|l_p|$.

On a finite lattice , we still expect that in the deconfined state the system will tunnel between the different degenerate vacua, that are equally spaced around the origin, making the VEV of the average Polyakov loop vanish $\langle l_p \rangle = 0$. In practise, to determine which phase the system is in, we will calculate the VEV of the absolute value of the average Polyakov loop, $\langle |l_p| \rangle_\beta$. Of course this will never be identically 0, however in the confined state it scales like $\mathcal{O}(1/\sqrt{V})$, therefore in the thermodynamic limit it is an good order parameter.

We can use the Polyakov loop to determine the phase of the system. Away from the phase transition, we expect that the VEV should be approximately flat. Around the phase transition, we expect the behaviour of the order parameter to depend on the order of the phase transition. For all $SU(N)$, and $Sp(2N)$ pure gauge theories, excluding the second order $SU(2) = Sp(2)$, the phase transition is first order. Therefore in the infinite volume limit, we expect there will be a discontinuity in the value Polyakov loop at the critical point, as it jumps from the finite value to 0. However, for finite volumes we expect a continuous change as the system can tunnel between the phases co-existing vacua. We characterise this change by the susceptibility of the Polyakov loop,

$$\chi_l(\beta) \equiv N_s^3 \left(\langle |l_p|^2 \rangle_\beta - \langle |l_p| \rangle_\beta^2 \right), \tag{2.2.19}$$

One definition for the critical point of the transition, $\beta_{CV}(\chi_l)$, for this lattice with volume V —as we will see there will be several definitions which should be equivalent in the thermodynamic limit— is the location of the peak of the of the susceptibility, $\chi_l(\beta_{CV}) = \chi_l^{max}$.

The behaviour of the VEV of the average plaquette has a similar behaviour around the phase transition. Away from the transition, the average plaquette will grow for increasing β, and shrink for $\beta \to 0$. For a system with finite volume, away from the critical region we expect the plaquette distribution, $P_\beta(u_p)$, to be approximately Gaussian [135],

$$P_\beta(u_p) = \sqrt{\frac{\tilde{V}\beta^2}{2\pi C}} \exp\left(-\frac{(u_p - u_{p0})^2 \beta^2 \tilde{V}}{2C} \right), \tag{2.2.20}$$

where C is related to the infinite volume specific heat, u_{p0} is the value of the plaquette at the peak of the distribution, which depends on the inverse coupling $u_{p0}(\beta)$. The exponent scales like $\tilde{V} = V/aN_t$, therefore making the amplitude of the Gaussian scale like, $P_\beta(u_p) \sim V^{\frac{1}{2}}$. In the thermodynamic limit, $V \to \infty$, this becomes a Dirac delta function.

In the critical region, in which we have co-existing solutions, and ignoring mixed phase

states, we can write the distribution approximately as a double Gaussian,

$$P_\beta(u_p) = A_\beta^{(c)} P_\beta(u_p^{(c)}) + A_\beta^{(d)} P_\beta(u_p^{(d)}), \tag{2.2.21}$$

where c and d denote contributions from the confined and deconfined states respectively, and $A_\beta^{(..)}$ controls the relative height of the two peaks. We define the critical point of the transition, for a spatial volume V, as $\beta_{CV}(P)$ the point at which both phases are equally likely. We approximate this as the point at which the heights of the peaks are equal, i.e. $A_{\beta_{CV}}^{(c)} P_{\beta_{CV}}(u_{p0}^{(c)}) = A_{\beta_{CV}}^{(d)} P_{\beta_{CV}}(u_{p0}^{(d)})$. We define the plaquette jump, $\Delta\langle u_p\rangle_{\beta_{CV}}$, as the plaquette difference between the two peaks.

On a finite sized lattice we can quantify the change in the plaquette by the specific heat,

$$C_V(\beta) \equiv \frac{6\tilde{V}}{a^4}\left(\langle u_p^2\rangle_\beta - \langle u_p\rangle_\beta^2\right), \tag{2.2.22}$$

this observable is related to the spread of the plaquette distribution. Again we can define the critical point of the transition as $\beta_{CV}(C_V)$, the inverse coupling corresponding to the peak of the specific heat for this lattice, $C_V(\beta_{CV}) = C_V^{(max)}$. We can compute the VEV of powers of the average plaquette using

$$\langle u_p^n\rangle = \int du_p P(u_p) u_p^n \tag{2.2.23}$$

as mentioned above, away from the phase transition in the thermodynamic limit the plaquette distribution becomes a Dirac delta, therefore the VEVs become $\langle u_p^n\rangle = u_{p0}^n$. At the critical point, which at finite volume we approximate the plaquette distribution as a double Gaussian with two peaks of equal height,

$$\lim_{V\to\infty} C_V^{(max)} = \frac{6\tilde{V}}{a^4}\left(\frac{(u_{p0}^{(d)})^2 + (u_{p0}^{(c)})^2}{2} - \frac{(u_{p0}^{(d)} + u_{p0}^{(c)})^2}{2}\right) = \frac{6\tilde{V}}{4a^4}(\Delta\langle u_p\rangle)^2, \tag{2.2.24}$$

this expression diverges in the thermodynamic limit with, $C_V^{(max)} \propto V$. By analysing the scaling of the peak of the specific heat we can determine the order of the transition. It will scale like $\propto (aN_s)^{\alpha/\nu}$, where α and ν are critical exponents. For second order transitions, α and ν will depend on the universality class of the transition, for first order transition it will be $\alpha/\nu = 3$, where 3 is the spatial dimension of the system. A more detailed calculation shows the first order corrections to $C_V^{(max)}/V$ are of order $1/V$ [136].

An important observable for determining the order of a phase transition is the Binder cumulant,

$$B_V(\beta) \equiv 1 - \frac{\langle u_p^4\rangle_\beta}{3\langle u_p^2\rangle_\beta^2}. \tag{2.2.25}$$

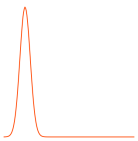

Away from the phase transition, when the system has a single vacua, it has a value of 2/3, in the thermodynamic limit. In first order transitions, where we can have mixed phase states with an interface, there will be a dip around the critical point, $B_V(\beta_{CV}) = B_V^{(min)} \neq 2/3$. Determining the location of the dip gives us an additional definition for the critical point, $\beta_{CV}(B_V)$. In second order transitions and cross-overs, we expect that in the thermodynamic limit the dip should disappear and $B_V(\beta_{CV}) \to 2/3$ for $V \to \infty$ [135].

All the definitions for the critical inverse coupling, β_{CV}, that we have discussed above, from the peak of the specific heat and Polyakov loop susceptibility, the minima of the Binder cumulant and the inverse coupling at which the two peaks of the plaquette distribution are of equal height, should coincide in the infinite volume limit, β_C. At finite spatial volume, the leading order correction of the definitions of the critical coupling are of order $\mathcal{O}(1/V)$. The form of these corrections will differ and therefore we expect these definitions will differ for a finite lattice [107, 135].

From the partition function we can define the internal energy of the lattice system, ϵ, and the pressure, p, using,

$$\epsilon = -\frac{1}{V}\frac{\partial \ln Z}{\partial T^{-1}}\bigg|_V, \quad p = -T\frac{\partial \ln Z}{\partial V}\bigg|_T. \tag{2.2.26}$$

Note that for the calculation of the these quantities we need to keep either the spatial volume, V, or the temperature, T, fixed. When we alter the temperature through the inverse coupling, $\beta(a)$, by indirectly changing the lattice spacing, the spatial volume will also change as, $V = (aN_s)^3$. A full analysis of these quantities generally involve the use of an anisotropic lattice, a lattice with different spatial and temporal lattice spacings, and the calculation of the Karch coefficients [137]. However, in this work we will assume that at the critical point, at which most of our analysis will be conducted, the pressure gap vanishes which is justified for $SU(3)$ in Ref. [103], proof for $Sp(4)$ is beyond the scope of this work.

Following Ref. [105], we rewrite the derivative of the temperature, $T = 1/aN_t$, in terms of the inverse coupling, $\beta(a)$,

$$\epsilon = \frac{T^2}{V}\frac{\partial\beta}{\partial T}\frac{\partial}{\partial\beta}\ln Z = \frac{T^2}{V}\left(-N_t a^2\frac{\partial\beta}{\partial a}\right)\left(6N_s^3N_t\left(1-\langle u_p\rangle_\beta\right)\right) = -6\frac{\left(1-\langle u_p\rangle_\beta\right)}{a^4}a\frac{\partial\beta}{\partial a}. \tag{2.2.27}$$

Thus the energy difference between the two phases at the critical point, the latent heat, in units of the critical temperature, T_c, is given by,

$$\frac{L_h}{T_c^4} \equiv \frac{\Delta\epsilon}{T_c^4} = -\left(N_t^4 a\frac{\partial\beta}{\partial a}6\Delta\langle u_p\rangle_\beta\right)_{\beta=\beta_C}. \tag{2.2.28}$$

In later chapters, we will discuss how to compute $\Delta\langle u_p\rangle_\beta$ using numerical simulations. To the calculate the beta function of the inverse coupling, $a\frac{\partial\beta}{\partial a}$, we write the derivative in terms of a quantity, μ, with physical units, $a\frac{\partial\beta}{\partial a} \to a\mu\frac{\partial\beta}{\partial a\mu}$. For pure gauge theory, μ will usually be chosen as the critical temperature, $T_c = 1/N_t a(\beta_C)$, or the square root of the string tension, $\sqrt{\sigma}$.

For large volumes the double Gaussian approximation we made above breaks down. In the meta-stable region between the two Gaussian there will be a flat region due to the presence of an interface. When the system tunnels between phases, it will move through an intermediary mixed phase state. Both phases will be present and separated by two interfaces, the minimal cross-section for each interfaces is $A = V^{\frac{2}{3}}$. Having the interface increases the energy of the system by a term $\propto \sigma_{cd}A$, where σ_{cd} is the surface tension of the interface, which is determined by the thermodynamic properties of the transition. To create an interface, the increase in energy due to the creation of the interface, $\propto V^{\frac{2}{3}}$, must be balanced by the reduction in energy from the latent heat,$\propto V$. The free energy of these interface states, will be higher than the pure phase states and thus they will be unstable. Therefore, one of the regions will grow until we return to a pure phase state. If this phase is different from our initial phase, the system has transitioned from one phase to the other.

If we assume the volume is large enough that at the critical point, the region between the two peaks contains only mixed phase configurations, we can relate the probability of tunneling through the potential barrier to the probability of being in the central region. Following Ref. [105], the probability of tunneling between phases, is related to the surface tension through,

$$P_t \propto \exp\left(-\frac{2\sigma_{cd}A}{T_c}\right) = \exp\left(-2a^3\sigma_{cd}N_s^2N_t\right), \tag{2.2.29}$$

as the area of the interface grows the probability of tunneling between phases decreases. This will lead to problems with our standard importance sampling methods, as will be discussed in the next section. This expression can be used to compute the interface tension from the equilibrium plaquette distribution. At the critical point, when the two Gaussian have an equal height, P_{max}, and assuming the central minima of the distribution, P_{min}, is due to the interface states, we have

$$\frac{P_{min}}{P_{max}} \propto \frac{N_s^2}{N_s^{\frac{3}{2}}}\exp\left(-2a^3\sigma_{cd}N_s^2N_t\right) = N_s^{\frac{1}{2}}\exp\left(-2a^3\sigma_{cd}N_s^2N_t\right) \tag{2.2.30}$$

the factor of N_s^2, comes from the translation of both interfaces and $N_s^{\frac{3}{2}}$ comes from the scaling of the plaquette distribution. As we have defined this at the critical temperature, T_c, we can

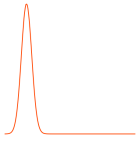

rewrite this as ,

$$\frac{P_{min}}{P_{max}} \propto N_s^{\frac{1}{2}} \exp\left(-2\frac{N_s^2}{N_t^2}\frac{\sigma_{cd}}{T_c^3}\right) = N_s^{\frac{1}{2}} \exp\left(-2\frac{N_s^2}{N_t^2}\hat{\sigma}_{cd}\right) \tag{2.2.31}$$

where we have defined the dimensionless surface tension , $\hat{\sigma}_{cd} = \sigma_{cd}/T_c^3$.

As we have used the critical temperature to set the scale, the surface tension calculated from this can be used to compare to the physics of the real world. The interface tension has units of a^{-3}, using the critical temperature T_c to set the scale, rather than calculating the interface tension directly we calculate the dimensionless tension.

Rearranging Eq. 2.2.31, gives,

$$\hat{\sigma}_{cd} = \frac{N_t^2}{2N_s^2}\ln\left(\frac{P_{min}}{P_{max}}\right) + \frac{N_t^2}{2N_s^2}\left(\frac{1}{2}\ln(N_s) + c\right) = \hat{I} + \frac{N_t^2}{2N_s^2}c \tag{2.2.32}$$

where c is a constant term and $\hat{I}$ has been defined such that in the limit of $\frac{N_t}{N_s} \to 0$, $\hat{\sigma}_{cd}$ becomes $\hat{I}$. Therefore, we can calculate $\hat{\sigma}_{cd}$ by calculating P_{min} and P_{max} from the plaquette distribution at the critical point, computing $\hat{I}$ and taking the thermodynamic at fixed N_t.

2.3 Numerical methods

Direct analytic computation of the path integral is not generally feasible. Instead, numerical methods, based on importance sampling techniques, are used to generate a representative set of configurations, $\{U_m\}_{m=1}^{N_{\text{cnfg}}}$, such that the mean value of an observable, $O[U_m]$, measured on these configurations corresponds to the VEV,

$$\langle O\rangle_\beta = \frac{1}{N_{\text{cnfg}}}\sum_{m=1}^{N_{\text{cnfg}}} O[U_m]. \tag{2.3.1}$$

If we are able to directly sample, and generate configurations, from the equilibrium distribution of the physical system,

$$dP[U] = \frac{1}{Z(\beta)}D[U]e^{-\beta S[U]}, \tag{2.3.2}$$

the error on the VEV decreases with the number of configurations, and is of order $\mathcal{O}(1/\sqrt{N_{\text{cnfg}}})$. The result is therefore iterably improvable, and becomes exact in the limit of infinite number of configurations, $N_{\text{cnfg}} \to \infty$.

To approximate this distribution Monte Carlo Markov chain (MCMC) methods are used. In this method a chain of configurations is generated, with each configuration only depending on the previous configuration, i.e. $U_1 \to U_2 \to U_3 \to ... \to U_{N_{\text{cnfg}}}$. We refer to the number

of configurations after the initial configuration as the simulation time. The transition probability to move one configuration (U_{m-1}) to the next (U_m), $P(U_m|U_{m-1})$, is chosen such that the distribution of configurations about the fixed point of the chain corresponds to Eq. 2.3.2. To ensure that any configuration can be reached, the transition probability obeys the strong ergodicity condition, $P(U_m|U_{m-1}) > 0$.

The transition probability obeys the detailed balance condition: the probability of being in state U_m, $P(U_m)$, and moving to state U_{m-1}, is the same as the probability of being in state U_{m-1} and moving to U_m, $P(U_m|U_{m-1})P(U_{m-1}) = P(U_{m-1}|U_m)P(U_m)$. This ensures that the fixed point of the Markov chain is unique.

Although the physical distribution is a fixed point of the Markov chain, the initial configuration, U_1, will usually be chosen randomly and hence will be unphysical. To ensure that our results are based on system's equilibrium distribution and not a product of our choice of arbitrary initial configuration we must thermalise the system. Before taking measurements we generate configurations until we reach the equilibrium distribution. Generally, it is not known a priori how many configurations are required to thermalise, but it can be checked by monitoring the energy against the simulation time. The energy will initially drift until it begins to oscillate around the physical point.

Although the continuum action is local, on the lattice, the action depends on the neighbouring links. Any link $U_\mu(n)$, contributes to 6 plaquettes. We define staple, $U_\sqcup$, as the combination of plaquettes that the link $U_\mu(n)$ contributes to, with the link $U_\mu(n)$ removed,

$$U_\sqcup = \sum_{\mu \neq \nu} \left(U_\nu(n+\hat{\mu}) U_\mu^\dagger(n+\hat{\nu}) U_\nu^\dagger(n) - U_\nu(n+\hat{\mu}) U_\mu^\dagger(n+\hat{\nu}) U_\nu^\dagger(n) \right). \tag{2.3.3}$$

From this we can calculate any links contribution to the action by,

$$S[U_\mu(n)] = -\frac{1}{N_c} \mathrm{Re}\left[\mathrm{Tr}\left(U_\mu \, U_\sqcup \right) \right]. \tag{2.3.4}$$

Therefore if we update the links individually according to,

$$dP(U_\mu) = dU_\mu \exp\left\{ -\frac{\beta}{N_c} \mathrm{Re}\left[\mathrm{Tr}\left(U_\mu \, U_\sqcup \right) \right] \right\}, \tag{2.3.5}$$

the generated configurations, when all links have been updated, and thermalised will obey the distribution in Eq. 2.3.2.

A classic example of an algorithm of this form is the Metropolis Monte Carlo Markov chain. In this case, we propose a change to each link of the lattice in turn, $U_\mu(n) \to U'_\mu(n)$. Changing the link will change the action, $S \to S' = S + \Delta S$. We will accept the change in the link with a probability $P_{U_\mu \to U'_\mu} = \min(1, \exp(-\beta(\Delta S)))$. If the change reduces the action,

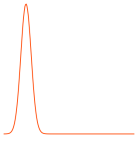

the new link will always be accepted. If the action is increased, we accept with the given probability. If the new link is not accepted, the link is reverted to $U_\mu(n)$. This is repeated on all links on the lattice, once changes on all links have been considered we have a new configuration. An improved algorithm which selects the new links more efficiently is discussed in the next section.

Generically, configurations generated using this MCMC methods will not be completely independent of each other, they will be correlated with prior configurations. The systematic error on the VEV, $\mathcal{O}(1/\sqrt{N_{\text{cnfg}}})$, requires completely independent configurations. The autocorrelation time τ, is the simulation time between independent configurations. The systematic error on the VEV is now $\mathcal{O}(\sqrt{\tau/N_{\text{cnfg}}})$. For an observable, $O[U]$, τ can be systematically estimated from the observables measured on the Markov chain,

$$\tau \approx \tau_{\text{int}} = \frac{1}{2} + \sum_{t=1}^{\infty} \frac{C(t)}{C(0)} \tag{2.3.6}$$

where $C(t)$ is the correlation function for the observable for configurations separated by a simulation time of t,

$$C(t) = \frac{1}{2(N_{\text{cnfg}} - t)} \sum_{m=1}^{N_{\text{cnfg}}-t} (O[U_m] - O[U_{m+t}])^2. \tag{2.3.7}$$

The sum in Eq. 2.3.6, will be truncated at some multiple of τ_{int}. The measurements of the observables are then put into sequential blocks of size $L > \tau_{\text{int}}$, the average of the observable is then calculated in each block. The error on the VEV is then estimated by calculating the error on the mean of the averages for these blocks.

To estimate the errors we use bootstrapping. We take our N_{samples} independent samples , i.e. for correlated data this is the mean of the blocks, and randomly select N_{samples} samples, not avoiding repeats, and calculate the average. This is repeated until we have a large number of random samples and we can approximate the results by Gaussian statistics. The standard error on the resampled data estimates the standard error on the mean of the original data set.

Around phase transition the autocorrelation time will increase and therefore more configurations are required to get independent measurements. For second order phase transitions this is particularly a problem due to the diverging correlation length, this is the critical slowing down problem.

Around first order transitions the meta-stable dynamics can lead to the obtained distribution of the Markov chain misrepresenting the physical distribution. To move from one phase to the other, the Markov chain will have to move through the region of phase space

that is exponentially suppressed, with an increased suppression as the volume grows. In addition the region between the peaks also scales with the volume. This can lead to the Markov chain getting stuck in one phase and not accurately representing the full phase space of the system. To ensure accurate results, the Markov chain must tunnel between the phases a sufficient number of times such that there is a representative number of configurations in each phase. Therefore, it can be difficult a priori to know how many configurations are required. This problem becomes intractable in the thermodynamic limit. This is the meta-stability problem, that is the basis for the methods discussed in the next chapter.

2.3.1 Heat bath

For $SU(2)$ gauge theory, Creutz in Ref. [138], proposed a more efficient method to sample the distribution in Eq. 2.3.5. Instead of randomly selecting a link variable and accepting it based on the distribution, as in the Metropolis method, the link variable is directly chosen according to the distribution. This can be done due to a special property of $SU(2)$, the sum of elements of $SU(2)$ is proportional to an element of $SU(2)$, i.e. if $A, B \in SU(2)$ then $A + B \propto C \in SU(2)$. Therefore the staple, introduced in Eq. 2.3.3, is proportional to an element of $SU(2)$, $U_{\sqcup}/k \in SU(2)$ with $k = \sqrt{\det[U_{\sqcup}]}$.

The term in the trace of Eq. 2.3.5, is now proportional to a group element. This allows us to rewrite the term in the exponent in terms of a single variable, $\tilde{U} = U_\mu U_{\sqcup}/k \in SU(2)$. We can also trivially rewrite the Haar measure in terms of this new variable, $dU_\mu \to d\tilde{U}$. Therefore, we can rewrite the distribution as

$$dP(\tilde{U}) = d\tilde{U} \exp\left\{-\frac{\beta k}{2}\mathrm{Re}\left[\mathrm{Tr}\left(\tilde{U}\right)\right]\right\} \tag{2.3.8}$$

which, for fixed β, only has dependence on one variable, $\tilde{U}$.

The new variable can be expressed in terms of the generators of the group, the Pauli matrices, σ_i, and a set of real numbers, u_μ, $\bar{U} = u_0 \mathbb{1} + \sum_{i=1}^{3} u_i \sigma_i$. This simplifies the trace to $\mathrm{Re}\left[\mathrm{Tr}\left(\bar{U}\right)\right] = 2u_0$, allowing the exponent to be written solely in terms of u_0. The condition $\det[\bar{U}] = 1$, causes the u_μ to lie on a 4-sphere with radius 1, i.e. $u_0^2 + |\mathbf{u}|^2 = u_0^2 + u_1^2 + u_2^2 + u_3^2 = 1$. We can rewrite the distribution as,

$$dP(\tilde{U}) = \frac{1}{2\pi^2} d^4u \delta(u_0^2 + |\mathbf{u}|^2 - 1) \exp\left\{-\beta k u_0\right\} , \tag{2.3.9}$$

decomposing the measure in terms of the u_0, the $|\mathbf{u}|$ and the solid angle $d^2\Omega$, and using a

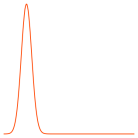

standard property of the Dirac delta we can write this as,

$$dP(\tilde{U}) = \frac{1}{2\pi^2} du_0 d|\mathbf{u}| d^2\Omega \frac{|\mathbf{u}|^2}{2\sqrt{1-u_0^2}} \exp\{-\beta k u_0\} \left(\delta(|\mathbf{u}| - \sqrt{1-u_0^2}) + \delta(|\mathbf{u}| + \sqrt{1-u_0^2})\right). \tag{2.3.10}$$

Integrating over $|\mathbf{u}|$ and the solid angle $d^2\Omega$, gives an expression in solely in terms of u_0,

$$d\tilde{P}(u_0) \sim du_0 \sqrt{1-u_0^2} \exp\left\{\beta\, k\, u_0\right\}. \tag{2.3.11}$$

The goal of sampling a random element of $SU(2)$ according to the distribution in Eq. 2.3.5, has now been simplified to sampling u_0 according to Eq. 2.3.11 and (u_1, u_2, u_3), to lie randomly on a sphere of radius $|\mathbf{u}| = \sqrt{1-u_0^2}$. To sample u_0, we select a random variable ξ uniformly between $\xi = 0$ and $\xi = 1$. From this we define u_0 to be,

$$u_0 = \frac{1}{\beta k} \ln\left(e^{-\beta k} + \xi(e^{\beta k} - e^{-\beta k})\right). \tag{2.3.12}$$

This will sample u_0 according to the correct exponent with the correct range for u_0, i.e. $\xi = 0$ ($\xi = 1$) gives $u_0 = -1$ ($u_0 = 1$). An accept reject step is added to enforce the $\sqrt{1-u_0^2}$ factor.

Once we have found $\bar{U}$, we can find our new link variable by $U_\mu(n) \to U'_\mu(n) = \bar{U}_\sqcup^{-1}$. This method will efficiently update the links of an $SU(2)$ pure gauge theory.

2.3.2 Over-relaxation

Another method to update the link variables in $SU(2)$ is given by the over-relaxation method, which was again proposed by Creutz in Ref. [139]. This method doesn't update the link variable according to the canonical distribution, but updates it micro-canonically, i.e. it leaves the action unchanged. Therefore this cannot be used in isolation, and should be used in combination with the heat-bath method, but it is very quick and can help to decorrelate the configurations.

The each link is updated according to $U_\mu(n) \to U'_\mu(n) = U_\sqcup^\dagger U_\mu^\dagger(n) U_\sqcup^\dagger / k^2$. By substituting this into the expression for the change in the action due to one link variable, Eq. 2.3.4, we can see that the action is unchanged,

$$\begin{aligned} S[U'_\mu(n)] &= -\frac{1}{2}\mathrm{Re}\left[\mathrm{Tr}\left(\frac{1}{k^2} U_\sqcup^\dagger U_\mu^\dagger(n) U_\sqcup^\dagger\, U_\sqcup\right)\right] && (2.3.13)\\ &= -\frac{1}{2}\mathrm{Re}\left[\mathrm{Tr}\left(U_\sqcup^\dagger\, U_\mu^\dagger(n)\right)\right] && (2.3.14)\\ &= S[U_\mu(n)], && (2.3.15) \end{aligned}$$

where in the second line we used $U_\sqcup^\dagger U_\sqcup = k^2$.

2.3.3 Cabibbo-Marinari method

These two methods of updating $SU(2)$ pure gauge theory were extended to general $SU(N)$ gauge theories by Cabibbo and Marinari in Ref. [140]. They proposed rather than directly updating the $SU(N)$ links, we should update the links by a set of $SU(2)$ subgroups of $SU(N)$. We select a set of $SU(2)$ subgroups embedded in $SU(N)$, $\{A_k \in SU(2), k = 1, ..., m\}$. We update each subgroup, A_k, of the link variables, through the heat-bath or over-relaxation method. The links are then fully updated by $U_\mu(n) \in SU(N) \rightarrow U'_\mu(n) = (\prod_{k=1}^{m} A_k)U_\mu(n) \in SU(N)$. We must ensure that we have selected the set of $SU(2)$ subgroups, such that no $SU(N)$, or $Sp(2N)$ group is left invariant under this transformation.

For $SU(3)$, we can use 3 $SU(2)$ subgroups, $A, B, C \in SU(3)$,

$$A = \begin{pmatrix} a_{11} & a_{12} & 0 \\ -a_{12}^* & a_{11}^* & 0 \\ 0 & 0 & 1 \end{pmatrix}, \quad B = \begin{pmatrix} b_{11} & 0 & b_{12} \\ 0 & 1 & 0 \\ -b_{12}^* & 0 & b_{11}^* \end{pmatrix}, \quad C = \begin{pmatrix} 1 & 0 & 0 \\ 0 & c_{11} & c_{12} \\ 0 & -c_{12}^* & c_{11}^* \end{pmatrix}, \tag{2.3.16}$$

where,

$$\begin{pmatrix} a_{11} & a_{12} \\ -a_{12}^* & a_{11}^* \end{pmatrix}, \begin{pmatrix} b_{11} & b_{12} \\ -b_{12}^* & b_{11}^* \end{pmatrix}, \begin{pmatrix} c_{11} & c_{12} \\ -c_{12}^* & c_{11}^* \end{pmatrix} \in SU(2). \tag{2.3.17}$$

We then select the new link according to $U'_\mu(n) \rightarrow ABCU_\mu(n)$.

This method was specialised in Ref. [72], to $Sp(2N)$ gauge theories. Now the embeddings are chosen to ensure that the block structure, Eq. 2.2.3, is enforced. We can break the embeddings down into 3 different categories, which will affect the action of the system in different ways. This difference between embedding will therefore change the exponent in the distribution in Eq. 2.3.11, to $\exp(-z\beta k u_0)$, and thus Eq. 2.3.12 becomes,

$$u_0 = \frac{1}{\beta k} \ln\left(e^{-z\beta k} + \xi(e^{z\beta k} - e^{-z\beta k})\right). \tag{2.3.18}$$

where the term z will depend on the trace of the embedding. For $Sp(4)$, we have

$$\begin{pmatrix} a & b & 0 & 0 \\ -b^* & a^* & 0 & 0 \\ 0 & 0 & a^* & b^* \\ 0 & 0 & -b & a \end{pmatrix}, \tag{2.3.19}$$

the trace, and therefore the effect on the action, of this subgroup is given by $4\mathrm{Re}(a)$, thus

$z = 2$. We also have the subgroup of the form,

$$\begin{pmatrix} a & 0 & 0 & b \\ 0 & -a^* & -b^* & 0 \\ 0 & -b^* & a^* & 0 \\ b & 0 & 0 & -a \end{pmatrix}, \tag{2.3.20}$$

which has a vanishing trace, and $z = 0$. Finally, the subgroups of the form,

$$\begin{pmatrix} a & 0 & b & 0 \\ 0 & 1 & 0 & 0 \\ -b^* & 0 & a^* & 0 \\ 0 & 0 & 0 & 1 \end{pmatrix}, \quad \begin{pmatrix} 1 & 0 & 0 & 0 \\ 0 & a & 0 & b \\ 0 & 0 & 1 & 0 \\ 0 & -b^* & 0 & a* \end{pmatrix} \tag{2.3.21}$$

has a trace of $2\mathrm{Re}(a)$, with $z = 1$.

Chapter 3

The density of states method

"I'm George. George McFly. I'm your density."
George McFly. Back to the Future (1985)

In the previous section we introduced how importance sampling, in particular MCMC, can be used to probe the properties of a system through the canonical ensemble. However, as mentioned ergodicity problems and critical slowing down around first order phase transitions can lead to intractable problems, and large systematic errors. In this section, we discuss a method to analyse the system through micro-canonical ensemble by the computation of the density of states, $\rho(E)$. This quantity will not only allow for the computation of expectation values, but it also gives access to additional quantities exponentially difficult to compute through importance sampling, such as the free energy and the partition function. We initially discuss several methods to solve the metastability problem, by sampling a flat energy distribution, before moving onto discuss the LLR algorithm, which is the primary technique used in this work. Much of this section is devoted to an in depth description of the LLR method, we discuss the background and analysis techniques, as well as the computational details for the simulations. Many of the algorithmic details of the LLR algorithm initially appeared in the Ref. [122], while details on our specific formulation were presented in Ref. [1].

3.0.1 The density of states

We define the density of states as

$$\rho(E) \equiv \int [DU]\delta(S[U] - E) \,, \tag{3.0.1}$$

heuristically this counts the number of configurations with the action, $S[U]$, equal to a given energy (value of the action), E. For very high energies, high temperatures, we expect this quantity to be very large number of disordered configurations, while at zero temperature

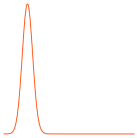

we expect there to be small number of configurations corresponding to the number of degenerate ground state energy. Between the high and low energy regimes, $\rho(E)$ is a continuous monotonically increasing function. This is a good assumption for a physically relevant range.

From the density of states we can calculate the probability for the system to be in any micro-state at inverse coupling β, and thus reconstruct the canonical ensembles plaquette distribution,

$$P_\beta(u_p) = \frac{1}{Z(\beta)}\rho(E)e^{-\beta E}\Big|_{E=(1-u_p)6\tilde{V}/a^4} = P_\beta(E = (1-u_p)6\tilde{V}/a^4). \tag{3.0.2}$$

This distribution can be used directly to analyse the thermodynamic properties of the system, and calculate observables such as the latent heat and surface tension. It can be used to calculate the Boltzmann weight of a micro-state, and therefore the contribution to the path integral. In this way, we can compute the VEV of an observable by sampling configurations with a flat energy distribution, therefore ensuring the Markov Chain cannot become stuck in one meta-stable vacua.

For an observable with explicit dependence on the energy, $O(E)$, the path integral over all possible configurations can be replaced with a one-dimensional integral over the energy of the system,

$$\langle O\rangle_\beta = \frac{1}{Z(\beta)}\int dE\rho(E)O(E)e^{-\beta E} = \int dE P_\beta(E)O(E), \tag{3.0.3}$$

where the partition function, $Z(\beta)$, is given by

$$Z(\beta) = \int dE\rho(E)e^{-\beta E}\,. \tag{3.0.4}$$

Both integrals run between 0 and $6\tilde{V}/a^4$.

From the plaquette distribution we also define an effective potential for the system as,

$$W_\beta(u_p) = -\ln\big(\langle\delta(S[U]-E)\rangle_\beta\big)\Big|_{E=(1-u_p)6\tilde{V}/a^4} = -\ln P_\beta(u_p). \tag{3.0.5}$$

Around first order transitions, we expect the effective potential will contain two minimas, one for each phase, corresponding to two peaks of the plaquette distribution.

3.0.2 Multicanonical method

The multicanonical method, see Refs. [116–118], is a method created to solve the metastability problem, by sampling an energy distribution with a flat distribution between the peaks. At the critical coupling, a cartoon of the desired distribution at the critical point can be seen

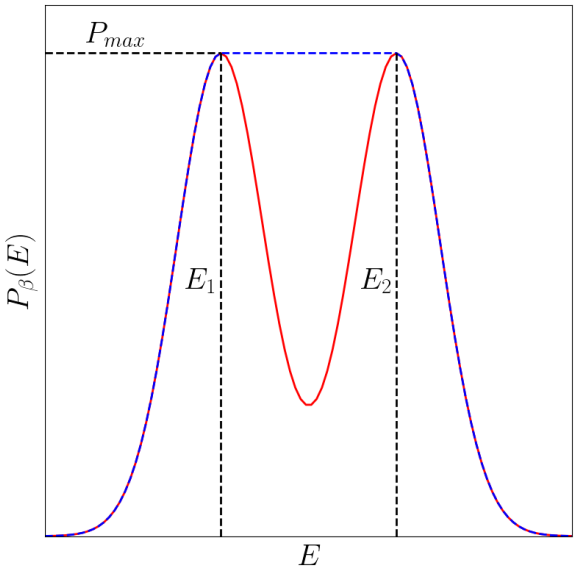

Figure 3.1. The desired energy distribution for the multicanonical method shown by the blue dashed line. The physical energy distribution at the critical coupling, $P_{\beta_{CV}}(E)$, is shown in red. The vertical dashed lines show the locations of the two peaks, E_1 and E_2, while the horizontal dashed black line shows the peak of the distribution of the peak.

in Fig. 3.1. The solid red line is the physical distribution of the system, however to sample the full distribution it will need to cross through the exponentially suppressed region of phase space. In this method, the goal is to sample the distribution shown by the blue dashed line. The desired distribution is given by,

$$P_\beta^{(MC)}(E) \propto \begin{cases} P_\beta(E) & E < E_1 \text{ or } E > E_2, \\ P_{max} & E_1 < E < E_2, \end{cases} \quad . \tag{3.0.6}$$

where E_1 and E_2, are the locations of the peaks of the distribution. The normalisation will ensure when integral over the full energy range is unity.

How do we sample this distribution using importance sampling methods? For the canonical ensemble, configurations are sampled according to the distribution $\propto e^{-\beta E}$, where $E = S[U]$. This distribution is changed by adding a weight function to it, $P_\beta^{(MC)}(E) \propto e^{-\beta E + W(E)}$. For $E < E_1$ and $E > E_2$, $W(E)$ will vanish. Between the peaks, to flatten the distribution we want $W(E) = -\ln\big(P_\beta(E)\big)$, where $P_\beta(E)$ is the canonical distribution. The canonical distribution in $W(E)$ will be approximated.

$P_\beta(E)$ can be approximated by the histogram of the measured energy values for a smaller lattice, in which the meta-stability problem is not an issue. The distribution will then be rescaled appropriately with the volume. Using the double Gaussian approximation, we can

approximate the scaling of the central region with the volume. This estimate for $P_\beta(E)$ is then used for $W(E)$, if the tunnelling is still suppressed an improved estimate is made. This is iterated until we have the desired energy distribution. The distribution does not have to be exactly what is shown in Fig. 3.1, the requirement is that it tunnels between the phases, and fully samples the full phase space.

Once we have our weight function, we can sample configurations according our new energy distribution $P_\beta^{(MC)}(E)$. However, we still need to convert this back into results relevant to original problem, i.e. we need to regain the canonical ensemble. This is can be done simply using the equation, $P_\beta(E) \propto P_\beta^{(MC)}(E)e^{-W(E)}$. Expectation values are then computed by reweighting the result.

For an observable with explicit dependence on the energy, we can rewrite the expectation value in Eq. 3.0.3 as,

$$\langle O\rangle_\beta = \int dE P_\beta^{(MC)}(E)O(E)\frac{P_\beta(E)}{P_\beta^{(MC)}(E)} \propto \int dE P_\beta^{(MC)}(E)O(E)e^{-W(E)}. \tag{3.0.7}$$

we can rewrite this as ,

$$\langle O\rangle_\beta = \frac{\int dE P_\beta^{(MC)}(E)O(E)\frac{P_\beta(E)}{P_\beta^{(MC)}(E)}}{\int dE P_\beta^{(MC)}(E)\frac{P_\beta(E)}{P_\beta^{(MC)}(E)}} = \frac{\int dE P_\beta^{(MC)}(E)O(E)e^{-W(E)}}{\int dE P_\beta^{(MC)}(E)e^{-W(E)}}, \tag{3.0.8}$$

this will remove the unknown normalisation. Using importance sampling methods, sampling the distribution $P_\beta^{(MC)}(E)$, the above equation can be written in terms of the expectation value of the new distribution, $\langle ...\rangle_\beta^{(MC)}$, giving

$$\langle O\rangle_\beta = \frac{\left\langle O(E)\frac{P_\beta(E)}{P_\beta^{(MC)}(E)}\right\rangle_\beta^{(MC)}}{\left\langle \frac{P_\beta(E)}{P_\beta^{(MC)}(E)}\right\rangle_\beta^{(MC)}} = \frac{\left\langle O(E)e^{-W(E)}\right\rangle_\beta^{(MC)}}{\left\langle e^{-W(E)}\right\rangle_\beta^{(MC)}}. \tag{3.0.9}$$

This method therefore can be used to sample a energy distribution, that avoids the metastability problems, $P_\beta^{(MC)}(E)$, ensuring we are ergodically sampling the energy distribution. On the generated configurations, the expectation values in Eq. 3.0.9 can be computed and the expectation values for the canonical ensemble can be estimated.

3.0.3 Wang-Landau method

A method for calculating the density of states for a system with discrete energy levels, was developed by Wang and Landau in Ref [119]. Their idea was to find an energy distribution, $P(E)$, that would allow for the configurations to be sampled with a flat distribution. If there are $\rho(E_n)$ configurations with a given energy, E_n, the probability we randomly select a configuration with this energy level from any possible configuration is proportional to $\rho(E_n)$. Therefore, if we want to sample configurations with a uniform energy distribution, we will need to select configurations with the reciprocal of this, i.e. $P(E) \propto 1/\rho(E_n)$.

In this method we sample according to an estimate for the density of states, $\tilde{\rho}(E)$, and improve our estimate until the histogram of sampled energies is flat. We set the probability to move from the state with energy, E_i, into a configuration with energy, E_f, to be,

$$P(E_f|E_i) = min\left(\frac{\tilde{\rho}(E_i)}{\tilde{\rho}(E_f)}, 1\right). \tag{3.0.10}$$

if the new configuration is accepted, we assume this configuration is more likely and thus we increase our estimate for $\tilde{\rho}(E_f)$, $\tilde{\rho}(E_f) \rightarrow f\tilde{\rho}(E_f)$, for $f > 1$. If the new configuration is not accepted our current configuration is more likely and we similarly increase $\tilde{\rho}(E_i)$, $\tilde{\rho}(E_i) \rightarrow f\tilde{\rho}(E_i)$. Initially, this algorithm will break the detailed balance condition, however as we approach the true value of the density of states, $\tilde{\rho}(E) \rightarrow \rho(E)$, it is recovered.

We keep track of the number of times an energy level is visited through the histogram, $H(E_n)$. We define the average histogram value to be $\bar{H} = \sum_n H(E_n)/N_{\text{int}}$, where N_{int} is the number of energy levels. The energy distribution is considered flat when the value of the histogram for all energy levels above some percentage, w, of the average histogram, i.e. $H(E_n) > w\bar{H}$, $\forall n$, with $w \sim 1$. In Ref [119], $w = 0.8$ was used.

Once we have a flat distribution, the error on the density of states will be proportional to $\ln(f)$ [119]. However, if we initially choose an infinitesimally small factor f, to get accurate results, the convergence to the true value will be very slow. Therefore, we start with a large $f = f_0$ value and run the algorithm until we have a flat distribution. The histogram is then reset, $H(E_n) = 0$ for all E_n, and we restart the algorithm using final estimate for the density of states and a new smaller $f = f_1$. This is repeated using, $f_0, f_1, .., f_M$, until we reach required error. The f_i values should be chosen systematically by some monotonically decreasing function that approaches 1 in the limit of an infinite number iterations, $\lim_{i\rightarrow\infty} f_i \rightarrow 1$. In the original paper, Ref. [119], $f_{i+1} = \sqrt{f_i}$, however in Ref. [141] this was shown to saturate and result in systematic errors, a function of the form $f_i \propto 1/i + 1$ was instead suggested.

An overview of the complete algorithm is given below:

1. Start in an initial configuration with energy E_i, $i = 0$. Set $\tilde{\rho}(E_n) = 1$ for all E_n.

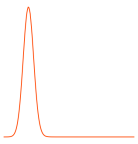

2. Set H(E) = 0 for all E, and $f = y(f_0, i)$, where y is a function that monotonically reduces to 1 as $i \to \infty$ and $y(f_0, 0) = f_0$.

3. Consider a new configuration with energy E_f. Accept new configuration with probability $P(E_i \to E_f) = min\left(\frac{\tilde{\rho}(E_i)}{\tilde{\rho}(E_f)}, 1\right)$.

   - If configuration not accepted, $H(E_i) = H(E_i) + 1$, $\tilde{\rho}(E_i) = \tilde{\rho}(E_i)f$.
   - If configuration accepted, $H(E_f) = H(E_f) + 1$, $\tilde{\rho}(E_f) = \tilde{\rho}(E_f)f$, $E_f = E_i$.

4. Repeat from Step 3 until $H(E_n) >= w\bar{H}$, for all E_n.

5. If we haven't reached the required error, increase i, $i = i + 1$, and return to Step 2.

3.1 LLR method

In Ref. [120] the logarithmic linear relaxation (LLR) method was introduced. It took the Wang-Landau method as inspiration and developed an algorithm for systems with continuous energy. Once again, the aim is to estimate the density of states by sampling a flat energy distribution. However, as we have continuous energy we can no longer calculate $\rho(E)$ directly for each energy level. Instead we break the systems energy into N_{int} intervals, with energy restricted to a given interval, $E_n - \Delta_E/4 \leq E < E_n + \Delta_E/4$. Within each interval we estimate the density of states, $\rho(E) \approx \tilde{\rho}(E)$, such that the energy distribution within each interval is approximately flat.

We assume the density of states is a continuous monotonically increasing function, where within each interval the natural log of $\rho(E)$, can be expanded as a Taylor series. For the *nth* interval it is given by,

$$\ln \rho(E) \equiv c_n + \left.\frac{\mathrm{d} \ln \rho(E)}{\mathrm{d}E}\right|_{E=E_n} (E - E_n) + \left.\frac{\mathrm{d}^2 \ln \rho(E)}{\mathrm{d}E^2}\right|_{E=E_n} (E - E_n)^2 + \mathcal{O}((E - E_n)^3). \tag{3.1.1}$$

We cutoff the Taylor series after the first term, defining,

$$a_n = \left.\frac{\mathrm{d} \ln \rho(E)}{\mathrm{d}E}\right|_{E=E_n}. \tag{3.1.2}$$

The coefficients have statistical mechanics interpretation of the inverse temperature, $a_n = 1/t_n$. This term is independent of the volume. The neglected higher order terms will scale inversely with the volume, $\mathrm{d}^{\mathrm{m}} \ln \rho(E)/\mathrm{d}E^m|_{E=E_n} \propto V^{-m+1}$ [122], and their contribution is small compared to the leading order. Thus we approximate the density of states as a piecewise log linear function, such that within an interval, $E_n - \Delta_E/4 \leq E \leq E_n + \Delta_E/4$, it is given

by,

$$\ln \tilde{\rho}(E) \equiv a_n \left(E - E_n\right) + c_n. \tag{3.1.3}$$

This should be true for the entire energy range $0 \leq E \leq 6\tilde{V}/a^4$. However, as we will calculate the coefficients, a_n, numerically, and we require the intervals to be small enough that the log linear approximation holds, it is not feasible to calculate $\rho(E)$ for the entire energy range. Instead, we will select a small energy range, $E_{min} \leq E \leq E_{max}$, such that all micro-states relevant to the physics we are studying are included. The effects of intervals outside this range will be exponentially suppressed. We define the centre of the intervals as, $E_n = E_{min} + (n+1)\Delta_E/2$.

The coefficients c_n are set by the continuity of $\rho(E)$,

$$c_n = c_1 + \frac{\Delta_E}{4} a_1 + \frac{\Delta_E}{2} \sum_{k=2}^{n-1} a_k + \frac{\Delta_E}{4} a_n \,. \tag{3.1.4}$$

A full calculation of the first term, c_1, requires the density of states of the ground state, E_0, and $\rho(E_0)$ to the number of degenerate ground states of the theory. However, generally this term will only appear as a constant factor that can be cancelled when divided by the partition function, thus we set $c_1 = 0$. Quantities with dependence on this will be treated differently.

To see how Eq. 3.1.3 leads to a flat distribution, we define the expectation value of an observable with explicit energy dependence, $O(E)$, at coupling a, for configurations restricted to the nth energy interval as,

$$\langle\langle O \rangle\rangle_n(a) \equiv \frac{1}{\mathcal{N}_n(a)} \int_{E_n - \frac{\Delta_E}{2}}^{E_n + \frac{\Delta_E}{2}} O(E)\rho(E)e^{-aE} dE \tag{3.1.5}$$

$$= \left\langle \left[\theta\left(E - E_n + \frac{\Delta_E}{2}\right) - \theta\left(E - E_n - \frac{\Delta_E}{2}\right) \right] O \right\rangle_a , \tag{3.1.6}$$

where $\theta(E)$ is the Heaviside step function, which ensures the distribution vanishes outside the interval. Note here the interval, $E_n - \Delta_E/2 \leq E < E_n + \Delta_E/2$, differs from the previously quoted interval size. Adjacent intervals are given an overlap, further details and the reasons are discussed later, when the replica exchange method is introduced. The normalisation, $\mathcal{N}_n(a)$, is the analogue of the partition function,

$$\mathcal{N}_n(a) \equiv \int_{E_n - \frac{\Delta_E}{2}}^{E_n + \frac{\Delta_E}{2}} \rho(E)e^{-aE} dE. \tag{3.1.7}$$

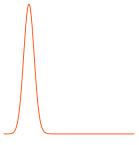

Substituting in our approximation, $\rho(E) \to \tilde{\rho}(E)$, gives

$$\mathcal{N}_n(a) \approx e^{c_n - a_n E_n} \int_{E_n - \frac{\Delta_E}{2}}^{E_n + \frac{\Delta_E}{2}} e^{(a_n - a)E} dE, \tag{3.1.8}$$

it should be clear that if we can select $a_n = a$, we integrate over a flat energy distribution. The integral gives $\mathcal{N}_n(a) \approx e^{c_n - a_n E_n} \Delta_E$. Substituting this into Eq. 3.1.5, gives

$$\langle\langle O \rangle\rangle_n(a) \approx \frac{1}{\Delta_E} \int_{E_n - \frac{\Delta_E}{2}}^{E_n + \frac{\Delta_E}{2}} O(E) dE \,. \tag{3.1.9}$$

Again, we are integrating over a flat energy distribution.

By cutting off the Taylor series after first order, Eq. 3.1.3, our expression, $\tilde{\rho}(E)$ will differ from the true density of states, $\rho(E)$, by the relation

$$\rho(E) = \tilde{\rho}(E) \exp\big(\mathcal{O}(\Delta_E^2 a^4 / \tilde{V})\big) \approx \tilde{\rho}(E) \left(1 + \mathcal{O}(\Delta_E^2 a^4 / \tilde{V})\right), \tag{3.1.10}$$

where $\Delta_E^2 a^4 / \tilde{V}$ is small. Therefore there will be a relative systematic error of the form, $1 - \tilde{\rho}(E)/\rho(E) = \mathcal{O}(\Delta_E^2 a^4 / \tilde{V})$[122].

To calculate the coefficients $a_n = a$, first we note that, $\langle\langle E \rangle\rangle_n(a) = E_n$, therefore the restricted expectation value of the energy difference, $E - E_n$, should vanish when we have correctly defined a_n,

$$\langle\langle \Delta E \rangle\rangle_n(a_n) = \frac{1}{\mathcal{N}_n(a_n)} \int_{E_n - \frac{\Delta_E}{2}}^{E_n + \frac{\Delta_E}{2}} (E - E_n)\, \rho(E) e^{-a_n E} dE = 0 \,, \tag{3.1.11}$$

We can therefore calculate $\tilde{\rho}(E)$, by solving this equation for all our intervals, $n_1, .., n_{N_{\text{int}}}$, to find, $a_1, ..., a_{N_{\text{int}}}$, and then use Eq. 3.1.4 and Eq. 3.1.3.

For later convenience, I introduce notation in terms of the average plaquette, as it will be the primary observable we focus on, and due to its direct relation to the action. It will also more easily allow for a discussion of results across different lattice volumes. I will denote the interval size as $\Delta_{u_p} = \frac{a^4 \Delta_E}{6\tilde{V}}$ and the plaquette values at the centre of each interval as $(u_p)_n = 1 - \frac{a^4}{6\tilde{V}} E_n$. The maximum and minimum plaquette values are given by $(u_p)_{min} = 1 - \frac{a^4}{6\tilde{V}} E_{max}$ and $(u_p)_{max} = 1 - \frac{a^4}{6\tilde{V}} E_{min}$.

3.1.1 Reconstructing the canonical ensemble

With the coefficients, $\{a_n\}_{n=1}^{N_{int}}$, for the intervals, $\{E_n\}_{n=1}^{N_{int}}$, we have a micro-canonical description of the system through the density of states. From this, a canonical description of the system can be reconstructed using the equations at the start of this chapter. By substituting in the approximation for $\rho(E)$, Eq. 3.1.3, into Eq. 3.0.4 we can calculate the partition function

for the system at inverse coupling β, up to a constant factor of e^{c_1},

$$Z(\beta) = \sum_{n=1}^{N_{int}} \int_{E_n-\Delta_E/4}^{E_n+\Delta_E/4} dE\tilde{\rho}(E)e^{-\beta E}, \tag{3.1.12}$$

$$= \sum_{n=1}^{N_{int}} \tilde{\rho}(E_n)e^{-\beta E_n} \int_{-\Delta_E/4}^{\Delta_E/4} dE e^{(a_n-\beta)E}. \tag{3.1.13}$$

$$\tag{3.1.14}$$

In the first expression, we exchanged our integral over all energy with a piece wise sum over the integrals in each interval, allowing us to use the numeric form of the density of states. In the second term we have taken all terms with no explicit dependence on the integration variable E, outside the integral and made the substitution $E \to E - E_n$. The integral is then solved, giving

$$Z(\beta) = \sum_{n=1}^{N_{int}} \tilde{\rho}(E_n)e^{-\beta E_n} \left\{ \frac{2}{a_n - \beta} \sinh\left((a_n - \beta)\frac{\Delta_E}{4} \right) \right\}, \tag{3.1.15}$$

where we note that when $a_n = \beta$, the term in the curly brackets becomes $\Delta_E/2$.

Similarly we can compute the VEV of observables with explicit dependence on the energy through a one dimensional integral over the energy,

$$\langle O \rangle_\beta \approx \sum_{n=1}^{N_{int}} \frac{\tilde{\rho}(E_n)e^{-\beta E_n}}{Z(\beta)} \int_{-\Delta_E/4}^{\Delta_E/4} dE O(E + E_n)e^{(a_n-\beta)E}. \tag{3.1.16}$$

Many of the observables we will study are functions of the average plaquette, we can rewrite this equation for an observable of this form,

$$\langle O \rangle_\beta \approx \sum_{n=1}^{N_{int}} \frac{\tilde{\rho}(E_n)e^{-\beta E_n}}{Z(\beta)} \int_{-\Delta_{u_p}/4}^{\Delta_{u_p}/4} du_p O(u_p + (u_p)_n)e^{-\frac{6\tilde{V}}{a^4}(a_n-\beta)u_p}. \tag{3.1.17}$$

The specific heat, and Binder cumulant, Eq. 2.2.22 and Eq. 2.2.25, are written in terms of the VEV of the powers of the average plaquette. By solving the integral for $O(u_p) = u_p^M$, gives

the expression,

$$\langle u_p^M \rangle_\beta = \sum_{n=1}^{N_{int}} \frac{\tilde{\rho}(E_n) e^{-\beta E_n}}{Z(\beta)} \int_{-\Delta_{u_p}/4}^{\Delta_{u_p}/4} du_p (u_p + (u_p)_n)^M e^{-\frac{6\tilde{V}}{a^4}(a_n - \beta)u_p}, \tag{3.1.18}$$

$$= \sum_{n=1}^{N_{int}} \frac{\tilde{\rho}(E_n) e^{-\beta E_n}}{Z(\beta)} \sum_{m=0}^{M} \frac{2(-1)^{M-m} M!}{(a_n - \beta)^{M-m+1}}$$

$$\left[\sum_{j=0}^{[\frac{m}{2}]} \frac{((u_p)_n)^{m-2j}}{(2j)!(m-2j)!} \left(\frac{\Delta_E}{4}\right)^{m-2j} \sinh\left(\frac{\Delta_E}{4}(a_n - \beta)\right) \right.$$

$$\left. + \sum_{j=1}^{[\frac{m}{2}]+1} \frac{((u_p)_n)^{m-2j+1}}{(2j-1)!(m-2j+1)!} \left(\frac{\Delta_E}{4}\right)^{m-2j+1} \cosh\left(\frac{\Delta_E}{4}(a_n - \beta)\right) \right], \tag{3.1.19}$$

which can be calculated numerically. The terms $[m/2]$, denote that the number in the square bracket is rounded down to the nearest integer. Using this equation we can numerically compute the specific heat and the Binder cumulant for inverse couplings within a range that is set by the chosen energy range.

The plaquette distribution can also be directly analysed for an inverse coupling β, for a plaquette value within the range $(u_p)_{min} \leq u_p \leq (u_p)_{max}$, through

$$P_\beta(u_p) = \frac{1}{Z(\beta)} \tilde{\rho}(E_n) e^{-a_n E_n} e^{(a_n - \beta)E} \Big|_{E=(1-u_p)6\tilde{V}/a^4} \tag{3.1.20}$$

where $E_n - \Delta_E/4 \leq E = (1-u_p)\frac{6\tilde{V}}{a^4} \leq E_n + \Delta_E/4$. From this we aim to demonstrate the characteristic double peak structure in the metastable region. This will also be used to find the critical coupling, the plaquette jump, and $\hat{I}$ in Eq. 2.2.31, through P_{min} and P_{max}. Using Eq. 3.0.5, we can also use this to calculate an effective potential for the system.

To compute the VEVs of more general observables, with explicit dependence on the lattice configuration, $B[U]$, we follow the method set out in Ref. [122], here we sketch the derivation. If we were to sample configurations from a completely flat energy distribution, to compute expectation values at an inverse coupling β we would have to weigh each measurement by the probability of having that given configuration, $P_\beta(S[U])$, where $S[U]$ is the action on a configuration, U. Therefore each measurement would contribute $B[U]P_\beta(S[U])$ to the expectation value,

$$\langle B \rangle_\beta = \langle B[U] P_\beta(E) \rangle^{(flat)}, \tag{3.1.21}$$

where $\langle ... \rangle^{(flat)}$, denotes the expectation value calculated on configurations sampled with a flat energy distribution. We approximate this distribution piecewise with $\langle ... \rangle^{(flat)} \approx \sum_n \langle\langle ... \rangle\rangle_n (a_n)$. The term in the double angle bracket is calculated numerically on a set of configurations,

$\{U\}$, restricted to the *nth* energy interval. Therefore, this equation becomes,

$$\langle B\rangle_\beta = \sum_{n=1}^{N_{int}} \frac{1}{2}\langle\langle B[U]P_\beta(S[U])\rangle\rangle_n(a_n), \tag{3.1.22}$$

the factor of $1/2$ is due to the overlap in the intervals. Using the Eq. 3.1.20 we can approximate the energy distribution for a small energy interval region around $E_n - \Delta_E/2 < E < E_n + \Delta_E/2$. Substituting this into the equation gives,

$$\langle B\rangle_\beta = \frac{1}{Z(\beta)} \sum_{n=1}^{N_{int}} \frac{1}{2}\langle\langle B[U]\tilde{\rho}(S[U])e^{-\beta S[U]}\rangle\rangle_n(a_n). \tag{3.1.23}$$

$$\langle B\rangle_\beta = \frac{1}{Z(\beta)} \sum_{n=1}^{N_{int}} \frac{1}{2}\tilde{\rho}(E_n)\langle\langle B[U]\exp(-\beta S[U] + a_n(S[U] - E_n))\rangle\rangle_n(a_n). \tag{3.1.24}$$

Following the normalisation in Ref. [122] gives,

$$\langle B\rangle_\beta = \frac{1}{Z(\beta)} \sum_{n=1}^{N_{int}} \frac{\Delta_E}{2}\tilde{\rho}(E_n)\tilde{B}[U]\,, \tag{3.1.25}$$

where

$$\tilde{B}[U] = \langle\langle B[U]\exp\{(-\beta S[U] + a_n(S[U] - E_n))\}\rangle\rangle_n(a_n)\,, \tag{3.1.26}$$

with the partition function being

$$Z(\beta) = \frac{1}{Z(\beta)} \sum_{n=1}^{N_{int}} \frac{\Delta_E}{2}\tilde{\rho}(E_n)\langle\langle\exp\{(-\beta S[U] + a_n(S[U] - E_n))\}\rangle\rangle_n(a_n)\,, \tag{3.1.27}$$

Further details on the calculation of this term is discussed when the fixed a_n iterations are introduced in the algorithmic details section.

Using the relation in Eq. 3.1.10, the error on the observables, calculated using Eq. 3.1.27 and Eq. 3.1.18, and the plaquette distribution, will also have also have an error $\mathcal{O}(\Delta_E^2)$. To ensure that we have accurately accounted for this systematic error, measured observables should be fit against Δ_E^2 and the limit of $\Delta_E \to 0$ should be taken.

Micro-canonical thermodynamics

Through analogies with statistical mechanics, we can define micro-canonical thermodynamic properties of the lattice system. In particular we define the internal energy as E, the

entropy s, the temperature t and the free-energy F, as

$$F = E - ts, \quad s = \ln(\rho), \quad t = \frac{\partial E}{\partial s} = \frac{1}{a_n}, \quad E = \frac{6\tilde{V}}{a^4}(1 - u_p), \tag{3.1.28}$$

from our estimate for $\rho(E)$ the entropy is given by

$$s(E) = c_n + a_n(E - E_n) \tag{3.1.29}$$

for $E_n - \Delta_E/4 \leq E \leq E_n + \Delta_E/4$. Note that this definition has an explicit dependence on the choice of c_1. The free-energy can be directly linked to the probability distribution through

$$\exp\left(-\frac{F(t)}{t}\right) = Z(\beta)P_\beta(E)\Big|_{\beta=1/t, E=F(t)+ts}, \tag{3.1.30}$$

it is also equivalent to the extrema of the effective potential, defined in Eq. 3.0.5.

Rather than computing the free-energy exactly, we generally compute the reduced free-energy defined as,

$$f(t) \equiv \frac{a^4}{\tilde{V}}(F(t) + \Sigma t). \tag{3.1.31}$$

The factor of the volume makes this an intensive quantity, and therefore will be more useful in comparing different spatial volumes. Σ is a constant term we choose to be equal to the average entropy across the intervals. It is used to remove the dependence on the arbitrary choice of c_1 and will allow for the characteristic swallow tail structure, that we expected to observe in the micro-canonical free-energy of the system, more visible.

3.1.2 Algorithmic details

Newton Raphson and Robbins Monro

To solve Eq. 3.1.11 we use two root-finding algorithms, the Newton-Raphson (NR) and the Robbins-Monro (RM) methods. We assume that for any given interval, there is one true solution, a_n, such that $\langle\langle \Delta E \rangle\rangle_n(a_n) = 0$. Initially we make a guess, $a_n = a_n^{(0)}$, assuming this guess is close to the true solution, we iteratively improve it, $a_n^{(0)} \to a_n^{(1)} \to \ldots \to a_n^{(M)}$, such that with infinite computational resources we reach the true answer, $\lim_{M\to\infty} a_n^{(M)} = a_n$.

For a function, $f(x)$, with root, $x = \tilde{x}$, i.e. $f(\tilde{x}) = 0$, the Newton-Raphson method finds $\tilde{x}$, iterably using $x^{(m)} \to x^{(m+1)}$, where

$$x^{(m+1)} = x^{(m)} - \frac{f(x^{(m)})}{f'(x^{(m)})}, \tag{3.1.32}$$

and $f'(x^{(m)}) = df(x)/dx|_{x=x^{(m)}}$. If the exact form of the function is known then the NR

method converges to the true solution quadratically. However, we do not know the exact form of $\langle\langle \Delta E \rangle\rangle_n(a_n^{(m)})$, instead we sample the distribution to approximate the expectation value. Away from the true solution this method will converge as expected. However close to the true value, the error on the expectation value will lead to the this algorithm oscillating around it. Robbins and Monro, in Ref [142], outlined an algorithm that will converge to the true solution when sampling a distribution to compute expectation values. The guess is now updated according to, $x^{(m+1)} = x^{(m)} - \epsilon_m f(x^{(m)})$, where $\sum_m \epsilon_m^2 < \infty$ and $\sum_m \epsilon_m = \infty$, we use $\epsilon_m \propto 1/m$.

To use the NR iterations, Eq. 3.1.32, to update our density of states, we take $x^{(m)} \to a_n^{(m)}$ and $f(x^{(m)}) \to \langle\langle \Delta E \rangle\rangle_n(a_n^{(m)})$. The differential term, in the denominator of the equation, can be simplified, as $\langle\langle \Delta E \rangle\rangle_n'(a_n^{(m)}) = \langle\langle \Delta E^2 \rangle\rangle_n(a_n^{(m)}) - \langle\langle \Delta E \rangle\rangle_n^2(a_n^{(m)})$. For $a_n^{(m)} \approx a_n$, this becomes $\langle\langle \Delta E \rangle\rangle_n^2(a_n) = 0$, then through explicit calculation $\langle\langle \Delta E \rangle\rangle_n'(a_n^{(m)}) \approx \langle\langle \Delta E^2 \rangle\rangle_n(a_n) = \Delta_E^2/12$. The NR iteration becomes,

$$a_n^{(m+1)} = a_n^{(m)} - \alpha \frac{\langle\langle \Delta E \rangle\rangle_n(a_n^{(m)})}{\langle\langle (\Delta E)^2 \rangle\rangle_n(a_n^{(m)})} \tag{3.1.33}$$

$$\simeq a_n^{(m)} - \alpha \frac{12}{\Delta_E^2} \langle\langle \Delta E \rangle\rangle_n(a_n^{(m)}) \,. \tag{3.1.34}$$

The RM iterations have the same form but with an additional suppression of $1/(m+1)$,

$$a_n^{(m+1)} = a_n^{(m)} - \frac{\alpha}{m+1} \frac{\langle\langle \Delta E \rangle\rangle_n(a_n^{(m)})}{\langle\langle (\Delta E)^2 \rangle\rangle_n(a_n^{(m)})} \tag{3.1.35}$$

$$\simeq a_n^{(m)} - \frac{\alpha}{m+1} \left(\frac{12}{\Delta_E^2} \right) \langle\langle \Delta E \rangle\rangle_n(a_n^{(m)}) \,. \tag{3.1.36}$$

For this work we set $\alpha = 1$.

Initially the NR method will converge to the true value much faster than the RM iterations. However, at later stages it will generally oscillate around the true value, with increasing iterations not reducing the error. Therefore, a combination of the methods is used. Initially we carry out $\bar{m}$ NR iterations, to bring the system close to the true value. This is followed by a set of $\tilde{m}$ RM iterations to refine our result and provide a better approximation to the true value. Generally, $\bar{m} \ll \tilde{m}$.

Choosing the initial values

In order to start using the NR and RM iterations, outlined above, we require initial guesses for the coefficients, $a_n^{(m)}$, for each interval. We also need to estimate the appropriate range of energy values to study the deconfinement phase transition. For both of these problems we carry out an initial parameter scan of inverse couplings, β, using standard importance

sampling methods. Generally, this can be carried out on a lattice with different number of spatial sites (a smaller N_s), but will need the same N_t.

For this scan we measure the VEV of the Polyakov loop, to determine the phase, and the average plaquette, for a set of evenly spaced β values around the critical point. If the critical point is known, i.e. it is in the literature we use this value. However, if it is unknown a larger scan of β values is used to find the critical point. We want to ensure that the chosen β values contain pure phase states in both the confined and deconfined phases.

Once a sufficient set of β values have been found, the histogram of the ensembles plaquette values can be used to determine the range of energy values, $E_{min} = E_1 - \Delta_E/2$ and $E_{max} = E_{N_{int}} + \Delta_E/2$, or equivalently the range of plaquette values $(u_p)_{min} = 1 - \frac{a^4}{6\tilde{V}} E_{max}$ and $(u_p)_{max} = 1 - \frac{a^4}{6\tilde{V}} E_{min}$. $(u_p)_{min}$ ($(u_p)_{max}$) is chosen to be location that the lowest (highest) plaquette value point at which the plaquette distribution for the lowest (highest) β appears to value vanish.

The number of intervals can also be estimated from the probability distribution, by choosing an interval size, Δ_E, which will make all the plaquette distribution approximately flat when restricted to an interval. However, this choice will be less rigorous and several interval sizes will be taken to ensure accurate results. The intervals should be equally spaced between E_{min} and E_{max}, with $E_n = E_1 + n\Delta_E/2$, for $N = 1, .., N_{int}$.

Once we have a set of intervals, $\{E_n\}_{n=1}^{N_{int}}$, we can estimate the initial a_n values, $a_n^{(0)}$. To do this we note that heuristically, away from the meta-stable region, the coefficients a_n will correspond to the β values that will give rise to a plaquette distribution centred at $(u_p)_n$. Therefore, we can invert this relation between the inverse coupling and the VEV of the average plaquette, by fitting a polynomial function to, $\beta(\langle u_p \rangle)$. We then use, $a_n^{(0)} = \beta((u_p)_n)$. This method will find values that are close enough for the RM and NR iterations to converge to the true value. As we will see when we discuss the results, this initial choice will not demonstrate the metastable dynamics characteristic of a first order transition, however after the iterations, this behaviour emerges.

Restricted heat bath method

To compute the coefficients a_n, we require a method to sample the energy distribution restricted to an interval, $E_n - \Delta/2 \leq E \leq E_n + \Delta/2$. The simplest method would be to add an accept reject steps after a full update, to check if the energy of the lattice is within the interval. For small interval sizes this will be massively inefficient and will involve throwing away many configurations. Alternatively, as is discussed in Ref. [122], the hard boundaries at the edge of each interval can be softened by reweighting the configurations outside the interval driving the systems back into the into the energy interval. This method also helps to resolve

ergodicity problems, that will be discussed further in Sec. 3.1.2. In the work presented here, we use the restricted heat bath method, discussed in Ref. [1]

To compute the VEVs in Eq. 3.1.34 and Eq. 3.1.36, we sample the energy restricted distribution, given by

$$dP_c(U) \propto dP(U)\theta(E - E_{n-1})\theta(E_{n+1} - E)\,, \tag{3.1.37}$$

where $dP(U)$ is the distribution in Eq. 2.3.2. The heaviside step functions, $\theta(E - E_{n-1})$ and $\theta(E_{n+1} - E)$, ensure the distribution vanishes when the energy is outside the interval, $E_{n-1} = E_n - \Delta/2 \leq E \leq E_n + \Delta/2 = E_{n+1}$. To efficiently sample this distribution we use an algorithm that is based on the heat-bath method discussed in Sec. 2.3.1, with modifications that impose the restrictions on the energy. For ease of notation, I will initially discuss how an $SU(2)$ lattice is updated using this method.

To impose the energy restriction, we consider a change on a link, $U_\mu(n) \to U'_\mu(n) = \bar{U}U_\square^{-1}$, for a lattice initially in configuration U, with energy E. The contribution to the total energy due to the link before and after the update is given by E_i and E_f, respectively. We denote the new variable as $\bar{U} = u_0\mathbb{1} + \sum_{i=1}^{3} u_i\sigma_i$. The variables u_1, u_2 and u_3, don't affect the energy so they are again selected to lie randomly on a sphere of radius, $\mathbf{u} = \sqrt{1-u_0^2}$. The energy contribution due the link after the update is given by $E_f = 6 - ku_0$, where $k = \sqrt{det[U_\square]}$. The energy restriction can be imposed on the range of u_0 values selected.

We can write the energy constraint as,

$$E_{n-1} \leq E - E_i + E_f \leq E_{n+1} \tag{3.1.38}$$

this is rearranged to find an expression for the range of u_0 values, denoted as $u_{\min} \leq u_0 \leq u_{\max}$, giving,

$$u_{\min} = \max\left(\frac{6 + (E - E_{n+1}) - E_i}{k}, -1\right), \tag{3.1.39}$$

$$u_{\max} = \min\left(\frac{6 + (E - E_{n-1}) - E_i}{k}, 1\right). \tag{3.1.40}$$

This restriction is imposed on the values of u_0, by randomly sampling a new variable ξ uniformly between 0 and 1, then setting

$$u_0 = \frac{1}{\beta k}\ln\left(e^{\beta k u_{\min}} + \xi(e^{\beta k u_{\max}} - e^{\beta k u_{\min}})\right). \tag{3.1.41}$$

This procedure is completed by adding the accept-reject step, to enforce the factor of $\sqrt{1-u_0^2}$.

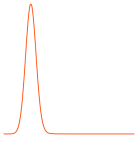

To update a lattice in a more general gauge group, $\mathcal{G}$, we again follow the Cabbibo-Marinari method, by updating the $SU(2)$ subgroups of each link. For $SU(N)$ no additional modification on the Cabbibo-Marinari method is required. However, recall for $Sp(2N)$ the form of the decomposition changes a link's contribution to the total energy. Following the notation in Sec. 2.3.3, the energy from the new link is given by, $E_f = 6 - zku_0$, where z depends on the form of the decomposition. Therefore, the new constraints on u_0 become,

$$u_{\min} = \max\left(\frac{6 + (E - E_{n+1}) - E_i}{zk}, -1\right), \tag{3.1.42}$$

$$u_{\max} = \min\left(\frac{6 + (E - E_{n-1}) - E_i}{zk}, 1\right). \tag{3.1.43}$$

The over-relaxation method, discussed in Sec. 2.3.2, is micro-canonical. Therefore, it can be used to update the lattice without alterations. Again, it cannot be used in isolation, but will be used concurrently with the restricted heat bath method to help decorrelate configurations.

Using these methods we can now compute the VEV, $\langle\langle \Delta E\rangle\rangle_n(a_n^{(m)})$. To ensure the measurements of the VEV are independent between iterations, and that the lattice has equilibrated to the new a_n value after they are updated, we carry out n_{Th} thermalisation updates on the configurations at the start of each NR/ RM step. Each update will consist of at least one restricted heat-bath update. This is followed by n_M measurement steps, in which we measure the value of ΔE and estimate its VEV.

Annealing and thermalisation

The method outlined above works once the system has entered the given energy interval. However, initially the lattice is setup in a completely randomly initial configuration. Therefore, before starting the restricted heat-bath updates, the system will need to be brought into the energy interval. We refer to this process as annealing.

To bring the system into a given interval, we update the lattice with standard importance sampling, i.e. we set $u_{\min} = -1$ and $u_{\max} = 1$, with the inverse coupling set to the initial a_n value, $\beta = a_n$. After each update we check if it is within the energy interval. If it is not, the lattice is updated again. After some number of updates, which we chose to be 10, if the system is still not within the interval the inverse coupling is changed, $\beta \to \beta - d\beta\frac{\Delta E}{|\Delta E|}$. This will increase (decrease) the inverse coupling by a fixed amount, $d\beta$, which is a fixed input parameter, if the energy is lower (higher) than the centre of the energy interval. This ensures the lattice hasn't become stuck in the wrong metastable vacua and will increase the speed of the convergence. Once the system is within the interval, we can begin using the restricted heat-bath iterations.

Following annealing, there will be a set of N_{ITh} thermalisation steps to ensure that the Markov chain is at the physical point. This will be a fixed number of restricted heat-bath and over-relaxation steps. After thermalising, the NR and RM iterations will begin.

Residual ergodicity problems

Restricting configurations to a small energy interval can lead to an ergodicity problem. Within an energy interval there can be disconnected regions of phase space separated by potential barriers. For example, in the deconfined phase there are multiple degenerate vacua due to the centre symmetry. To tunnel between these vacua, the system may need to leave the energy interval to overcome the potential barrier. To resolve this problem we use replica exchange, introduced for the Wang-Landau method in Ref. [143].

The LLR algorithm is ran on a lattice system in each interval in parallel. The intervals are given an overlap region, the centres of the intervals are separated by $\Delta_E/2$, but the interval width is Δ_E. Therefore the energy of the nth and $(n-1)th$ interval overlap for E in $E_{n-1} \leq E \leq E_n$. After each NR and RM iteration, if both replicas in neighbouring intervals (n and $n-1$) are in the overlap region we add a Metropolis step to consider exchanging configurations between the intervals, with probability

$$P_{\text{swap}} = \min\left(1, e^{(a_n^{(m)} - a_{n-1}^{(m)})(S_n^{(m)} - S_{n-1}^{(m)})}\right) . \tag{3.1.44}$$

$S_n^{(m)}$ is the action of the configuration in the nth replica at the mth RM iteration number, when the exchange is considered. Therefore, the replicas are able to move between intervals, allowing the configurations to escape and rejoin energy intervals. This should allow the system to fully explore the phase space of a given interval as we carry out the NR and RM updates.

There remains an additional residual ergodicity problem. After implementing the replica exchange, there is still a hard cutoff on the action at E_{min} and E_{max}. To resolve this issue, we remove the hard cutoffs in the boundary intervals, E_1 and $E_{N_{int}}$. The energy intervals at the boundaries becomes, $0 \leq E \leq E_1 + \Delta_E/2$ and $E_{N_{int}} - \Delta_E/2 \leq E \leq 6\tilde{V}/a^4$. This change is implemented by altering value of $u_{\min}$ and $u_{\max}$ in the restricted heat-bath algorithm. The energy distribution explored by all replicas will be a flat distribution between E_1 and $E_{N_{int}}$, with a two Gaussian tails at the boundaries, allowing the energy to escape the set energy range.

Arbitrarily implementing this algorithm will cause a_1 and $a_{N_{int}}$ to drift, as the intervals are no longer symmetric about E_1 and $E_{N_{int}}$, leading to an error in the calculation of $\langle\langle \Delta E \rangle\rangle_n(a_n^{(m)})$. Instead of updating the boundary intervals according to NR and RM iterations, we will instead assume that away from the transition and for a sufficiently small interval size, the relation between E_n and a_n, is approximately linear. After carrying out an

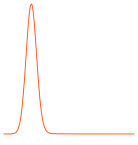

NR or RM iteration, the boundary intervals are updated according to,

$$a_1 = 2a_2 - a_3 \tag{3.1.45}$$

$$a_{N_{int}} = 2a_{N_{int}-1} - a_{N_{int}-2} \tag{3.1.46}$$

Domain decomposition

To improve the scalability of lattice simulations using importance sampling methods, when moving to larger lattice sizes, domain decomposition is used. A single lattice is broken down into N_D subdomains. The subdomains are independently updated using the heat-bath or over-relaxation method. When using the restricted heat-bath method this cannot directly be used. The restricted heat-bath method requires prior knowledge of the total energy of the system. When a link in one of the subdomains is changed the total energy of full lattice is changed. Simultaneously updating the links in multiple subdomains can therefore lead to configurations escaping the energy interval.

To use the restricted heat-bath method, we can only change the energy in one subdomain at a time. The inherently micro-canonical over-relaxation update is then used to update the links in the other subdomains. Therefore, the action is only changed in one subdomain at a time, while the over-relaxation step reduces the correlation between the updates.

For each lattice sweep, we chose one of the N_D subdomains and update it using the restricted heat-bath method, in the other $N_D - 1$ subdomains we carry out over-relaxation steps. The next subdomain is then chosen for the restricted heat-bath update. A full sweep is completed once all N_D subdomains have received one restricted heat-bath update. Therefore, in each sweep each link is updated $N_D - 1$ times with the over-relaxation method and once with the restricted heat-bath.

Fixed a_n iterations

To compute expectation values of observables that depend on the configuration, and not directly on the energy, we use Eq. 3.1.27. The double angle brackets in the expression for $\tilde{B}[U]$, denote that we are calculating the expectation value of a set of configurations restricted to a given energy interval, $E_n - \Delta_E/2 \leq E \leq E_n + \Delta_E/2$, when the inverse coupling is given by $a_n = a_n^{(\hat{m})}$. After completing the RM iterations, within each interval we generate a set of configurations using the restricted heat-bath, and over relaxation, updates, using $a_n^{(\hat{m})}$ fixed to the final value. On these configurations, we measure the observable of interest, in this work we use the Polyakov loop.

We will measure the observables on n_{fxa} configurations, after which to ensure ergodicity, we again use a replica exchange step. This is repeated $\hat{m}$, times. Therefore, for each interval we have $n_{fxa}\hat{m}$ measurements for the computation of $\tilde{B}[U]$.

The fixed a_n iterations also allow us to verify our results. We can compute the restricted expectation value, $\langle\langle \Delta E \rangle\rangle_n(a_n)$, which as a requirement of our results should equal 0, within error. We can also analyse the energy distribution of the configurations generated, to ensure it is approximately flat, within the range $E_1 \leq E \leq E_{N_{int}}$.

Estimating errors

In computing the coefficients a_n, we have statistical errors in the computation of the VEVs, $\langle\langle \Delta E \rangle\rangle_n(a_n^{(m)})$, as we sample a finite number of configurations. We also truncate after a finite number of RM iterations, $\tilde{m} < \infty$, leading to an additional error. To estimate these errors we repeat the computation of the coefficients n_R times, using different random seeds. This will give n_R statistically independent estimates for the density of states. For a sufficient number of RM iterations, the values of $a_n^{(m)}$ are expected to be normally distributed with a standard deviation $\sigma(a_n^{(m)})$, this has a theoretical best scaling behaviour of $\sigma(a_n^{(m)}) \sim 1/\sqrt{m}$ [126].

In this work we assume that the primary source of error is in the determination of the coefficients. To estimate the error on an observable, we calculate the observable on all of the n_R repeats, treating them as independent samples. We then use bootstrapping on the results to estimate the error on the mean.

Overview of algorithm

An overview of the complete algorithm is given below:

- Find initial values: Choose the energy range, $[E_{\min}, E_{\max}]$, that includes all physically relevant energy micro-states for the temperature range of interest. Divide the energy range into N_{int} intervals, with width $\Delta_E = 2(E_{\max} - E_{\min})/(N_{int} + 1)$, centred at $E_n = E_{\min} + n\Delta_E/2$, for $n = 1, .., N_{int}$. From importance sampling, or prior LLR results, choose an initial a_n value for each interval.

- Repeat n_R times with different random sequences:

  1. Start each replica in a random configuration and anneal. Then thermalise with n_{ITh} action-constrained updates.
  2. Carry out $\bar{m}$ NR updates:
     (a) Thermalise with n_{Th} action-constrained updates.
     (b) Measure $(E - E_n)$ on n_M action-constrained updates to calculate the VEV in Eq. 3.1.34 and update a_n.
     (c) Consider configuration swaps using Eq. 3.1.44.
  3. Carry out $\tilde{m}$ RM updates:
     (a) Thermalise with n_{Th} action-constrained updates.

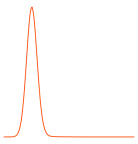

(b) Measure E on n_M action-constrained updates to calculate the VEV in Eq. 3.1.36 and update a_n.

(c) Consider configuration swaps using Eq. 3.1.44.

4. Carry out $\hat{m}$ fixed a_n steps:

(a) Fixing a_n to their final values, generate n_{fxa} configurations restricted to each interval and measure an observable $B[U]$ on them, for this work $B[U] = l_p[U]$.

(b) Consider configuration swaps using Eq. 3.1.44.

We summarise the parameters for this algorithm in Tab. 3.1.

Table 3.1. Parameters of the LLR algorithm used for the numerical computation of the density of states as formulated for N_{int} overlapping subintervals, each of amplitude Δ_E, covering the relevant action interval, $[E_{\min}, E_{\max}]$. This table is an expanded version of Tab.1 in Ref. [1].

Symbol	Name/Role	Description/Purpose
$E_{\min}$	minimal action	lower limit of the relevant action interval
$E_{\max}$	maximal action	upper limit of the relevant action interval
Δ_E	amplitude of intervals	controls the local first-order expansion of $\ln \rho(E)$
$\bar{m}$	number of NR steps	enables to refine the initial guess for the a_n
$\tilde{m}$	number of RM updates	controls the tolerance on the convergence of the a_n
n_{Th}	number of thermalisation steps per NR/RM update	controls decorrelation between two RM updates
n_M	number of measurements per NR/ RM update	controls the accuracy of the expectation values in Eq. 3.1.36
n_P	number of action-constrained updates per NR/ RM update	$n_{Th} + n_M$
n_R	number of determinations of a_n	enables to estimate statistical errors
n_{fxa}	number of fixed a_n updates between replica exchange steps	measurements allow computation of general observables using Eq. 3.0.3
$\hat{m}$	number of sets of n_{fxa} fixed a_n updates	fixed a_n updates will have $\hat{m} n_{fxa}$ configurations
n_{ITh}	number of initial thermalisation steps	thermalises from annealed initial configuration
$(u_p)_{\min}$	minimal plaquette	$1 - \left(E_{\max} a^4/6\tilde{V}\right)$
$(u_p)_{\max}$	maximal plaquette	$1 - \left(E_{\min} a^4/6\tilde{V}\right)$
Δ_{u_p}	plaquette interval size	$\Delta_E a^4/6\tilde{V}$
N_{int}	number of intervals	$N_{int} = \frac{2(E_{\max} - E_{\min})}{\Delta_E} - 1$
N_D	number of subdomains	to improve scalability, each update will have 1 RHB update, and $N_D - 1$ OR updates

3.2 Density of States Functional Fit Approach

Finally, before moving onto the results of the LLR study, for completeness we mention an alternative density of states method, used in lattice gauge theory, the Density of States Functional Fit Approach (DoS FFA). This approach has been used to study the sign problem for finite chemical potentials, see for example Ref. [121]. It has also been used to study gauge theories with a topological term, see for example Ref. [144].

Based on Ref. [121], we will briefly discuss the basic concept of DoS FFA, in the context of $SU(3)$ gauge theory with finite chemical potential, μ. The physical interpretation of the

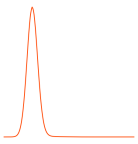

system is $SU(3)$ with static colour sources, the coupling strength of these colour sources is given by a parameter η. We have an action of the form,

$$S_\mu[U] = \beta S[U] - \eta N_s^3 (e^{\mu N_t} l_p + e^{-\mu N_t} l_p^\dagger) \tag{3.2.1}$$

where $S[U]$ is the standard Wilson action, and l_p is the Polyakov loop. Collecting together the real components of the action gives,

$$S_\rho[U] = \beta S[U] - 2\eta N_s^3 \cosh(\mu N_t)\, \mathrm{Re}(l_p), \tag{3.2.2}$$

while for the imaginary components we define,

$$X[U] = N_s^3 \,\mathrm{Im}(l_p), \quad \xi_\mu = 2\eta \sinh(\mu N_t). \tag{3.2.3}$$

where $X[U]$ has the range $-x_{max} \le X[U] \le x_{max}$.

The density of states for the parameter, $X[U]$, is given by

$$\rho(x) = \int [DU] e^{-S_\rho[U]} \delta(X[U] - x), \tag{3.2.4}$$

which is counts the number of configurations with $X[U] = x$, weighted by a Boltzmann factor given by the real part of the action. We can define the partion function as,

$$Z = \int_{-x_{max}}^{x_{max}} dx \rho(x) e^{i\xi_\mu x} = 2 \int_0^{x_{max}} dx \rho(x) \cos\left(\xi_\mu x\right) \tag{3.2.5}$$

where in the second equality we used that $\rho(x)$ is an even function.

To approximate the density of states, the parameter space of $X[U]$ is broken down into intervals, i.e. for the n^{th} interval $x_n \le x < x_{n+1}$. These intervals are of size $\Delta_j = x_{j+1} - x_j$, which can generally be different for each interval. The density of states is then approximated as a piecewise log linear function, for each interval,

$$\ln \rho(x) = c_n - k_n x, \quad \text{with} \quad c_n = -\sum_{j=0}^{n-1} \Delta_j (k_j - k_n), \quad \text{for} \quad x_n \le x < x_{n+1} \tag{3.2.6}$$

The vacuum expectation value restricted to the n^{th} interval is given by,

$$\begin{aligned} \langle\langle X \rangle\rangle_n(\lambda) &= \frac{1}{\mathcal{N}_n(\lambda)} \int [DU] e^{-S_\rho[U] + \lambda X[U]} X[U] \left[\theta\left(X[U] - x_n\right) - \theta\left(X[U] - x_{n+1}\right)\right], \\ &= \frac{1}{\mathcal{N}_n(\lambda)} \int_{x_n}^{x_{n+1}} dx \rho(x) x e^{\lambda x}. \end{aligned} \tag{3.2.7}$$

where $\theta(y)$ is the Heaviside step function with $\theta(y) = 0$ for $y < 0$ and $\theta(y) = 1$ for $y > 0$. The normalisation is given by,

$$\begin{aligned}\mathcal{N}_n(\lambda) &= \int [DU] e^{-S_\rho[U]+\lambda X[U]} \left[\theta\left(X[U]-x_n\right) - \theta\left(X[U]-x_{n+1}\right)\right], \\ &= \int_{x_n}^{x_{n+1}} dx \rho(x) e^{\lambda x}. \end{aligned} \tag{3.2.8}$$

Using the restricted vacuum expectation value, the function $Y_n(\lambda)$ is defined as,

$$Y_n(\lambda) = h((\lambda - k_n)\Delta_n) = \frac{\langle\langle X\rangle\rangle_n(\lambda) - \sum_{j=0}^{n-1}\Delta_j}{\Delta_n} - \frac{1}{2} = \frac{1}{1-e^{-(\lambda-k_n)\Delta_n}} - \frac{1}{(\lambda-k_n)\Delta_n} - \frac{1}{2} \tag{3.2.9}$$

Other than the input parameter λ, this function only depends on one parameter, the k_n value for that interval. To compute these coefficients, several simulations are carried out with configurations restricted to each interval, at several different λ values. From this the function $h((\lambda - k_n)\Delta_n)$ is computed at different λ values, and the parameter k_n can be fitted to the results. This is repeated for each interval, and the density of states is estimated.

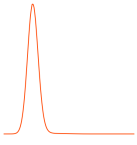

Chapter 4

$SU(3)$

> "I've always found that writing comes from a great inner pain."
> Barton Fink. Barton Fink (1991)

In the past the LLR method has been used to study a variety of statistical mechanics systems, and some initial work on gauge theories have been presented [120, 122, 128, 129]. However, many of the methods outlined in the last chapter had not been tested before we began our work. In particular our work was the first to implement the restricted heat bath algorithm, the partial form of domain decomposition and the use of a single sequence of half overlapping intervals, as opposed to two non-overlapping half-shifted replica sequences used in Ref. [145]. Our implementation of the method [5], through a modification to HiRep [146][1], was also new. As a verification for the method and the implementation, we chose to study the best tested non-Abelian gauge theory, $SU(3)$ pure gauge theory, as our first project.

The literature on the finite temperature deconfinement transition in $SU(3)$ pure gauge theory is extensive, see for example Ref. [103] and Ref. [104], and references therein. It corresponds to the infinite quark mass limit of QCD and is therefore phonologically interesting to standard model physics. As there are no dynamic fermions it is computationally less demanding than full QCD, and is used as an initial testbed for methods that aim to probe QCD. However, deconfinement in pure $SU(3)$ gauge theory is first order whereas QCD at the physical point is a cross-over, therefore it poses unique challenges. Although the pure gauge system is generally expected to have a weak first order transition, the meta-stability problems make precision studies of the thermodynamic and continuum limits difficult.

Another aim of this study was to determine the effects of the systematic error due to a finite interval size, Δ_E. We therefore focus on one lattice size, 4×20^3, with several interval sizes, and take the limit of $\Delta_E \to 0$. We aim to show that for a sufficiently small interval size,

[1] See Ref. [147] for an original description of the code.

the systematic error due to a finite interval, is $\propto \Delta_E^2$ and is smaller than the stochastic error from the repeats.

Most of the results reported in this chapter have appeared in Ref. [1], and the proceedings Ref. [130], Ref. [131] and Ref. [94]. The LLR code used for this work has been released in Ref. [5] and the analysis code is released in Ref. [4].

4.1 Initial importance sampling and finding the critical region

Before a full run of the LLR algorithm we require a study using importance sampling methods to determine the input parameters. In particular we need to know the range of the β values we are interested in studying, and from this the action range, E_{min} and E_{max}. These results will also allow further verification of the LLR method, by direct comparison.

In the literature for $N_t = 4$, in the thermodynamic limit, the critical coupling is given by $\beta_C = 5.69236(15)$, see Ref. [107]. Initially we carried out a scan of β values around this point, to determine the region of interest. We studied ensembles with lattice volume, $\tilde{V}/a^4 = 4 \times 20^3$, at inverse couplings $\beta = 5.660$, 5.680, 5.690, 5.700 and 5.720. For each β, we carry out 10,000 thermalisation steps followed by 500,000 measurements. Each update consisted of 1 heat-bath step followed by 4 over-relaxation steps. On each configuration we measured the Polyakov loop and the average plaquette. The error on the importance sampling results was found by binning the configurations into blocks length $5\tau_{int}$, and bootstrapping over the results. τ_{int} was estimated using Eq. 2.3.6, with the sum truncated when $t >= 4\tau_{int}$.

As mentioned in Chap. 2, the absolute value of the Polyakov loop is the order parameter of the transition. In the confined state, we expect it will vanish and in the deconfined state it will tend to a finite value. If a system is evolved in real time, across a first order phase transition we expect a discontinuity in this value. However, as we are analysing the equilibrium distribution on a finite sized lattice, we expect a smooth change in the VEV as we vary the inverse coupling across the transition. This corresponds to a finite value for the peak of the Polyakov loop susceptibility. In our LLR analysis, we want to encompass the β range in which this change is most prominent. Fig 4.1, shows the VEV of the absolute value of the Polyakov loop, $\langle |l_p| \rangle_\beta$, and the susceptibility, $\chi_l(\beta)$, against the inverse coupling, β. From this figure we determined the region of interest to be between $\beta = 5.68$ and 5.70. The susceptibility for points outside this region appear to plateau. We therefore added extra ensembles in this region, with $\beta = 5.685$ and 5.695. These points are also included in the plot.

Fig. 4.2 shows the VEV of the average plaquette, $\langle u_p \rangle_\beta$, and the specific heat, $C_V(\beta)$, against the inverse coupling. Again there appears to be an increased change in average plaquette around $\beta = 5.69$, as demonstrated by the specific heat peaking at this point.

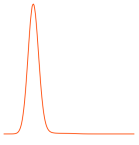

A histogram of the measured plaquette values is shown in Fig. 4.3. The four ensembles further from the critical point, β = 5.660, 5.680, 5.700 and 5.720, all appear to obey the expected Gaussian structure, hence they likely correspond to pure phase configurations. The two intermediate ensembles, β = 5.690 and 5.695, both appear to show the first indications of a divergence from this structure, with an initial display of coexisting phases due to a possible double peak structure.

To study the thermodynamic properties of the phase transition, we choose a range of β values between 5.680 and 5.700. To ensure we include all relevant micro-states, we choose the plaquette value at which the lower end of the distribution for the ensemble with β = 5.680 vanishes, $(u_p)_{min} \approx 0.54$, and the higher end of the β = 5.700 ensemble vanishes, $(u_p)_{max} \approx 0.56$. A selection of interval sizes, Δ_{u_p}, as set by the number of intervals, N_{int}, was chosen allowing the $\Delta_{u_p} \to 0$ limit to be taken. We chose N_{int} = 8, 15, 28, 55, 108.

A full list of the parameters chosen for this study is shown in Tab. 4.1. Most of the parameters were chosen through a combination of trial and error, and comparable values chosen elsewhere in the literature. For each interval size, we carry out twenty repeats with different random seeds. This should allow for the results to be analysed with Gaussian statistics. The lattice for each replica was broken down into 4 subdomains, such that each lattice update consisted of 1 restricted heat-bath update and 3 over-relaxation updates. For each update we chose 200 thermalisation steps and 500 measurements. We chose to carry out 500 RM iterations, followed fixed a_n steps with parameters $\hat{m}$ = 20 and n_{fxa} = 2000.

In this work we use no NR iterations, $\bar{m}$ = 0. When this work was carried out, NR iterations were not implemented in the code, instead several sets of RM iterations were taken with $\tilde{m}$, very small. The final values were inputted as the initial values of the next set. This gave a_n values sufficiently close to the expected true value, removing the need for the NR iterations.

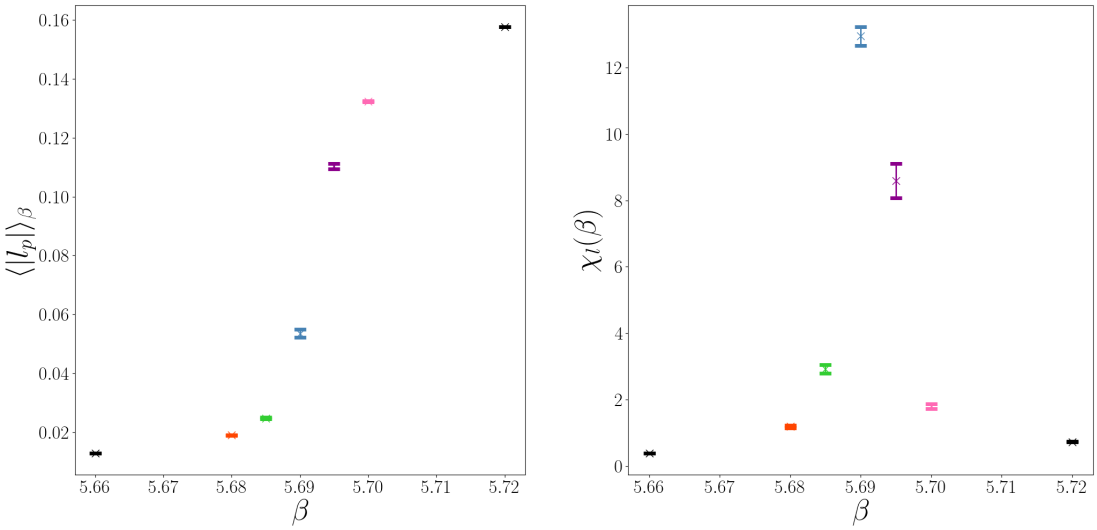

Figure 4.1. Importance sampling results for the VEV of the absolute value of the Polyakov loop (left), $\langle |l_p| \rangle_\beta$, and the susceptibility (right), $\chi_l(\beta)$, against the inverse coupling, β, for $SU(3)$ pure gauge theory on a lattice of size 4×20^3. For each ensemble 500,000 measurements were taken after 10,000 thermalisation steps. Each update involved 1 heat-bath, followed by 4 over-relaxation steps. The errors were computed by binning and bootstrapping the results.

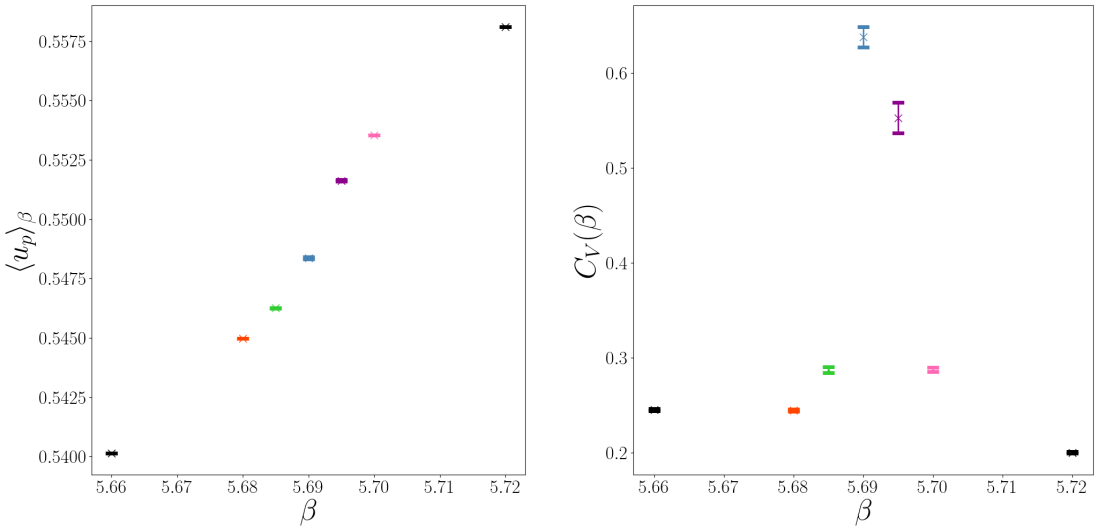

Figure 4.2. Importance sampling results for the VEV of the average plaquette (left), $\langle u_p \rangle_\beta$, and the specific heat (right), $C_V(\beta)$, against the inverse coupling, β, for $SU(3)$ pure gauge theory on a lattice of size 4×20^3. For each ensemble 500,000 measurements were taken after 10,000 thermalisation steps. Each update involved 1 heat-bath, followed by 4 over-relaxation steps. The errors were computed by binning and bootstrapping the results.

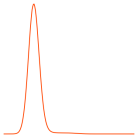

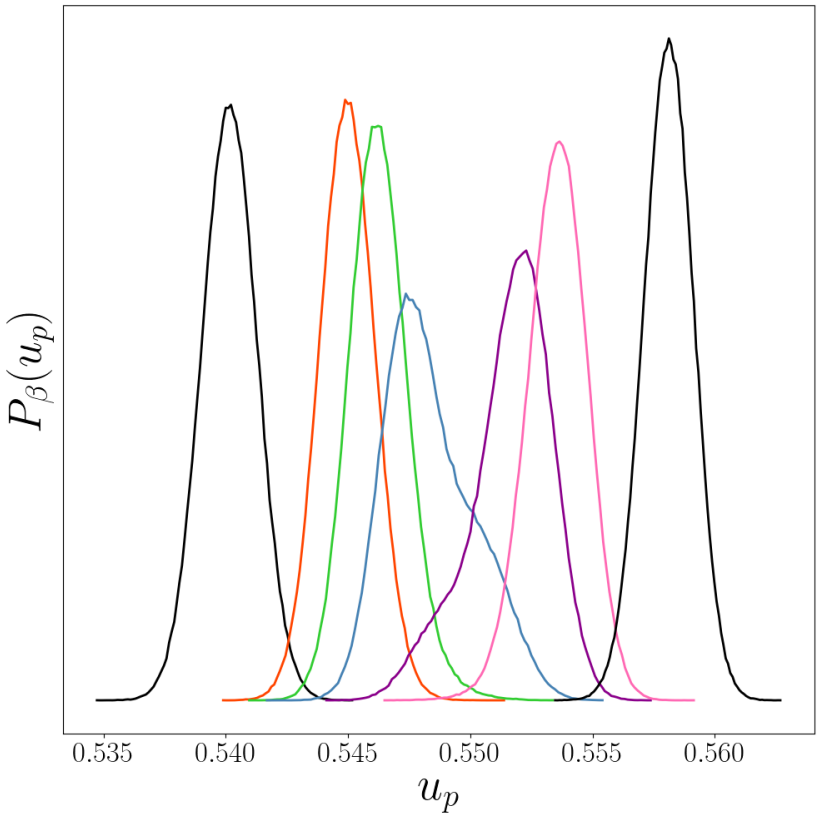

Figure 4.3. The histogram of the measured average plaquette values, u_p, at a range of inverse couplings, from left to right β = 5.660, 5.680, 5.685, 5.690 , 5.695, 5.700, 5.720, for $SU(3)$ pure gauge theory on a lattice of size 4×20^3. For each ensemble 500,000 measurements were taken after 10,000 thermalisation steps. Each update involved 1 heat-bath, followed by 4 over-relaxation steps. The colours of these histogram match the colour of the points in Fig. 4.1 and Fig. 4.2.

Table 4.1. A list of parameters for the study of the deconfinement transition in $SU(3)$ pure gauge theory on a lattice of size 4×20^3, using the LLR method. The parameters were chosen such that the $\Delta_{u_p} \to 0$ limit could be taken. The interval size, Δ_{u_p}, and the centre of each interval, $(u_p)_n$, have been quoted to 4 decimal places for convenience. The definitions for the variables of this table are given in Tab. 3.1.

$\tilde{V}/a^4$	N_D	N_{int}	n_R	Δ_{u_p}	$(u_p)_{\min}$	$(u_p)_{\max}$	$\bar{m}$	$\tilde{m}$	$\hat{m}$	n_{Th}	n_M	n_{fxa}	n_{ITh}
4×20^3	4	8	20	0.0063	0.5373	0.5594	0	500	20	200	500	2000	10000
4×20^3	4	15	20	0.0030	0.5396	0.5605	0	500	20	200	500	2000	10000
4×20^3	4	28	20	0.0015	0.5403	0.5605	0	500	20	200	500	2000	10000
4×20^3	4	55	20	0.0007	0.5403	0.5605	0	500	20	200	500	2000	10000
4×20^3	4	108	20	0.0004	0.5404	0.5604	0	500	20	200	500	2000	10000

4.2 Verification of the method

The results for the coefficients, a_n, for all intervals, $(u_p)_n$, at each interval size, Δ_{u_p}, are shown for $SU(3)$ pure gauge theory on a lattice of size 4×20^3, in Fig. 4.4. Each interval size is represented by a different colour. The top plot shows the full range of plaquette values, while the bottom plot is focused on the critical region, $\beta \approx 5.692$. Around the critical point, the function $a_n(u_p)$ becomes non-invertible. As we will show later, this indicates co-existing vacua at the same temperature. This behaviour is seen in all but the largest interval size, $\Delta_{u_p} = 0.0063$. This underpins the importance of analysing the results in the $\Delta_{u_p} \to 0$ limit, as for this ensemble the statistical error on a_n is much smaller than the systematic error due to a finite Δ_{u_p}. This can be seen from the difference between the curves at different interval sizes, particularly for the two largest interval sizes. However, as expected, the results appear to converge as the interval size vanishes.

After running all the ensembles, we verified that the results were consistent with our expectations. First we checked that for each interval, n, the coefficients, $a_n^{(m)}$, for each repeat behaved as expected, as it is updated through the RM iterations. Fig. 4.5 shows an example RM trajectory for an interval centred at $(u_p)_n = 0.540676$, with $\Delta_{u_p} = 0.0007$, through 500 iterations. In the figure, twenty independent trajectories are shown, one from each repeat, in different colours. Initially, the trajectories follow large oscillations around their final value, the oscillations then dampen and converge to their final value. The distribution of final values $a_n^{(\tilde{m})} = a_n$, is shown in the inset of the figure. This is compatible with a Gaussian distribution.

Fig. 4.6, shows the same trajectory plot for all intervals. With the results for different intervals being shown in different colours. Colours are repeated if the intervals don't overlap. For all intervals, it demonstrates the results converge to their final value. In the centre of the plot around, $a_n \sim 5.692$, the results for different intervals begin to overlap, corresponding to the non-invertibility of $a_n(u_p)$ at the critical point.

The standard deviation of $a_n^{(m)}$ values through m RM trajectories across the repeats, $\sigma(a_n^{(m)})$, has a theoretical best scaling behaviour of $\sigma(a_n^{(m)}) \sim 1/\sqrt{m}$ [126]. We want to ensure we are close to this asymptotic behaviour, and have therefore carried out sufficient RM iterations. Fig. 4.7 shows a plot of the natural log of the standard deviation, $\ln\left(\sigma(a_n^{(m)})\right)$, against the natural log of the iteration number, for all intervals in different colour. If we have reached the asymptotic convergence we expect the gradient of this line to be $-1/2$. We have taken a linear fit of $\ln\left(\sigma(a_n^{(m)})\right)$ against $\ln m$ for all the intervals, $\ln\left(\sigma(a_n^{(m)})\right) = M \ln m + c$. The mean gradient for all intervals was found to be $M = -0.497(68)$, where the error is the standard deviation. We can therefore verify that we have approached the asymptotic regime and all trajectories are likely converging to the same value. Therefore, our statistical error on

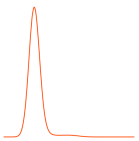

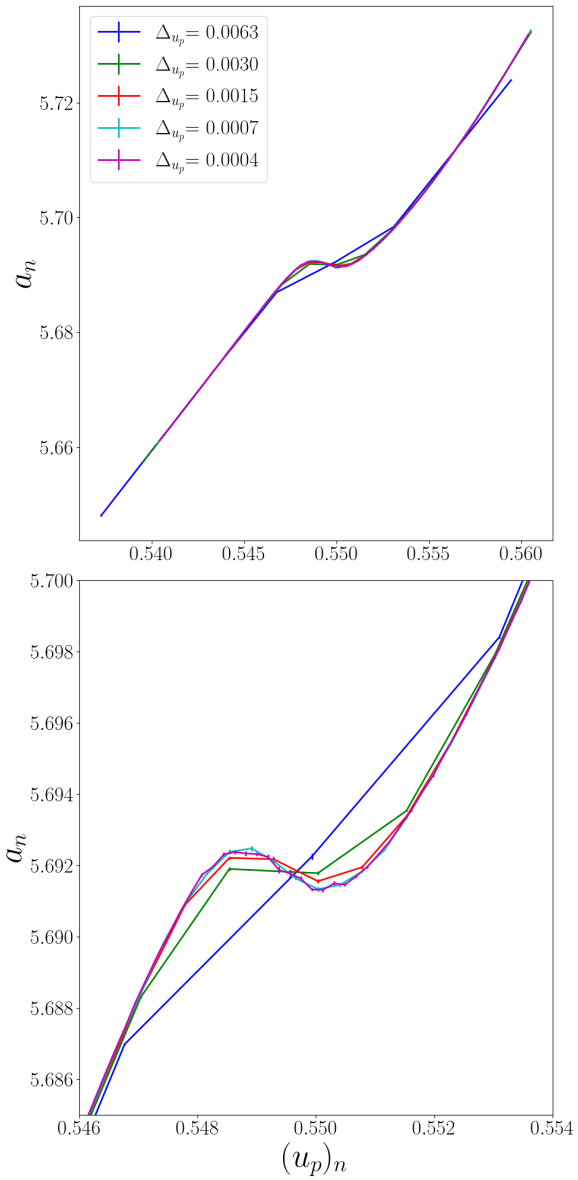

Figure 4.4. The final values of the coefficient, a_n, after 500 RM iterations, are shown against the centre of their interval, $(u_p)_n$, with different interval sizes, Δ_{u_p}, are shown in different colours. The bottom panel shows identical data to the top panel but focused on the critical region, which shows the non-invertible structure of $a_n(u_p)$. The figure originally appeared in Ref. [1].

the final values of a_n should be a good estimate for the truncation error.

The above plots indicate that in this case, far fewer iterations would be required to gain a good estimate for a_n. The standard deviation of $a_n^{(m)}$ appears to reach the asymptotic behaviour very quickly, however further iterations decrease the error. For larger volumes, a

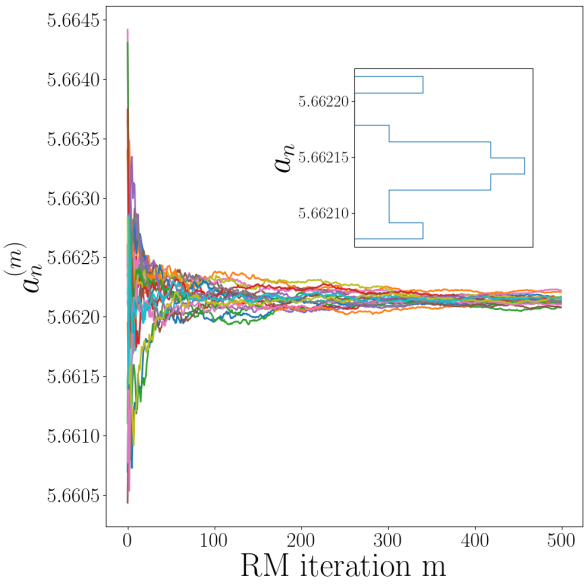

Figure 4.5. The history of an example coefficient $a_n^{(m)}$ is shown against the iteration number m, for 500 RM iterations. 20 repeats are shown by the different colours. The interval is centred at $(u_p)_n$ = 0.540676, for a system with interval size Δ_{u_p} = 0.0007. The distribution of the final a_n values is shown in the inset. The figure originally appeared in Ref. [1].

smaller number of iterations should be used, with a balance considered between improvements in error and computational cost.

Between RM updates, to ensure the method is ergodic, replicas can be exchanged between neighbouring intervals, as discussed in Sec. 3.1.2. Fig. 4.8, demonstrates this process through the 500 RM iterations. It shows an example history of one repeat for the coefficient, $a_n^{(m)}$, for all intervals. The colours of the lines follow the trajectory of a replica as it is exchanged between intervals, the colours have rainbow colour map and depend on the initial interval. Although all the trajectories are swapped between intervals, few of the replicas move between phases, this is due to the different microscopic structure of the configurations in each phase. The clustering of values around $a_n \sim 5.692$, is due to non-invertibility of $a_n(u_p)$ around the critical point.

After completing the RM iterations, we carried out a set of fixed a_n iterations measuring the value of the Polyakov loop and the average plaquette on configurations with their action restricted to the interval. This will allow us to reconstruct the VEV of the Polyakov loop and the susceptibility using Eq. 3.1.27. It also allows for a direct verification that the RM iterations have solved Eq. 3.1.11, by directly calculating the average of $\Delta E = E - E_n$, on the configurations in each interval. The results are shown in Fig. 4.9. The blue dots show the results for each repeat, the black dots show the mean of this value and the red region shows the error on the mean. Away from the phase transition all intervals appear to be within error

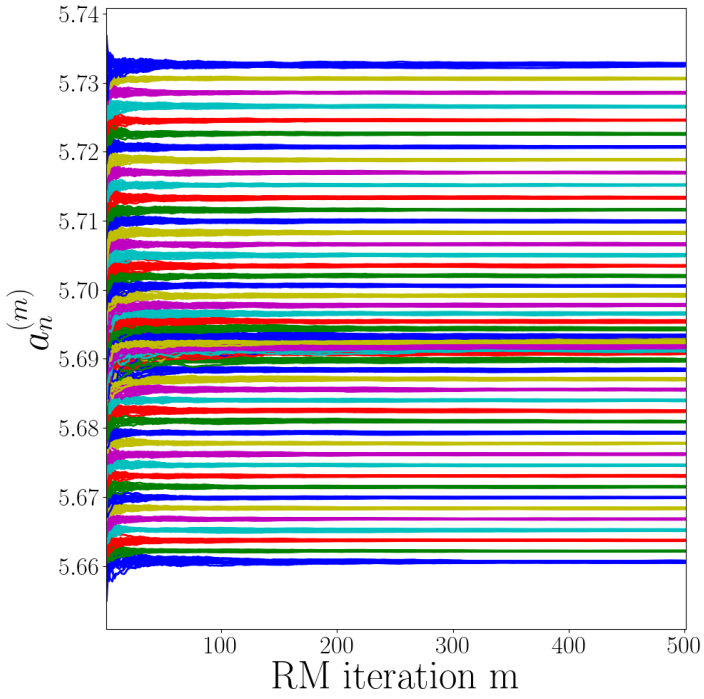

Figure 4.6. The history of the coefficients $a_n^{(m)}$ are shown for all intervals and all repeats, against the iteration number m, for 500 RM iterations. The colours show the results for different intervals, with colours repeated when the intervals will not overlap. This results is for a system with interval size $\Delta_{u_p} = 0.0007$.

of 0, as we expect. Some of the points around the critical point, between $(u_p)_n \approx 0.5475$ and 0.5525, are outside one error of the mean of 0, however the spread of results for these intervals is largest.

The goal of the density of states method is to sample a flat energy distribution to avoid the meta-stability problems of the standard importance sampling approach. In Fig. 4.10, we demonstrate an example of the distribution of the measured values plaquette values during the fixed a_n iterations. Between $(u_p)_1$ and $(u_p)_{N_{int}}$, the distribution appears to be approximately flat. Outside this region, we have the Gaussian tails, as discussed in Sec. 3.1.2, allowing the system to escape our energy boundaries and to ensure ergodicity of the algorithm.

Fig. 4.5, Fig. 4.6 and Fig. 4.7, show that in each interval the coefficients a_n appear to converge to the same value, at the rate expected for the asymptotic regime of RM iterations, and the final values for across the repeats for each interval an approximately Gaussian distribution around the mean. The final values are plotted against the centre of the interval in Fig. 4.4, for all interval sizes. Excluding the ensemble with the coarsest interval size, $\Delta_{u_p} = 0.0063$, the functional form of $a_n(u_p)$ appears to be the same, single valued away from the transition, with a non-invertibility in the critical region, between $u_p \approx 0.547$ and

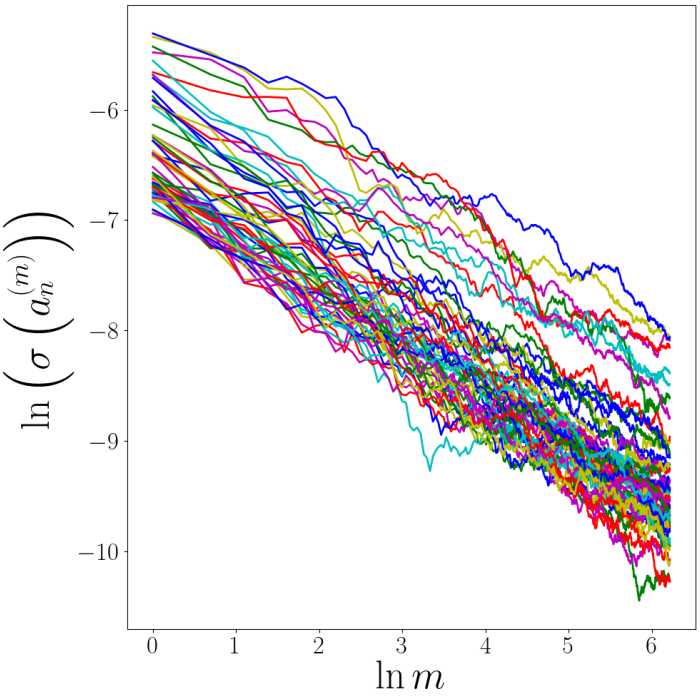

Figure 4.7. The natural log of the standard deviation across the repeats of the value of $a_n^{(m)}$, $\ln\left(\sigma(a_n^{(m)})\right)$, as a function of the natural log of the iterations number, $\ln m$, is plotted with each interval, n, in a different colour. These results are for a system with interval size, $\Delta_{u_p} = 0.0007$. A linear fit was taken of this function, $\ln\left(\sigma(a_n^{(m)})\right) = M \ln m + c$, mean gradient across the intervals was found to be $M = -0.497(68)$. This demonstrates the expected scaling behaviour of the standard deviation as a function of iteration number, $\sigma(a_n^{(m)}) \sim 1/\sqrt{m}$.

0.552, we will later demonstrate that this indicates the meta-stable dynamics characteristic of a first order transition. The coarsest interval size does not contain the non-invertibility, which demonstrates the importance of carefully taking the limit of vanishing interval size. By analysing the fixed a_n iterations, Fig. 4.9 and Fig. 4.10, we verified that our final values of a_n solves Eq. 3.1.11 and leads to a flat energy distribution. Our results will give an estimate for the density of states, with statistical error given by the independent repeats and a systematic error, due to finite interval size, that can be estimated through the limit, $\Delta_{u_p} \to 0$.

4.2.1 Comparison with Importance Sampling

After verifying the algorithm has given results consistent with our expectations for the LLR method, we confirm it agrees with conventional importance sampling methods. We use the results for the importance sampling ensembles discussed in Sec. 4.1, with $\beta = 5.68000$, 5.68500, 5.69000, 5.69500 and 5.70000. To this we add an additional ensemble with $\beta =$

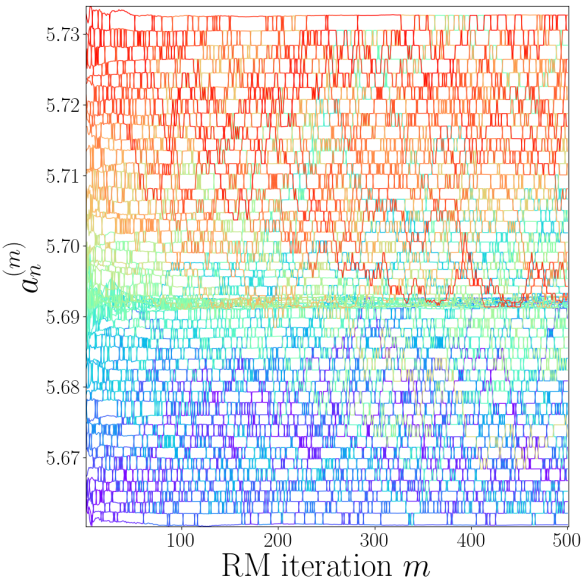

Figure 4.8. The history for the coefficients $a_n^{(m)}$ are shown for all intervals, $m = 1, ..., N_{int}$, as they are updated through 500 RM iterations for the system with interval size $\Delta_{u_p} = 0.0007$. The trajectories of the replicas are shown as they are exchanged between intervals, the colour of each trajectory shows the replica's initial interval. The figure originally appeared in Ref. [1].

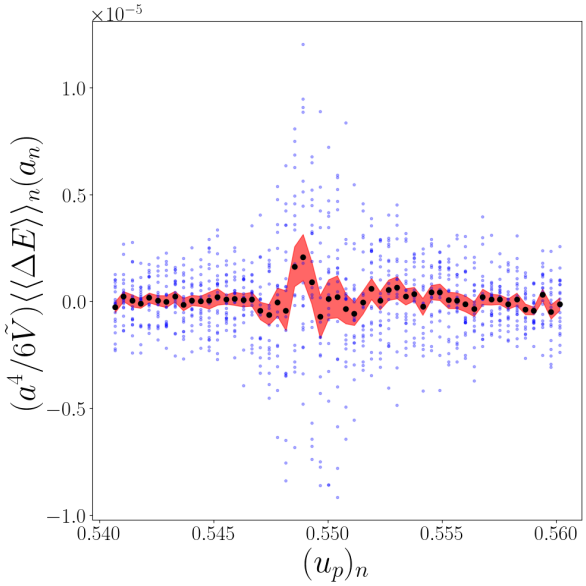

Figure 4.9. The ensemble average of the difference between the measured energy and the centre of the interval, ΔE, measured on configurations with their action restricted to a given interval with fixed a_n value, is plotted for each interval, centred on $(u_p)_n$. This system has an interval width, $\Delta_{u_p} = 0.0007$. Results for each of the 20 repeats are shown by blue dots, the black dots show the mean value, and the red shaded region shows the error on the mean.

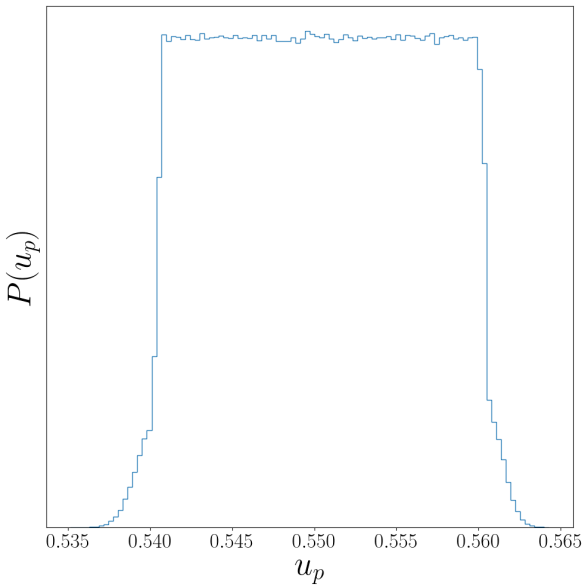

Figure 4.10. The combined histogram for all intervals of the measured average plaquette values for configurations restricted to each energy interval with fixed a_n values. Between $(u_p)_1$ and $(u_p)_{N_{int}}$, the distribution is approximately flat, while outside this region the distribution has Gaussian tails. These results are for a single repeat with interval width $\Delta_{u_p} = 0.0007$. The figure originally appeared in Ref. [1].

5.69187, the critical point as determined by the LLR method, more details on the determination of this value will be given in the next section. This new ensemble has the same parameters as the other ensembles, with 10,000 thermalisation steps followed by 500,000 measurements, and 4 over-relaxation updates and heat-bath step per update. For this ensemble we have ensured that the system has tunneled between the different phases many times, and therefore we don't expect any large systematic errors associated with the meta-stability.

On the LLR results we expect a systematic error that scales with the square of the interval size, Δ_E^2 $(= (\Delta_{u_p} 6\tilde{V}/a^4)^2)$. We compare the limit of vanishing interval size with the importance sampling results. We are particularly interested in testing whether the results for ensembles with the smallest interval sizes ($\Delta_{u_p} = 0.0007$ and 0.0004) are within the error on the extrapolated results. This will verify whether a full extrapolation is required for every lattice size to obtain accurate results.

Through Eq. 3.1.20 we can compute the plaquette distribution, $P_\beta(u_p)$, for a inverse couplings between $\beta = 5.68$ and 5.70. In the left plot Fig. 4.11, we directly compare the LLR results, solid blue line, with the histogram from importance sampling, orange dashed line, for one interval size $\Delta_{u_p} = 0.0007$. There is very good agreement, particularly for the $\beta = 5.68, 5.685$ and 5.700, the ensembles away from the meta-stable region. The agreement

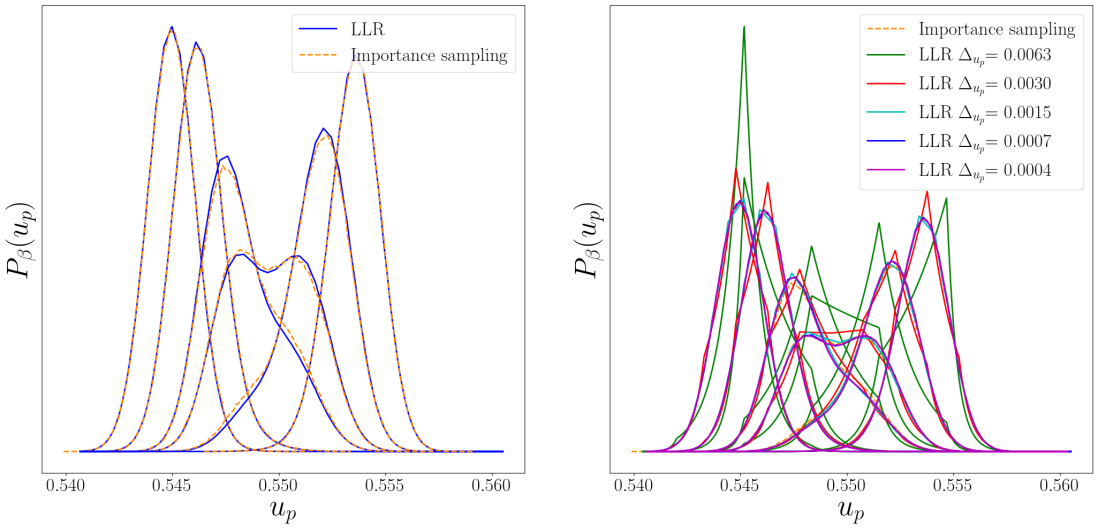

Figure 4.11. Comparison between the plaquette distribution, $P_\beta(u_p)$, calculated with the LLR method (solid line), and the histogram from importance sampling results (orange dashed line). The left plot, which originally appeared in Ref. [1], shows the results for one interval size, $\Delta_{u_p} = 0.0007$, whereas the right plot shows the results for all interval sizes, in different colours. The plaquette distributions are shown for six β values, from left to right: $\beta = 5.68000$, 5.68500, 5.69000, 5.69187, 5.69500 and 5.70000.

between the other ensembles with other inverse couplings is still evident, however there are small discrepancies around the peaks. However, it is not clear if the difference is due to the large auto-correlation time close the phase transition, which has not been accounted for in the histogram of the importance sampling results, or if it is from the LLR method results. The right plot of this figure shows the plaquette distribution for the other different interval sizes, shown in different colours. For the larger interval sizes, $\Delta_{u_p} = 0.0063$ and 0.0030, it cannot correctly resolve the structure of the distributions, particularly for $\beta = 5.69187$, in which the double peak structure, clearly visible for the smaller interval sizes, does not appear at all.

Using Eq. 3.1.18, we can compute the average plaquette, the specific heat (Eq. 2.2.22) and the Binder cumulant (Eq. 2.2.25). We calculate these values for 1000 β values in the critical region, between $\beta = 5.690$ and 5.695, in order to determine the peak of the specific heat and the minima of the Binder cumulant. We also calculated these observables at inverse couplings directly comparable with the importance sampling ensembles. The error on the LLR results is calculated by calculating the observable for a given β value on all repeats at a given interval size, then bootstrapping the final results, to estimate the error on the mean.

The results for the average plaquette, specific heat and Binder cumulant are shown in the left plots of Fig. 4.12, Fig. 4.13, Fig. 4.14, respectively. The solid lines show the mean value across the repeats of the fine scan of β values, with different interval sizes shown in different colours. The errors on these values are given by the dashed line. The black dots

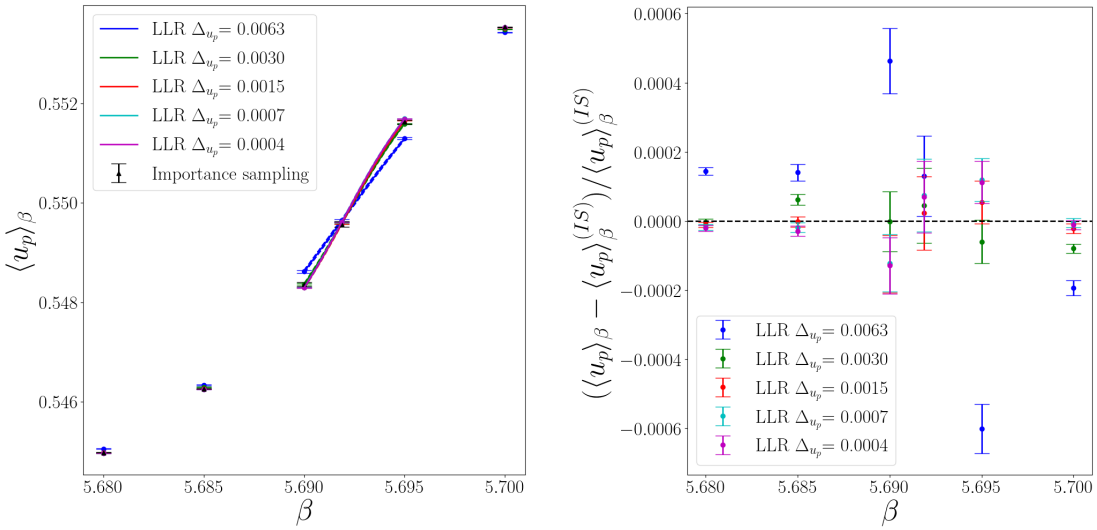

Figure 4.12. The VEV of the average plaquette, computed at different couplings, from the LLR method, at different interval widths, Δ_{u_p}, shown in different colours, is compared with the importance sampling results. The importance sampling results are for ensembles calculated at β = 5.68000, 5.68500, 5.69000, 5.69187, 5.69500, and 5.70000. The left plot shows the VEV of the average plaquette against β, when calculated with both methods. The coloured dots show the LLR results with direct comparison to the importance sampling results and the solid lines shows the LLR results for a fine scan of 1000 points evenly spaced between β = 5.690 and 5.695. Note the coloured dots and the solid lines overlap within the region of the fine scan. The black dots show the importance sampling results. The right plot shows the percentage difference between the LLR results and the importance sampling results. The figures originally appeared in Ref. [1].

show the importance sampling results, while the coloured dots show the LLR results at the same inverse coupling.

The peak of the specific heat and minima of the Binder cumulant are shown by the dashed vertical lines, while the shaded region shows the corresponding errors. These extremal values are found by determining the inverse coupling that gives the maximum (minima) value of the observable. We choose the range and number of β values in this fine scan to ensure that the error on the peak is due to statistical difference between the a_n values in each repeat, rather than the difference between measured β values. This was ensured by plotting the histogram of measured values and checking it was approximately Gaussian.

In the right hand plots of Fig. 4.12, Fig. 4.13 and Fig. 4.14, the direct comparison between importance sampling and the LLR results are shown. These figures show the percentage difference between the two methods, the superscript (IS) denotes the importance sampling result. The errors are calculated by propagating the error from LLR and IS. The LLR results are consistent with the importance sampling result if the points are within error of the dashed black line at 0.

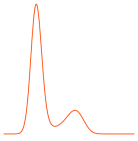

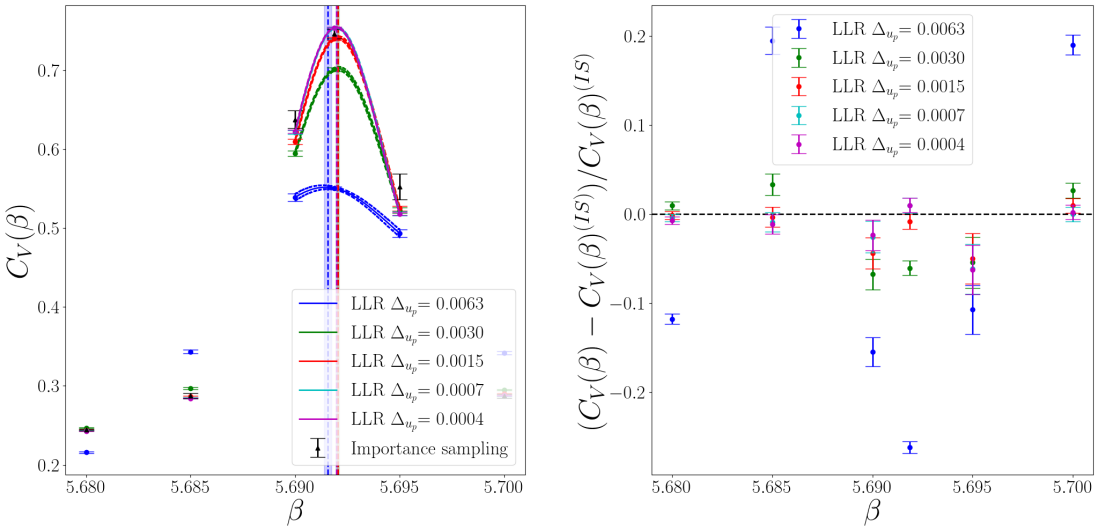

Figure 4.13. The specific heat, computed at different inverse couplings, from the LLR method, at different interval widths, Δ_{u_p}, shown in different colours, is compared with the importance sampling results. The importance sampling results are for ensembles calculated at β = 5.68000, 5.68500, 5.69000, 5.69187, 5.69500, and 5.70000. The left plot shows the specific heat against β, when calculated with both methods. The coloured dots show the LLR results with direct comparison to the importance sampling results and the solid lines shows the LLR results for a fine scan of 1000 points evenly spaced between β = 5.690 and 5.695. Note the coloured dots and the solid lines overlap within the region of the fine scan. The inverse coupling corresponding to the peak is shown by the dashed line and the surrounding shaded region shows the error. The black dots show the importance sampling results. The right plot shows the percentage difference between the LLR results and the importance sampling results. The figures originally appeared in Ref. [1].

For all observables, $\langle u_p \rangle_\beta$, $C_V(\beta)$ and $B_V(\beta)$, the behaviour of the system with the largest interval size, Δ_{u_p} = 0.0063, differs from the other interval sizes. The change in all observables is smooth, and the extrema of the Binder cumulant and specific heat are lower and shifted to a smaller β. This is due to the difference in structure of the function of $a_n(u_p)$. The non-invertibility of this function in the other systems leads to the meta-stable dynamics and therefore the behaviour characteristic of the a first order transition. Whereas for this system no double peak structure was observed in the plaquette distribution, leading to a completely different behaviour of the value of the observables.

As the interval size decreases, the value of the observables tend to the same value, around the value for the smallest interval size, Δ_{u_p} = 0.0004. The results for the two smallest intervals are consistent with each other. This can be seen in both the left and right hand plots. The right hand plots in particular show that, generally, as the interval size is decreased the result tends towards the importance sampling value, giving a good posterior justification of the method. However, not all points are consistent with importance sampling.

Using Eq. 3.0.3, we can calculate the Polyakov loop and the susceptibility (Eq. 2.2.19).

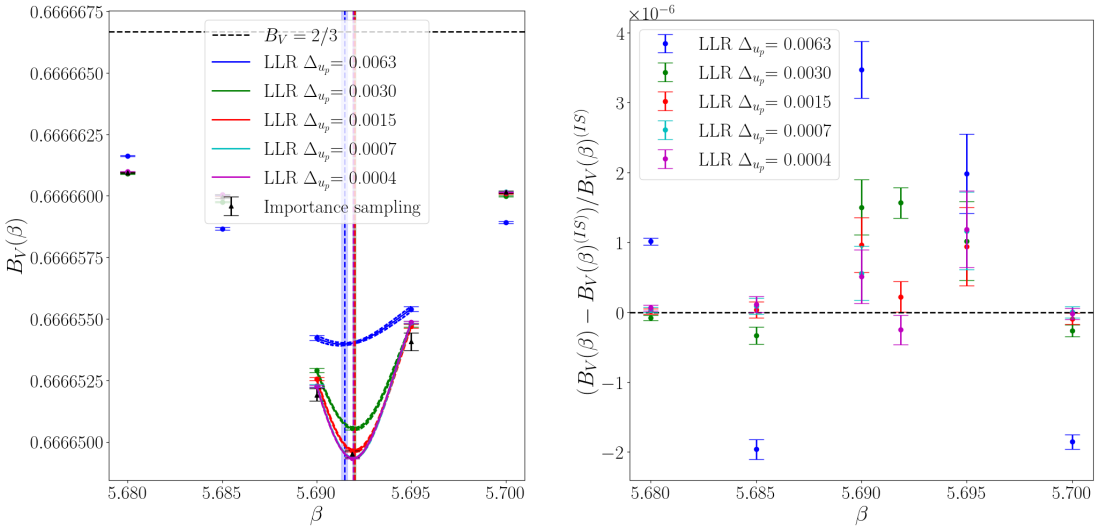

Figure 4.14. The Binder cumulant, computed at different inverse couplings, from the LLR method, at different interval widths, Δ_{u_p}, shown in different colours, is compared with the importance sampling results. The importance sampling results are for ensembles calculated at β = 5.68000, 5.68500, 5.69000, 5.69187, 5.69500, and 5.70000. The left plot shows the Binder cumulant against β, when calculated with both methods. The coloured dots show the LLR results with direct comparison to the importance sampling results and the solid lines shows the LLR results for a fine scan of 1000 points evenly spaced between β = 5.690 and 5.695. Note the coloured dots and the solid lines overlap within the region of the fine scan. The inverse coupling corresponding to the peak is shown by the dashed line and the surrounding shaded region shows the error. The black dots show the importance sampling results. The dashed horizontal black line in the left plot is at 2/3. The right plot shows the percentage difference between the LLR results and the importance sampling results. The left figure originally appeared in Ref. [1].

To compute the value in the double angle bracket, we carry out fixed a_n iterations, in which we measure the value of the Polyakov loop for configurations with action restricted to each interval. The results are shown in Fig. 4.15 and Fig. 4.16. The solid lines in the left plots show the values calculated for 100 β values between 5.690 and 5.695, while the dots show the results directly comparable with our importance sampling ensembles. The errors on the fine scan, shown by the dashed lines, are found by bootstrapping the results for the repeats. The colours show the results for different interval sizes. The vertical lines in the plots of the Polyakov loop susceptibility shows the inverse coupling corresponding to the peak the of the curve. The right plots again show the percentage difference between the LLR results and the importance sampling results, with errors found through propagation of the LLR and IS errors. These observables also appear to tend towards the same value, given by the smallest interval size. However, the results in this case seem more stable, with even largest interval size system agreeing.

The limit of vanishing interval size has been analysed for the peaks of the specific heat,

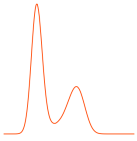

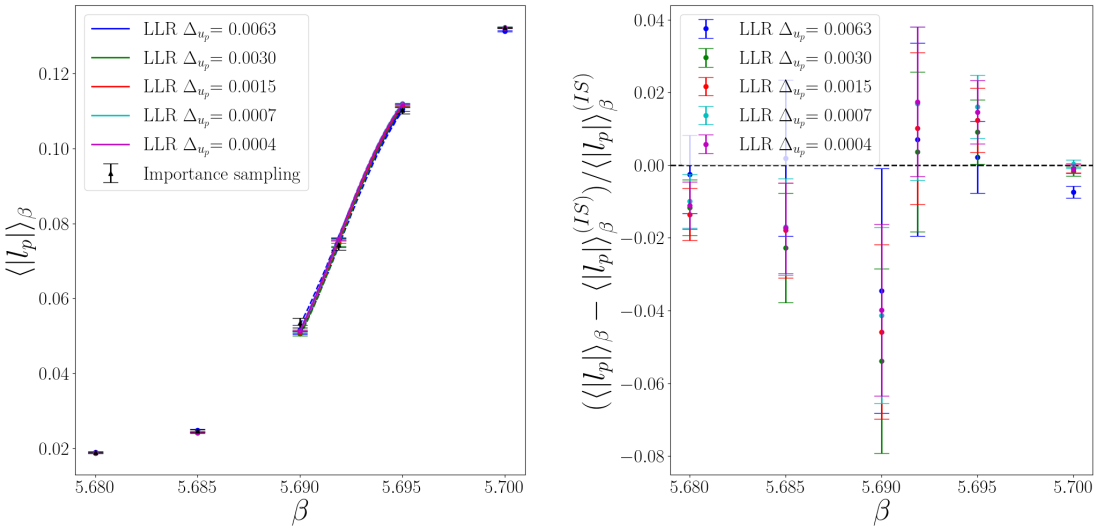

Figure 4.15. The VEV of the absolute value of the Polyakov loop, computed at different inverse couplings, from the LLR method, at different interval widths, Δ_{u_p}, shown in different colours, is compared with the importance sampling results. The importance sampling results are for ensembles calculated at β = 5.68000, 5.68500, 5.69000, 5.69187, 5.69500, and 5.70000. The left plot shows the absolute value of the Polyakov loop against β, when calculated with both methods. The coloured dots show the LLR results with direct comparison to the importance sampling results and the solid lines shows the LLR results for a fine scan of 100 points evenly spaced between β = 5.690 and 5.695. Note the coloured dots and the solid lines overlap within the region of the fine scan. The black dots show the importance sampling results. The right plot shows the percentage difference between the LLR results and the importance sampling results. Figures originally appeared in Ref. [1].

$C_V^{(max)}$, the Polyakov loop susceptibility, $\chi_L^{(max)}$, and the minima of the Binder cumulant, $B_V^{(min)}$. Fig. 4.17 and Fig. 4.18 show the measured value at the extrema of these curves against the square of the interval size. The colours of the points in this plot correspond directly to the colours of the curves in the previous figures showing the values of these observables. The black dashed line shows a linear extrapolation of the four finest interval sizes to $\Delta_{u_p} \to 0$. We choose not to use the interval Δ_{u_p} = 0.0063 in this extrapolation, as it clearly obeys a different behaviour to the other systems and is therefore not in the asymptotic regime of the $\Delta_{u_p} \to 0$ limit. The extrapolated point is shown by a black dot, the error was calculated from the error on the intercept of the extrapolation.

The extrapolation of the LLR results for the peak of the specific heat was given by $C_V^{(max)}$ = 0.7553(7), with a reduced chi-square of χ_ν^2 = 1.76. This value is within the error of the measured value for the two smallest interval sizes, Δ_{u_p} = 0.0007 and 0.0004, with values $C_V^{(max)}$ = 0.7546(11) and 0.7553(7), respectively. Similarly, the results for the two smallest interval sizes for the minima of the Binder cumulant are consistent with the extrapolation, $B_V^{(min)}$ = 0.66664931(1) with χ_ν^2 = 1.45, compared with 0.66664932(3) and 0.66664933(2) for

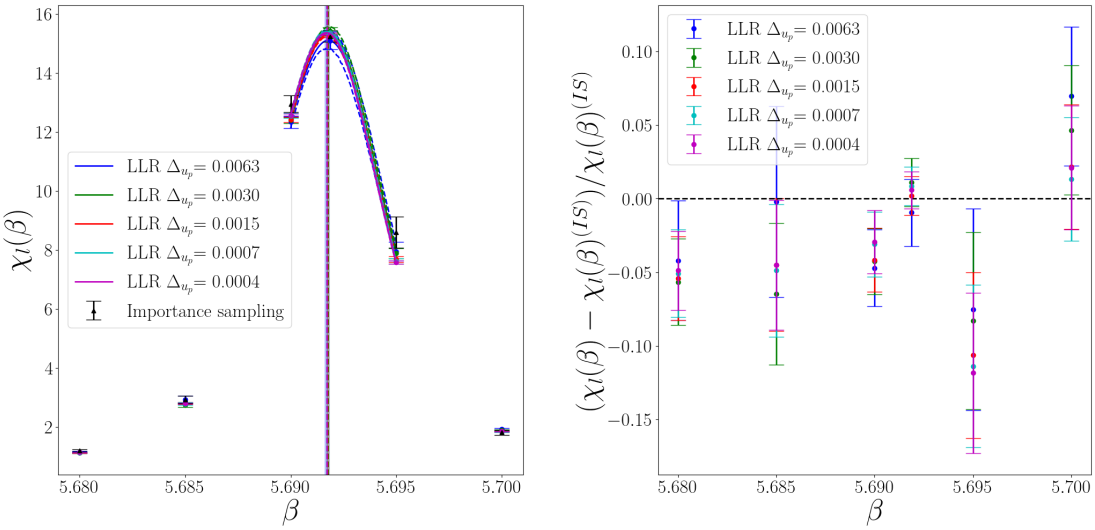

Figure 4.16. The Polyakov loop susceptibility, computed at different inverse couplings, from the LLR method, at different interval widths, Δ_{u_p}, shown by different colours is compared with the importance sampling results. The importance sampling results are for ensembles calculated at β = 5.68000, 5.68500, 5.69000, 5.69187, 5.69500, and 5.70000. The left plot shows the Polyakov loop susceptibility against β, when calculated with both methods. The coloured dots show the LLR results with direct comparison to the importance sampling results and the solid lines shows the LLR results for a fine scan of 100 points evenly spaced between β = 5.690 and 5.695. Note the coloured dots and the solid lines overlap within the region of the fine scan. The inverse coupling corresponding to the peak is shown by the dashed line and the surrounding shaded region shows the error. The black dots show the importance sampling results. The right plot shows the percentage difference between the LLR results and the importance sampling results. The figures originally appeared in Ref. [1].

Δ_{u_p} = 0.0007 and 0.0004. These results indicate that we can use the smallest two interval sizes to accurately estimate the observable without taking the $\Delta_{u_p} \to 0$ limit, although it is difficult to know a priori the required interval size.

As with the previous analysis of the Polyakov loop susceptibility, the results for the peak have less dependence on the Δ_{u_p}, with the results of all interval sizes being consistent with the extrapolation, $\chi_l^{(max)}$ = 15.37(3) with a reduced chi-square of χ^2_ν = 0.85. However, as we decrease the interval size there is a large decrease in the error, therefore considering the $\Delta_{u_p} \to 0$ limit is still important for accurate results.

We carry out the same analysis for the values of the coupling at the peak of the specific heat, $\beta_{CV}(C_V)$, the minima of the Binder cumulant, $\beta_{CV}(B_V)$, and the peak Polyakov loop susceptibility, $\beta_{CV}(\chi_l)$, the results are shown in Fig. 4.19. The different colours show the results for the different observables. In the thermodynamic limit we expect these quantities to converge, to the critical coupling β_C, however at a finite volume there will be a systematic error on the value. The extrapolations are given by $\beta_{CV}(C_V)$=5.69197(2), $\beta_{CV}(B_V)$=5.69194(1) and $\beta_{CV}(\chi_l)$=5.69171(1), with reduced chi-squares of χ^2_ν = 1.19, 1.29 and 0.47 respectively. In

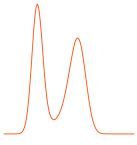

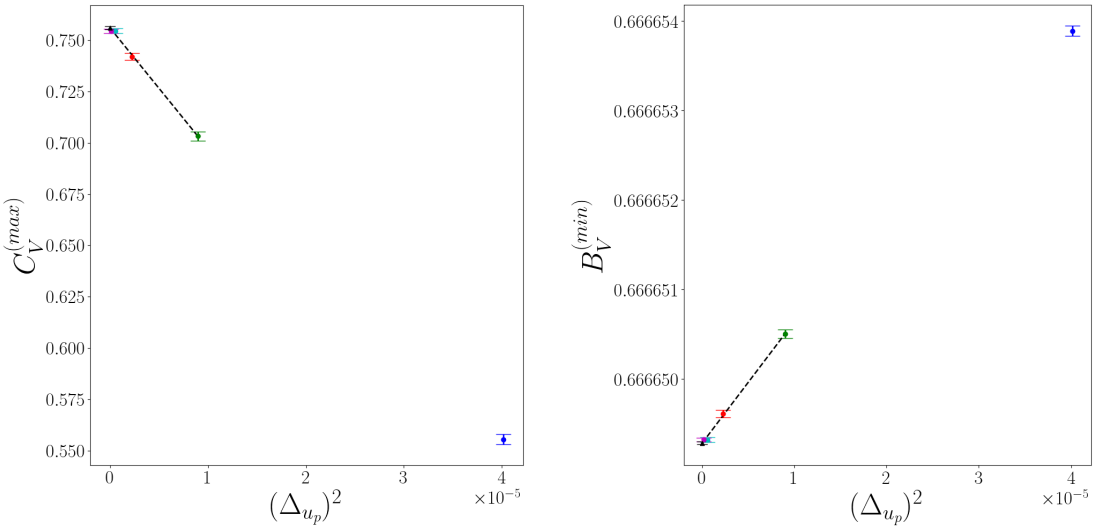

Figure 4.17. The peak of the specific heat (left), $C_V^{(max)}$ (left), and the minima of the Binder cumulant (right), $B_V^{(min)}$, are plotted against the square of the interval size, $\Delta_{u_p}^2$. The extrema were found by taking the maximum value of a fine a scan of 1000 β values between $\beta = 5.690$ and 5.695, for each repeat, then bootstrapping the results to estimate the error. In both plots the limit of vanishing interval width, $\Delta_{u_p} \to 0$, is taken, by taking a linear fit of the observable against $\Delta_{u_p}^2$, for the results of the four finest interval sizes. The fit is shown by the black dashed line, while the black triangle shows the value extrapolated to $\Delta_{u_p} = 0$. The fit of the specific heat had a reduced chi-square of $\chi_\nu^2 = 1.76$, and the extrapolation gave $C_V^{(max)} = 0.7553(7)$. The fit of the Binder cumulant had a reduced chi-square of $\chi_\nu^2 = 1.45$, and the extrapolation gave $B_V^{(min)} = 0.66664931(1)$. These figures originally appeared in Ref. [1].

all cases the two finest interval sizes are consistent with the extrapolations. The values of the extrema of the observables and their the corresponding couplings are shown in Tab.4.2.

We have demonstrated that for all observables, and for the plaquette distribution, the LLR results converge towards the results for the smallest interval size, and that they all agree well with our importance sampling results. The behaviour of the system with the largest interval size, $\Delta_{u_p} = 0.0063$, differs greatly from the others. The non-invertibility in the function $a_n(u_p)$, for the other interval sizes leads to the co-existing phases in the critical region, this idea will be discussed further in the next section. The two smallest interval sizes $\Delta_{u_p} = 0.0007$ and 0.0004, are consistent with our extrapolations to $\Delta_{u_p} \to 0$, for all of the observables we have studied, and therefore give a good estimation for the observable without requiring the extrapolation.

4.2.2 Finding the critical coupling from the double Gaussian

We have verified our method agrees well with importance sampling results, and that our two finest interval sizes are consistent with the limit of vanishing interval size. We now use

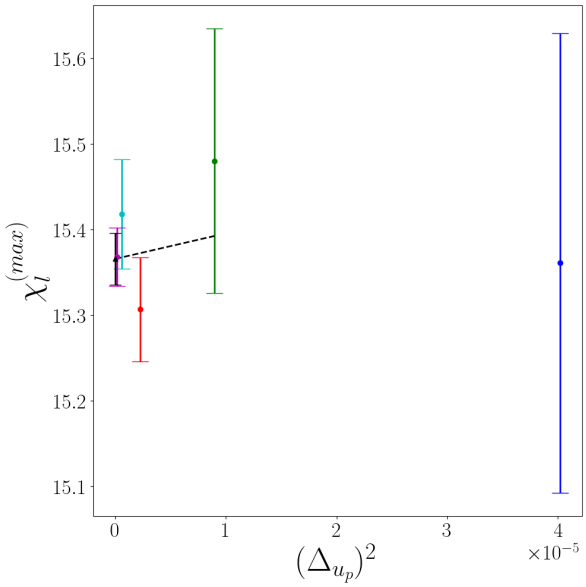

Figure 4.18. The maxima of the Polyakov loop susceptibility, $\chi_l^{(max)}$, plotted against the square of the interval width $\Delta_{u_p}^2$. The peak was found by taking the maximum value in a fine a scan of 100 β values between β = 5.690 and 5.695, for each repeat, then bootstrapping the results to estimate the error. The limit of vanishing interval width, $\Delta_{u_p} \to 0$, is taken, by taking a linear fit of the observable against $\Delta_{u_p}^2$, for the results of the four finest interval sizes. The fit is shown by the black dashed line, while the black triangle shows the value extrapolated to Δ_{u_p} = 0. The fit of the specific heat had a reduced chi-square of χ_ν^2 = 0.85, and the extrapolation gave $\chi_l^{(max)}$ = 15.37(3).

Table 4.2. The maximum of the specific heat, $C_V^{(max)}$, the minimum Binder cumulant, $B_V^{(min)}$, and the peak of the Polyakov loop susceptibility, $\chi_l^{(max)}$, and their corresponding inverse couplings, $\beta_{CV}(C_V)$, $\beta_{CV}(B_V)$ and $\beta_{CV}(\chi_l)$, are presented for each interval size. They are found by taking the maximum (minimum) value of a fine scan of β values evenly spaced between 5.690 and 5.695. Measurements were carried out at 1000 β values for C_V and B_V, while for χ_l 100 values were scanned. In all cases a linear fit of the value against $\Delta_{u_p}^2$ was taken, and used to extrapolate to $\Delta_{u_p} \to 0$, the result are shown in the final row of the table.

Δ_{u_p}	$\beta_{CV}(C_V)$	$\beta(B_V)$	$\beta(\chi_l)$	$C_V^{(max)}$	$B_V^{(min)}$	$\chi_l^{(max)}$
0.0063	5.69156(17)	5.69147(16)	5.69172(10)	0.5555(26)	0.66665389(6)	15.36(30)
0.0030	5.69205(5)	5.69201(4)	5.69176(5)	0.7033(21)	0.66665050(5)	15.48(16)
0.0015	5.69205(3)	5.69201(3)	5.69175(3)	0.7420(19)	0.66664961(5)	15.31(6)
0.0007	5.69198(3)	5.69194(3)	5.69170(3)	0.7546(11)	0.66664932(3)	15.42(6)
0.0004	5.69197(2)	5.69193(2)	5.69170(2)	0.7545(9)	0.66664933(2)	15.37(4)
$\to 0$	5.69197(2)	5.69194(1)	5.69171(1)	0.7553(7)	0.66664931(1)	15.37(3)

the LLR method to analyse the thermodynamic properties of the phase transition. First we

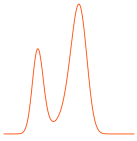

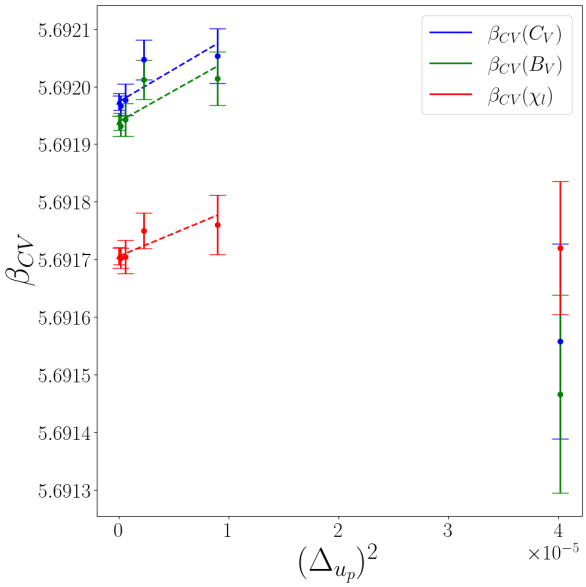

Figure 4.19. The inverse coupling corresponding to the extrema of the specific heat (blue), $\beta_{CV}(C_V)$, Binder cumulant (red), $\beta_{CV}(B_V)$, and the Polyakov loop susceptibility (green), $\beta_{CV}(\chi_l)$, is plotted against the square of the interval size, $\Delta^2_{u_p}$. In each case a linear fit has been taken, this is shown by a dashed line, and the value at $\Delta_{u_p} = 0$, is given by the triangle. The extrapolation to vanishing interval size limit for the specific heat gave, $\beta_{CV}(C_V) = 5.69197(2)$ with a reduced chi-square $\chi^2_\nu = 1.19$. The extrapolation of the Binder cumulant gave $\beta_{CV}(B_V) = 5.69194(1)$ with a reduced chi-square $\chi^2_\nu = 1.29$. The extrapolation of the Polyakov loop susceptibility gave $\beta_{CV}(\chi_l) = 5.69171(1)$, with a reduced chi-square $\chi^2_\nu = 0.47$. These values are the inverse couplings corresponding the peaks value of the observables measured in the fine scan between $\beta = 5.690$ and 5.695, with errors calcuated by bootstrapping over the repeats.

want to find the critical inverse coupling, $\beta_{CV}(P)$, at which the plaquette distribution has a double Gaussian structure with two peaks of equal height. By analysing the plaquette distribution at this point, we can find the plaquette jump, $\Delta\langle u_p\rangle_{\beta_{CV}}$, the difference in the plaquette values at the peaks of the distribution, through Eq. 2.2.28, this can be related to the latent heat of the transition. We are also interested in $-\ln(P_{min}/P_{max})$, the natural logarithm of the ratio of the height of the two degenerate peaks, P_{max}, and the central minima, P_{min}, this is used in Eq. 2.2.32. Through infinite volume and continuum extrapolations this can be related to the interface tension.

As shown in Fig. 4.11, in the critical region the plaquette distribution will obey a double Gaussian like structure, while away from the phase transition, it will be approximately a single Gaussian. We can see this change in structure in Fig. 4.20, which shows the plaquette distribution as a colour map as a function of both inverse coupling, along the horizontal axis, and plaquette value, on the vertical. The lighter colours correspond to a more probable plaquette value. If we look at the vertical slices, corresponding to the distribution for a given β

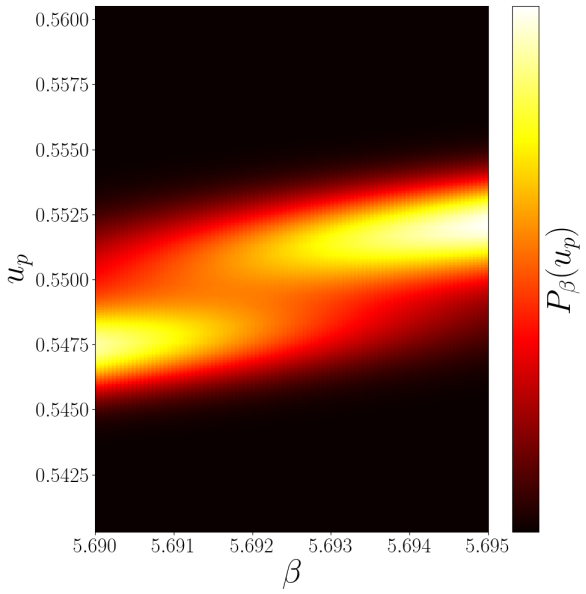

Figure 4.20. The plaquette distribution, $P_\beta(u_p)$, is shown by the colour map, for plaquette values between $u_p = 0.5403$ and 0.5605, and couplings between $\beta = 5.690$ and 5.6950. These results are from the LLR method with interval width, $\Delta_{u_p} = 0.0007$. The lighter colour corresponds o a more probable plaquette value.

value, it begins with one peak, the distribution then spreads out and a second peak appears. This second peak grows and starts to dominate as we continue to increase β. Finally, the original peaks disappears and we are left with a single Gaussian distribution, in the new phase.

We can directly see the meta-stable region from the coefficients a_n and their corresponding plaquette values, $(u_p)_n$. From Eq. 3.1.20, we can see that the extrema of the plaquette distribution, $\partial P_\beta(u_p)/\partial u_p = 0$, correspond to the points at which $a_n = \beta$. Therefore, when the function $u_p(a_n)$ is single valued, we have a single Gaussian peak centred at $u_p(a_n)|_{a_n=\beta}$. Similarly, if it is multi-valued we will have an extrema in the plaquette distribution centred at each of the points where $u_p(a_n)|_{a_n=\beta}$.

Fig. 4.21 directly demonstrates this property. The top plot shows the a_n as a function of the plaquette $(u_p)_n$. The middle plot shows the plaquette distribution, $P_\beta(u_p)$, while the bottom plot shows the effective potential, $W_\beta(u_p)$, as defined in Eq. 3.0.5. The dashed red line shows the line of $a_n = \beta$ value, the left figure has $\beta = \beta_{CV}(P) = 5.6918$, while the right plot has a $\beta = 5.689$. The vertical dashed magenta lines shows the corresponding plaquette values, $u_p(a_n)|_{a_n=\beta}$. At the critical point, left plot, the line $a_n = \beta$, intercepts the curve of a_n against $(u_p)_n$ three times, the first and the last correspond to the (meta-)stable Gaussian distribution from the single phase, whereas the middle intercept corresponds to an unstable

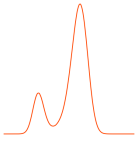

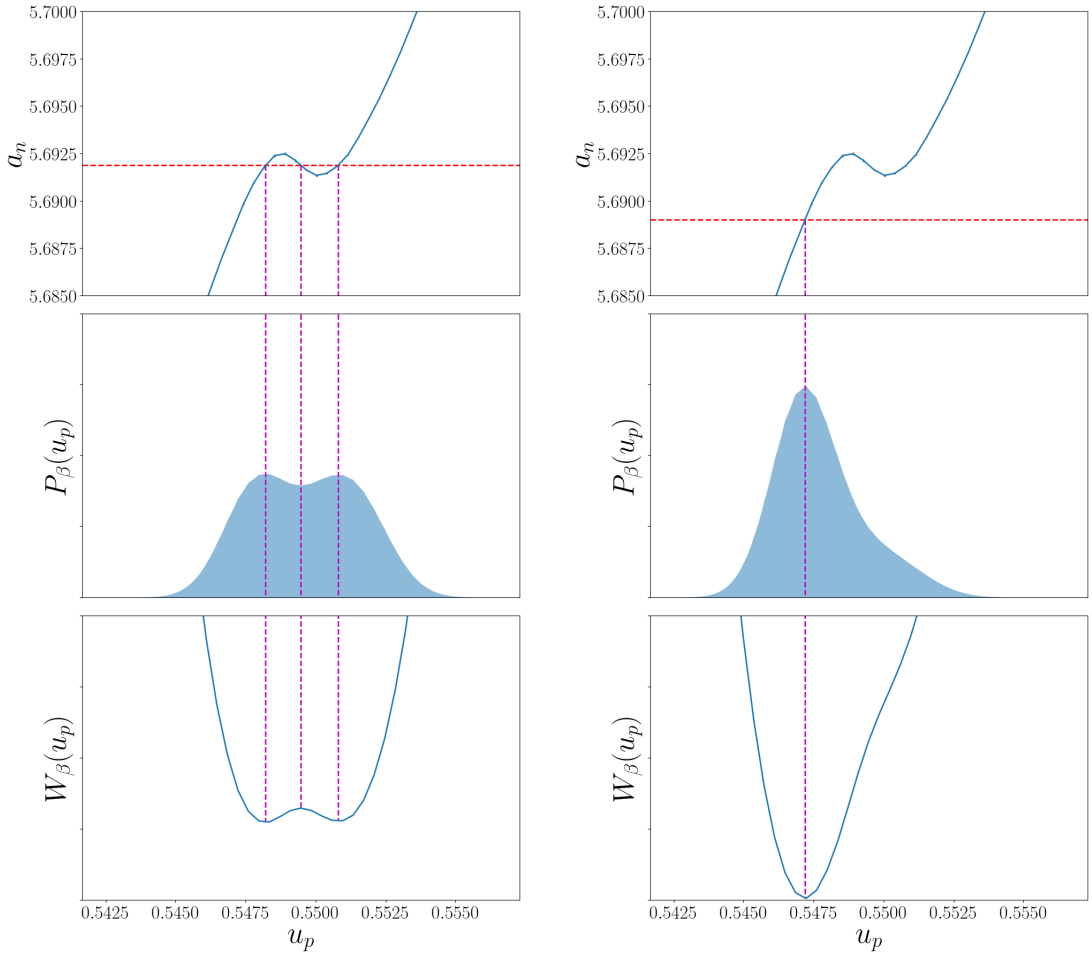

Figure 4.21. The top panel shows the coefficients a_n against the centre of the intervals, $(u_p)_n$, from the LLR method with interval width $\Delta_{u_p} = 0.0007$. The middle panel and bottom panel show the plaquette distribution, $P_\beta(u_p)$, and the quantum effective potential, $W_\beta(u_p)$, respectively. The left figure shows the critical point (left), $\beta_{CV}(P) = 5.69187$, and the right plot shows an arbitrary inverse coupling away from the meta-stable region, $\beta = 5.689$. The value of the inverse coupling in relation to the coefficients, a_n, is shown by the horizontal dashed red line. The vertical magenta dashed line shows the plaquette values corresponding to the points at which $a_n = \beta$, in the top panel, and equivalently the locations of the extrema of the distribution, and the effective potential. The left figure originally appeared in Ref. [1].

point in the distribution. In the right panel, we can see that although the distribution is not Gaussian, it has a single peak and a single minima of the effective potential, therefore it will not exhibit meta-stable dynamics.

To find the critical point, $\beta_{CV}(P)$, we use the bisection method to iteratively solve the equation, $P_{\beta_{CV}}(u_{p0}^{(+)}) = P_{\beta_{CV}}(u_{p0}^{(-)})$, where $u_{p0}^{(-)}$ ($u_{p0}^{(+)}$) denotes the value of the plaquette at the peak of the distribution in (de)confined phase. This gives us an estimate for the point

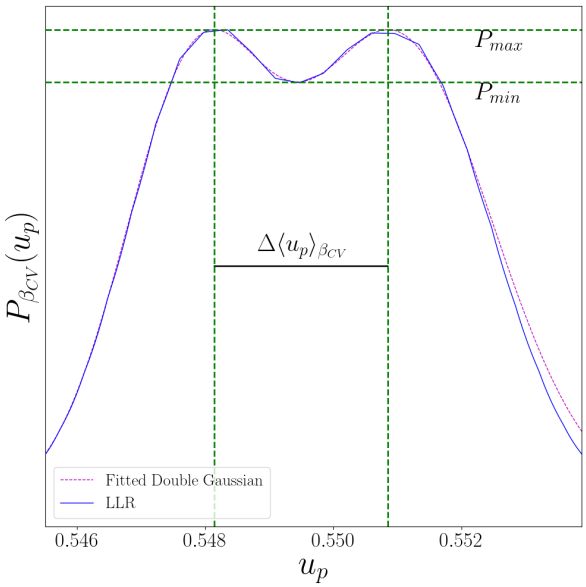

Figure 4.22. The plaquette distribution, $P_\beta(u_p)$, at the critical point, $\beta = \beta_{CV}(P)$. The results for one repeat of the LLR method for a interval of width of $\Delta_{u_p} = 0.0007$, is shown in blue, while the red curve shows a double Gaussian fitted to this distribution. The vertical dashed green lines show the locations of the peaks of the distribution, we define $\Delta\langle u_p\rangle_{\beta_{CV}}$ as the difference between the locations of these peaks. The horizontal dashed line shows the height of the degenerate peaks of the distribution,P_{max}, and the central minima of the distribution, P_{min}.

at which the double Gaussian distribution has two peaks of equal height. Full details on finding the critical point can be found in App. A.

An example of the plaquette distribution at the critical inverse coupling is shown by the solid blue line in Fig. 4.22, for one repeat with $\Delta_{u_p} = 0.0007$. To this distribution we have fitted a double Gaussian, red dashed line, which has very good agreement, therefore demonstrating at this volume we are not observing an effects from mixed phase states. The vertical dashed green lines show the locations of the peaks, the difference between them gives the plaquette jump $\langle u_p\rangle_{\beta_{CV}}$. The horizontal dashed green line shows the location of the degenerate maxima, P_{max}, and the central local minima, P_{min}.

We carried out this analysis for the systems with the interval sizes, Δ_{u_p}= 0.0015, 0.0007, and 0.0004, calculating $\beta_{CV}(P)$, $\langle u_p\rangle_{\beta_{CV}}$ and $\ln(P_{min}/P_{max})$, with error computed by bootstrapping over the results for all the repeats. We choose to carry out the analysis on only these points as the systems with larger interval sizes cannot accurately resolve the critical region. The results are shown blue the orange dots in Fig. 4.23. A linear fit of the result, as a function of the square of the interval size was taken, as shown by the green dashed line, the extrapolation to the limit of vanishing interval size is shown by the green triangle.

We found that the reduced chi-square for the fit of the critical inverse coupling was much

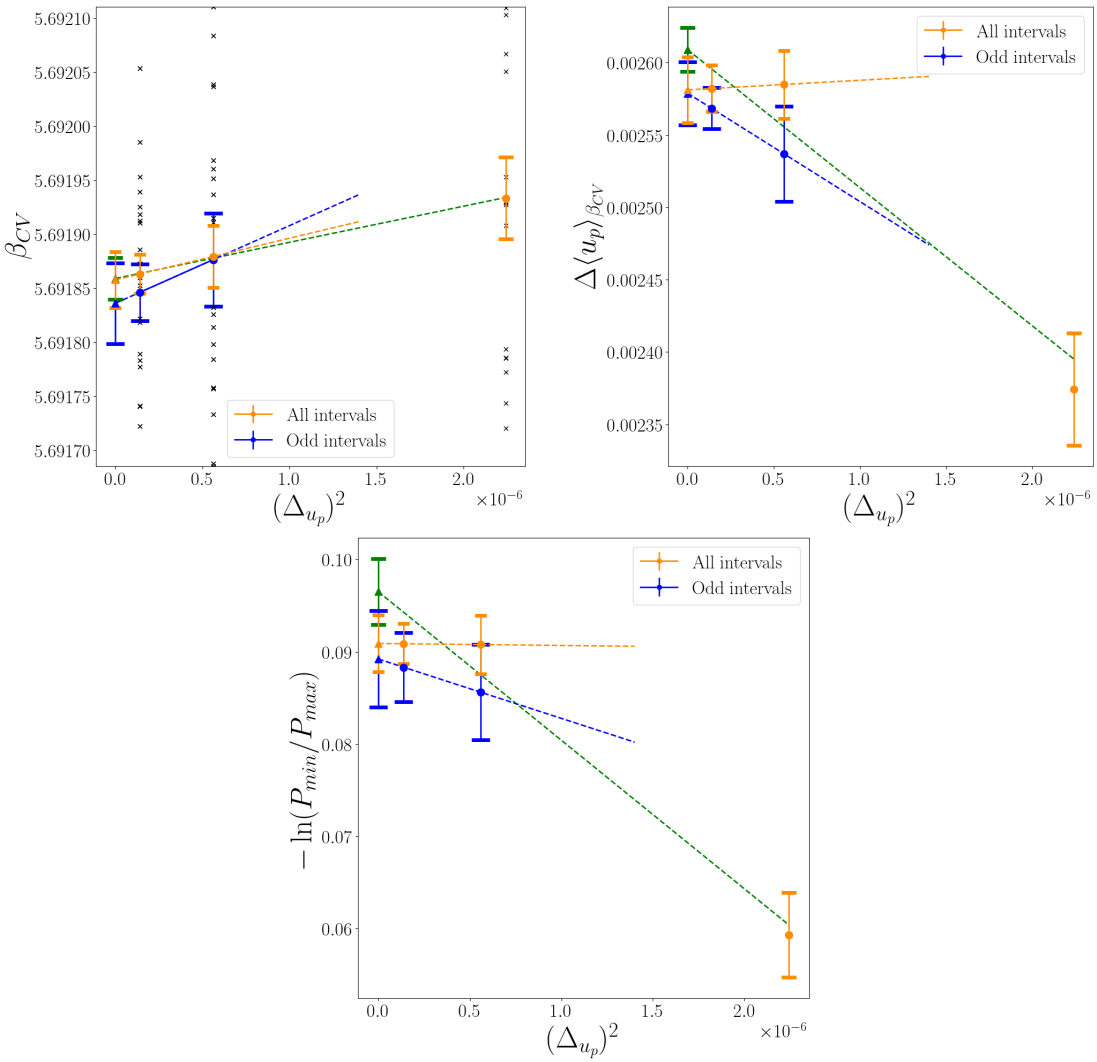

Figure 4.23. The critical inverse couplings, $\beta_{CV}(P)$, the plaquette jump, $\Delta\langle u_p\rangle_{\beta_{CV}}$, and the natural log of the ratio of the heights of the extrema of the plaquette distribution, $-\ln(P_{min}/P_{max})$, plotted against the square of the interval, $\Delta_{u_p}^2$, are shown in the top left, top right and bottom figures respectively. The critical inverse coupling calculated by fitting a double Gaussian to the plaquette distribution and tuning the coupling until the two peaks have equal height, then the other observables are found by analysing the distribution at this point. Errors are found by bootstrapping over the repeats. The results are shown by the orange dots, while the blue dots show the results when only using the odd numbered intervals, i.e. $\{a_{2n-1}, E_{2n-1}\}_{n=1}^{N_{int}/2}$. In all cases an extrapolation of the results for the two smallest interval sizes in the limit $\Delta_{u_p} \to 0$ is taken and shown by the dashed lines and the triangles. In green is an additional extrapolation of the full LLR results using all interval sizes. The values are presented in Tab. 4.3, the reduced chi-square of the extrapolations of all intervals with all interval sizes is given by $\chi_\nu^2 = 0.004, 3.05, 2.09$ for the top left, top right and bottom plots respectively. The top two figures originally appeared in Ref. [1].

Table 4.3. The values of the critical coupling, $\beta_{CV}(f)$, and the difference between the peaks of the plaquette distribution, $\Delta\langle u_p\rangle_{\beta_{CV}}$, and the natural logarithm of the ratio of the height of degenerate meta-stable peaks and the local minima, $-\ln(P_{min}/P_{max})$, for different energy interval sizes Δ_E.. The values calculated by fitting a double Gaussian to the plaquette distribution and tuning the coupling until the two peaks have equal height. The other observables are found by analysing the distribution at this point. Errors are found by bootstrapping over the repeats.The table shows results obtained in two ways. Either all intervals are included or only the odd intervals, $\{a_{2n-1}, E_{2n-1}\}_{n=1}^{N_{int}/2}$. The symbol '$\to 0$' is used to denote the result of an extrapolation. The table contains three extrapolations. An extrapolation using the results when only odd intervals are considered, an extrapolation when all points with all the intervals are used and an extrapolation of the two finest interval sizes when all intervals are used.

	Δ_{u_p}	$\beta_{CV}(P)$	$\Delta\langle u_p\rangle_{\beta_{CV}}$	$-\ln\left(\frac{P_{min}}{P_{max}}\right)$
Odd intervals	0.0007	5.69188(4)	0.00254(3)	0.0856(55)
Odd intervals	0.0004	5.69185(3)	0.00257(2)	0.0883(34)
All intervals	0.0015	5.69193(4)	0.00237(4)	0.0593(43)
All intervals	0.0007	5.69188(3)	0.00258(2)	0.0932(45)
All intervals	0.0004	5.69186(2)	0.00258(2)	0.0910(38)
Odd intervals	$\to 0$	5.69184(4)	0.00258(2)	0.0892(49)
All intervals all points	$\to 0$	5.69186(3)	0.00258(2)	0.0966(34)
All intervals 2 points	$\to 0$	5.69186(2)	0.00261(2)	0.0909(32)

less than one, $\chi^2_\nu = 0.004$. This over-fitting is likely due to an overestimation of the error at fixed interval size. Many contributions to this error have been accounted for, however we have not considered the to correlations between different intervals, i.e. correlations across each set of a_n values from a repeat, due to the replica exchange. In order to partially account for this we additionally considered results found by using only the odd numbered intervals, $\{a_{2n-1}, E_{2n-1}\}_{n=1}^{N_{int}/2}$, these are shown by the blue dots. The blue point at $\Delta_{u_p} = 0.0015$ (0.0007) is using the odd numbered intervals from $\Delta_{u_p} = 0.007$ (0.0004). A linear fit of these results was taken against $\Delta^2_{u_p}$, this is shown in blue. As we are fitting to only two points here, the reduced chi-square diverges.

The reduced chi-square on the fit of the other observables, $-\ln(P_{min}/P_{max})$ and $\langle u_p\rangle_{\beta_{CV}}$, using all intervals and all interval sizes was greater than 1, with $\chi^2_\nu = 2.0$ and 3.05 respectively. The behaviour of these observables in the $\Delta_{u_p} \to 0$ limit, appears to differ between the $\Delta_{u_p} = 0.0015$ and the finer points. The two finer points are within error of each other and the general trend is downward with decreasing Δ_{u_p}. Whereas the coarser point, is below the others and outside their error. It is therefore possible that the results for the coarser interval size are outside the asymptotic regime for the $\Delta_{u_p} \to 0$ limit. To account for this we also considered an extrapolation using only the two finest interval sizes, this is shown by the orange dashed line and the orange triangle. Once again, as we are fitting to only two points here,

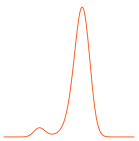

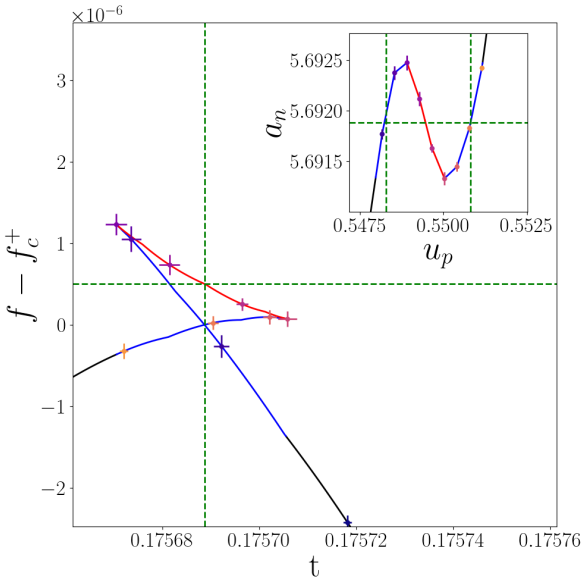

Figure 4.24. The micro-canonical (reduced) free-energy, f, is shown as a function of the micro-canonical temperature, $t = 1/a_n$. The inset shows the coefficients a_n, against the centre of the interval $(u_p)_n$. The dots show the points directly from the LLR algorithm, while the solid line shows an interpolation between them. The solid lines show the stable region in black, the unstable region in red, and the meta-stable region in blue. The colour of the dots in the main plot and inset match. In the main figure, the vertical green dashed line shows the location of the critical point $t_c = 1/\beta_{CV}(f)$, while the horizontal dashed line shows the value of unstable branch of the (reduced) free-energy at the critical point. The quantity f_c^+ corresponds to the value of the (reduced) free-energy at the points at which the two meta-stable branches cross. The horizontal green dashed lines in the inset shows the critical point (horizontal line), $a_n = \beta_{CV}(f)$, and the corresponding plaquette values (vertical lines) of the meta-stable branches. These results are from the LLR method with an interval width of $\Delta_{u_p} = 0.0007$.

the reduced chi-square diverges

The results for fixed interval size and the all three extrapolation are shown in Tab. 4.3, and Fig. 4.23. Comparing each of the extrapolations allows us to quantify the effects of the correlation between intervals. As can be seen all extrapolations differ, but they are consistent, suggesting that although the error is still likely being overestimated, the final results are not affected by the correlation between the neighbouring intervals. The systems with the two finest interval sizes are consistent with all extrapolations.

4.2.3 Thermodynamic potentials

As discussed in Sec. 3.1.1, we can use our numerical approximation of the density of states to compute thermodynamics potentials for the bulk of the system. In particular, we can compute the free-energy, $F(t)$, the entropy, s, the (microcanonical) temperature t, and the energy, $E(t)$, which we compute by piece wise inverting our function $u_p(a_n) \to a_n(u_p)$, which leads

to an expression for $t(E)$. All of these potentials are defined in Eq. 3.1.28

Rather than direct computation of $F(t)$, we calculate the reduced free-energy, defined in Eq. 3.1.31. We choose the constant Σ to be the average entropy for each interval, averaged across all the repeats for a given system, $\Sigma = \frac{1}{n_R}\sum_{m=1}^{n_R}\{\frac{1}{N_{int}}\sum_{n=1}^{N_{int}} s(E_n)\}_m$. This removes the dependence on our arbitrary choice of c_1. Our choice of Σ is also equivalent to the average gradient of $F(t)$. Generally, we are interested in the difference of free-energies at the same temperature, our choice of Σ, will therefore not change our results. In addition to calculating the reduced free-energy by subtracting a term linear in temperature, we subtract a constant term, the reduced free-energy at the point at which the two meta-stable branches of the free-energy are equal, f_c^+. This allows more direct comparison of the free-energy across different systems.

The reduced free-energy is plotted against the temperature in Fig. 4.24, for the system with interval size $\Delta_{u_p} = 0.0007$, focused on the critical point. The values at the centre of each interval are shown by the coloured points, with the errors in both directions. Between the points, we have the free-energy calculated through a linear interpolation of $a_n(u_p)$. In black is the stable region, in which only one solution is present. The blue lines show the meta-stable regimes, which correspond to minima of the effective potential and maxima of the plaquette distribution, when multiple solutions are present. The red line shows the unstable branch, this corresponds to the maxima of the effective potential and the central minima of the plaquette distribution. The inset of the plot shows the coefficients a_n against the centre of the intervals $(u_p)_n$, in the same region, with the colour of the points and lines matching those of the main figure. The unstable branch corresponds to the region with a negative gradient in $a_n(u_p)$. This 'swallow tail' structure is characteristic of a first order phase transition, this demonstrates the first order nature of the phase transition on a single lattice size.

To give further physical interpretation to the free-energy, and in particular to the specified regimes, we measure the ensemble average of the Polyakov loop, $\langle\langle|l_p|\rangle\rangle_n(a_n)$, and the susceptibility, $(\chi_l)_n(a_n)$, on configurations restricted to the nth energy interval, using the fixed a_n iterations. The results for the system with interval size, $\Delta_{u_p} = 0.0007$, plotted against the plaquette value at the centre of the interval, $(u_p)_n$, are shown in Fig. 4.25. The errors are the standard deviation of the values across the repeats. The shaded regions match the colour of the lines in Fig. 4.24, the blue region corresponds to the meta-stable branches, the red region corresponds to the unstable region, while the unshaded region correspond to the stable, single phase solutions. The majority of the peak of the Polyakov loop susceptibility, and therefore the region with the largest change in the Polyakov loop, corresponds to the critical region (shaded).

From Fig. 4.24, we can determine the same observables as calculated in the last section.

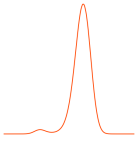

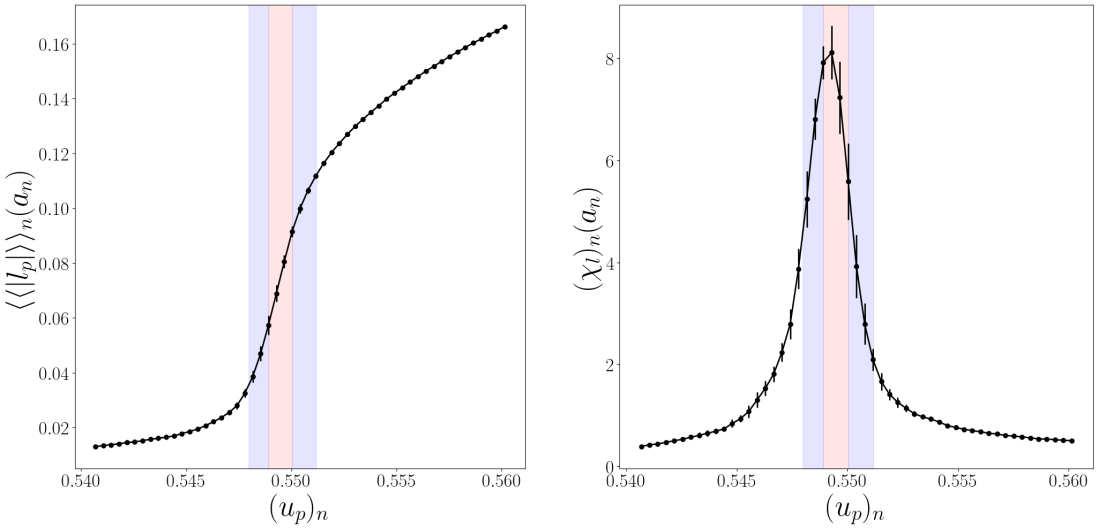

Figure 4.25. The ensemble average for configurations restricted to the *nth* energy interval of the absolute value of the Polyakov loop (left), $\langle\langle|l_p|\rangle\rangle_n(a_n)$, and the susceptibility (right), $(\chi_l)_n(a_n)$, plotted against the plaquette value at the centre of the interval, for the fixed a_n iterations of the LLR method with $\Delta_{u_p} = 0.0007$. The shaded blue region corresponds to intervals in the meta-stable branches of Fig. 4.24, while the red region is the unstable branch.

The point at which the meta-stable branches cross corresponds to the critical (microcanonical) temperature, t_c, the corresponding critical coupling is equivalent to the reciprocal of this, $\beta_{CV}(f) = 1/t_c$. This is calculated by piecewise linearly interpolating $a_n(u_p = \beta)$ on the meta-stable branches, and finding the temperature that minimises the free-energy difference between them. At the critical point, there will be three plaquette values when $a_n = \beta$, $u_p(a_n = \beta_{CV}(f))$ will have three intercepts. These correspond to the two meta-stable peaks to the plaquette distribution, and the unstable central minima. The difference between two intercepts on the meta-stable branches correspond to the plaquette jump, $\Delta\langle u_p\rangle_{\beta_{CV}}$. Using Eq. 3.1.30, the natural logarithm of the ratio of the minima and maxima of the plaquette distribution can be directly related to the difference between the meta-stable and the unstable branch in free-energy at the critical point, $-\ln(P_{min}/P_{max}) = \Delta F(t_c)/t_c$. All errors are calculated by bootstrapping over the results for each repeat.

The free-energy was calculated for LLR results for interval sizes $\Delta_{u_p} = 0.0015$, 0.0007 and 0.0004. The results are shown in left plot of Fig. 4.26, with the colours denoting the different interval sizes. Again the vertical dashed line shows t_c, while the horizontal dashed line shows the (reduced) free energy difference between the meta-stable branches and the unstable branch at the critical point. The coefficients a_n as a function plaquette value at the centre of the interval for these systems are shown in right figure. The horizontal dashed line shows the critical coupling, $a_n = \beta_{CV}(f) = 1/t_c$, while the vertical dashed lines show the

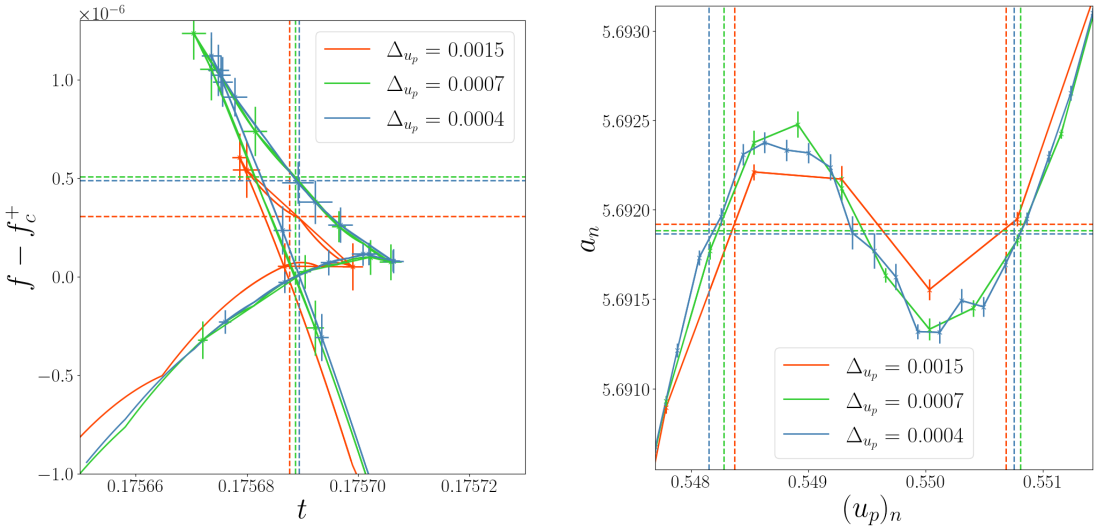

Figure 4.26. The left plot shows the micro-canonical (reduced) free-energy, f, as a function of the micro-canonical temperature, $t = 1/a_n$. The right plot shows the coefficients a_n, against the centre of the interval $(u_p)_n$. The dots show the points directly from the LLR algorithm, while the solid line shows an interpolation between them. The colour of the plots show the value of the interval size, $\Delta_{u_p} = 0.0015$, 0.0007 and 0.0004 in red, green and blue respectively. In the left figure, each vertical dashed line shows the location of the critical point $t_c = 1/\beta_{CV}(f)$, for the corresponding interval size, while the horizontal dashed line shows the value of the (reduced) free-energy on the unstable branch at the critical point. The quantity f_c^+ corresponds to the value of the (reduced) free-energy at the points at which the two meta-stable branches cross. The horizontal dashed line in the right figure shows the critical point, $a_n = \beta_{CV}(f)$, and the corresponding plaquette values (vertical lines) of the meta-stable branches.

points at which the meta-stable branch intercepts this. The behaviour of the systems with the two finer intervals are very similar, whereas the other system appears to not to resolve all the relevant information in the critical region. This agrees with our previous discussion of these systems.

From these systems we also calculate the quantities of interest for the phase transition: the critical coupling, $\beta_{CV}(f)$, the plaquette jump, $\Delta\langle u_p\rangle_{\beta_{CV}}$, and the change in free-energy, $\Delta F(t_c)/t_c = -\ln(P_{min}/P_{max})$. The results are presented in Tab. 4.4 and Fig. 4.27. The errors are calculated by bootstrapping the results for each repeat. For each of these observables, we fit a function linear in the square of the interval size, $\Delta_{u_p}^2$, and extrapolate to the limit of vanishing interval size. The reduced chi-square for $\beta_{CV}(f)$ and $\Delta\langle u_p\rangle_{\beta_{CV}}$ are very low, $\chi^2_\nu = 0.086$ and $\chi^2_\nu = 0.101$, respectively. Again this is likely due to an overestimation of the errors. The reduced square for $-\ln(P_{min}/P_{max})$ is $\chi^2_\nu = 1.603$. This might be driven by the largest interval size not being in the asymptotic regime, as demonstrated by the difference in behaviour in Fig. 4.26. The systems with the two finest interval sizes are consistent with all extrapolations.

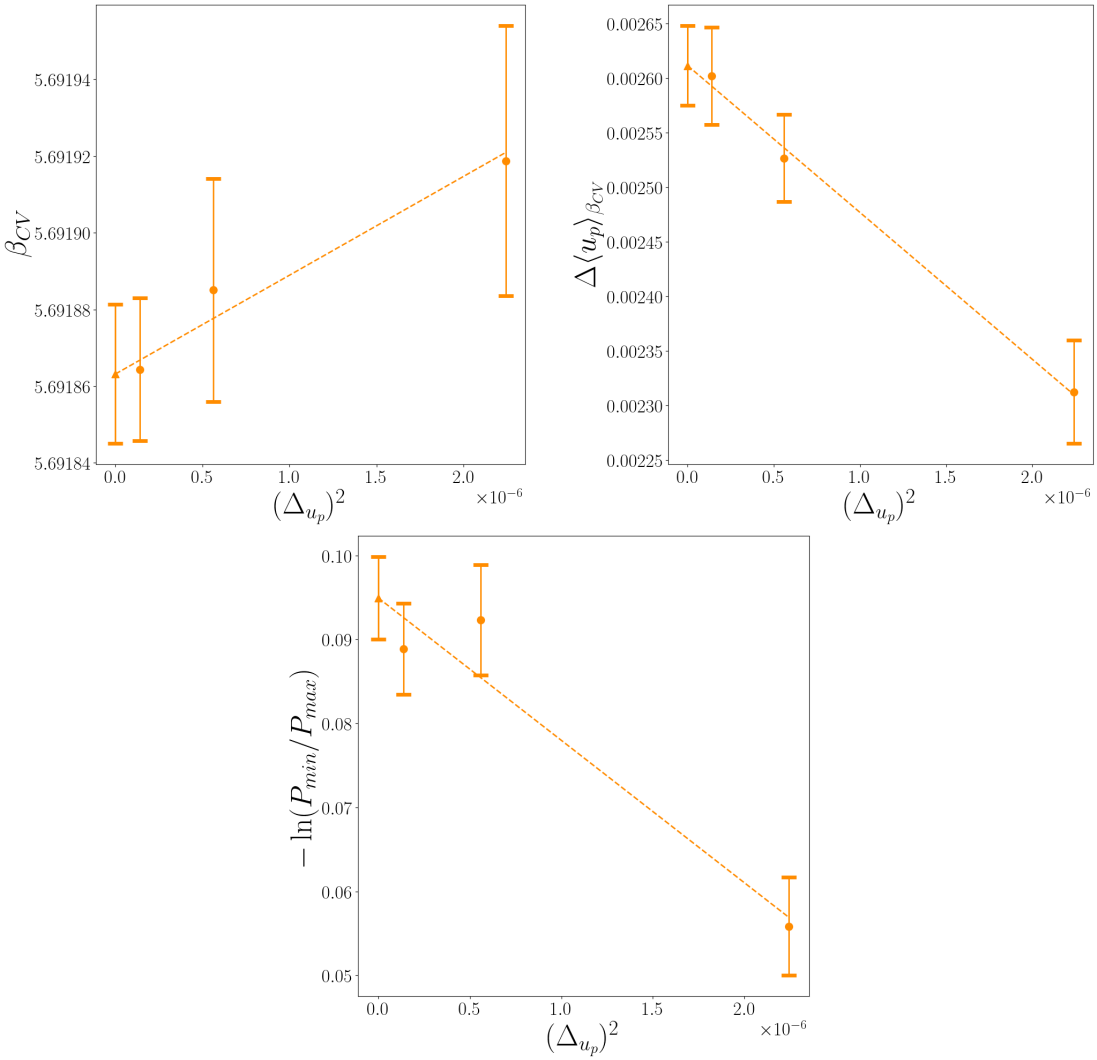

Figure 4.27. The critical couplings, $\beta_{CV}(f)$, the plaquette jump, $\Delta\langle u_p\rangle_{\beta_{CV}}$, and the natural log of the ratio of the heights of the extrema of the plaquette distribution, $-\ln(P_{min}/P_{max})$, calculated at different interval sizes, Δ_{u_p}, are shown in the top left, top right and bottom figures respectively. The values calculated by finding the 'temperature', $t = 1/a_n$, at which the two meta-stable branches cross on the free-energy plot, Fig. 4.24, $\beta_{CV}(f) = 1/t_c$. $-\ln(P_{min}/P_{max})$ is calculated as the free-energy difference between the meta-stable branches, $-\ln(P_{min}/P_{max}) = \Delta F/t_c$, and the unstable branch at the critical coupling, and the plaquette jump is the difference in the plaquette value between the two meta-stable branches when $u_p(a_n = 1/t_c)$. Errors are found by bootstrapping over the repeats. The results are shown by the orange dots, and an extrapolation in the limit of $\Delta_{u_p} \to 0$ is taken and shown by the dashed lines and the triangle. The values are presented in Tab. 4.4, the reduced chi-square of the extrapolations are given by $\chi^2_\nu = 0.086$, 0.101 and 1.603, for the top left, top right and bottom plots respectively.

The results presented in Tab. 4.4, are directly comparable to the results presented in Tab. 4.3. They are calculated in different ways, the former through the free-energy and the

Table 4.4. The values of the critical coupling, $\beta_{CV}(f)$, and the difference between the peaks of the plaquette distribution, $\Delta\langle u_p\rangle_{\beta_{CV}}$, and the natural logarithm of the ratio of the height of degenerate meta-stable peaks and the local minima, $-\ln(P_{min}/P_{max})$, for different energy interval sizes Δ_E. The values calculated by finding the 'temperature', $t_=1/a_n$, at which the two meta-stable branches cross on the free-energy plot, Fig. 4.24, $\beta_{CV}(f) = 1/t_c$. $-\ln(P_{min}/P_{max})$ is calculated as the free-energy difference between the meta-stable branches, $-\ln(P_{min}/P_{max}) = \Delta F/t_c$, and the unstable branch at the critical coupling, and the plaquette jump is the difference in the plaquette value between the two meta-stable branches when $u_p(a_n = 1/t_c)$. Errors are found by bootstrapping over the repeats. The symbol '$\to 0$' is used to denote the result of an extrapolation.

Δ_{u_p}	$\beta_{CV}(f)$	$\Delta\langle u_p\rangle_{\beta_{CV}}$	$-\ln\left(\frac{P_{min}}{P_{max}}\right)$
0.0015	5.69192(4)	0.00231(5)	0.0559(58)
0.0007	5.69189(3)	0.00253(4)	0.0923(66)
0.0004	5.69186(2)	0.00260(4)	0.0889(54)
0.0000	5.69186(2)	0.00261(4)	0.0950(49)

other by fitting double Gaussian. In all cases the results are consistent within error. It also confirms the validity of our formation of the free-energy in Eq. 3.1.30.

4.3 Conclusion

The aim of this study was to verify our methodology for analysis of non-Abelian gauge theories using the LLR method, to better understand the limit of vanishing interval size, and to gain some insight into the deconfinement transition in $SU(3)$ gauge theory. We chose to study $SU(3)$ pure gauge theory on a relatively small lattice 4×20^3, as the meta-stability problems that plague larger lattice volumes and in larger gauge groups could be better controlled. Therefore, the systematic error in standard importance sampling methods could be better understood.

By analysing the trajectories of the coefficients $a_n^{(m)}$, as they are updated using the RM iterations, in Fig. 4.5, Fig. 4.6 and Fig. 4.7, we verified that in each interval all repeats converge to the same value with the expected asymptotic scaling, $\sigma(a_n^{(m)}) \sim 1/\sqrt{m}$. By analysing the results of the fixed a_n iterations we have ensured that Eq. 3.1.11 is solved, through Fig. 4.9, and that we have obtained a flat energy distribution as shown in Fig. 4.10. The ergodicity of the algorithm has been ensured through a combination of replica exchange, Fig. 4.8, and the soft boundary conditions, in intervals 1 and N_{int}, leading to Gaussian tails in the distribution in Fig. 4.10. This demonstrated that our methodology was consistent with expectation.

Next we analysed the limit of vanishing interval size. The LLR results for all interval sizes demonstrate that the coefficients a_n appear to converge to the value of the smallest interval size, as shown in Fig. 4.4. Most of the systems have the same structure, away from

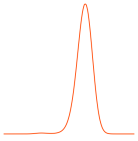

the phase transition the function $u_p(a_n)$ is single values, while around the phase transition it is multi-valued. In Fig. 4.11 and Fig. 4.21, we demonstrated that the non-invertibility of this function leads to the meta-stable dynamics characteristic of the first order transition. However, the largest interval size $\Delta_{u_p} = 0.0063$ differed greatly from the others, due to large systematic errors due to the coarse discretisation of the plaquette range.

In the limit of vanishing interval size our results largely agree with importance sampling. To verify this, we reconstructed the average plaquette, specific heat, Binder cumulant, average Polyakov loop and Polyakov loop susceptibility, using the LLR results with several interval sizes. These results are shown in Fig. 4.12, Fig. 4.13, Fig. 4.14, Fig. 4.15 and Fig. 4.16. In all cases the results appear to tend toward the value for the smallest interval size, which is generally within error of the importance sampling results. The plaquette distribution, reconstructed from the LLR results is also in good agreement with the histograms of plaquette values from importance sampling.

Using the results for each of the observables, we found estimates for the critical inverse coupling. By finding the peak of the specific heat, $\beta(C_V^{(max)})$, the minimum of the Binder cumulant, $\beta(B_V^{(min)})$, and the peak of the Polyakov loop susceptibility, $\beta(\chi_l^{(max)})$. In the thermodynamic limit we expect these results to converge to the same value, however at finite volume they generally differ. We analysed these variables in the limit of vanishing interval size, and found that the extrapolation is generally consistent with the two smallest interval sizes, Fig. 4.19. Similar results were found for the values of the observables at the peak, $C_V^{(max)}$, $B_V^{(min)}$ and $\chi_l^{(max)}$. These results are shown in Tab. 4.2 and Fig. 4.17 and Fig. 4.18.

Using the results of the LLR algorithm, we can reconstruct the plaquette distribution for an arbitrary inverse coupling, between a range set by our chosen range of energy intervals, $E_1 \to E_{N_{int}}$. Using the plaquette distribution we can also define an effective potential as shown in Fig. 4.21. By tuning the inverse coupling until the plaquette distribution gives a double Gaussian like structure with two peaks of equal height, we were able to find another value for the critical inverse coupling, $\beta_{CV}(P)$. From the distribution at this point, we demonstrated the ability to determine the quantities $\Delta\langle u_p\rangle_{\beta_{CV}}$ and $-\ln(P_{min}/P_{max})$, which can be related to the latent heat and surface tension, through infinite volume and continuum extrapolations. For these observables, we extrapolated to the limit of vanishing interval size. For this we found a very small reduced-chi square, and discussed the affects of correlation between intervals. We found in all cases the results for the two smallest interval sizes agree well with the extrapolation. These results are shown in Tab. 4.3 and Fig. 4.23.

Using the density of states, we demonstrated that we can compute thermodynamic properties that are inaccessible to standard importance sampling methods. In particular, we compute the micro-canonical free-energy and demonstrate that it obeys the swallow tail

structure characteristic of a first order phase transition, Fig. 4.24, demonstrating the first order nature on a single lattice size. Using this definition for the free-energy we were able to compute the same observables as before, $\beta_{CV}(f)$, $\Delta\langle u_p\rangle_{\beta_{CV}}$ and $-\ln(P_{min}/P_{max})$. We again extrapolated the results to the limit of vanishing interval size, again the results for the two smallest interval sizes were shown to be consistent with the extrapolated results. These results are shown in Tab. 4.4 and Fig. 4.27. These results were shown to be consistent with the values calculated from the plaquette distribution.

We have shown that our results are consistent with expectation of the LLR algorithm and it agrees well with other lattice methods of analysing the system. We have also demonstrated that this method gives accurate results for thermodynamic properties. It also gives access to other observables that are otherwise inaccessible. In addition we demonstrated our expectation that the leading order correction to the observables is $\propto \Delta_E^2$, and verified that the results for a finite interval size agree with the extrapolation to vanishing interval size, therefore a full extrapolation may not be required if we can ensure we are in the asymptotic regime. This study focused on a system that is very weakly first order on a small lattice and therefore the meta-stability problems that the method was developed for are easily overcame through standard importance sampling methods. In the next chapter we study systems in the thermodynamic limit, in which these issues are more apparent.

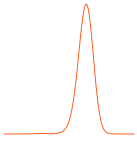

Chapter 5

$Sp(4)$

> "Do some real life physics and I'll give you a quote."
> S. Pandey private correspondence

In the previous chapter we demonstrated and verified our methodology on a well tested problem, the finite temperature deconfinement phase transition in $SU(3)$ pure gauge theory. We now move onto a less studied problem of the finite temperature deconfinement phase transition in $Sp(4)$ pure gauge theory. Most of our discussion will revolve around a system with $N_t = 4$, with an in depth analysis on the thermodynamic limit, using finite size scaling and considering the effects of mixed phase states. We also discuss an initial exploration of $N_t = 5$ and $N_t = 6$, with the aim of taking the continuum limit in future work. We aim to compute the thermodynamic properties which are of particular interest for the study of the gravitational wave phenomenology: the critical inverse coupling, the plaquette jump and the surface tension.

Preliminary forms of the results presented in this chapter have appeared in the proceeding Ref. [94]. This analysis will also form the basis for an upcoming research paper Ref. [2], proceeding Ref. [95], and the data and code releases, Ref. [3] and Ref. [6].

5.1 $N_t = 4$

5.1.1 Initial importance sampling exploration

To find the range relevant range of plaquette values, and the initial parameters, $a_n^{(0)}$, we carry out a scan of inverse couplings around the critical region using standard importance sampling techniques. For the critical inverse couplings in the thermodynamic limit for $N_t = 4$ Ref. [86] found $\beta_C = 7.339(1)$. We carry out our importance sampling analysis on a lattice of size 4×20^3, for inverse couplings $\beta = 7.32$, 7.33, 7.34 and 7.35. For each ensemble we measure the average plaquette, u_p, and absolute value of the Polyakov loop, $|l_p|$, on 500,000 configurations, after 50,000 thermalisation steps. For each update we carry out 1 heat-bath followed by 4 over-relaxation iterations.

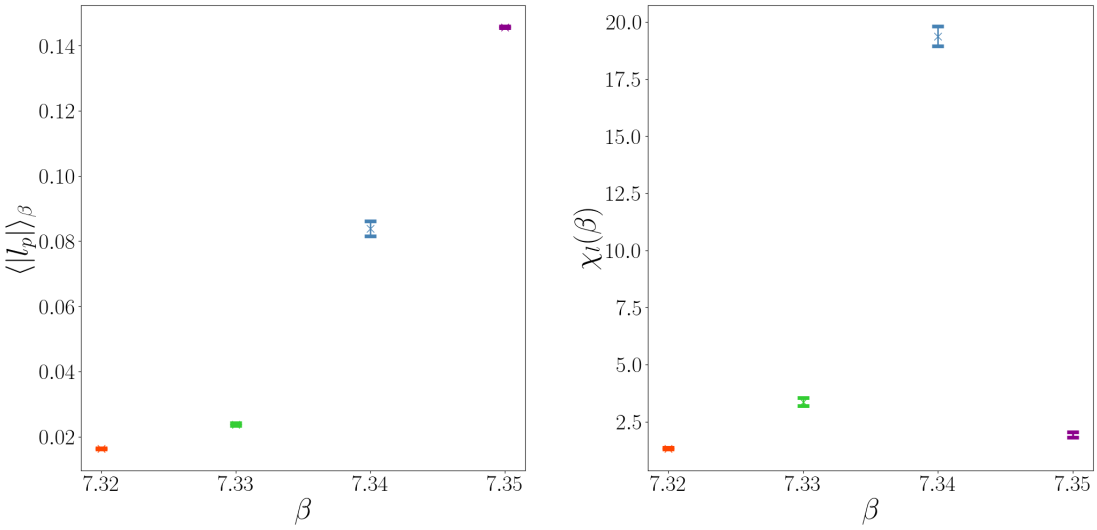

Figure 5.1. Importance sampling results for the VEV of the absolute value of the Polyakov loop (left), $\langle |l_p| \rangle_\beta$, and the susceptibility (right), $\chi_l(\beta)$, against the inverse coupling, β, for $Sp(4)$ pure gauge theory on a lattice of size 4×20^3. For each ensemble we take 500,000 measurements, after 50,000 thermalisation steps. For each update we carry out 1 heat-bath update followed by 4 over-relaxation steps. The errors were computed by binning and bootstrapping the results.

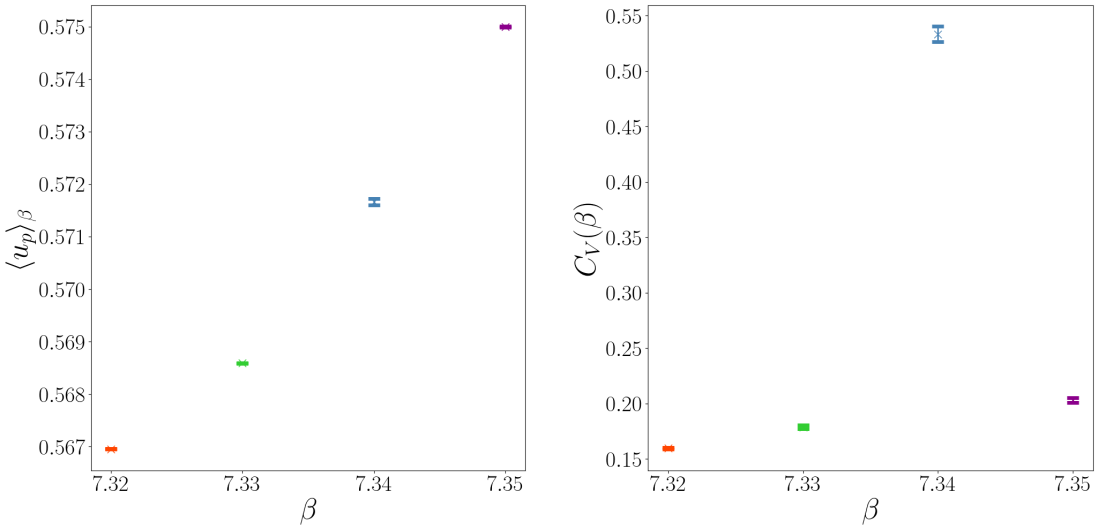

Figure 5.2. Importance sampling results for the VEV of the average plaquette (left), $\langle u_p \rangle_\beta$, and the specific heat (right), $C_V(\beta)$, against the inverse coupling, β, for $Sp(4)$ pure gauge theory on a lattice of size 4×20^3. For each ensemble we take 500,000 measurements, after 50,000 thermalisation steps. For each update we carry out 1 heat-bath update followed by 4 over-relaxation steps. The errors were computed by binning and bootstrapping the results.

The measured value of the VEV of absolute value of the Polyakov loop, $\langle |l_p| \rangle_\beta$, and the

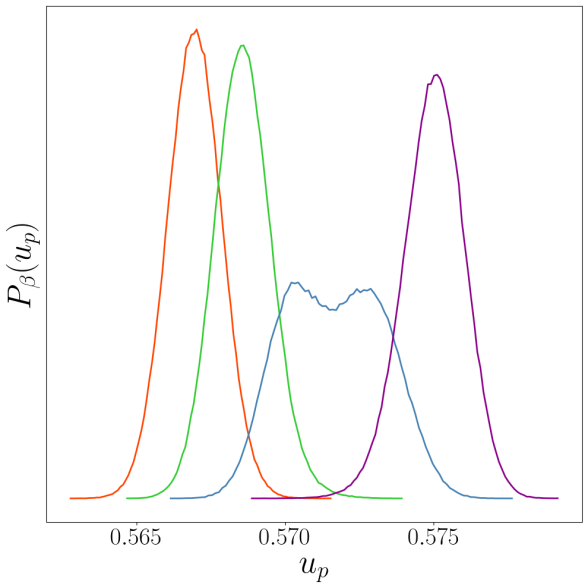

Figure 5.3. The histogram of measured average plaquette values, $P_\beta(u_p)$, for a range of inverse couplings, from left to right β = 7.32, 7.33, 7.34 and 7.35. For each ensemble 500,000 measurements were taken after 10,000 thermalisation steps. For each update we carry out 1 heat-bath, followed by 4 over-relaxation steps. The colours of the histograms match the colour of the points in Fig. 5.1 and Fig. 5.2.

Polyakov loop susceptibility, $\chi_l(\beta)$, are shown for each ensemble, against their inverse coupling, in Fig. 5.1. The two ensembles with the smallest inverse couplings are in the confined phase, and are likely away from the critical region, as both the Polyakov loop and the susceptibility are small. The configurations in the ensemble with the largest inverse coupling, are likely deconfined pure phase states, as the Polyakov loop has a larger value, but again the susceptibility is small. The final ensemble with β = 7.34, appears to be very close to the transition, as it has a large susceptibility and an intermediate Polyakov loop value. A similar story is told by the VEV of the average plaquette, $\langle u_p \rangle_\beta$, and the specific heat, $C_V(\beta)$, in Fig. 5.2.

We can further verify the interpretation of these results by analysing the plaquette distribution, Fig. 5.3. We can see that the ensembles with β = 7.32, 7.33 and 7.35, are to a good approximation described by a single Gaussian, again showing that they are likely pure phase states. The ensemble at β = 7.34 appears to be very close to the critical point. It displays the characteristic double Gaussian structure, with two peaks of approximately equal height. We choose to select plaquette values which include all of the relevant micro-states for all these inverse couplings. We therefore select $(u_p)_{min}$ = 0.565 and $(u_p)_{max}$ = 0.58 as these are the plaquette values in which the plaquette distribution for the ensembles with β = 7.32 and 7.35 become highly suppressed.

In this study we focus on the thermodynamic limit, by analysing the transition at several spatial volumes, all with the same temporal size. We choose : $\tilde{V}/a^4 = 4\times20^3$, 4×24^3, 4×28^3, 4×40^3, and 4×48^3. In the thermodynamic limit we expect that the plaquette distribution will become more constrained, i.e. the width scales inversely with the volume, therefore we can use an equal, or smaller plaquette range for each volume. To ensure we are adequately resolving the critical region, at each volume we choose multiple interval sizes, Δ_{u_p}. We do this by varying the number of intervals, and by reducing the plaquette range. For the largest lattice volumes, 4×40^3, and 4×48^3, we reduce the plaquette range to $(u_p)_{min} = 0.568$ and $(u_p)_{max} = 0.576$, as the width of the plaquette distribution has decreased, and the micro-states outside this range are now suppressed for the inverse couplings we are interested in studying.

We find the initial coefficients, $a_n^{(0)}$, by fitting a cubic polynomial to our importance sampling results for the inverse coupling as a function of the measured VEV of the average plaquette, $\beta(u_p)$. We select the centre of the intervals, $(u_p)_n$, to be N_{int} plaquette values evenly spaced between $(u_p)_{min}$ and $(u_p)_{max}$ intervals. The initial coefficients are then taken directly from our polynomial fit, $a_n^{(0)} = \beta((u_p)_n)$. From initial tests we find that 10 NR iterations are sufficient to refine our initial estimate, in order for the RM iteration to converge. For the smaller lattice volumes we carry out 300 RM iterations, then as the volume, and therefore the computational time per iteration increases, we reduce the number of iterations. The values of the other parameters, were informed from our previous work and preliminary tests. A full list of the ensembles and the LLR parameters used for this study are shown in Tab. 5.1.

In Fig. 5.4, we show the importance sampling results (black points), initial values of a_n (black dashed line), the mean values a_n after completing the NR iterations (coloured dashed line), and the final a_n values after completing the RM iterations. This example is for a lattice of volume, 4×24^3. Although there is large difference between the initial values of a_n, and the final values, especially outside the range of the fit at the edges of the plaquette range, after 10 NR iterations the results are sufficiently close to the final values for the RM iterations to converge accurately. We also note that the results for each interval size, shown in different colours, are consistent with each other, particularly for the two finest intervals. Therefore we believe we are in the asymptotic regime and we can take the limit of vanishing interval size by extrapolating in $\Delta_{u_p}^2$. It is also clear that the although our initial approximation for $a_n(u_p)$, is single valued, after completing the RM iterations the non-invertible structure has emerged. Similar results were found for all lattice volumes.

At each spatial size we carefully consider the limit of vanishing interval size to ensure accurate results for each lattice size. For the ensembles $\tilde{V}/a^4 = 4\times20^3$ with $\Delta_{u_p} = 0.00025$, and $\tilde{V}/a^4 = 4\times24^3$ with $\Delta_{u_p} = 0.00025$, we have incorrectly chosen the plaquette range, and

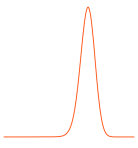

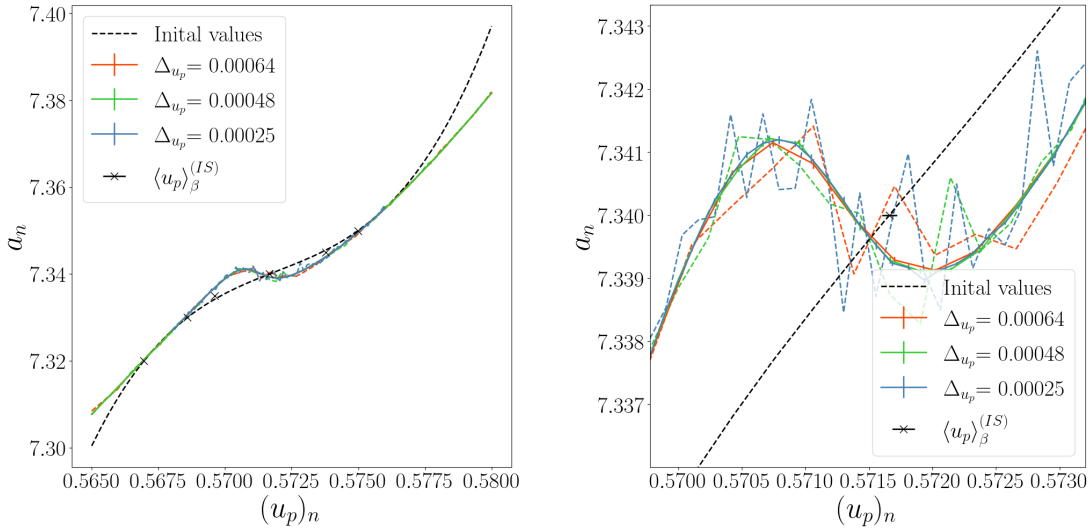

Figure 5.4. The final values of the coefficients, a_n, against the plaquette values at the centre of the intervals, $(u_p)_n$, for the $Sp(4)$ pure gauge theory on a lattice of volume 4×24^3, for three different interval sizes, Δ_{u_p}, shown in different colours. The coloured points show the results directly from the LLR method, with error calculated by bootstrapping over the repeats, while the solid line shows a linear interpolation between them. The black points show the importance sampling results, the vertical axis are the β values, and the horizontal axis is the VEV of the average plaquette, $\langle u_p \rangle_\beta$. The black dashed line shows the initial a_n values, before starting the NR iterations, found from a cubic fit of the importance sampling results. The coloured dashed lines show the mean a_n values after completing the NR iterations, before starting the RM iterations. The right plot is identical to the left, but focuses on the critical region, this more clearly shows the difference between the results after the NR iterations and after the RM iterations, which are difficult to resolve in the left plot.

have thus cut-off relevant micro-states. Results for these systems are not considered in our extrapolations to $\Delta_{u_p} \to 0$, due to the new systematic errors. Further details on the analysis of errors due to finite interval size for the systems studied are presented in App. B.

5.1.2 $N_t = 4$, $N_s \to \infty$

In this section we will discuss the thermodynamic limit, and finite size effects for the deconfinement phase transition in $Sp(4)$ pure gauge theory on a lattice with four temporal sites, $N_t = 4$, by analysing the system for several spatial sizes, $N_s = 20$, 24, 28, 40 and 48. We will demonstrate the LLR algorithm's ability to resolve the critical region, where we see the effects of mixed phase configurations. We analyse the thermodynamic limit for the important thermodynamic observables, the critical inverse coupling, β_{CV}, the plaquettte jump, $\Delta\langle u_p \rangle_{\beta_{CV}}$, the interface tension term, $\hat{I}$, as well as extrema of the specific heat, $C_V^{(max)}$, Polyakov loop susceptibility, $\chi_l^{(max)}$, and the Binder cumulant, $B_V^{(min)}$.

The final values of the coefficients a_n, after completing all NR and RM iterations, are plotted as a function of the plaquette value at the centre of each interval, $(u_p)_n$, in Fig. 5.5.

Table 5.1. A list of LLR parameters for the study of the deconfinement phase transition in $Sp(4)$ pure gauge theory on a lattice with four temporal sites, for several spatial volumes. For each volume we chose several interval sizes, Δ_{u_p}, such that the limit of vanishing interval size could be analysed. The interval size has been quoted to 5 decimal places for convenience. The definitions for the variables of this table are given in Tab. 3.1.

$\tilde{V}/a^4$	N_D	N_{int}	n_R	Δ_{u_p}	$(u_p)_{\min}$	$(u_p)_{\max}$	$\bar{m}$	$\tilde{m}$	$\hat{m}$	n_{Th}	n_M	n_{fxa}	n_{ITh}
4×20^3	4	48	20	0.00064	0.565	0.580	10	300	100	300	700	100	1000
4×20^3	4	64	20	0.00048	0.565	0.580	10	300	100	300	700	100	1000
4×20^3	4	64	20	0.00025	0.568	0.576	10	300	100	300	700	100	1000
4×24^3	4	48	20	0.00064	0.565	0.580	10	300	100	300	700	100	1000
4×24^3	4	64	20	0.00048	0.565	0.580	10	300	100	300	700	100	1000
4×24^3	4	64	20	0.00025	0.568	0.576	10	300	100	300	700	100	1000
4×28^3	4	64	20	0.00048	0.565	0.580	10	200	100	300	700	100	1000
4×28^3	4	64	20	0.00025	0.568	0.576	10	200	100	300	700	100	1000
4×40^3	4	96	25	0.00017	0.568	0.576	10	100	50	300	700	100	1000
4×40^3	4	128	25	0.00013	0.568	0.576	10	100	50	300	700	100	1000
4×48^3	4	128	25	0.00013	0.568	0.576	10	100	50	300	700	100	1000

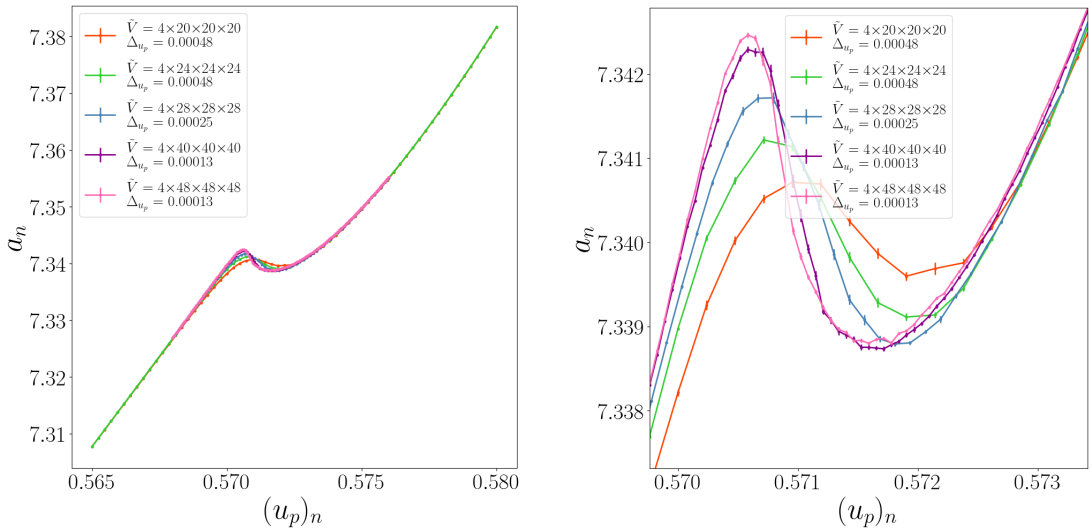

Figure 5.5. The final values of the coefficients, a_n, against the plaquette values at the centre of the intervals, $(u_p)_n$, for $Sp(4)$ pure gauge theory on lattice with $N_t = 4$ and a various spatial volumes in different colours for a single interval size, Δ_{u_p}. The coloured points show the results directly from the LLR method, with errors calculated by bootstrapping over the repeats, while the solid line shows a linear interpolation between them. The points in the right plot are identical to the left, but focuses on the critical region.

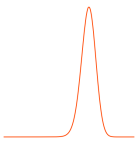

We plot the results for different volumes in different colours, and showing only the results for the one interval size at each volume. The right plot shows identical results to the left plot, but focuses on the critical region. Away from the phase transition the results for all volumes are in very good agreement, this can be seen at the edges of the left hand plot. Around the phase transition, in the region we observe the non-invertibility in $a_n(u_p)$, the results differ for each volume. As we increase the volume the non-invertible region appears to grow, as the gradient of the unstable branch becomes more negative. This indicates that the metastable dynamics will affects a larger range of inverse couplings. There is an indication that it will converge in the infinite volume limit, as for each successive increase the volume, the change between the curves appears to decrease. As we expect a_n to be volume independent, this indicates that for the smaller volumes we are seeing systematic effects.

The plaquette distribution, $P_\beta(u_p)$, is shown as a colour map in Fig. 5.6, the lighter colours correspond to a high value of the plaquette distribution, as a function of both the inverse coupling, β, along the horizontal axis, and the plaquette value, u_p, on the vertical axis. Each subplot shows the results for a different spatial volume, with the same range of plaquette values, $0.568 \leq u_p \leq 0.576$, and range of inverse couplings, $7.337 \leq \beta \leq 7.343$. At each volume we show the results for a single interval size. Vertical slices correspond to the plaquette distribution for an individual inverse coupling value. The general behaviour of all the distributions are the same. For the lowest couplings, the system only has one peak, at a plaquette value around $u_p \approx 0.570$, this corresponds to pure phase configurations in the confined phase. As β increases a new peak appears, at a plaquette value around $u_p \approx 0.573$, corresponding to the pure phase configurations in the deconfined phase, between the two peaks is area with a lower probability. As we increase the inverse coupling further, the peak from the confined phase disappears, as the deconfined phase dominates. As we increase the spatial volume of the system, the peaks become more prominent. This is due to the scaling of the width of the plaquette distribution inversely with the volume.

In Fig. 5.6, the plaquette distribution in the region between the peaks appears to completely disappear for the largest volumes. To analyse this region further, in Fig. 5.7, we plot the plaquette distribution at the critical inverse coupling, $P_{\beta_{CV}}(u_p)$, where we have two peaks of equal height, with each subplot showing the results for a different spatial volume. As we saw previously, as the volume is increased the width of the peaks decreases and their height increases. However, we now see that the unstable region between the peaks does not disappear, it appears to begin to plateau. This corresponds to a break down of the double Gaussian approximation, as we start to see the effects of mixed phase configurations. To each distribution we have fit a double Gaussian distribution, shown by the black dashed line. When fitting to the distribution we do not include the area between the two vertical black lines, to ensure we only fit to the pure phase configurations, in which the double

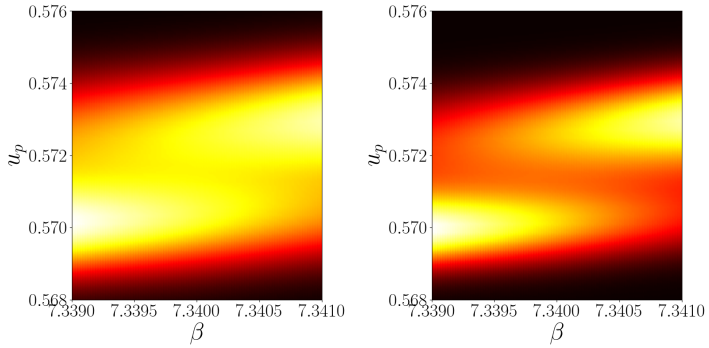

(A) $\tilde{V}/a^4 = 4 \times 20^3$, $\Delta_{u_p} = 0.00048$ (B) $\tilde{V}/a^4 = 4 \times 24^3$, $\Delta_{u_p} = 0.00048$

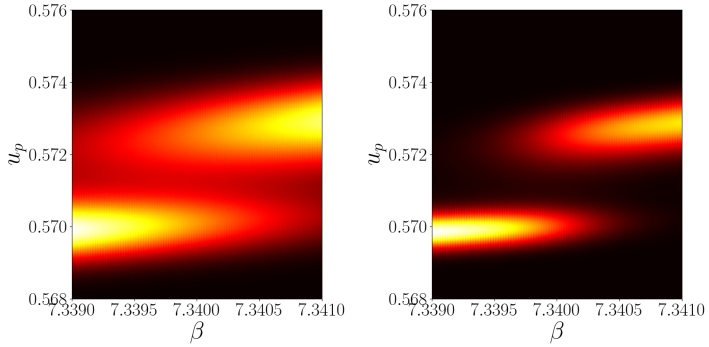

(C) $\tilde{V}/a^4 = 4 \times 28^3$, $\Delta_{u_p} = 0.00025$ (D) $\tilde{V}/a^4 = 4 \times 40^3$, $\Delta_{u_p} = 0.00013$

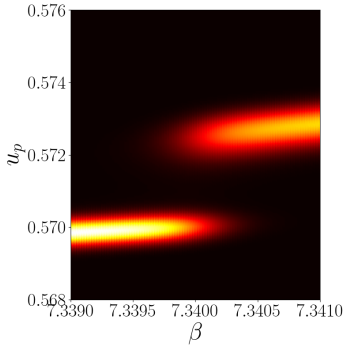

(E) $\tilde{V}/a^4 = 4 \times 48^3$, $\Delta_{u_p} = 0.00013$

Figure 5.6. The plaquette distribution, $P_\beta(u_p)$, is shown by the colour map, lighter colours correspond to a more probable plaquette value, against the plaquette value, u_p, on the vertical axis and the inverse coupling on the horizontal, β. We show the results for a plaquette range $0.568 \to 0.576$, and a inverse coupling, $7.337 \to 7.343$, for a selection of spatial volumes, N_s = 20, 24, 28, 40 and 48, for one interval size, Δ_{u_p} at each volume. Vertical slices show the plaquette distribution for a single inverse coupling.

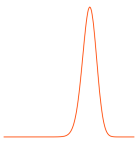

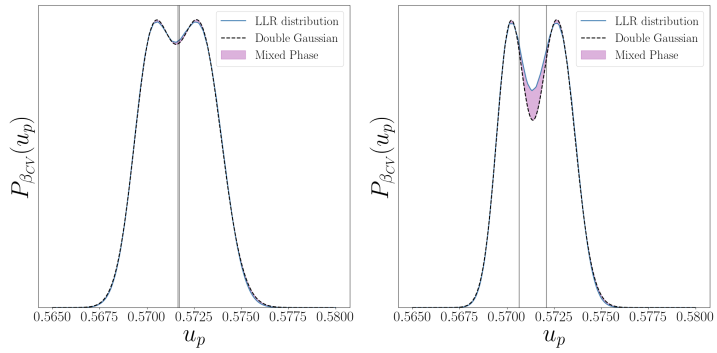

(A) $\tilde{V}/a^4 = 4 \times 20^3$, $\Delta_{u_p} = 0.00048$ (B) $\tilde{V}/a^4 = 4 \times 24^3$, $\Delta_{u_p} = 0.00048$

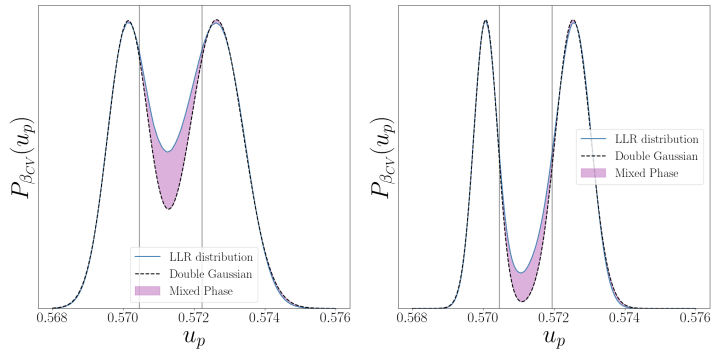

(C) $\tilde{V}/a^4 = 4 \times 28^3$, $\Delta_{u_p} = 0.00025$ (D) $\tilde{V}/a^4 = 4 \times 40^3$, $\Delta_{u_p} = 0.00013$

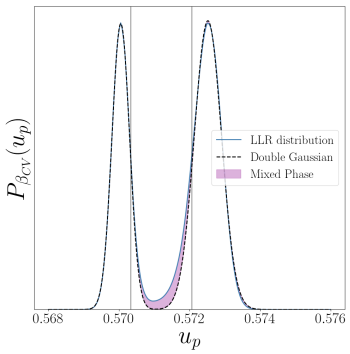

(E) $\tilde{V}/a^4 = 4 \times 48^3$, $\Delta_{u_p} = 0.00013$

Figure 5.7. The plaquette distribution at the critical coupling, $P_\beta(u_p)|_{\beta=\beta_{CV}(f)}$, shown in blue, for each spatial volume $N_s = 20, 24, 28, 40$ and 48, for the smallest interval size, Δ_{u_p}, at each volume. The black dashed line shows a fit of a double Gaussian to each distribution, excluding the central region between the two vertical lines. The area between the fitted double Gaussian and the reconstructed plaquette distribution are shown in pink.

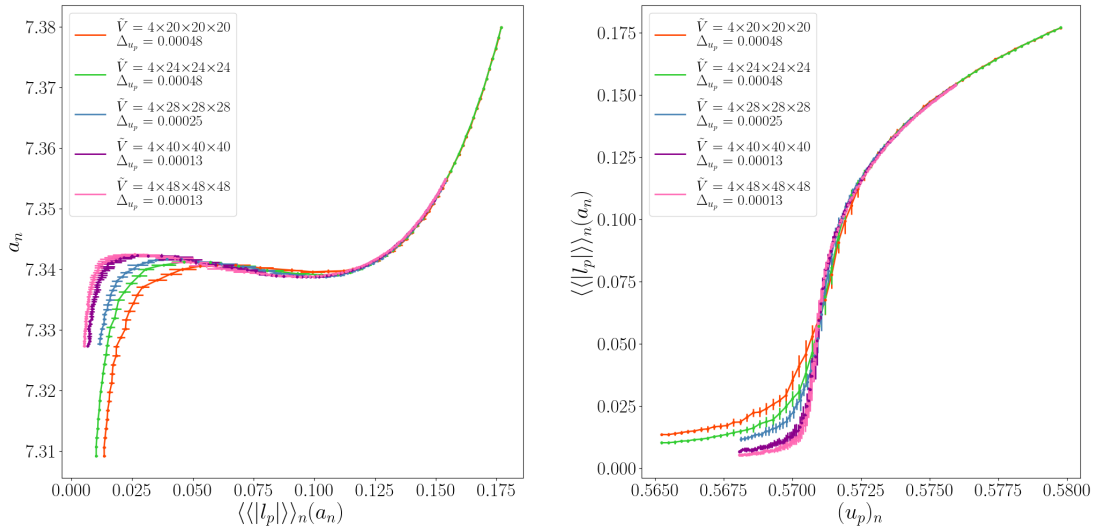

Figure 5.8. The ensemble average of the absolute value of the Polyakov loop for configurations restricted to the nth interval from the fixed a_n iterations, $\langle\langle|l_p|\rangle\rangle_n(a_n)$, plotted against the coefficients, a_n, in the left plot, and the plaquette value at the centre of the interval, $(u_p)_n$, in the right plot. Results are shown for $Sp(4)$ pure gauge theory on a lattice with $N_t = 4$, and spatial sizes, $N_s = 20$, 24, 28, 40 and 48, in different colours, for one interval size at each volume. Errors on the Polyakov loop, are the standard deviation of the results across the repeats.

Gaussian approximation is expected to hold. For the region included in the fit, the double Gaussian approximation holds well. However, between the two peaks it differs greatly, as shown by the pink shaded region. Particularly for the largest volume, $N_s = 48$, where we see that the plaquette distribution for pure phase configurations has almost completely disappeared, while we are still visibly observe a non-zero probability to have configurations in this region. This is a strong indication that within the intervals in this region, we will get mixed phase configurations.

After completing all NR and RM iterations, we again use fixed a_n iterations, as described in Sec. 3.1.2, measuring the Polyakov loop and average plaquette on configurations with their action restricted to each energy interval. In each interval we carry out 10,000 measurements. We have plotted the ensemble average of the action restricted absolute value of the Polyakov loop, $\langle\langle|l_p|\rangle\rangle_n(a_n)$, against the centre of the interval, $(u_p)_n$, and the coefficients a_n, in the right and left plots of Fig. 5.8 respectively. We notice that in the structure of the function $a_n(\langle\langle|l_p|\rangle\rangle_n)$, mirrors that of the $a_n(u_p)$, demonstrating the non-invertibility that we have shown leads to the meta-stable dynamics in the critical region. As the spatial volume increases the value of the Polyakov loop vanishes as expected, and range of a_n values in the critical region grows as the change across the transition grows. We also show the value of the Polyakov loop as a function of the plaquette value at the centre of the interval remains

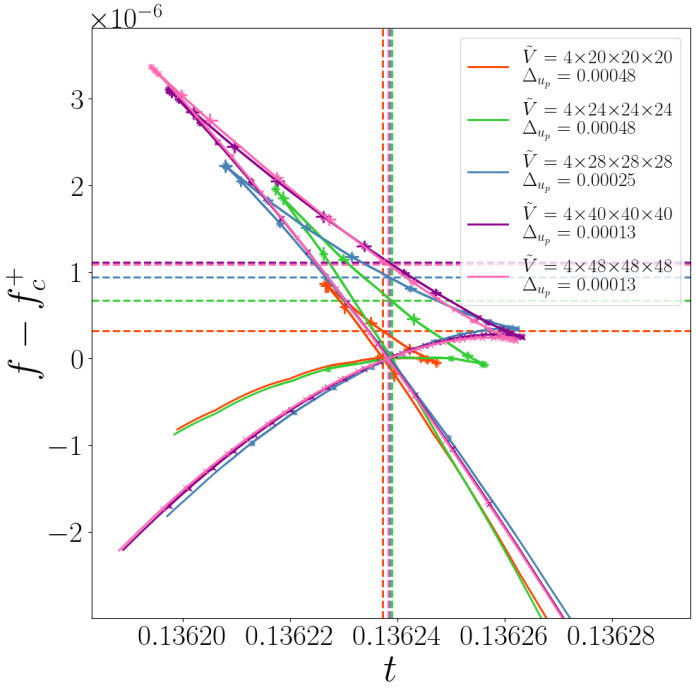

Figure 5.9. The reduced free-energy, f, against the (micro-canonical) temperature, t, for N_t = 4 and spatial volumes N_s = 20, 24, 28, 40, 48, for one interval size, Δ_{u_p}, at each volume. The vertical line shows the critical (micro-canonical) temperature, t_c, where the two meta-stable branches cross. We have subtracted from the reduced free-energy, the reduced free-energy of the meta-stable branch at the critical point, f_c^+. The horizontal line shows the value of the reduced free-energy on the unstable branch at the critical temperature.

single valued. The change in this function also becomes steeper as we increase the volume.

Through Eq. 3.1.28, we calculate the micro-canonical reduced free-energy by locally inverting $a_n(u_p)$, to give a numerical expression for the function $E(t)$, s(t), and therefore F(t). We choose the constant Σ, in Eq. 3.1.31, to be the average entropy across all intervals, and repeats, this is the average gradient of the $F(t)$. The results are plotted in Fig. 5.9, against the (micro-canonical) temperature, t, for each lattice volume, with N_t = 4, using the results for one interval size at each volume. The points on the plot are directly from our LLR results, with errors in both the free-energy and temperature found by bootstrapping over the results for each repeat. Between the points we have linearly interpolated in the function $E(t)$, shown by the lines. Using this interpolation, we find the critical (micro-canonical) temperature, t_c, as the temperature at which the two meta-stable branches of the free-energy cross. This is shown by the dashed vertical lines. The errors for this quantity are again calculated by bootstrapping over the repeats. We verify the linear interpolation is accurate by carrying out the analysis on several interval sizes, this will reduce the distance between

the points, making the approximation more accurate. We then take the limit of $\Delta_{u_p} \to 0$ for the results at each spatial volume, as described in App. B. The values for the critical inverse couplings, $\beta_{CV}(f) = 1/t_c$, are shown in Tab. 5.2. This table also includes the results for the other definitions of the critical inverse coupling, which will be discussed later. In the plot, we have subtracted the reduced free-energy of the meta-stable branch at the critical point, f_c^+, this makes the plots for different spatial volumes more directly comparable. The size of the swallow tail structure grows with the volume, but it appears to converge in the thermodynamic limit, the reduced free-energy at volume 4×48^3 almost overlapping that of 4×40^3. The gradient of the swallow tail structure of the reduced free energy for 4×20^3 and 4×24^3, differ from the others, due to the different plaquette range.

Using the free-energy, and this definition for the critical point, we can compute the difference in free-energy between the meta-stable and unstable branches at the critical point, ΔF. The change in free-energy can be related to the logarithmic term in Eq. 2.2.32, $\Delta F/t_c = \ln(P_{min}/P_{max})$. Therefore by calculating this quantity we can compute the term $\hat{I}$, which allows us to determine the interface tension for this lattice spacing, $\hat{\sigma}_{cd}$, through the thermodynamic limit. We find the change in free-energy by finding the point, in the interpolation of the free-energy, on the unstable and meta-stable branches with (micro-canonical) temperature closest to our numerically defined value of t_c, for that given repeat. The difference between these numbers is ΔF $(= \Delta f \tilde{V})$. Errors are found by repeating the calculation on all the repeats, and bootstrapping the results. The horizontal lines in Fig. 5.9, show the values of change in reduced free-energy, Δf, for each volume. We present the results for the values of $\hat{I}$, from Eq. 2.2.32, in Tab. 5.3.

To compute the surface tension, $\hat{\sigma}_{cd}$, for this N_t, we take the limit $N_t^2/N_s^2 \to 0$, for $\hat{I}$, as can be seen from Eq. 2.2.32. In Fig. 5.10, we plot the measured value of $\hat{I}$, as a function of the square of the inverse of the aspect ratio. For each volume we use the results extrapolated to the limit of vanishing interval size, except for $N_s = 48$ in which we only have results for one interval size. We fit a quadratic polynomial in N_t^2/N_s^2 to the results for spatial sizes, $N_s = 24, 28, 40$ and 48. We find a reduced chi-square for this fit of $\chi_\nu^2 = 1.0$, with an extrapolation of $\hat{\sigma}_{cd} = \lim_{N_t/N_s \to 0} \hat{I} = 0.01718(32)$. The small reduced chi-square indicates that to a good approximation our results scale with N_s^2, this indicates that we are seeing the effects of an interface on the plaquette distribution. Although we note only for the final two points does the term containing $-\ln(P_{min}/P_{max})$ dominates the $(N_t/N_s)^2 \ln(N_s)$ term in Eq. 2.2.32.

After finding the critical inverse coupling, $\beta_{CV}(f)$, through the free-energy, we can also compute the plaquette jump, $\Delta\langle u_p \rangle_{\beta_{CV}}$. This is the plaquette difference between the peaks of the plaquette distribution at the critical inverse coupling. We compute this by finding the points at which the function $u_p(a_n)$ intercepts with $a_n = \beta_{CV}(f)$. This is again done with our linear interpolation, and by finding the points on the two meta-stable branches with a_n

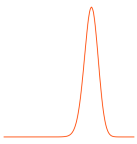

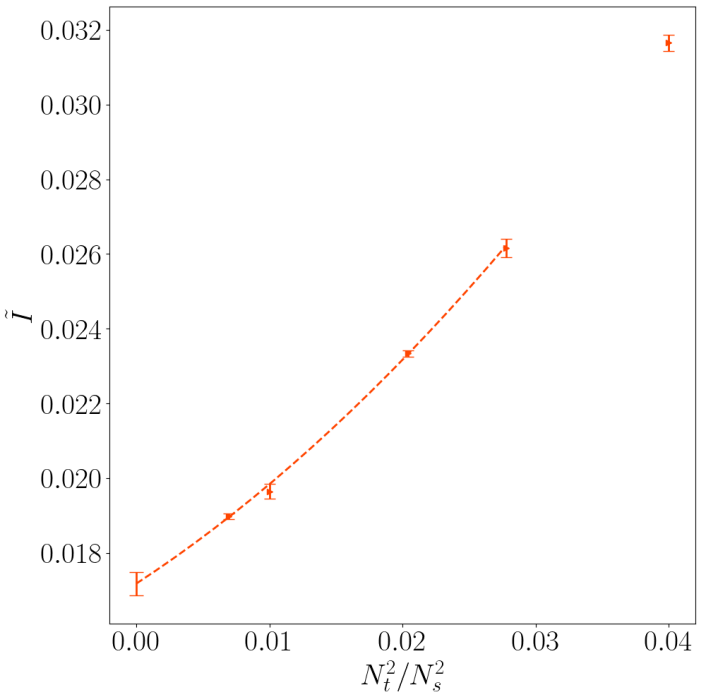

Figure 5.10. The interface tension term, $\hat{I}$, defined in Eq. 2.2.32, is calculated for $Sp(4)$ pure gauge theory with four temporal sites and spatial sizes, $N_s = 20, 24, 28, 40, 48$. For $N_s = 20$, 24, 28 and 40, the presented results are for the limit $\Delta_{u_p} \to 0$, for $N_s = 48$ we present the results for the only interval size, this is discussed further in App. B. It is plot as a function of the square of the inverse of the aspect ratio, N_t^2/N_s^2, to this we fit a quadratic polynomial, for $N_s = 24, 28, 40$ and 48, as shown by the dashed line. We have extrapolated to the limit of $N_t^2/N_s^2 \to 0$, and shown this in the plot. We find a reduced chi-square for the fit $\chi_\nu^2 = 1.0$.

value closest to $\beta_{CV}(f)$. These plaquette values correspond to the two peaks of the plaquette distribution at $\beta_{CV}(f)$. The plaquette jump is then the difference between these plaquettte values. The left plot in Fig. 5.11 shows the coefficients a_n against the plaquette values at the centre of the interval, $(u_p)_n$, and right plot shows the plaquette distribution at the critical point. We show the results for one interval size at each volume. The horizontal line in the left plot shows the line of the critical inverse coupling, $a_n = \beta_{CV}(f)$, while the vertical dashed lines shows the intercepts of this. The vertical dashed line in the right plot are at the same plaquette values as in the left plot, and correspond to the locations of the peaks. In Tab. 5.3, we present the results of the plaquette jump, for all ensembles with $N_t = 4$.

Using Eq. 3.1.18, we can compute the VEV of the average plaquette, $\langle u_p \rangle_\beta$, the specific heat, $C_V(\beta)$, and the Binder cumulant, $B_V(\beta)$, for the canonical ensemble, for a range inverse couplings set by the range of plaquette values we use. For the systems with $N_s = 20$, 24 and 28, we compute these observables for 1000 inverse couplings between $\beta = 7.337$ and 7.343, and for the systems with $N_s = 40$ and 48, we use 1000 inverse couplings between $\beta = 7.339$

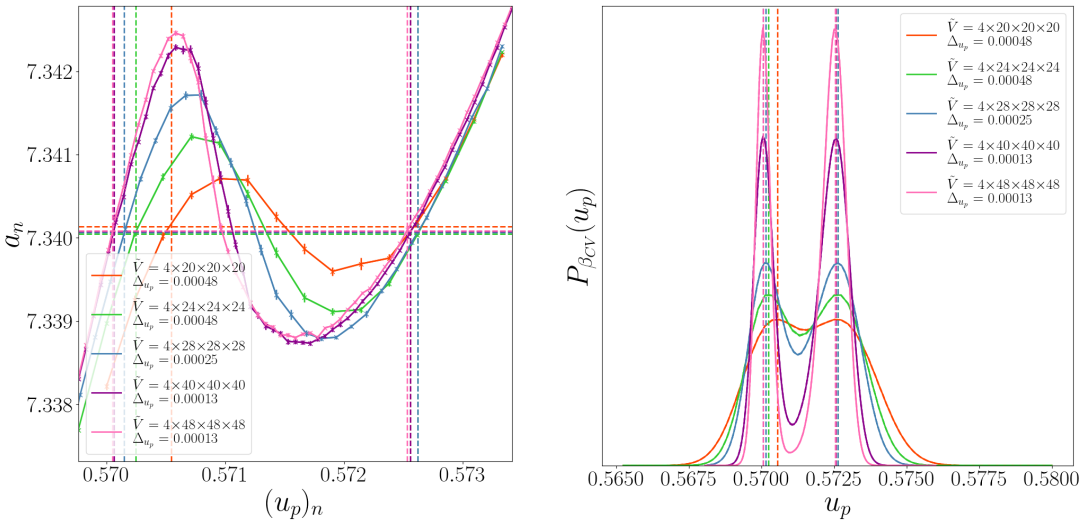

Figure 5.11. The left plot shows the coefficients, a_n, against the plaquette values at the centre of the intervals, $(u_p)_n$, focused on the critical region, for $N_t = 4$ and spatial volumes $N_s = 20$, 24, 28, 40, 48 in different colours, for one interval size, Δ_{u_p}, at each volume. The horizontal dashed line in this plot shows the critical couplings, $\beta_{CV}(f)$, found as the inverse of the (micro-canonical) temperature at which the two meta-stable branches of the free-energy cross, $\beta_{CV}(f) = 1/t_c$. The right plot shows the plaquette distribution at the critical inverse coupling, $P_\beta(u_p)$, for each volume. At this inverse coupling the plaquette distribution is approximately a double Gaussian, with two peaks of equal height. The vertical dashed lines, in both plots, show the peaks of the plaquette distribution.

and 7.341. At each β value and for each ensemble, we compute the error by bootstrapping over the results for each repeat. The results are presented against the inverse couplings in Fig. 5.12 for the VEV of the average plaquette, and the left plot of Fig. 5.13 and Fig. 5.14 for specific heat and the Binder cumulant respectively. Each plot contains results for all spatial sizes, shown in different colours, with one interval size at each volume.

As the spatial volume of the system increases, the rate of change of the plaquette distribution across the transitions increases. This can be seen directly from the VEV of the average plaquette in Fig. 5.12, and the height of the peak of the specific heat in the left plot of Fig. 5.13. We can see that the VEV of the average plaquette approaches a discrete jump, that we expect from a first order transition. The height of the peak of the specific heat grows with the volume and is expected to diverge in the thermodynamic limit, while its width reduces. In the thermodynamic limit the peak of the specific heat divided by the volume is expected to tend to a value proportional to the square of the plaquette jump at the critical point, $4a^4 C_V^{(max)}/\tilde{V} \to (\langle u_p \rangle_{\beta_{CV}})^2$. The leading corrections to this are polynomials in the inverse of the spatial volume, $1/V$ [107]. We find the peak of the specific heat, $C_V^{(max)}$ and the corresponding inverse coupling, $\beta_{CV}(C_V)$, as the maximum value measured in the our scan of β values, the errors for both are found by bootstrapping over the results for the repeats.

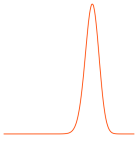

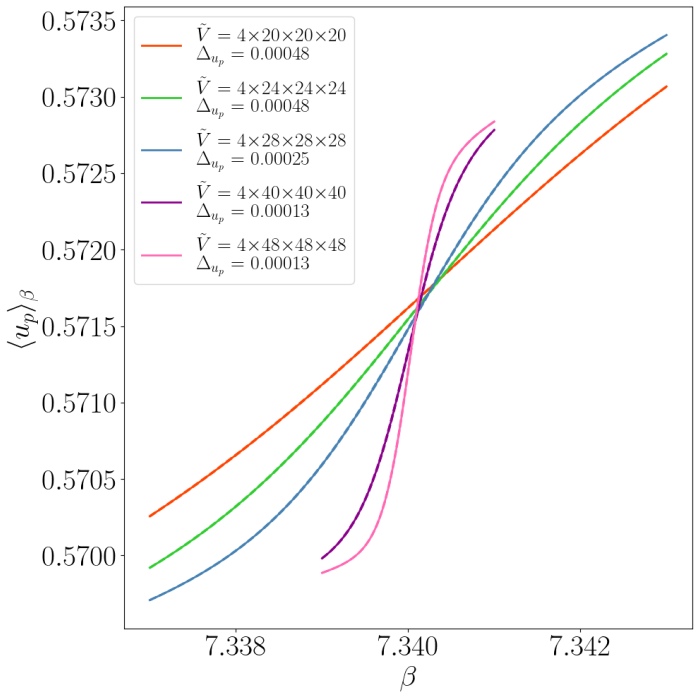

Figure 5.12. The VEV of the average plaquette, $\langle u_p \rangle_\beta$, against the inverse coupling, β, for $Sp(4)$ pure gauge theory with $N_t = 4$ and spatial sizes N_s =20, 24, 28, 40 and 48, shown in different colours. We present results for one interval size for each volume. We calculate the VEV for 1000 evenly spaced inverse couplings between $\beta = 7.337$ and 7.343, for $N_s = 20$, 24 and 28, and $\beta = 7.339$ and 7.341, for $N_s = 40$ and 48. The solid line shows the mean value across the repeats while the errors, found by bootstrapping over the results for each repeat, are shown by the dashed line.

To ensure there are no systematic error related to our choice of parameters in the scan, we repeat the calculation with a finer scan of β values and ensure the results are unchanged. For each spatial volume we extrapolate the results to the limit of vanishing interval size, see App. B. The results for $\beta_{CV}(C_V)$ and $a^4 C_V^{(max)}/\tilde{V}$, and presented in Tab. 5.2 and Tab. 5.3 respectively.

To verify the expectation for the scaling of $C_V^{(max)}$ in the thermodynamic limit, we plot $4a^4 C_V^{(max)}/6\tilde{V}$ against the cube of the inverse of the aspect ratio N_t^3/N_s^3, this is shown by the green points in the right hand plot of Fig. 5.13. On this plot we also show the square of the plaquette jump, $(\Delta\langle u_p \rangle_{\beta_{CV}})^2$, in red. All results presented in this plot are the values found by extrapolating to the limit of vanishing interval size, except $N_s = 48$ in which we only have one interval size. We fit a quadratic polynomial in N_t^3/N_s^3 to both sets of results for $N_s = 24$, 28, 40 and 48, as shown by the dashed lines, and take the thermodynamic limit, $N_t/N_s \to 0$, as shown by the point at $N_t^3/N_s^3 = 0$. The reduced chi-square for the fit of the peak of the specific heat is given by $\chi_\nu^2 = 5.5$, with an extrapolation of $4a^4 C_V/6\tilde{V} = 5.85(2) \times 10^{-6}$. The

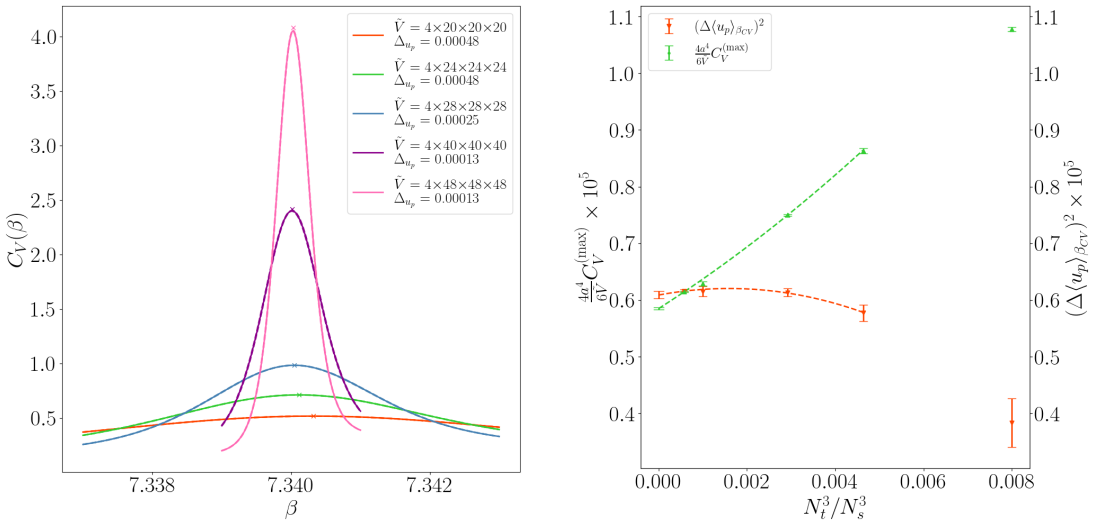

Figure 5.13. The left plot shows the specific heat, $C_V(\beta)$, against the inverse coupling, β, for $Sp(4)$ pure gauge theory with $N_t = 4$ and spatial sizes N_s =20, 24, 28, 40 and 48, shown in different colours. We present results for one interval size for each volume. We calculate the observable for 1000 evenly spaced inverse couplings between $\beta = 7.337$ and 7.343, for $N_s = 20$, 24 and 28, and $\beta = 7.339$ and 7.341, for $N_s = 40$ and 48. The solid line shows the mean value across the repeats while the errors, found by bootstrapping over the results for each repeat, are shown by the dashed line. The right plot shows the maximum measured value of of the specific heat (scaled by $4/6\tilde{V}$), $a^4C_V^{(max)}/\tilde{V}$, and the square of the plaquette jump, $(\Delta\langle u_p\rangle_{\beta_{CV}})^2$, in green and red respectively, against the cube of the inverse of the aspect ratio N_t^3/N_s^3. The points have been extrapolated to the limit of vanishing interval size, see App. B. To each we fit a quadratic polynomial in N_t^3/N_s^3, to the points at N_s = 24, 28 , 40 and 48, dashed line, and extrapolated to the thermodynamic limit, $N_t/N_s \to 0$.

reduced chi-square for the fit of the square of the plaquette jump is given by $\chi^2_\nu = 0.18$, with an extrapolation of $(\Delta\langle u_p\rangle_{\beta_{CV}})^2 = 6.09(7) \times 10^{-6}$. The results for extrapolation of $C_V/\tilde{V}$ and $\Delta\langle u_p\rangle_{\beta_{CV}}$ are given in Tab. 5.3.

We note that, although the extrapolated results are close, they are not consistent with each other. The difference between the extrapolated values could indicate that we are seeing higher order effects on the scaling, and in particular the effects due to the presence of the mixed phase states, leading to a divergence from the double Gaussian approximation. This could also be a contributing factor in the relatively poor fit, as shown by the reduced chi-square. However, the results for both observables for the largest volume, $N_s = 48$, are consistent within error, and the results for the $N_s = 40$ are only two standard deviations away. Without further analysis at larger spatial volumes, we cannot know whether the results for $C_V^{(max)}/\tilde{V}$ will continue to decrease below that of the plaquette jump, or if it will plateau and tend to the same value as the plaquette jump. We also note that the very small reduced chi-square for the fit of the square of the plaquette jump could indicate that we are

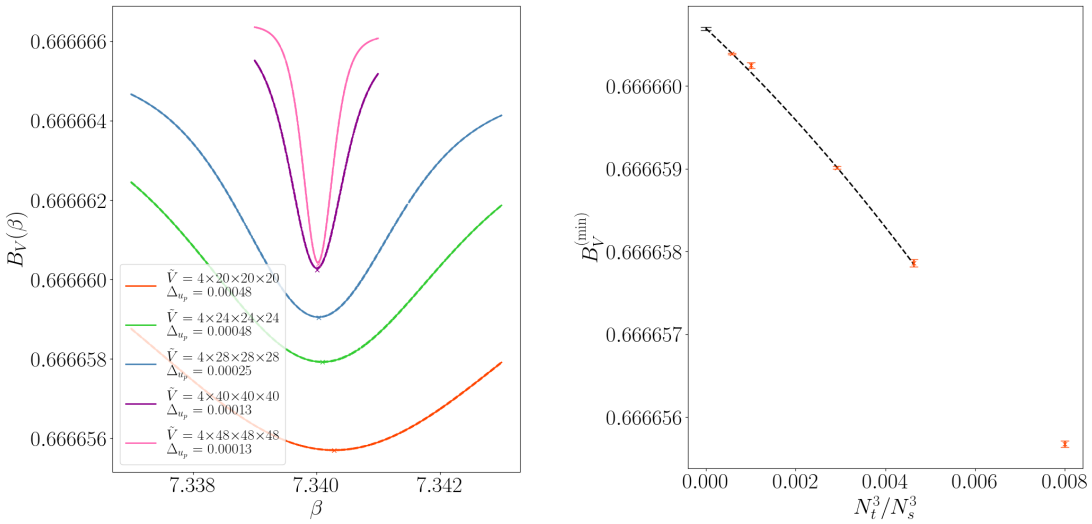

Figure 5.14. The left plot shows the Binder cumulant, $B_V(\beta)$, against the inverse coupling, β, for $Sp(4)$ pure gauge theory with N_t = 4 and spatial sizes N_s =20, 24, 28, 40 and 48, shown in different colours. We present results for one interval size for each volume. We calculate the observable for 1000 evenly spaced inverse couplings between β = 7.337 and 7.343, for N_s = 20, 24 and 28, and β = 7.339 and 7.341, for N_s = 40 and 48. The solid line shows the mean value across the repeats while the errors, found by bootstrapping over the results for each repeat, are shown by the dashed line. The right plot shows minimum measured value of the Binder cumulant, $B_V^{(min)}$, against the cube of the inverse of the aspect ratio N_t^3/N_s^3. The points have been extrapolated to the limit of vanishing interval size, see App. B. To the results we fit a quadratic polynomial in N_t^3/N_s^3, to the points at N_s = 24, 28 , 40 and 48, dashed line, and extrapolated to the thermodynamic limit, $N_t/N_s \to 0$.

over-estimating the error. Alternatively, it could suggest that, as the plaquette jump doesn't depend on the region between the peaks, and is less effected by the higher-order effects to the scaling due to the mixed-phase configurations.

Using the parameter scan of β values we also find the minima of the Binder cumulant, $B_V^{(min)}$ these values are presented in Tab. 5.3, with the corresponding inverse coupling, $\beta_{CV}(B_V)$, presented in Tab. 5.2. In the thermodynamic limit we expect the minima of the Binder cumulant to marginally increase as the width of the dip decreases, this can be seen from the left plot of Fig. 5.14. As this is a first order transition, the dip should never disappear and the minima should not approach a value of 2/3 [135]. In the right plot we take the thermodynamic limit of the minima of the Binder cumulant. As with the peak of the specific heat, it is expected that the error on the value of the minima of the Binder cumulant scales inversely with the spatial volume [135], we therefore plot it against the inverse of the aspect ratio, N_t^3/N_s^3. The results for each spatial volume, except N_s = 48, have been extrapolated to the limit of vanishing interval size. To the results for N_s = 24, 28, 40 and 48, we fit a quadratic polynomial in N_t^3/N_s^3, as shown by the dashed line, this had a reduced chi-square of χ^2_ν = 6.2.

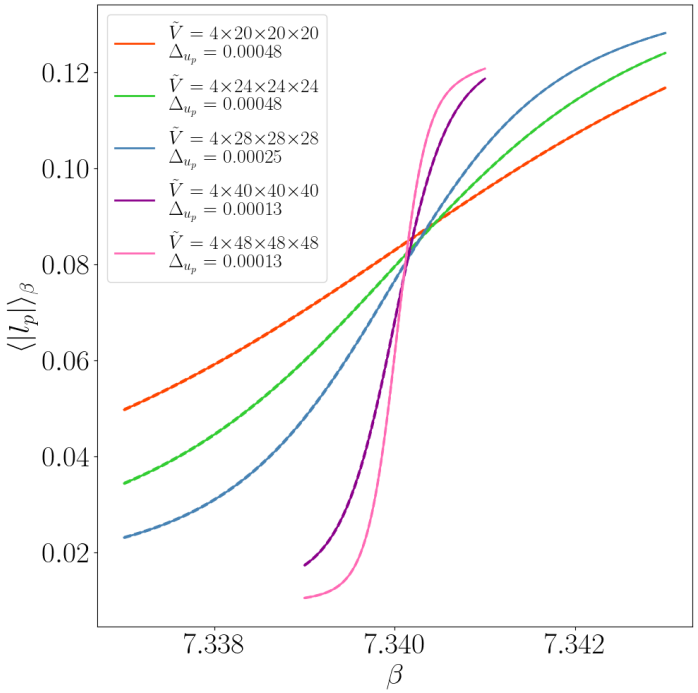

Figure 5.15. The VEV of the average of the absolute value of the Polyakov loop, $\langle |l_p| \rangle_\beta$, against the inverse coupling, β, for $Sp(4)$ pure gauge theory with N_t = 4 and spatial sizes N_s =20, 24, 28, 40 and 48, shown in different colours. We present results for one interval size for each volume. We calculate the VEV for 100 evenly spaced inverse couplings between β = 7.337 and 7.343, for N_s = 20, 24 and 28, and β = 7.339 and 7.341, for N_s = 40 and 48. The solid line shows the mean value across the repeats while the errors, found by bootstrapping over the results for each repeat, are shown by the dashed line.

For this fit we have a high reduced chi-square, this could again indicate that we are starting to see higher order effects to the scaling at larger volumes. Using this fit, we extrapolate to the thermodynamic limit giving a value of $B_V^{(min)}$ = 0.66666069(2), showing that this is a first order transition, as 2/3 is well outside the error of this extrapolation.

Using Eq. 3.1.27 and the results of the fixed a_n iterations, we are able to compute the VEV of the absolute value of the Polyakov loop, $\langle |l_p| \rangle_\beta$, and the susceptibility, $\chi_l(\beta)$. We measure their value for 100 evenly spaced inverse couplings between β = 7.337 and 7.343, for N_s = 20, 24 and 28, and between β = 7.339 and 7.341, for N_s = 40 and 48. The results are presented in Fig. 5.15 and the left hand plot of Fig. 5.16. In different colours we show the results for one interval size for each volume. Much as we observed for the average plaquette, the value of the Polyakov loop appears to tend towards a discrete jump, as we expect from first order transition in the large volume limit. This is quantified by the susceptibility, the width of the peak shrinks as the height increases. We again expect the height of the peak to scale with the volume, with leading order effects on the height of the peak inversely proportional to

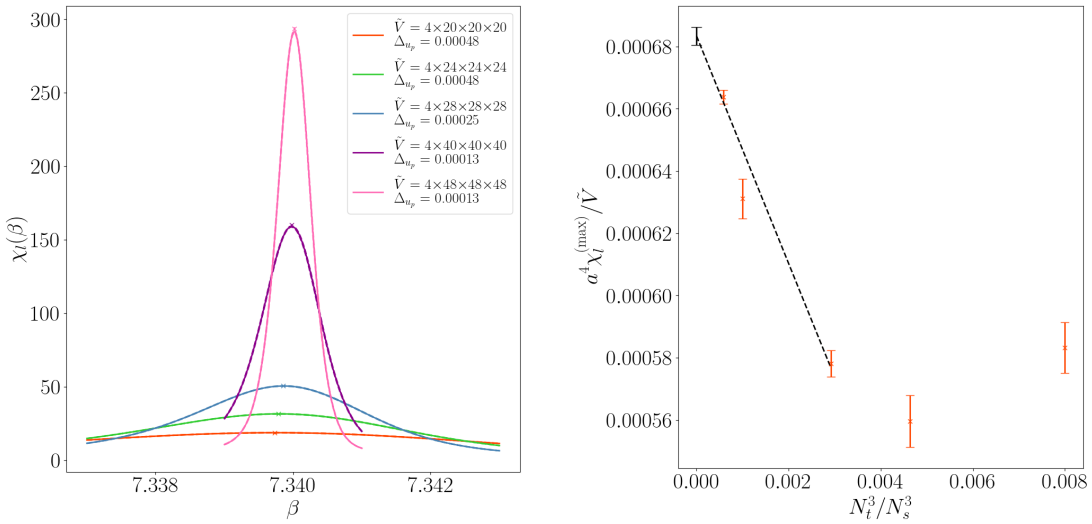

Figure 5.16. The left plot shows the Polyakov loop susceptibility, $\chi_l(\beta)$, against the inverse coupling, β, for $Sp(4)$ pure gauge theory with $N_t = 4$ and spatial sizes $N_s = 20$, 24, 28, 40 and 48, shown in different colours. We present results for one interval size for each volume. We calculate the observable for 100 evenly spaced inverse couplings between $\beta = 7.337$ and 7.343, for $N_s = 20$, 24 and 28, and $\beta = 7.339$ and 7.341, for $N_s = 40$ and 48. The solid line shows the mean value across the repeats while the errors, found by bootstrapping over the results for each repeat, are shown by the dashed line. The right plot shows maximum measured value of the Binder cumulant (scaled by the volume), $a^4\chi_l^{(max)}/\tilde{V}$, against the cube of the inverse of the aspect ratio N_t^3/N_s^3. The points are results that have been extrapolated to the limit of vanishing interval size. To the results at $N_s = 28$, 40 and 48, we carry out a linear fit in N_t^3/N_s^3, shown by the dashed line, and extrapolated to the thermodynamic limit, $N_t/N_s \to 0$.

the volume [107]. We find the peak value of the Polyakov loop susceptibility, $\chi_l^{(max)}$, and the corresponding inverse coupling, $\beta_{CV}(\chi_l)$, by taking the largest measured value in the scan of β values, and calculate errors by bootstrapping over the results for the repeats. For $C_V(\beta)$ and $B_V(\beta)$ we determined that 100 measurements was sufficient to obtain accurate results for the location and value of the peak, however the computation of observables in that case was fast enough for 1000 measurements to be easily achieved. The calculation of the Polyakov loop susceptibility is more computationally intensive, we therefore choose to only make 100 measurements. We present the results in Tab. 5.3 and Tab. 5.2, for $\chi_l^{(max)}$ and $\beta_{CV}(\chi_l)$ respectively. We discuss the limit of vanishing interval size in App. B.

In the right hand plot of Fig. 5.16, we show the peak value of the Polyakov loop susceptibility scaled by the inverse volume, $a^4\chi_l^{(max)}/\tilde{V}$, against the cube of the inverse of the aspect ratio, N_t^3/N_s^3. To the results for $N_s = 28$, 40 and 48, we carry out a linear fit in N_t^3/N_s^3, as shown by the black dashed line. We choose to omit the points at $N_s = 20$ and 24, as there is a clear change in behaviour between these and the later points, possibly indicating the results are still not in the asymptotic regime of the scaling. The fit to the data is still not good,

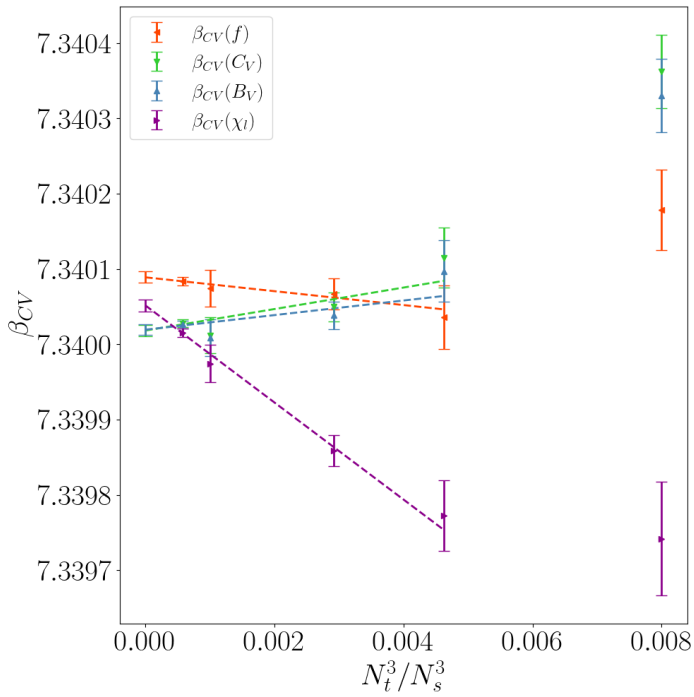

Figure 5.17. The critical couplings defined as: the intersection point of the meta-stable branches of the free-energy, $\beta_{CV}(f)$, the inverse coupling at the peak of the specific heat, $\beta_{CV}(C_V)$, the peak of the Polyakov loop susceptibility, $\beta_{CV}(\chi_l)$, and the minima of the Binder cumulant, $\beta_{CV}(B_V)$, against the cube of the inverse of the aspect ratio, N_t^3/N_s^3. The result for each volume have been extrapolated to the limit of vanishing interval size, see App. B. We linearly fit in N_t^3/N_s^3 to the points at N_s = 24, 28, 40 and 48, dashed line, and extrapolate to the thermodynamic limit, $N_t/N_s \to 0$.

with a reduced chi-square $\chi^2_\nu = 6.7$. This could indicate that the results are being affected by the higher order corrections. We extrapolate the results to the thermodynamic limit, and get a result of $a^4\chi_l^{(max)}/\tilde{V} = 6.83(3) \times 10^{-4}$.

Using the free-energy, specific heat, Binder cumulant and Polyakov loop susceptibility, we have computed four different definitions for the critical inverse couplings, $\beta_{CV}(f)$, $\beta_{CV}(C_V)$, $\beta_{CV}(B_V)$, and $\beta_{CV}(\chi_l)$, respectively. In the thermodynamic limit we expect that these definitions will converge. The results for all of these quantities are given in Tab. 5.2. A discussion of the results in the limit of vanishing interval size, for each volume is given in App. B. As with the values at the peak, we expect that the leading order finite volume corrections to the quantities scale with the inverse of the volume [107, 135], at least for the observables from the reconstructed canonical ensemble $\beta_{CV}(C_V)$, $\beta_{CV}(B_V)$, and $\beta_{CV}(\chi_l)$. In Fig. 5.17 we present the results for each definition of the critical inverse coupling, shown in different colours, against the inverse of the cube of the aspect ratio, N_t^3/N_s^3. To each we carry out a linear fit in N_t^3/N_s^3 to the results for N_s = 24, 28, 40 and 48, these are shown by the

dashed lines, and extrapolate the results to the thermodynamic limit. The fits for all result are in good agreement, with reduced chi-squares χ^2_v = 0.08, 0.84, 0.81, and 0.25 for $\beta_{CV}(f)$, $\beta_{CV}(C_V)$, $\beta_{CV}(B_V)$, and $\beta_{CV}(\chi_l)$, respectively.

The extrapolated results for the critical couplings are given by $\beta_{CV}(f)$ = 7.340089(8), $\beta_{CV}(C_V)$ = 7.340018(7), $\beta_{CV}(B_V)$ = 7.340019(7) and $\beta_{CV}(\chi_l)$ = 7.340052(8). We note that the results from the specific heat and Binder cumulant are in very good agreement, this is not unexpected as they are both based on the behaviour of the average plaquette. Their results for the three largest volumes are also consistent with each other. Although the results had a good fit, the final two points may indicate that the behaviour of the observable is changing. The results for N_s = 20, 24 and 28, all appear to decrease from the previous result, while the final two increase. This could be another indication that we are seeing the effects of the mixed phase states on the finite size error. The extrapolation of the result for the Polyakov loop susceptibility is not consistent with the extrapolation of the Binder cumulant and the specific heat. However, we see that the results for finite volume, are converging with the results for the largest volume being within error. Without considering $N_s > 48$, it is difficult to determine whether the sub-leading affects of the scaling will lead to these results converging.

The reduced chi-square for $\beta_{CV}(f)$ is very small, this indicates we are likely over-estimating the errors on these points. This definition depends on the meta-stable branches, and therefore the pure phase states, only with a indirect dependence on the mixed phase states. This could explain the difference between this inverse coupling and the others.

Table 5.2. The critical couplings defined as: the intersection point of the meta-stable branches of the free-energy, $\beta_{CV}(f)$, the inverse coupling at the peak of the specific heat, $\beta_{CV}(C_V)$, the peak of the Polyakov loop susceptibility, $\beta_{CV}(\chi_l)$, and the minima of the Binder cumulant, $\beta_{CV}(B_V)$, for $Sp(4)$ pure gauge theory at $N_t = 4$, for each spatial size, N_s, and interval size, Δ_{u_p}. The results for the vanishing interval size limit are denoted by $\to 0$, in the Δ_{u_p} column, details on these results are presented in App. B. The final row with $N_s \to \infty$, shows the results of extrapolations to the thermodynamic limit.

N_s	Δ_{u_p}	$\beta_{CV}(C_V)$	$\beta_{CV}(B_V)$	$\beta_{CV}(\chi_l)$	$\beta_{CV}(f)$
20	0.00064	7.340282(23)	7.340246(24)	7.339721(25)	7.340102(25)
20	0.00048	7.340317(17)	7.340283(17)	7.339730(30)	7.340136(19)
20	0.00025	7.340356(16)	7.340325(15)	7.339739(24)	7.340150(19)
20	$\to 0$	7.340362(49)	7.340330(49)	7.339742(75)	7.340178(54)
24	0.00064	7.340111(19)	7.340095(19)	7.339800(20)	7.340058(20)
24	0.00048	7.340113(14)	7.340096(15)	7.339788(18)	7.340048(15)
24	0.00025	7.340120(10)	7.340105(10)	7.339785(13)	7.340056(10)
24	$\to 0$	7.340115(40)	7.340097(41)	7.339773(47)	7.340036(43)
28	0.00048	7.340036(17)	7.340028(16)	7.339855(17)	7.340055(16)
28	0.00025	7.340046(13)	7.340035(12)	7.339858(14)	7.340064(14)
28	$\to 0$	7.340050(19)	7.340038(18)	7.339859(21)	7.340067(21)
40	0.00017	7.340011(9)	7.340009(8)	7.339978(8)	7.340079(9)
40	0.00013	7.340011(9)	7.340009(10)	7.339976(10)	7.340077(10)
40	$\to 0$	7.340012(24)	7.340009(24)	7.339974(25)	7.340074(24)
48	0.00013	7.340028(5)	7.340026(5)	7.340015(6)	7.340084(5)
$\to \infty$		7.340018(7)	7.340019(7)	7.340052(8)	7.340089(8)

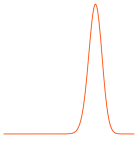

Table 5.3. The values for observables at the critical point for $Sp(4)$ pure gauge theory at $N_t = 4$, for each spatial size, N_s, and interval size, Δ_{u_p}. $a^4 C_V^{(max)}/\tilde{V}$ and $a^4 \chi_l^{(max)}/\tilde{V}$, are the maximum measured values of the specific heat and Polyakov loop susceptibility scaled by the inverse of the volume. $B_V^{(min)}$ is the minimum measured value of the Binder cumulant. $\Delta\langle u_p\rangle_{\beta_{CV}}$ is the plaquette jump at the critical point, and $\hat{I}$ is related to the interface tension defined in Eq. 2.2.32. The results for the vanishing interval size limit are denoted by $\to 0$, in the Δ_{u_p} column, details on these results are presented in App. B. The final row with $N_s \to \infty$, shows the results of extrapolations to the thermodynamic limit.

N_s	Δ_{u_p}	$a^4 C_V^{(max)}/\tilde{V}$	$B_V^{(min)}$	$a^4 \chi_l^{(max)}/\tilde{V}$	$\Delta\langle u_p\rangle_{\beta_{CV}}$	$\hat{I}$
20	0.00064	$1.611(3)\times10^{-5}$	0.66665571(2)	$5.86(4)\times10^{-4}$	0.002056(33)	0.03135(10)
20	0.00048	$1.614(2)\times10^{-5}$	0.66665570(1)	$5.85(3)\times10^{-4}$	0.002013(45)	0.03148 (8)
20	0.00025	$1.587(2)\times10^{-5}$	0.66665588(1)	$5.87(2)\times10^{-4}$	0.002048(47)	0.03146(10)
20	$\to 0$	$1.617(6)\times10^{-5}$	0.66665568(4)	$5.83(8)\times10^{-4}$	0.001958(109)	0.03165(22)
24	0.00064	$1.280(2)\times10^{-5}$	0.66665796(2)	$5.79(4)\times10^{-4}$	0.002352(10)	0.02561(10)
24	0.00048	$1.286(3)\times10^{-5}$	0.66665792(2)	$5.70(3)\times10^{-4}$	0.002375(12)	0.02586(10)
24	0.00025	$1.284(2)\times10^{-5}$	0.66665793(1)	$5.70(4)\times10^{-4}$	0.002399(12)	0.02588(8)
24	$\to 0$	$1.294(7)\times10^{-5}$	0.66665786(4)	$5.60(8)\times10^{-4}$	0.002403(30)	0.02616(25)
28	0.00048	$1.109(2)\times10^{-5}$	0.66665912(2)	$5.69(4)\times10^{-4}$	0.002461(8)	0.02278(8)
28	0.00025	$1.120(1)\times10^{-5}$	0.66665905(1)	$5.76(3)\times10^{-4}$	0.002472(10)	0.02318(5)
28	$\to 0$	$1.125(2)\times10^{-5}$	0.66665901(1)	$5.78(4)\times10^{-4}$	0.002477(14)	0.02334(8)
40	0.00017	$0.944(2)\times10^{-5}$	0.66666024(1)	$6.21(2)\times10^{-4}$	0.002509(6)	0.01973(8)
40	0.00013	$0.944(2)\times10^{-5}$	0.66666024(1)	$6.25(2)\times10^{-4}$	0.002497(7)	0.01969(8)
40	$\to 0$	$0.943(5)\times10^{-5}$	0.66666025(3)	$6.31(6)\times10^{-4}$	0.002481(18)	0.01965(20)
48	0.00013	$0.922(1)\times10^{-5}$	0.66666039(1)	$6.64(2)\times10^{-4}$	0.002482(5)	0.01897(8)
$\to \infty$		$0.878(3)\times10^{-5}$	0.66666069(2)	$6.83(3)\times10^{-4}$	0.002468(13)	0.01718(32)

5.2 $N_t = 5$

In order to study the continuum theory, we analyse the behaviour of the system as we increase N_t. This section will present an initial analysis for the deconfinement phase transition in $Sp(4)$ pure gauge theory with five temporal sites, using the LLR method. We begin with an exploration of the system using standard importance sampling methods. Before finding the initial parameters $a_n^{(0)}$, and the plaquette range, we want to determine the aspect ratio, N_s/N_t, required for us to observe the meta-stable dynamics. In the double Gaussian approximation, the width of the peaks scales with the square root of the inverse volume of the system. However, as we increase the N_t, the lattice spacing decreases and we need to increase N_s to fully resolve the separate peaks. In App. C, we analysis the importance sampling results for 5×20^3, 5×32^3 and 5×40^3, and determine that we begin to see indications of meta-stable dynamics at $N_s = 40$. In this work we focus study 5×48^3 and 5×56^3.

5.2.1 Initial importance sampling exploration

Using importance sampling methods we determine the plaquette range of interest and the initial coefficients, $a_n^{(0)}$, for the full LLR analysis. The infinite volume critical inverse couplings for $N_t = 5$ was determined to be $\beta_C = 7.486(4)$, in Ref. [86]. We therefore carry out a parameter scan of the inverse couplings $\beta = 7.480, 7.490, 7.493, 7.495$ and 7.500. For each ensemble we measure the Polyakov loop and average plaquette on 10,000 configurations, after 5,000 thermalisation steps. For each update we carry out 1 heat-bath and 4 over-relaxation updates. For accurate results, more configurations would likely be required. In particularly around the meta-stability, as we don't ensure that it tunnels between the vacua. However, for the purpose of determining the initial parameters for a more detailed study, we do not require precise results.

The VEV of the absolute value of the Polyakov loop, $\langle |l_p| \rangle_\beta$, and the susceptibility, $\chi_l(\beta)$, are shown in Fig. 5.18. From our limited scan of β values, we can see that the susceptibility peaks around $\beta = 7.493$. Between the $\beta = 7.490$ and 7.493, there is also a clear change in the value of the Polyakov loop. From this rudimentary analysis we conclude that the critical inverse coupling is likely somewhere between $\beta = 7.490$ and 7.493. These results are also mirrored in the VEV of the average plaquette, $\langle u_p \rangle_\beta$ and specific heat, $C_V(\beta)$, in Fig. 5.19.

In selecting our plaquette range, we want to include the micro-states relevant to the ensembles with inverse couplings $\beta = 7.480, 7.490, 7.493$ and 7.495. We have chosen to include $\beta = 7.480$, to ensure that we can study the previously quoted critical coupling from the literature, $\beta_C = 7.486(4)$[86]. The plaquette distributions, found from the histograms of measured plaquette values of the importance sampling analysis, is shown in Fig. 5.20.

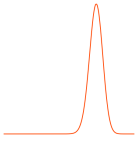

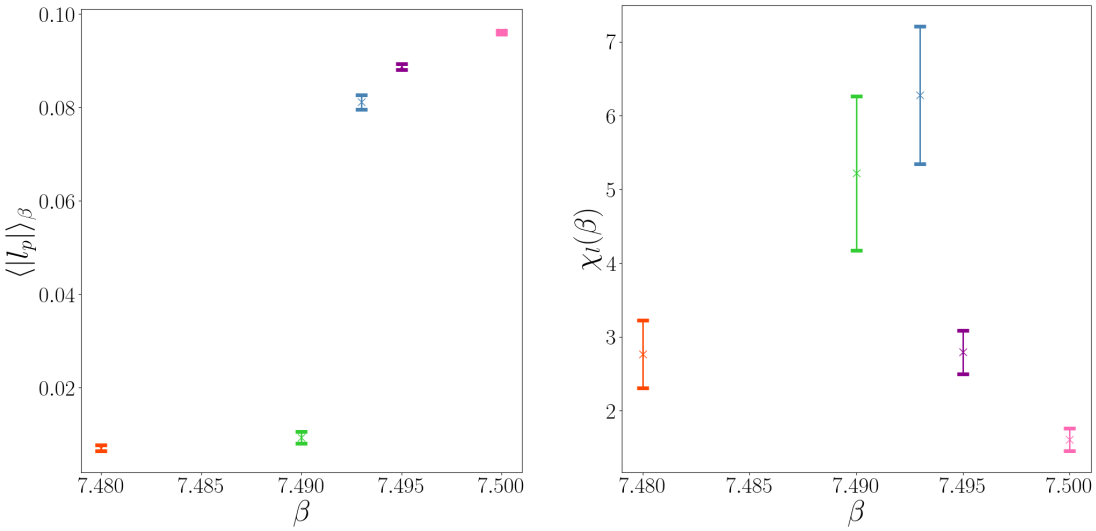

Figure 5.18. Importance sampling results for the VEV of the absolute value of the Polyakov loop (left), $\langle |l_p| \rangle_\beta$, and the susceptibility (right), $\chi_l(\beta)$, against the inverse coupling, β, for $Sp(4)$ pure gauge theory on a lattice of size 5×48^3. For each ensemble we take 10,000 measurements, after 5,000 thermalisation steps. For each update we carry out 1 heat-bath update followed by 4 over-relaxation steps. The errors were computed by binning and bootstrapping the results.

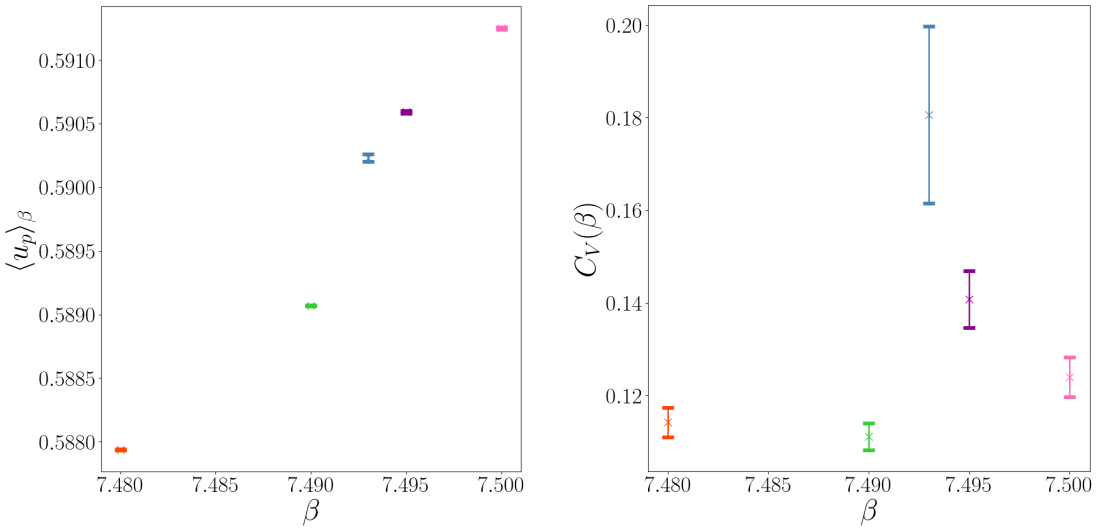

Figure 5.19. Importance sampling results for the VEV of the average plaquette (left), $\langle u_p \rangle_\beta$, and the specific heat (right), $C_V(\beta)$, against the inverse coupling, β, for $Sp(4)$ pure gauge theory on a lattice of size 5×48^3. For each ensemble we take 10,000 measurements, after 5,000 thermalisation steps. For each update we carry out 1 heat-bath update followed by 4 over-relaxation steps. The errors were computed by binning and bootstrapping the results.

From this we can see that the required plaquette range is approximately $(u_p)_{min} = 0.587$ and $(u_p)_{max} = 0.595$.

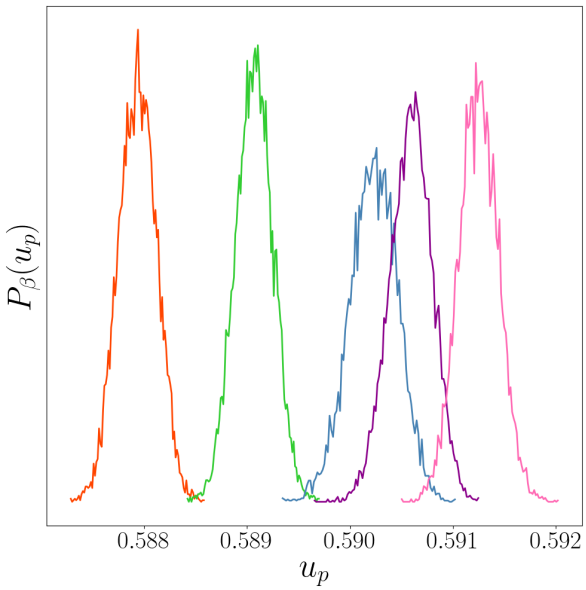

Figure 5.20. The histogram of measured average plaquette values, u_p, for a range of inverse couplings, from left to right $\beta = 7.480, 7.490, 7.493, 7.495$ and 7.500. For each ensemble we take 10,000 measurements, after 5,000 thermalisation steps. For each update we carry out 1 heat-bath, followed by 4 over-relaxation steps. The colours of the histograms match the colour of the points in Fig. 5.18 and Fig. 5.19.

We use the same plaquette range for both $\tilde{V}/a^4 = 5 \times 48^3$ and 5×56^3. For each volume, in order to study the limit of vanishing interval size we vary the number of intervals. For $N_s = 48$ we have $N_{int} = 48$ and 96, while for $N_s = 56$ we have $N_{int} = 96$ and 128. We largely choose to keep the LLR parameters used in the study of $N_t = 4$, however due to computational resources we only carry out 50 RM iterations. A full list of systems and their LLR parameters is given in Tab. 5.4.

To find the initial $a_n^{(0)}$ coefficients, we fit a cubic polynomial to the inverse coupling as a function of the measured VEV of the average plaquette, $\langle u_p \rangle_\beta^{(IS)}$. The importance sampling results and the initial $a_n^{(0)}$ values are shown by the black points and the black dashed line in Fig. 5.21, for 5×56^3. The mean over the repeats, for the coefficients a_n after 10 NR iterations are shown by the coloured dashed line, while the solid line shows the final results after completing all RM iterations. We observe that 10 NR iterations is sufficient to bring the coefficients close to the true solution, such that the RM iterations refine our results and converge. The results for each interval size, Δ_{u_p}, are shown in different colours.

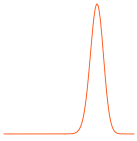

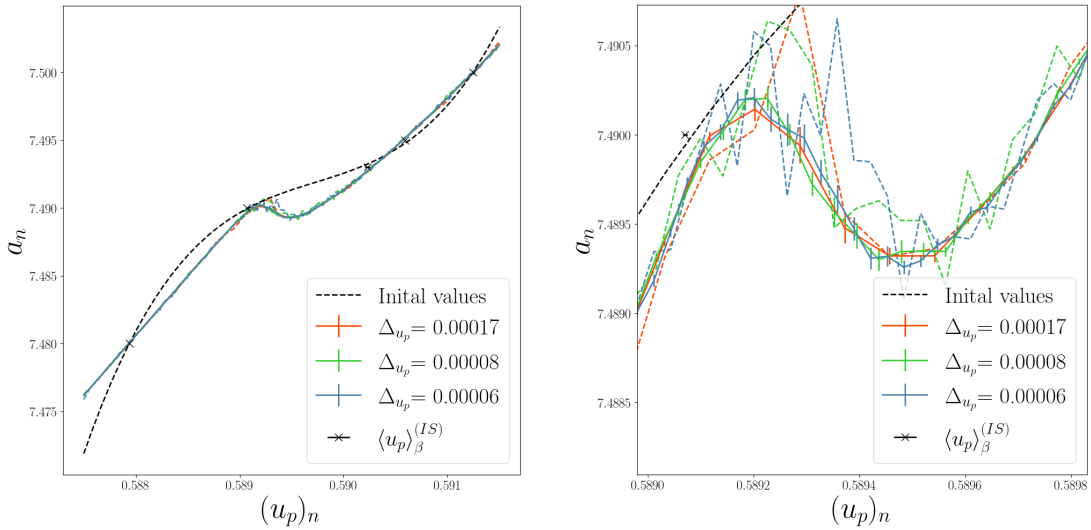

Figure 5.21. The final values of the coefficients, a_n, against the plaquette values at the centre of the intervals, $(u_p)_n$, for the $Sp(4)$ pure gauge theory on a lattice of volume 5×56^3, with three different interval sizes, Δ_{u_p}, shown in different colours. The coloured points show the results directly from the LLR method, with error calculated by bootstrapping over the repeats, while the solid line shows a linear interpolation between them. The black points show the importance sampling results, with β on the vertical axis and the measured VEV of the average plaquette, $\langle u_p \rangle_\beta^{(IS)}$, on the horizontal axis. The black dashed line shows the initial a_n values, before starting the NR iterations, found from a cubic fit of the importance sampling results. The coloured dashed lines show the mean a_n values after completing the NR iterations, before starting the RM iterations. The right plot is identical to the left, but focuses on the critical region.

Table 5.4. A list of LLR parameters for the study of the deconfinement phase transition in $Sp(4)$ pure gauge theory on a lattice with five temporal sites, for several spatial volumes. For each volume we chose several interval sizes, Δ_{u_p}, such that the limit of vanishing interval size could be analysed. The interval size has been quoted to 5 decimal places for convenience. The definitions for the variables of this table are given in Tab. 3.1.

$N_t \times N_s^3$	N_{int}	n_R	Δ_{u_p}	$(u_p)_{\min}$	$(u_p)_{\max}$	$\bar{m}$	$\tilde{m}$	$\hat{m}$	n_{Th}	n_M	n_{fxa}
5×48^3	48	25	0.00017	0.5875	0.5915	10	50	50	300	700	100
5×48^3	96	25	0.00008	0.5875	0.5915	10	50	50	300	700	100
5×56^3	48	25	0.00017	0.5875	0.5915	10	50	50	300	700	100
5×56^3	96	25	0.00008	0.5875	0.5915	10	50	50	300	700	100
5×56^3	128	25	0.00006	0.5875	0.5915	10	50	50	300	700	100

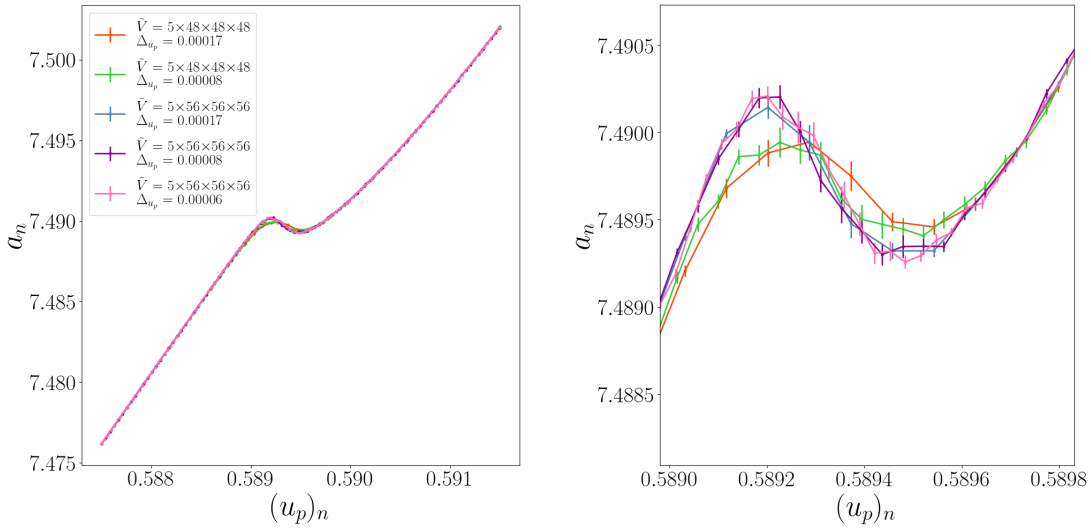

Figure 5.22. The final values of the coefficients, a_n, against the plaquette values at the centre of the intervals, $(u_p)_n$, for $Sp(4)$ pure gauge theory on lattice with $N_t = 5$, for $N_s = 48$ and 56 with all interval sizes, Δ_{u_p}, shown in different colours. The coloured points show the results directly from the LLR method, with error calculated by bootstrapping over the repeats, while the solid line shows a linear interpolation between them. The points in the right plot are identical to the left, but focuses on the critical region.

5.2.2 LLR analysis

The final values for the coefficients, a_n, after completing the NR and RM iterations, are shown against the plaquette values at the centre of the interval, $(u_p)_n$, for all spatial volumes and interval sizes with $N_t = 5$, in Fig. 5.5. The general behaviour of all systems is the same. Away from the critical region, all results are consistent. Around the non-invertibility in $a_n(u_p)$, as we saw for $N_t = 4$, the region that exhibits the meta-stable dynamics and the rate of change of the coefficients a_n grows with the volume. We also note that the results for the largest interval size, $\Delta_{u_p} = 0.00017$, for both volumes is likely not in the asymptotic regime of the limit of vanishing interval size. As the change in a_n is smoother for both and rather than simply appearing to interpolate the results with smaller interval sizes, it appears to average the results within the intervals.

Using Eq. 3.1.28, we can again compute the reduced free-energy, $f(t)$, by computing $s(t)$ directly from a_n, then locally inverting the function $a_n(u_p)$, to find an expression for $E(t)$. We can find values at the centres of the intervals, then between them we interpolate in $E(t)$. Σ, in Eq. 3.1.31, is the average entropy across the intervals and repeats, this is average gradient of the free-energy. Fig. 5.23 shows the reduced free-energy for both the system at $N_s = 48$ and 56, using results for the smallest interval size at each volume. By finding the two closest

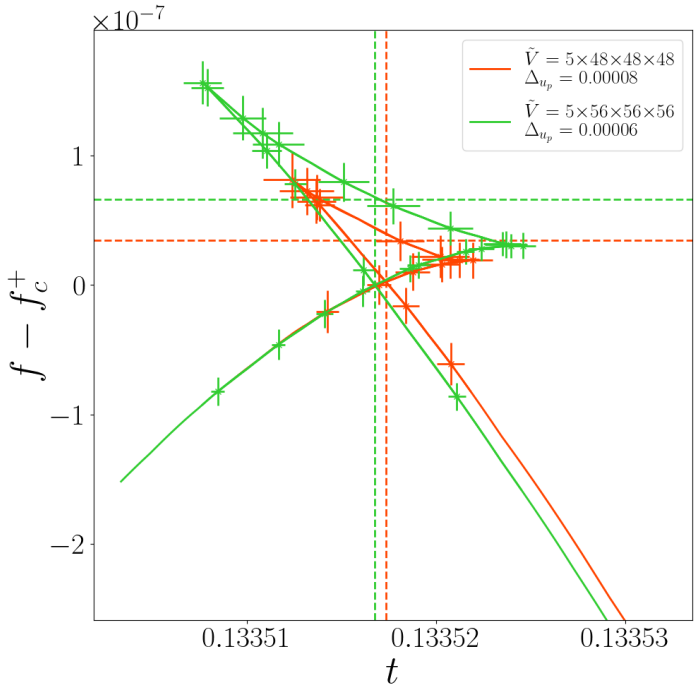

Figure 5.23. The reduced free-energy, f, against the (micro-canonical) temperature, t, for $N_t = 5$ and spatial volumes $N_s = 48$ and 56, for one interval size, Δ_{u_p}, at each volume. The vertical line shows the critical (micro-canonical) temperature, t_c, where the two meta-stable branches cross. We have subtracted from the reduced free-energy, the reduced free-energy of the meta-stable branch at the critical point, f_c^+. The horizontal line shows the value of the unstable branch of the reduced free-energy at the critical temperature.

points from the two different meta-stable branches in the interpolation of the reduced free-energy, we can determine the location of the critical (micro-canonical) temperature and thus the critical inverse coupling, $\beta_{CV}(f) = 1/t_c$. This is shown by the dashed horizontal line. In this plot, to the value of the reduced free-energy we subtract the free-energy at the point the two meta-stable branches cross, f_c^+. The horizontal dashed line shows the value on the unstable branch at the critical (micro-canonical) temperature, therefore this is equal to the jump in the reduced free-energy across the transition, $\Delta f = a^4 \Delta F/\tilde{V}$. The measured values of $\hat{I}$, defined in Eq. 2.2.32, calculated using the change in the free-energy at the critical point, $\Delta F/t_c = -\ln(P_{min}/P_{max})$, are presented in Tab. 5.6. The critical inverse coupling is presented in Tab. 5.5.

To find the peaks of the plaquette distribution, and compute the plaquette jump, we find the points at which the line $u_p(a_n = \beta_{CV}(f))$, for each interval size and volume. We show this in Fig. 5.24. The left hand plot shows the plaquette values at the centre of the energy intervals, $(u_p)_n$, against the coefficients a_n, and the right plot shows the plaquette

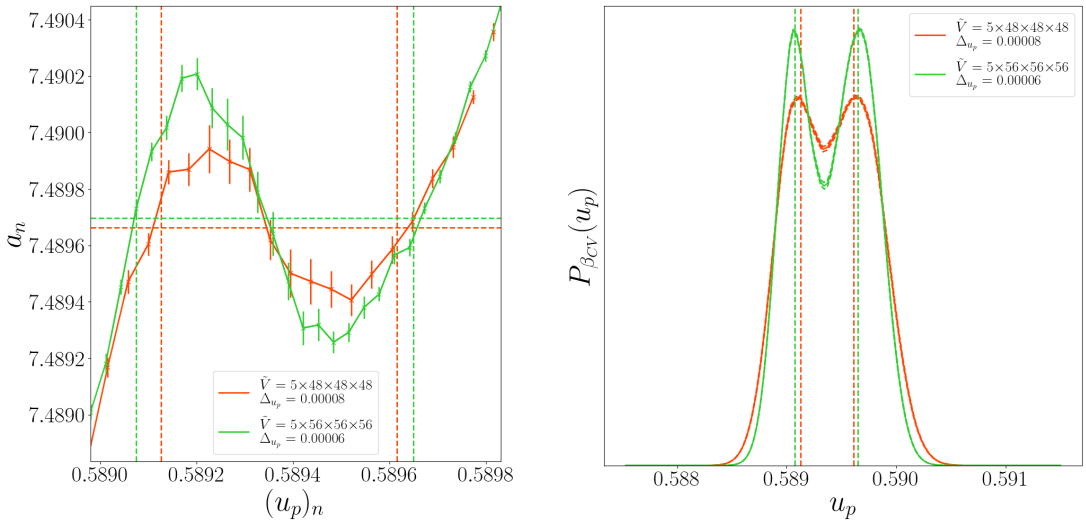

Figure 5.24. The left plot shows the coefficients, a_n, against the plaquette values at the centre of the intervals, $(u_p)_n$, focused on the critical region, for $N_t = 5$ and spatial volumes $N_s = 48$ and 56, in different colours, for the smallest interval size, Δ_{u_p}, at each volume. The horizontal dashed line in this plot shows the critical couplings, $\beta_{CV}(f)$, found as the inverse of the (micro-canonical) temperature at which the two meta-stable branches of the free-energy cross, $\beta_{CV}(f) = 1/t_c$. The right plot shows the plaquette distribution at the critical inverse coupling, $P_\beta(u_p)$, for each volume. At this inverse coupling the plaquette distribution is approximately a double Gaussian, with two peaks of equal height. The vertical dashed lines, in both plots, show the peaks of the plaquette distribution.

distribution at the critical inverse coupling, $P_\beta(u_p)|_{\beta=\beta_{CV}(f)}$. The horizontal dashed line in left plot shows the line of $a_n = \beta_{CV}(f)$, while the vertical lines shows the intersection points. The right plot has vertical dashed lines at the same points, showing that they correspond to the peaks of the plaquette distribution. We find that the lines visibly do not intersect the curve of the mean value of $u_p(a_n)$. The error on the curve of $u_p(a_n)$, is only in one direction, as we fix the values of $(u_p)_n$. However, both the horizontal line of the critical coupling and the vertical lines of the intersection points, have errors. The plot does not show the error on these values. The fact that we can visibly see this divergence indicates that more RM iterations should be carried out to refine our coefficients, a_n further. The difference between the two vertical lines gives an estimate for the plaquette jump at the critical point, $\Delta\langle u_p\rangle_{\beta_{CV}}$ These preliminary measured results are presented in Tab. 5.6.

We also compute the specific heat, $C_V(\beta)$, Binder cumulant, $B_V(\beta)$, and the Polyakov loop susceptibility, $\chi_l(\beta)$, for evenly spaced inverse couplings between $\beta = 7.4880$ and 7.4910. For the specific heat and Binder cumulant as they depend explicitly on the energy, we compute them using Eq. 3.1.18, this calculation is very fast, and we therefore carry out a scan of 1000 β values. The computation of $\chi_l(\beta)$ requires the use the of the results of the fixed a_n iterations, and Eq. 3.1.27. this is slower and therefore we choose to only carry out

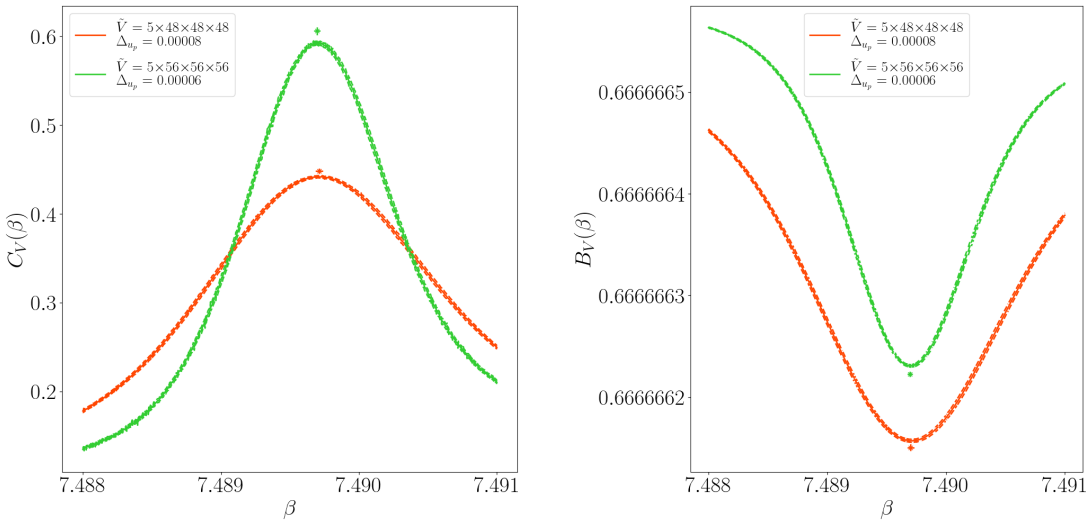

Figure 5.25. The specific heat (left), $C_V(\beta)$, and the Binder cumulant (right)), $B_V(\beta)$, against the inverse coupling, β, for $Sp(4)$ pure gauge theory with $N_t = 5$ and spatial sizes $N_s = 48$, and 56, shown in different colours. We present results for one interval size for each volume. We calculate the observable for 1000 evenly spaced inverse couplings between $\beta = 7.4880$ and 7.4910. The solid line shows the mean value across the repeats while the errors, found by bootstrapping over the results for each repeat, are shown by the dashed line. The points show the value of the observable and the inverse coupling at the extrema of the observable (left) $(\beta_{CV}(C_V), C_V^{(max)})$ and (right) $(\beta_{CV}(B_V), B_V^{(min)})$.

a scan of 100 β values. The results for $C_V(\beta)$ and $B_V(\beta)$,is shown in Fig. 5.25, and $\chi_l(\beta)$ is shown in Fig. 5.26. We present the results for the smallest interval size for each volume, shown in different colours. The solid line shows the mean value for the results, and the dashed line shows the errors, calculated by bootstrapping over the results from the repeats for each inverse coupling.

The individual points in these plots, show the value at the extrema of each observable, $C_V^{(max)}$, $B_V^{(min)}$ and $\chi_l^{(max)}$, and the corresponding critical inverse coupling, $\beta_{CV}(C_V)$, $\beta_{CV}(B_V)$ and $\beta_{CV}(\chi_l)$. The points are outside the errors of the observables. The extrema are found by finding the extremal measured value for each observable in the scan of inverse couplings. The errors on these points have errors in both the inverse coupling and the value of the observable, whereas for the parameter scan we set the inverse couplings, and there is therefore only error in the value of the observable. The correlation between the value of a_n, within a single repeat can lead to the curve of the peak shifting across to different β values. This has led to the measured peak values being outside the error of the measured observable. We likely require more RM iterations, to further refine our a_n results, to improve our estimate for these observables. The preliminary results for these observables are given in Tab. 5.6, with the corresponding inverse couplings in Tab. 5.5.

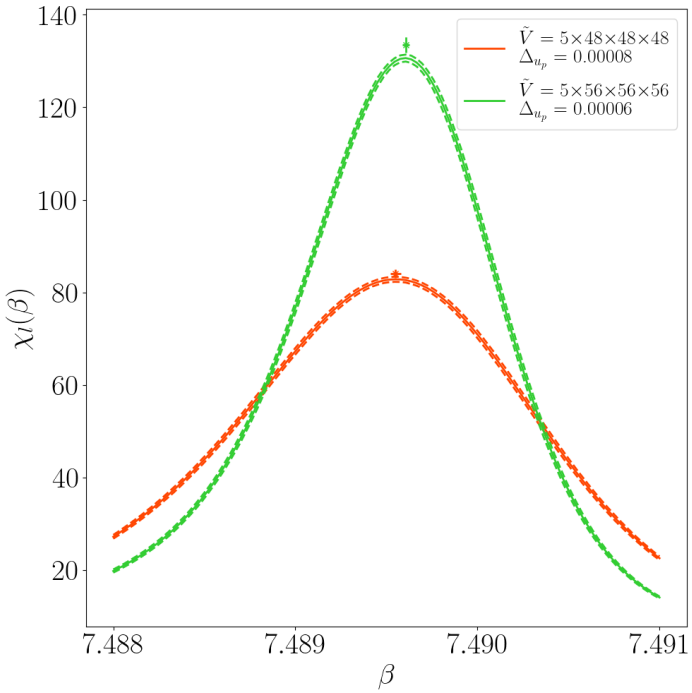

Figure 5.26. The Polyakov loop susceptibility, $\chi_l(\beta)$, against the inverse coupling, β, for $Sp(4)$ pure gauge theory with $N_t = 5$ and spatial sizes $N_s = 48$, and 56, shown in different colours. We present results for one interval size for each volume. We calculate the observable for 100 evenly spaced inverse couplings between $\beta = 7.4880$ and 7.4910. The solid line shows the mean value across the repeats while the errors, found by bootstrapping over the results for each repeat, are shown by the dashed line. The points show the value of the observable and the inverse coupling at the extrema of the observable $(\beta_{CV}(\chi_l), \chi_l^{(max)})$.

In future work, results for these lattice volumes should be refined to gain values estimates for thermodynamic observables that are more self-consistent. Larger spatial volumes should be studied to give access to surface tension, and the other thermodynamic observables in the thermodynamic limit for this lattice spacing. Larger volumes are also required to start to fully gain the advantage of the LLR method, and start to further study the effects of mixed phase states.

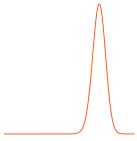

Table 5.5. The critical couplings defined as: the intersection point of the meta-stable branches of the free-energy, $\beta_{CV}(f)$, the inverse coupling at the peak of the specific heat, $\beta_{CV}(C_V)$, the peak of the Polyakov loop susceptibility, $\beta_{CV}(\chi_l)$, and the minima of the Binder cumulant, $\beta_{CV}(B_V)$, for $Sp(4)$ pure gauge theory at $N_t = 5$, for each spatial size, N_s, and interval size, Δ_{u_p}.

N_s	Δ_{u_p}	$\beta_{CV}(C_V)$	$\beta_{CV}(B_V)$	$\beta_{CV}(\chi_l)$	$\beta_{CV}(f)$
48	0.00017	7.489736(34)	7.489730(33)	7.489581(36)	7.489665(36)
48	0.00008	7.489711(27)	7.489702(28)	7.489550(30)	7.489664(31)
56	0.00017	7.489675(30)	7.489676(29)	7.489617(28)	7.489672(32)
56	0.00008	7.489679(23)	7.489682(24)	7.489600(25)	7.489677(26)
56	0.00006	7.489697(21)	7.489696(21)	7.489606(20)	7.489698(21)

Table 5.6. The values for observables at the critical point for $Sp(4)$ pure gauge theory at $N_t = 5$, for each spatial size, N_s, and interval size, Δ_{u_p}. $a^4 C_V^{(max)}/\tilde{V}$ and $a^4 \chi_l^{(max)}/\tilde{V}$, are the maximum measured values of the specific heat and Polyakov loop susceptibility scaled by the inverse of the volume. $B_V^{(min)}$ is the minimum measured value of the Binder cumulant. $\Delta\langle u_p\rangle_{\beta_{CV}}$ is the plaquette jump at the critical point, and $\hat{I}$ is the related to the surface tension defined in Eq. 2.2.32.

N_s	Δ_{u_p}	$a^4 C_V^{(max)}/\tilde{V}$	$B_V^{(min)}$	$a^4 \chi_l^{(max)}/\tilde{V}$	$\Delta\langle u_p\rangle_{\beta_{CV}}$	$\hat{I}$
48	0.00017	$0.806(7)\times10^{-6}$	0.666666152(4)	0.000156(3)	0.000503(18)	0.01140(12)
48	0.00008	$0.811(5)\times10^{-6}$	0.666666151(3)	0.000152(2)	0.000488(15)	0.01128(13)
56	0.00017	$0.693(8)\times10^{-6}$	0.666666224(5)	0.000159(3)	0.000583(10)	0.00993(17)
56	0.00008	$0.694(7)\times10^{-6}$	0.666666227(4)	0.000156(2)	0.000560(13)	0.00983(15)
56	0.00006	$0.690(5)\times10^{-6}$	0.666666223(3)	0.000152(2)	0.000575(9)	0.00975(12)

5.3 $N_t = 6$

To continue our goal of reaching the continuum limit, we began a study of $N_t = 6$. In this case we have been unable to get results that demonstrate the meta-stable dynamics we expect from a first order transition. In this section, we will discuss an initial exploration of $N_t = 6$ with $N_s = 72$. We discuss our initial findings, some issues that have become apparent at this lattice size, and the direction of future study. At $N_t = 4$ and $N_t = 5$, we found that an aspect ratio of $N_s/N_t = 10$ was sufficient to resolve the two peaks of the energy distribution, and start to observe the first order nature of the system. We therefore selected 6×72^3, with $N_s/N_t = 12$ as a lattice size that we expected to observe these features for this temporal extent. As we saw for $N_t = 4$ and 5, we can use results at smaller spatial volumes to determine initial parameters for the LLR analysis. For initial importance sampling analysis, we select a lattice of size 6×48^3, with ensembles at $\beta = 7.610, 7.615, 7.620, 7.625$ and 7.630. The infinite volume critical inverse coupling in Ref. [86] was determined to be 7.611(14). For each inverse

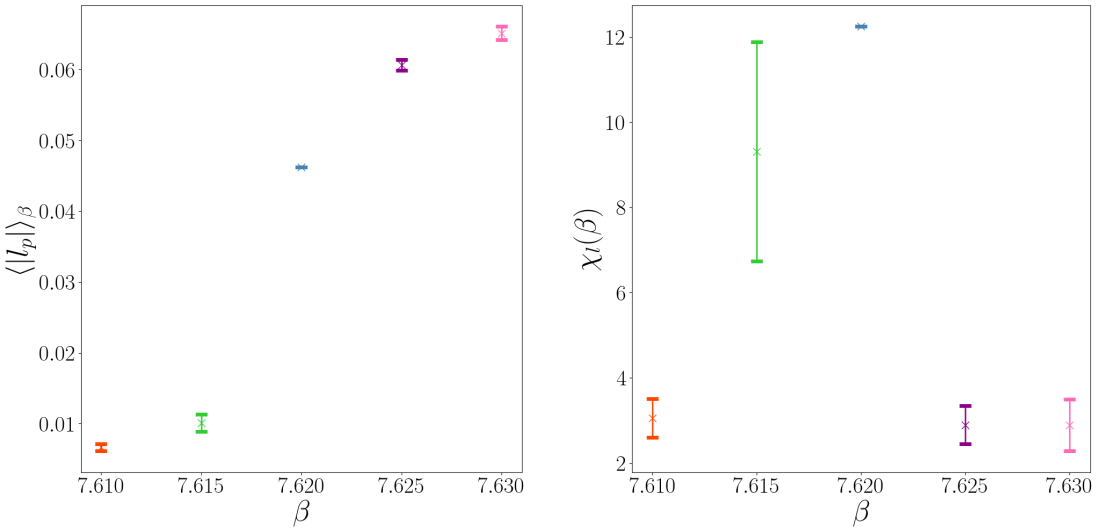

Figure 5.27. Importance sampling results for the VEV of the absolute value of the Polyakov loop (left), $\langle |l_p| \rangle_\beta$, and the susceptibility (right), $\chi_l(\beta)$, against the inverse coupling, β, for $Sp(4)$ pure gauge theory on a lattice of size 6×48^3. For each ensemble we take 50,000 measurements, after 10,000 thermalisation steps. For each update we carry out 1 heat-bath update followed by 4 over-relaxation steps. The errors were computed by binning and bootstrapping the results.

coupling, we measure the Polyakov loop and average plaquette on 50,000 configurations, after 10,000 thermalisation steps. For each lattice update we carry out 1 heat-bath and 4 over-relaxation updates.

From the VEV of the absolute value of the Polyakov loop, $\langle |l_p| \rangle_\beta$, the susceptibility, $\chi_l(\beta)$, Fig. 5.27, the VEV of the average plaquette, $\langle u_p \rangle_\beta$, and specific heat, $C_V(\beta)$, Fig. 5.28, we can see that the critical point appears to be around $\beta = 7.620$. Both the specific heat and the Polyakov loop susceptibility peak at this inverse couplings, and between $\beta = 7.615$ and 7.620, there appears to be a clear jump in the value of the Polyakov loop. To ensure we include the micro-states for at least one of the ensembles in the confined and deconfined phases, we choose a plaquette range that encompasses all the relevant the micro-states for $\beta = 7.615$ and 7.620, and covers the majority of the relevant range for $\beta = 7.625$. The plaquette distribution for all ensembles are shown by the histograms in Fig. 5.29. The plaquette range we chose is given by $(u_p)_{min} = 0.6010$ and $(u_p)_{min} = 0.6030$. In order to study the systematic affects of finite interval size, we study the system with two interval sizes, as set by the number of intervals, $N_{int} = 48$ and 96.

We again select largely the same LLR parameters as for the previous studies. However, due to the increased computational complexity of this lattice size, we only carry out 9 NR iterations, followed by 30 RM iterations for $\Delta_{u_p} = 0.00008$ and 20 RM iterations for $\Delta_{u_p} = 0.00004$. We were also unable to complete the fixed a_n iterations. A full list of the LLR

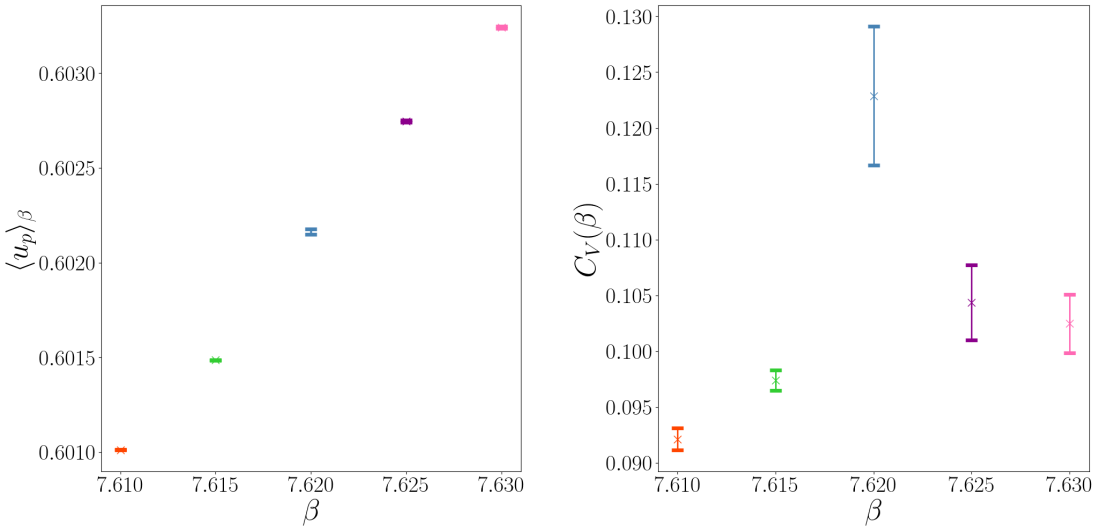

Figure 5.28. Importance sampling results for the VEV of the average plaquette (left), $\langle u_p \rangle_\beta$, and the specific heat (right), $C_V(\beta)$, against the inverse coupling, β, for $Sp(4)$ pure gauge theory on a lattice of size 6×48^3. For each ensemble we take 50,000 measurements, after 10,000 thermalisation steps. For each update we carry out 1 heat-bath update followed by 4 over-relaxation steps. The errors were computed by binning and bootstrapping the results.

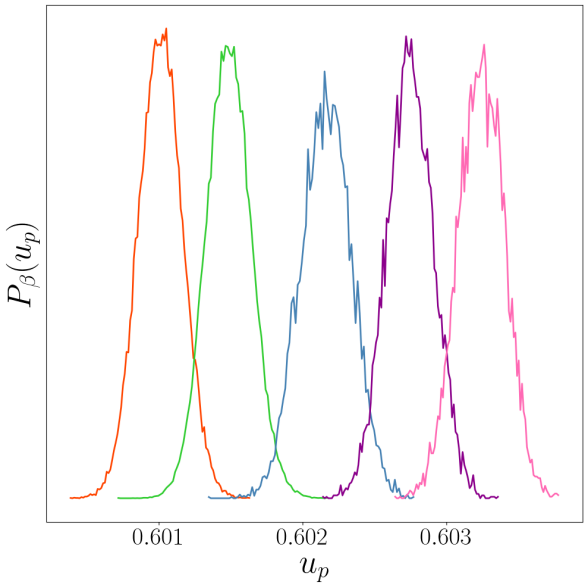

Figure 5.29. The histogram of measured average plaquette values, u_p, for a range of inverse couplings, from left to right β = 7.610, 7.615, 7.620, 7.625 and 7.630. For each ensemble 50,000 measurements were taken after 10,000 thermalisation steps. For each update we carry out 1 heat-bath, followed by 4 over-relaxation steps. The colours of the histograms match the colour of the points in Fig. 5.27 and Fig. 5.28.

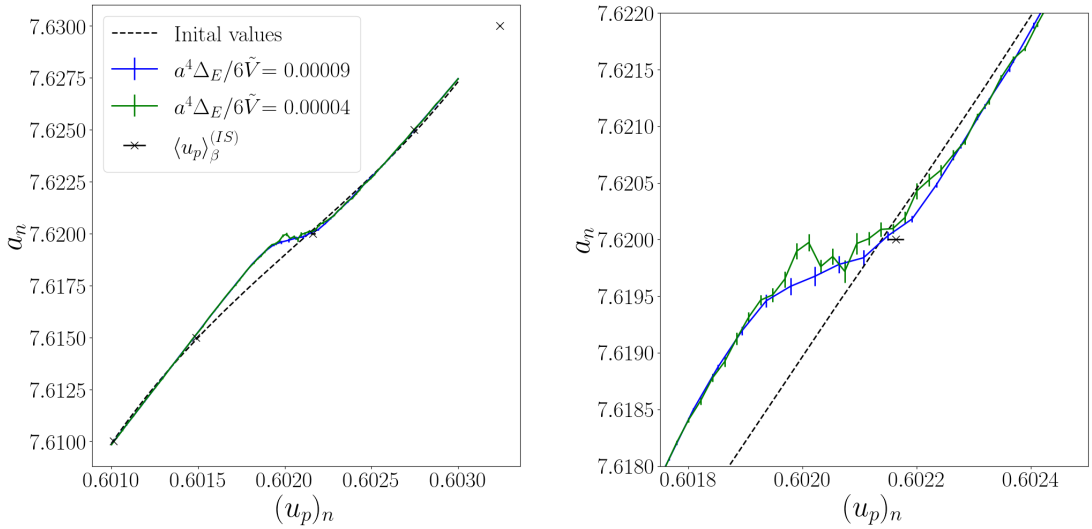

Figure 5.30. The final values of the coefficients, a_n, against the plaquette values at the centre of the intervals, $(u_p)_n$, for the $Sp(4)$ pure gauge theory on a lattice of volume 6×72^3, with two different interval sizes, Δ_{u_p}, shown in different colours. The coloured points show the results directly from the LLR method, with errors calculated by bootstrapping over the repeats, while the solid line shows a linear interpolation between them. The black points show the importance sampling results, the vertical axis are the β values, and the horizontal axis is the VEV of the average plaquette, $\langle u_p\rangle_\beta$. The black dashed line shows the initial a_n values, before starting the NR iterations, found from a cubic fit of the importance sampling results. The right plot is identical to the left, but focuses on the critical region.

parameters used for this study are shown in Tab. 5.7. The final values for the coefficients a_n are shown in Fig. 5.30 against the plaquette values at the centre of the intervals, $(u_p)_n$. The errors on the points are computed by bootstrapping over the results from each repeat. Also shown in this plot are the initial a_n value before the NR iterations, in black, and the importance sampling results used to find the initial values. Again the initial values are found by fitting a cubic polynomial to the inverse couplings as a function of the measured VEV of the plaquette values from importance sampling.

The results for the $\Delta_{u_p} = 0.00008$ do not show any evidence of the non-invertibility in $a_n(u_p)$, while $\Delta_{u_p} = 0.00004$, hints at it. However, the large errors on these point could lead to the non-invertibility disappearing if we carry out more RM iterations. This is likely due to the large width of the double Gaussian distributions, causing the region between the two peaks to be very small and flat. This would lead to difficulties in computing the coefficients a_n, at the point at which the energy distribution is flat. For the smaller N_t values, we found that the results for the larger N_s values were better able to refine the coefficients. Therefore, these initial results indicate that a larger volume should be studied to continue the extrapolation to the continuum limit.

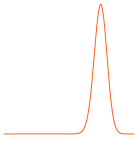

Table 5.7. A list of LLR parameters for the study of the deconfinement phase transition in $Sp(4)$ pure gauge theory on a lattice of volume $\tilde{V}/a^4 = 6 \times 72^3$, for two interval sizes, Δ_{u_p}. The interval size have been quoted to 5 decimal places for convenience. The definitions for the variables of this table are given in Tab. 3.1.

$N_t \times N_s^3$	N_{int}	n_R	Δ_{u_p}	$(u_p)_{\min}$	$(u_p)_{\max}$	$\bar{m}$	$\tilde{m}$	$\hat{m}$	n_{Th}	n_M	n_{fxa}
6×72^3	48	25	0.00008	0.6010	0.6030	9	30	0	300	700	0
6×72^3	96	25	0.00004	0.6010	0.6030	9	20	0	300	700	0

5.4 Conclusion

We have studied the finite temperature deconfinement phase transition in $Sp(4)$ pure gauge theory on lattices with temporal sizes, $N_t = 4$, 5 and 6. For $N_t = 4$, we presented an in depth analysis of the thermodynamic limit, while we only presented preliminary results for finer lattice spacing. At each lattice size, we used the LLR method to determine the coefficients a_n, in order to compute the density of states. This allowed us to directly determine various thermodynamic observables, such as the critical inverse coupling, the plaquette jump and the surface tension. We also reconstructed the canonical ensemble at a range of inverse couplings and compute the VEV of various observables.

For $N_t = 4$ we studied systems with spatial sizes $N_s = 20$, 24, 28, 40 and 48. At each spatial volume, we ensure we accurately account for the systematic errors due to finite interval size, Δ_{u_p}, by repeating our calculations at multiple interval sizes and take the limit $\Delta_{u_p} \to 0$, more details on this are given in App.B. A full list of systems used for this study are given in Tab. 5.1. For each system, we compute the VEV of the average plaquette, $\langle u_p \rangle_\beta$, the specific heat, $C_V(\beta)$, the Binder cumulant, $B_V(\beta)$, the VEV of the absolute value of the Polyakov loop, $\langle |l_p| \rangle_\beta$, and the susceptibility, $\chi_l(\beta)$, for a range of inverse couplings around the critical point, these results are presented in Fig. 5.12, Fig. 5.13, Fig. 5.14 and Fig. 5.16, respectively. Using these results we found the extremal values of the specific heat, $C_V^{(max)}$, Binder cumulant, $B_V^{(min)}$, and Polyakov loop susceptibility, $\chi_l^{(max)}$, and the corresponding inverse couplings, $\beta_{CV}(C_V)$ $\beta_{CV}(B_V)$ and $\beta_{CV}(\chi_l)$. All of these results are presented in Tab. 5.3 and Tab. 5.2. In the thermodynamic limit, these couplings are expected to be equivalent to each other, and give a definition for the critical inverse coupling.

Directly from the micro-canonical information, we were also able to compute the thermodynamic potentials presented in Eq. 3.1.28, in particular we calculate the free-energy. This gave access a new definition for the finite volume critical inverse coupling, $\beta_{CV}(f)$, as the point at which the two meta-stable branches of the free-energy cross. We then compute the plaquette jump, $\Delta\langle u_p \rangle_{\beta_{CV}}$ and the free-energy interface between the two equilibrium states, ΔF, at this inverse coupling. Physically $\beta_{CV}(f)$, is the inverse coupling that gives rise to a

plaquette distribution with two peaks of equal height. The plaquette jump is the difference between the plaquette values at the peaks of this distribution, and the ΔF can be related to the ratio of the height of the peaks of the plaquette distribution to the central minima, $\Delta F \beta_{CV}(f) = -\ln(P_{min}/P_{max})$. This final expression can be used in Eq. 2.2.32, to compute the term $\hat{I}$. These results are also presented in Tab. 5.3 and Tab. 5.2.

Using the results for finite volume we take the thermodynamic limit. From finite scaling analysis we expect that the error on the finite volume critical inverse couplings will scale inversely with the spatial volume. In Fig. 5.17, we plot the results against the cube of the inverse of the aspect ratio N_t^3/N_s^3. By fitting a linear function in N_t^3/N_s^3 to the results, we found good agreement between these and the expected scaling, indicating that this is likely a first order transition. However, we found the results for each definition differed when extrapolated to the infinite volume limit, we believe this is due to the high-order corrections to the scaling from the mixed phase states affecting the extrapolations.

The peaks of the specific heat and the Polyakov loop susceptibility are expected to scale with the volume, with corrections that scale inversely with the volume. The error on the minima of the Binder cumulant is also expected to scale inversely with the volume. Fig. 5.13, Fig. 5.14, and Fig. 5.16, we present the results for $a^4 C_V^{(max}/\tilde{V}$, $B_V^{(min}$ and $a^4 \chi_l^{(max}/\tilde{V}$ against N_t^3/N_s^3, respectively. We fit a quadratic polynomial in N_t^3/N_s^3 to all of these results. The fit in all cases were not good, with a reduced chi-square around 5, this could be due to an underestimation of errors. However, we believe that this divergence is coming from the sub-leading finite volume effects due to mixed phase states. In Fig. 5.7, we demonstrate that the double Gaussian approximation, in which the plaquette distribution is made up of the combination of two pure phase Gaussian distributions, breaks down as we are likely seeing mixed phase states. Although we have a relatively large reduced chi-square we extrapolate our results to the infinite volume limit giving $a^4 C_V^{(max)}/\tilde{V} = 878(3) \times 10^{-5}$ $a^4 \chi_l^{(max)}/\tilde{V} = 6.83(3) \times 10^{-4}$ and $B_V^{(min)} = 0.66666069(2)$. As the first two results are non-zero, again we have some indication of the first order nature of the transition. If the transition was not first order we would expect that the Binder cumulant would tend to a value of $2/3$ in the infinite volume limit, we do not observe this, again indicating the first order nature.

In the thermodynamic limit, it is expected that the peak of the specific heat will be proportional to the square of the plaquette jump, $4a^4 C_V^{(max)}/6\tilde{V} = (\Delta\langle u_p \rangle_{\beta_{CV}})^2$. In right plot of 5.13, we also show the square of the plaquette jump against N_t^3/N_s^3, again we fit a quadratic to this and take the large volume limit, the extrapolation. We find that the relation between the extrapolation of $\langle u_p \rangle_{\beta_{CV}}$ and $a^4 C_V^{(max)}/\tilde{V}$, doesn't match our expectation. However, results at finite volume are consistent. We expect again that we are seeing affects of mixed phase states. Finally, we also took the thermodynamic limit of $\hat{I}$, to get an expression for the

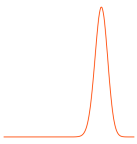

surface tension $\hat{\sigma}_{cd}$. As this is a surface term we fit the results to a quadratic in N_t^2/N_s^2, finding a good agreement, with a reduced chi-square of 1. As this term has good agreement with the expected scaling, this indicates we are seeing the effects on a interface. The extrapolated results are presented in Tab. 5.3.

After a detailed analysis of the system at $N_t = 4$, we began to study the system with a smaller lattice spacing. In App. C, using importance sampling methods, we determined $N_s = 48$ was sufficient to observe the meta-stability for $N_t = 5$. We carry out initial LLR analysis for lattices volumes 5×48, and 5×56. For both volumes we use several interval sizes. A full list of LLR parameters for $N_t = 5$ is presented in Tab. 5.4. For these systems we again compute the thermodynamic observables, $\beta_{CV}(f)$, $\Delta\langle u_p \rangle_{\beta_{CV}}$ and $\hat{I}$. By reconstructing the canonical ensemble and carrying out a parameter scan of β values between $\beta = 7.4880$ and 7.4910, we determined the extrema and corresponding inverse couplings of specific heat, Binder cumulant and Polyakov loop susceptibility. All these results are presented in Tab. 5.5 and Tab. 5.6. However, we found that location of the peaks of the observables are outside the error of the observable for each inverse coupling. Therefore, more RM iterations are likely required to better refine our values of a_n, to get self-consistent results.

For $N_t = 6$, we studied a lattice of volume 6×72^3. Due to computational limitations, we did not carry out a large number of RM iterations and have correspondingly large errors on our estimations for a_n. With these preliminary results, it is unclear whether this spatial volume is sufficient to observe the meta-stability that is characteristic of a first order transition.

In future work, we plan to add additional systems to our study, particularly focusing on taking the thermodynamic limit in $N_t = 5$. For $N_t = 6$, studies at larger spatial volumes, in particular with an aspect ratio of at least $N_s/N_t = 14$. A study of larger spatial volumes for $N_t = 4$, could also allow for a more direct understanding of the effects of the mixed-phase states, and whether the results for all of the critical inverse couplings begin to converge in this limit.

Chapter 6

Conclusion

"Yang-Mills on Lattice
First order phase transition
Thermal properties "
Research Haiku. L. Cole, S. Pandey, et al.

Early universe first order phase transitions can generate a background of long wavelength gravitational waves and produce some of the observed matter-antimatter asymmetry, through bubble nucleation. The transitions in the standard model of particle physics don't contain the desired properties, we therefore look to BSM physics. The thermodynamic properties of these transitions should allow the possible gravitational wave power-spectrums to be estimated. The aim of the work presented in this thesis was to analyse the thermodynamic properties of first order deconfinement phase transitions, for various pure non-Abelian gauge theories, particularly focusing on $SU(3)$ pure gauge theory, as a well studied testbed for the analysis methods, and then $Sp(4)$, as the infinitely heavy quark mass limit of phenomenologically interesting models of BSM physics. This work has taken steps toward the ultimate goal of determining continuum thermodynamic properties that can be used in the gravitational wave physics.

In Chap. 2, we introduced the lattice formalism, in which spacetime is discretised onto a finite set of points on a hypercubic lattice. Using Euclidean spacetime with periodic boundary conditions, the lattice system can be interpreted as a statistical mechanics system at a temperature that is controlled by the temporal extent. Important thermodynamic quantities and properties of the phase transition were discussed. The lattice observables like the plaquette jump, $\Delta\langle u_p\rangle_{\beta_{CV}}$, the interface tension, $\hat{\sigma}_{cd}$, and the critical inverse coupling, β_{CV}, were introduced, and the methods of computing them were discussed. Then technical details on the computation of VEVs using importance sampling techniques were discussed and specific problems in these methods due to the meta-stable dynamics, that lead to the rich phenomenology, were introduced.

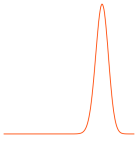

Chap. 3 gave background on the density of states methods, that aim to solve the metastability problem, by sampling a flat energy distribution. The primary focus was to introduce the LLR method, which is the main computational technique for this work. The method aims to reconstruct the density of states as a piecewise log linear function. In-depth technical details on the computation of the density of states were given. We discussed how to reconstruct the canonical ensemble from the density of states, allowing for the reconstruction of the plaquette distribution and VEVs. Directly from the microcanonical information, contained within the density of states, we defined thermodynamic potentials like the free-energy.

In order to test our implementation of the LLR algorithm, we analysed the deconfinement phase transition in $SU(3)$ pure gauge theory, for a single lattice size 4×20^3, this was presented in Chap. 4. The main aim of this work was to analyse the systematic effects of having a finite interval size, Δ_{u_p}, and verify the expectation for observables, of a relative error of order $\Delta_{u_p}^2$. Initially, we verified that the LLR coefficients $a_n^{(m)}$, behaved as expected as we updated them through the RM iterations. In Fig. 4.7, we demonstrated that the standard deviation of the coefficients have the expected scaling with the iteration number, $\sigma(a_n^{(m)}) \sim 1/\sqrt{m}$ demonstrating the convergence of the results. The convergence of the results was further demonstrated in Fig. 4.5, which further showed the approximately Gaussian nature of the final results, a_n. To ensure ergodicity of the algorithm, we utilised replica exchange, in Fig. 4.8 we showed the systems as they were exchanged between energy intervals. We notice that although all replicas are exchanged, there are very few systems that cross between phases, this is due to the difference in the microscopic degrees of freedom between phases. To compute the density of states, we needed to find coefficients, a_n, that lead to a flat energy distribution, and solve Eq. 3.1.11. This was verified using fixed a_n iterations, upon finishing the RM iterations. The measured energy distribution from the fixed a_n iterations were shown to be flat in Fig. 4.10, and the VEV $\langle\langle \Delta E \rangle\rangle_n(a_n)$, was shown to vanish in Fig. 4.9. This verified our results were consistent with our expectation of the algorithm.

As the size of this lattice was small and the phase transition for this system is weak, the metastability problems can be adequately accounted for in standard importance sampling methods. To ensure that our LLR results were accurately describing the physical system, we compared our results with importance sampling results. We compared the plaquette distribution, Fig. 4.11, the VEV of the average plaquette, Fig. 4.12, the specific heat, Fig. 4.13, Binder cumulant, Fig. 4.14, the VEV of the absolute value of the Polyakov loop, Fig. 4.15, and the Polyakov loop susceptibility, Fig. 4.16. In all cases we found good agreement with the importance sampling results, with the results generally converging towards the importance sampling result in the limit of vanishing interval size.

After ensuring that our results are consistent with the algorithmic expectation and comparing them with more established methods, we began to compute thermodynamic quantities of interest. We found the extrema of the specific heat, $C_V^{(max)}$, the Binder cumulant, $B_V^{(min)}$, and the Polyakov loop susceptibility, $\chi_l^{(max)}$, and the corresponding critical inverse coupling, $\beta_{CV}(C_V)$, $\beta_{CV}(B_V)$ and $\beta_{CV}(\chi_l)$, respectively. The limit of vanishing interval size was taken for all of these observables, as shown in Fig. 4.17, Fig. 4.18 and Fig. 4.19, and presented in Tab. 4.2. In all cases the reduced chi square for a linear fit against $\Delta_{u_p}^2$ was $\chi_\nu^2 \sim 1$, indicating that our expectation for the scaling of the error is appropriate.

By tuning the inverse coupling, and computing the plaquette distribution we were able to determine an additional definition for the critical inverse coupling, $\beta_{CV}(P)$, the inverse coupling that gives rise to a plaquette distribution with two peaks of equal height, details of the determination of this parameter is given in App. A. At this coupling, we were also able to compute the plaquette jump, $\Delta\langle u_p\rangle_{\beta_{CV}}$, which appears in Eq. 2.2.28 and can be related to the latent heat, and $-\ln(P_{min}/P_{max})$, which appears in Eq. 2.2.32 and can be related to the tension of the interface that separates regions of the system in different vacua. All of these quantities were calculated at each interval size and the limit of vanishing interval size was taken, as shown in Fig. 4.23. For the critical inverse coupling $\beta_{CV}(P)$, we found very low reduced chi square for the fit against $\Delta_{u_p}^2$. Therefore we expect we might be overestimating the errors, so we considered a possible source of correlation from the data, from the exchange of replicas. We considered results with only odd numbered intervals and found that the these results, and the extrapolation gave consistent results with comparable errors.

Finally, for $SU(3)$, we computed the thermodynamic potentials, defined in Eq. 3.1.28. From this we demonstrated the characteristic swallow tail structure, Fig. 4.24, that we expect from a first order phase transition, containing two meta-stable branches and an unstable branch. By analysing the behaviour of the free-energy, we can determine the same thermodynamic properties, $\beta_{CV}(f)$, $\Delta\langle u_p\rangle_{\beta_{CV}}$ and $-\ln(P_{min}/P_{max})$, we found from the plaquette distribution. We linearly fit the results to $\Delta_{u_p}^2$ and took the limit of vanishing interval size. These results are shown in Fig. 4.27 and Tab. 4.4. We note that the results computed using the plaquette distribution, and from the free-energy are consistent.

In all cases for our analysis of $SU(3)$ pure gauge theory on a 4×20^3 lattice the results were consistent with our expectations. The coefficients $a_n^{(m)}$ converged as we expected. They agreed well with importance sampling. The scaling of the systematic error with the interval size appeared to agree well with the expectation of a leading order contribution $\propto \Delta_{u_p}^2$. Using this we moved onto the less well studied system of pure $Sp(4)$ gauge theory. We focused on $N_t = 4$ in the thermodynamic limit, however preliminary results for systems with reduced lattice spacing, $N_t = 5$ and $N_t = 6$, were considered.

First, we analyse how the plaquette distribution is affected by the increase in volume

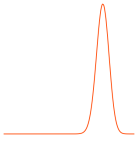

at $N_t = 4$. We find that, as expected the peaks height grows and the width decreases with increasing volume. For smaller volumes, the double Gaussian approximation, in which the plaquette distribution is approximated as the sum of two Gaussian pure phase distributions, is a good approximation for the data. However, as the volume grows, we see a clear divergence from this as the region between the peaks plateaus. This likely indicates we are seeing the effects of mixed phase states on the distribution.

We again compute observables relevant for the deconfinement transition and analysed how they changed with increasing volume. The change in the VEV of the average plaquette and the absolute value of the Polyakov loop, both appear to approach the discrete jump we expect from a first order transition in the thermodynamic limit. This jump is quantified by the specific heat and the Polyakov loop susceptibility. From the finite size scaling, the peaks of the specific heat and the Polyakov loop susceptibility are expected to scale with the volume, with leading order corrections to $C_V^{(max)} a^4/\tilde{V}$ and $\chi_l^{(max)} a^4/\tilde{V}$ scaling with $1/V$. In Fig. 5.13 and Fig. 5.16, we verified the expectation of the scaling. However, when fitting a polynomial in $(N_t/N_s)^3$, to $C_V^{(max)} a^4/\tilde{V}$ and $\chi_l^{(max)} a^4/\tilde{V}$, we found large reduced chi-squares $\chi^2_\nu \sim 5$. This could be due to an underestimation of the error, however we believe this is due to subleading effects from the mixed phase states. A similar problem was found for the minima of the Binder cumulant, shown in Fig. 5.14. However, from the Binder cumulant we were able to determine that the results are consistent with a first order transition, as the dip at the critical point did not disappear and it did not extrapolate to a value of 2/3, which is expected for high order transitions. All of these results are presented in Tab. 5.3, and demonstrate the first order nature of the transition.

Another expectation of the peak of the specific heat, is that in the thermodynamic limit, it should tend to a value related to the square of the plaquette jump, $\lim_{V\to\infty} C_V^{(max)} = \frac{6\tilde{V}}{4a^4}(\Delta\langle u_p\rangle_{\beta_c})^2$. Using the thermodynamic potentials, we again compute the plaquette jump for each volume, and fit a polynomial in $(N_t/N_s)^3$. This had a very good fit. These results are also shown in Fig. 5.13, with a direct comparison between $C_V^{(max)} \frac{4a^4}{6\tilde{V}}$ and $(\Delta\langle u_p\rangle_{\beta_c})^2$. Although they don't agree in the thermodynamic limit, they do agree for the largest spatial volume. We therefore expect that further consideration of the subleading effects when taking the limit, could lead to agreement between the results. However, without further calculations, at larger volumes, this is difficult to confirm.

Using the term $-\ln(P_{min}/P_{max})$, we compute $\hat{I}$, from Eq. 2.2.32. By fitting this quantity against $(N_t/N_s)^2$, and extrapolating the thermodynamic limit, we were able to compute the surface tension $\hat{\sigma}_{cd}$, for this lattice spacing. Both $\hat{I}$ and $\Delta\langle u_p\rangle_{\beta_c}$, are given in Tab. 5.3 for $N_t = 4$.

We computed several different definitions for the critical inverse coupling, from the observables $\beta_{CV}(C_V)$, $\beta_{CV}(B_V)$, $\beta_{CV}(\chi_l)$, and from the free-energy $\beta_{CV}(f)$. It is expected that in the thermodynamic limit these results should converge to the same value. From finite

scaling analysis, the leading order correction to the results are of order $(N_t/N_s)^3$, for first order transitions. We therefore fit a linear function in $(N_t/N_s)^3$ to the results, and extrapolate to the thermodynamic limit. These results are presented in Tab. 5.2. In each case we found quite low reduced chi-squares, especially for $\beta_{CV}(f)$, this could again indicate that we are overestimating the errors. The extrapolations for $\beta_{CV}(C_V)$ and $\beta_{CV}(B_V)$ agree well, this is expected as they are both based on the behaviour of the plaquette. The extrapolations of the other definitions are not consistent. Although, the results for $\beta_{CV}(\chi_l)$, for the largest volume are consistent with $\beta_{CV}(C_V)$ and $\beta_{CV}(B_V)$. This could again indicate that including higher order effects on the extrapolation could lead to a correspondence between these results.

Initial results for $N_t = 5$ were also presented. The peaks of the observables $C_V^{(max)}$, $B_V^{(min)}$ and $\chi_l^{(max)}$ are given in Tab. 5.6, while the corresponding inverse couplings are presented in Tab. 5.5. However, we find that the peaks are outside the error of observables of the parameter scan of β. This likely indicates that correlation between intervals is leading to the peaks of the observables shifting. Therefore, these results likely have not carried out an adequate number of RM iterations to sufficiently reduce the errors on a_n. For $N_t = 6$ we began to analyse a lattice of volume 6×72^3, however we were unable to resolve the non-invertibility in the function $a_n(u_p)$, therefore larger volumes are likely required to observe the meta-stable dynamics that are characteristic of a first order transition.

In future work, we plan to analyse systems with larger lattice volumes. For $N_t = 4$, we plan on adding at least one larger lattice size, to better observe the effects of the mixed phase configurations. Additional spatial volumes would allow us to determine whether the peak of the specific heat continues to agree with the expectation, for finite lattice volumes. We could also determine whether the critical inverse coupling $\beta_{CV}(C_V)$ and $\beta_{CV}(\chi_l)$, also continue to agree at finite volumes, and check if the results for $\beta_{CV}(f)$ continues to disagree with the other definitions. Detailed analysis of $N_t = 5$ and $N_t = 6$, with additional volumes would allow for the determination of the thermodynamic parameters for smaller lattice spacing, and allow us to start considering the continuum limit. We are particularly interested in $N_t = 6$, as this may allow us to estimate the required aspect ratio to resolve the double peak structure for $N_t > 6$. With an in-depth analysis of these lattice volumes, the continuum limit of the latent heat, critical temperature and the surface tension can begin to be determined.

Moving to larger lattice volumes would open up interesting physics, and start to realise the aims of the project. However, an open problem for this method is parallelisation. Although, we have implemented a form of domain decomposition that helps to decorrelate configurations, due to the microcanonical nature of the updates in most of the sub-lattices, it does not reduce the time for a full canonical update. Therefore the computational time scales poorly with an increase in volume. More algorithmic development is required for this

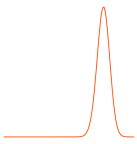

method to become fully viable for larger lattices.

Further algorithmic improvement could be made by treating intervals differently. The behaviours of the function $a_n(u_p)$ is more linear away from the transition, and therefore larger intervals could be used there. Allowing for a different number of measurements per RM iteration away from the transition, could also help to reduce the required computational resources.

All of the phenomenologically interesting models will contain fermions, and it is known that the inclusion of fermions generally leads to a weaker transition. Therefore it is important that the effects of fermionic matter on the thermodynamics are studied. Our current method is based on the heat bath update, which is for pure gauge systems, an alternative approach based on hybrid Monte Carlo, as used in Ref. [128] and Ref. [125], might be required in order to study the system with dynamical fermions. The addition of fermionic matter also adds to the complexity to the problem in the form of an additional parameter, the quark masses.

Appendix A

Finding $\beta_{CV}(P)$

"Does each appendix really require a quote?"
David Mason in a letter to Robert Mason

This appendix will discuss the method used to find the critical inverse coupling $\beta_{CV}(P)$, from the plaquette distribution by tuning the inverse coupling β until the height peaks have an equal height within some tolerance, ϵ_t, which is a parameter in the code. We begin by guessing the critical coupling by assuming $\beta_{CV}(P) \approx \beta_{CV}(C_V)$. To the plaquette distribution at $\beta = \beta' = \beta_{CV}(C_V)$ we fit a double Gaussian function, of the form

$$P_\beta(u_p) = A^{(c)} \exp\left(-\frac{(u_p - B^{(c)})^2}{2C^{(c)}}\right) + A^{(d)} \exp\left(-\frac{(u_p - B^{(d)})^2}{2C^{(d)}}\right), \tag{A.0.1}$$

where $A^{(c)}$, $B^{(c)}$, $C^{(c)}$, $A^{(d)}$, $B^{(d)}$ and $C^{(d)}$, are fitting parameters. We then find the peaks of this distribution, $P^{(c)}_{max}$ and $P^{(d)}_{max}$. If the percentage difference between these peaks, $\epsilon_\beta = (P^{(d)}_{max} - P^{(c)}_{max}))/P^{(c)}_{max}$, is below the tolerance, then we have found the correct β. If not, we try a new β.

First we change the inverse coupling by a tunable parameter $d\beta$. If $P^{(c)}_{max} > P^{(d)}_{max}$, we set $\beta' \to \beta' + d\beta$, else we set $\beta \to \beta - d\beta$. Using this new coupling, we compute the plaquette distribution and fit the double Gaussian function to it. If the percentage difference between $P^{(c)}_{max}$ and $P^{(d)}_{max}$ is below a tolerance we stop. If not we repeat this process, changing β by $d\beta$, until it overshoots $\beta_{CV}(P)$, therefore giving us one β value either side of the critical inverse coupling. We want to choose $d\beta$, such that this happens as quickly as possible. We define β_- and β_+ to be the smaller and larger out of β' and $\beta_{CV}(C_V)$, respectively, i.e. $\beta_- = \min(\beta', \beta_{CV}(C_V))$ and $\beta_+ = \max(\beta', \beta_{CV}(P))$, such that $\beta_- < \beta_{CV}(C_V) < \beta_+$. Using these two inverse couplings we can use the bisection method to refine our result.

We compute the mid point of the two inverse couplings $\beta' = \frac{\beta_+ + \beta_-}{2}$. From this we compute the plaquette distribution, fit the double Gaussian and check if the height difference of the peaks is below the tolerance. If not, if $P^{(c)}_{max} > P^{(d)}_{max}$, for $P_{\beta'}(u_p)$, we set $\beta_- = \beta'$, else we

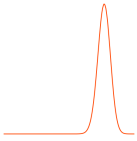

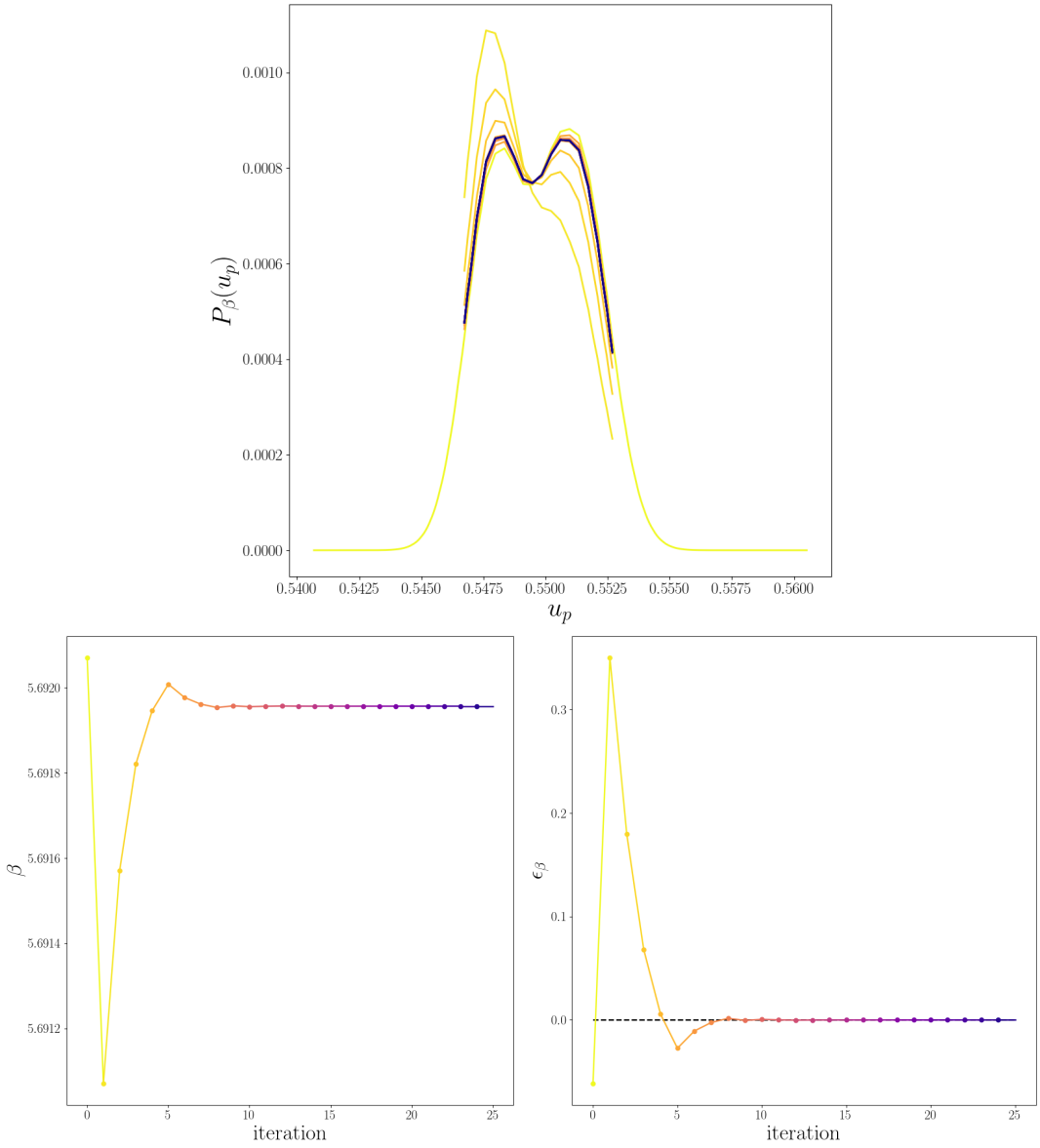

Figure A.1. The bisection method is used to find the critical point, the top the top panel shows the plaquette distribution, $P_\beta(u_p)$, reconstructed from the LLR method, for each iteration, shown in a different colour. The inverse coupling, β, for each iteration is shown in the bottom left panel, while the percentage error between the height of the peaks is shown for each iteration in the bottom right, $\epsilon_\beta = (P^{(d)}_{max} - P^{(c)}_{max}))/P^{(c)}_{max}$, where $P^{(c)}_{max}$ ($P^{(d)}_{max}$) is the peak value of the plaquette distribution in the (de)confined phase. The colours of the points in the bottom plots, correspond to the colour of the plaquette distribution in the top plot. This result is for $SU(3)$ pure gauge theory on a lattice of size 4×20^3 for one repeat with an interval size of $\Delta_{u_p} = 0.0007$.

set $\beta_+ = \beta'$. This is repeated until the difference in the height between the peaks is below a tolerance, then setting $\beta_{CV}(P) = \beta'$.

A diagrammatic representation of this is shown in Fig. A.1. The top figure shows how the plaquette distribution changes as we iteratively change our guess for $\beta_{CV}(P)$. The bottom left plot shows how beta is changed, while the bottom right plot shows how the percentage difference, ϵ_β changes. The colour of the points in the bottom two plots match the colour of the plaquette distribution in the top plot. Initially, the plaquette distribution clearly favours the confined phase, but as we change β the two peaks become approximately equal height. Once the bisection method kicks in the results converge quickly to the correct $\beta_{CV}(P)$.

An overview of the complete algorithm is given below:

1. Set the tolerance ϵ_t and choose initial guess for $\beta_{CV}(P)$, setting $\beta' = \beta_{CV}(C_V)$
2. Compute $P'_\beta(u_p)$, fit the function Eq. A.0.1 to it and find the peaks $P^{(c)}_{max}$ and $P^{(d)}_{max}$
3. If $\epsilon_{\beta'} = (P^{(d)}_{max} - P^{(c)}_{max}))/P^{(c)}_{max} < \epsilon_t$, move to Step 9;
4. If $\epsilon_{\beta'}$ and $\epsilon_{\beta_{CV}(C_V)}$ have different signs, move to Step 6;
5. If $P^{(c)}_{max} > P^{(d)}_{max}$ set $\beta' \to \beta' + d\beta$, else $\beta' \to \beta' + d\beta$, return Step 2;
6. Set $\beta_- = \min(\beta', \beta_{CV}(C_V))$ and $\beta_+ = \max(\beta', \beta_{CV}(C_V))$, such that $\beta_- < \beta_{CV}(P) < \beta_+$;
7. Set $\beta' = \frac{\beta_+ + \beta_-}{2}$, compute $P'_\beta(u_p)$, fit the function Eq. A.0.1 to it and find the peaks $P^{(c)}_{max}$ and $P^{(d)}_{max}$;
8. If $\epsilon_{\beta'} = (P^{(c)}_{max} - P^{(d)}_{max}))/P^{(c)}_{max} < \epsilon_t$, move to Step 9;
9. If $P^{(c)}_{max} > P^{(d)}_{max}$ set $\beta_- = \beta'$, else $\beta_+ = \beta'$, return Step 7;
10. Set $\beta_{CV}(P) = \beta'$ and end.

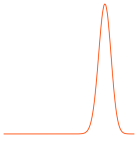

Appendix B

$\Delta_{u_p} \to 0$ limit for $Sp(4)$ with $N_t = 4$

"Of course"
Robert Mason private correspondence

In this section we analyse the systematic error of having a finite Δ_{u_p} size, and take the limit of $\Delta_{u_p} \to 0$, for many observables computed for $Sp(4)$ pure gauge theory. We consider the results for all lattice sizes, in which we have more than one interval size at $N_t = 4 : 4 \times 20^3$, 4×24^3, 4×28^3, and 4×40^3. We also discuss our results for 4×48^3. For the two smallest lattice sizes, we demonstrate systematic errors for the results with the smallest interval size, due to the chosen energy range E_{min} and E_{max}.

B.1 4×20^3

We begin our study of the systematic effects of a finite interval size for $Sp(4)$ pure gauge theory with a lattice of size 4×20^3. We choose three interval sizes, $\Delta_{u_p} = 0.00064$, 0.00048 and 0.00025. The two larger interval sizes have the same plaquette ranges, with $(u_p)_{min} = 0.565$ and $(u_p)_{max} = 0.580$, but differ due to a different number of intervals $N_{int} = 48$ and 64. The smallest interval size has a smaller plaquette range, with $(u_p)_{min} = 0.568$ and $(u_p)_{max} = 0.576$, with $N_{int} = 64$. The final values of the coefficients a_n are shown against the plaquette value at the centre of the interval in Fig. B.1. We have focused on the critical region as this is where we expect the largest difference across interval sizes. We see that they are all in good agreement, with the larger interval sizes appearing to approximately interpolate between the results for smaller intervals sizes.

To verify that for all systems we can accurately reconstruct the canonical ensemble, we compute the plaquette distribution, $P_\beta(u_p)$, at the critical inverse couplings, $\beta_{CV}(f)$, $\beta_{CV}(C_V)$, $\beta_{CV}(\chi_l)$ and $\beta_{CV}(B_V)$, the results are shown in Fig. B.2 for each interval size. For the systems with the larger interval sizes, $\Delta_{u_p} = 0.00064$ and 0.00048, which have the larger plaquette range, we can see that the plaquette distribution appears to vanish on both sides

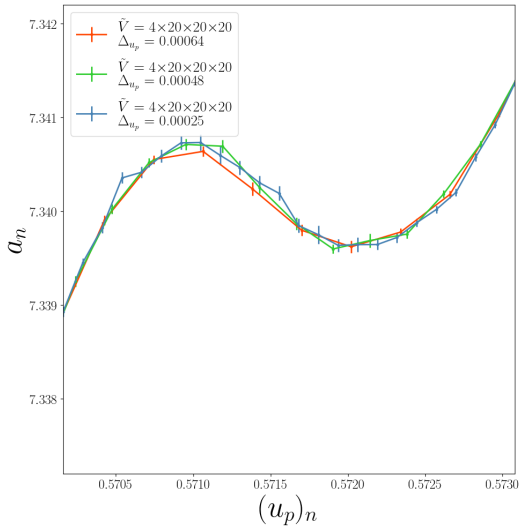

Figure B.1. The coefficients a_n, against plaquette value at the centre of the interval, $(u_p)_n$, focused on the critical region, for $Sp(4)$ on a lattice of size 4×20^3, for several interval sizes, Δ_{u_p}, shown in different colours.

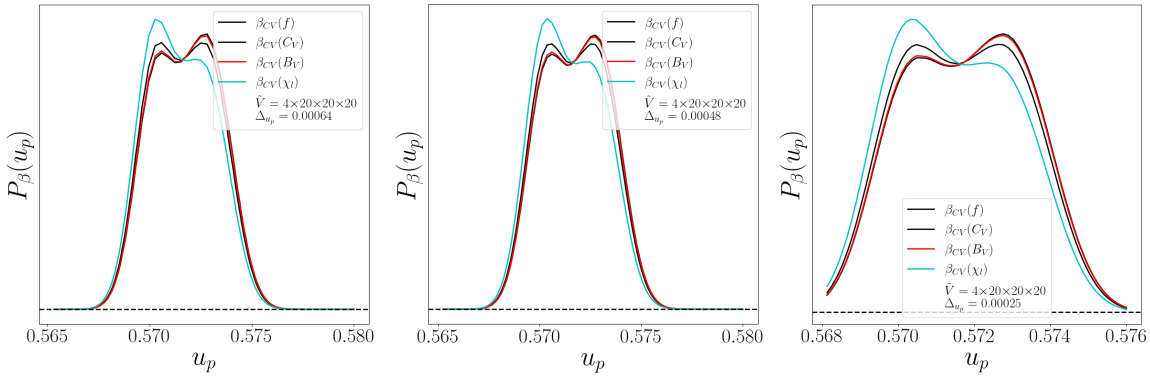

Figure B.2. The plaquette distribution for the critical inverse couplings: $\beta_{CV}(f)$, $\beta_{CV}(C_V)$, $\beta_{CV}(B_V)$ and $\beta_{CV}(\chi_l)$, for $Sp(4)$ on a lattice of size 4×20^3, for several interval widths, (left) $\Delta_{u_p} = 0.00064$, (centre) $\Delta_{u_p} = 0.00048$ and (right) $\Delta_{u_p} = 0.00025$. The dashed line is at $P_\beta(u_p) = 0$.

of the distribution, for all inverse couplings. Therefore, the effect of the cutoff of the microstates will be minimal and we can accurately reconstruct observables with these systems. However, for $\Delta_{u_p} = 0.00025$, we see that the plaquette distribution still visibly has a finite value at the cutoff. In this case, reconstructed observables will be affected by the cutoff, and therefore it will lead to inaccurate results. We will not include these results in extrapolations to the limit of vanishing interval size.

To find the inverse couplings at the peak of the specific heat, $\beta_{CV}(C_V)$, and the minimum

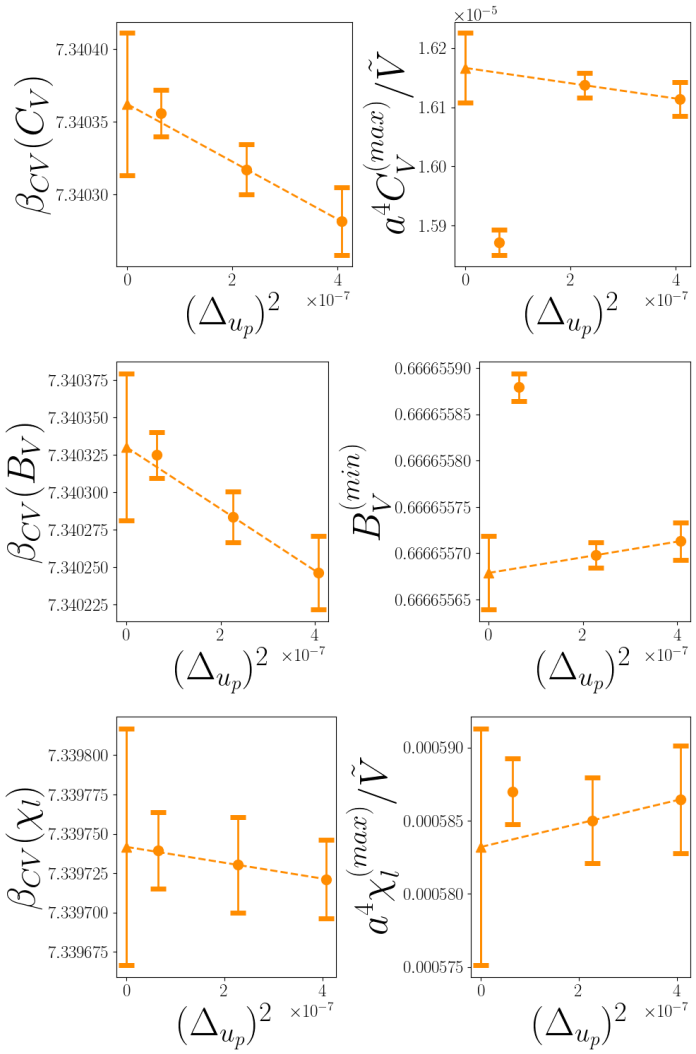

Figure B.3. The critical inverse couplings and the corresponding observables: $\beta_{CV}(C_V)$, $a^4 C_V^{(max)}/\tilde{V}$, $\beta_{CV}(B_V)$, $B_V^{(min)}$, $\beta_{CV}(\chi_l)$, $a^4 \chi_l^{(max)}/\tilde{V}$, against the square of the interval size, $(\Delta_{u_p})^2$, for $Sp(4)$ gauge theory on a lattice of size 4×20^3. The error on each point with finite interval size is the error on the mean found by bootstrapping over the repeats. We carry out a linear extrapolation, orange dashed line, on each observable in $(\Delta_{u_p})^2$, using the points $\Delta_{u_p} = 0.00064$ and 0.00048, and take the limit of vanishing interval size, orange triangle.

Binder cumulant, $\beta_{CV}(B_V)$, for each interval size we carry out a scan of 1000 inverse couplings between $\beta = 7.337$ and 7.343, and take the value that gives rise to the extremal value of the observables, $C_V^{(max)}$ and $B_V^{(min)}$. We verify that our results, and errors are not affected by our choice of β values by comparing results with a different number of inverse couplings in the scan. We find that 100 values are sufficient to get accurate results, for these observables we use 1000 values to be conservative. We also carry out a fine scan of the Polyakov loop

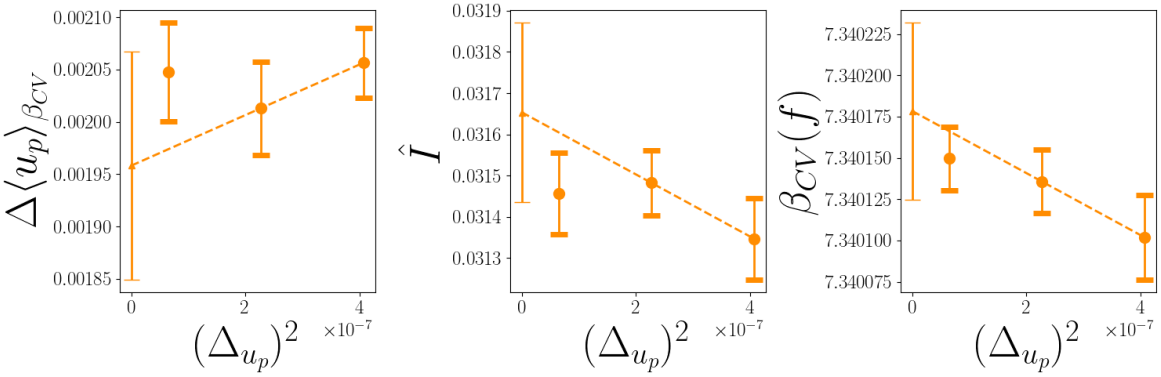

Figure B.4. The observables and their critical inverse coupling: $\Delta\langle u_p\rangle_{\beta_{CV}}$, $\hat{I}$, and $\beta_{CV}(f)$, against the square of the interval size, $(\Delta_{u_p})^2$, for $Sp(4)$ gauge theory on a lattice of size 4×20^3. The error on each point with finite interval size is the error on the mean found by bootstrapping over the repeats. We carry out a linear extrapolation, orange dashed line, on each observable in $(\Delta_{u_p})^2$, using the points $\Delta_{u_p} = 0.00064, 0.00048$, and take the limit of vanishing interval size, orange triangle.

susceptibility, $\chi_l(\beta)$, and find the value at the peak, $\chi_l^{(max)}$, and the corresponding inverse coupling, $\beta_{CV}(\chi_l)$. However for this observable we only measure 100 inverse couplings between $\beta = 7.337$ and 7.343, as the computation of this observable is more time consuming. The results for these critical inverse couplings and observables are given in Tab. 5.2 and Tab. 5.3, and presented in Fig. B.3 against the square of the interval size, $(\Delta_{u_p})^2$. The error on each point with finite interval size is the error on the mean found by bootstrapping over the repeats. We expect a systematic error on the observables proportional to the square of the interval size, $\Delta_{u_p}^2$. We carry out a linear extrapolation, dashed line, on the results for $\Delta_{u_p} = 0.00064$ and 0.00048, and take the limit of vanishing interval size, triangle. Based on the work presented in Chap. 4, we expect that this extrapolation is valid for sufficiently small interval sizes.

For the extrapolation of the specific heat we found $\beta_{CV}(C_V) = 7.340362(49)$ and $a^4 C_V^{(max)}/\tilde{V} = 1.6166(59) \times 10^{-5}$. For the Binder cumulant we found, $\beta_{CV}(B_V) = 7.340330(49)$ and $B_V^{(min)} = 0.66665568(4)$. For the Polyakov loop susceptibility we found, $\beta_{CV}(\chi_l) = 7.339742(75)$ and $a^4\chi_l^{(max)}/\tilde{V} = 5.832(81) \times 10^{-4}$. For all of these quantities our best results, $\Delta_{u_p} = 0.00048$, are consistent with the extrapolation.

We also compute the critical inverse coupling, $\beta_{CV}(f)$, the plaquette jump, $\Delta\langle u_p\rangle_{\beta_{CV}}$, and the interface term, $\hat{I}$, from Eq.2.2.32, for each interval size. These results are given in Tab. 5.2 and Tab. 5.3, and presented in Fig. B.4, against the interval size squared, $\Delta_{u_p}^2$. The error on each point with finite interval size is the error on the mean found by bootstrapping over the repeats. We carry out a linear extrapolation in $\Delta_{u_p}^2$ to the limit of vanishing interval size using results for $\Delta_{u_p} = 0.00064$ and 0.00048, as shown by the dashed line and triangle. For

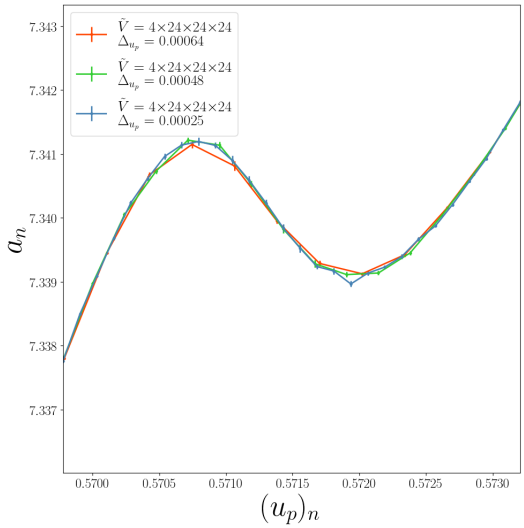

Figure B.5. The coefficients a_n, against plaquette value at the centre of the interval, $(u_p)_n$, focused on the critical region, for $Sp(4)$ on a lattice of size 4×24^3, for several interval sizes, Δ_{u_p}, shown in different colours.

the critical inverse coupling we get an extrapolation of $\beta_{CV}(f) = 7.340178(54)$. The plaquette jump has an extrapolation of $\Delta\langle u_p\rangle_{\beta_{CV}} = 0.001958(109)$. The quantity $\hat{I}$ has an extrapolated value of $\hat{I} = 0.03165(22)$. For all of these quantities our best results, $\Delta_{u_p} = 0.00048$, are consistent with the extrapolation.

B.2 4×24^3

For $Sp(4)$ gauge theory on a lattice of size 4×24^3, we choose three interval sizes, $\Delta_{u_p} = 0.00064$, 0.00048 and 0.00025. The two larger interval sizes have the same plaquette range, with $(u_p)_{min} = 0.565$ and $(u_p)_{max} = 0.580$, but differ due to a different number of intervals $N_{int} = 48$ and 64. The smallest interval size has a smaller plaquette range, with $(u_p)_{min} = 0.568$ and $(u_p)_{max} = 0.576$, with $N_{int} = 64$. The final values of the coefficients a_n are shown against the plaquette value at the centre of the interval in Fig. B.5. We have focused on the critical region as this is where we expect the largest difference between interval sizes to be observed. We see that they are all in good agreement, with the larger interval sizes appearing to approximately interpolate between the results for smaller intervals sizes.

To verify that for all systems we can accurately reconstruct the canonical ensemble, we compute the plaquette distribution, $P_\beta(u_p)$, at the critical inverse couplings, $\beta_{CV}(f)$, $\beta_{CV}(C_V)$, $\beta_{CV}(\chi_l)$ and $\beta_{CV}(B_V)$, the results are shown in Fig. B.6 for each interval size. For the systems with the larger interval sizes, $\Delta_{u_p} = 0.00064$ and 0.00048, which have the larger plaquette range, we can see that the plaquette distribution appears to vanish on both sides

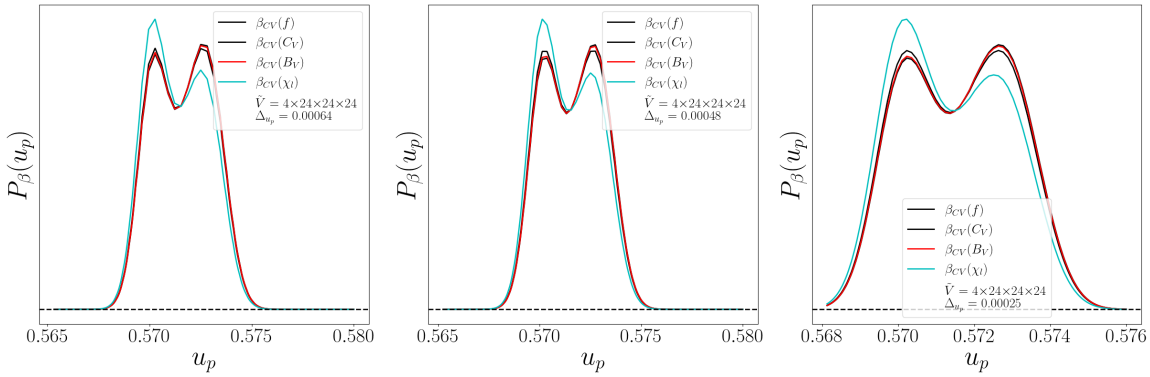

Figure B.6. The plaquette distribution for the critical inverse couplings: $\beta_{CV}(f)$, $\beta_{CV}(C_V)$, $\beta_{CV}(B_V)$ and $\beta_{CV}(\chi_l)$, for $Sp(4)$ on a lattice of size 4×24^3, for several interval widths, (left) $\Delta_{u_p} = 0.00064$, (centre) $\Delta_{u_p} = 0.00048$ and (right) $\Delta_{u_p} = 0.00025$. The dashed line is at $P_\beta(u_p) = 0$.

of the distribution, for all inverse couplings. Therefore, the effect of the cutoff of the microstates will be minimal and we can accurately reconstruct observables with these systems. However, for $\Delta_{u_p} = 0.00025$, we see that the plaquette distribution still visibly has a finite value at the cutoff. Although this value is smaller than the value at the previous volume, 4×20^3, the reconstructed observables will still be affected by the cutoff, and therefore it will lead to inaccurate results. We will therefore not include these results in extrapolations to the limit of vanishing interval size.

To find the inverse couplings at the peak of the specific heat, $\beta_{CV}(C_V)$, and the minimum Binder cumulant, $\beta_{CV}(B_V)$, for each interval size we carry out a scan of 1000 inverse couplings between $\beta = 7.337$ and 7.343, and take the value that gives rise to the extremal value of the observables, $C_V^{(max)}$ and $B_V^{(min)}$. We verify that our results, and errors are not affected by our choice of β values by comparing results with a different number of inverse couplings in the scan. We find that 100 values are sufficient to get accurate results, for these observables we use 1000 values to be conservative. We also carry out a fine scan of the Polyakov loop susceptibility, $\chi_l(\beta)$, and find the value at the peak, $\chi_l^{(max)}$, and the corresponding inverse coupling, $\beta_{CV}(\chi_l)$. However for this observable we only measure 100 inverse couplings between $\beta = 7.337$ and 7.343, as the computation of this observable is more time consuming. The results for these critical inverse couplings and observables are given in Tab. 5.2 and Tab. 5.3, and presented in Fig. B.7 against the square of the interval size, $(\Delta_{u_p})^2$. The error on each point with finite interval size is the error on the mean found by bootstrapping over the repeats. We expect a systematic error on the observables proportional to the square of the interval size, $\Delta_{u_p}^2$. We carry out a linear extrapolation, dashed line, on the results for $\Delta_{u_p} = 0.00064$ and 0.00048, and take the limit of vanishing interval size, triangle. Based on the work presented in Chap. 4, we expect that this extrapolation is valid for sufficiently small

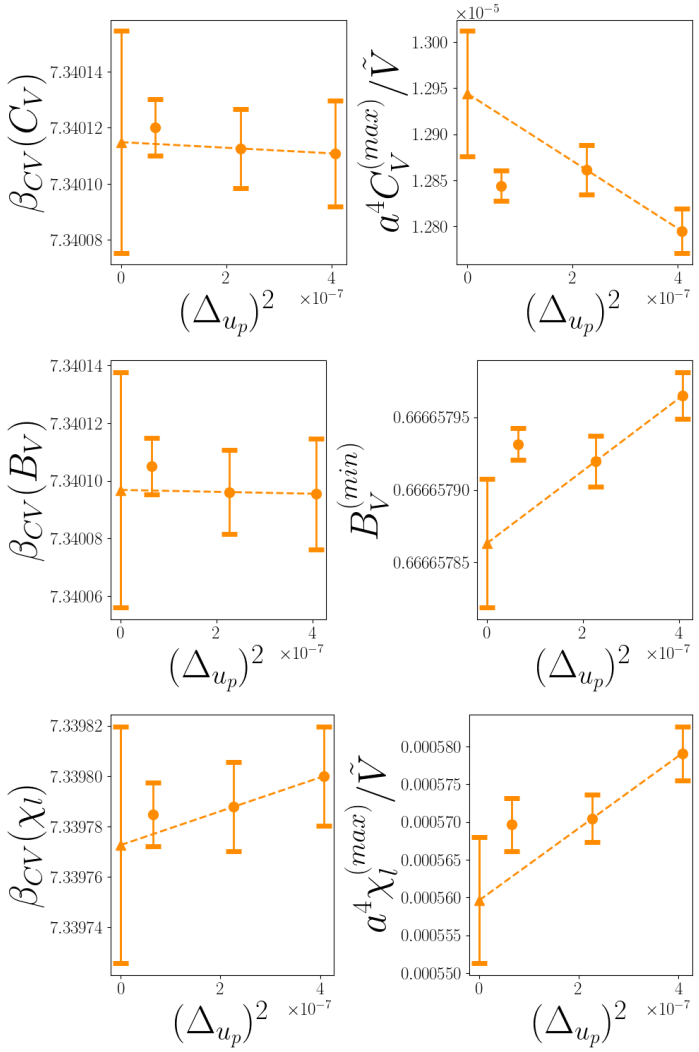

Figure B.7. The critical inverse couplings and the corresponding observables: $\beta_{CV}(C_V)$, $a^4 C_V^{(max)}/\tilde{V}$, $\beta_{CV}(B_V)$, $B_V^{(min)}$, $\beta_{CV}(\chi_l)$, $a^4 \chi_l^{(max)}/\tilde{V}$, for $Sp(4)$ gauge theory on a lattice of size 4×24^3, against the square of the interval size, $(\Delta_{u_p})^2$.The error on each point with finite interval size is the error on the mean found by bootstrapping over the repeats. We carry out a linear extrapolation, orange dashed line, on each observable in $(\Delta_{u_p})^2$, using the points $\Delta_{u_p} = 0.00064$ and 0.00048, and take the limit of vanishing interval size, orange triangle.

interval sizes.

The extrapolation of the inverse coupling at the peak of the specific heat was found to be $\beta_{CV}(C_V)) = 7.340115(40)$. The value of the specific heat at the peak was found to be $a^4 C_V^{(max)}/\tilde{V} = 1.2944(68) \times 10^{-5}$. For the Binder cumulant we found, $\beta_{CV}(B_V) = 7.340097(41)$ and $B_V^{(min)} = 0.66665786(4)$. For the Polyakov loop susceptibility we found, $\beta_{CV}(\chi_l) = 7.339773(47)$, and $a^4 \chi_l^{(max)}/\tilde{V} = 5.596(83) \times 10^{-4}$.

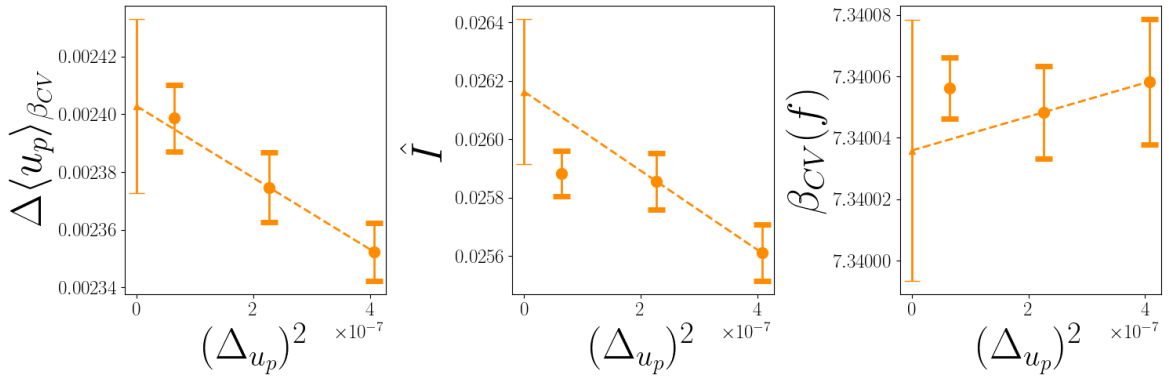

Figure B.8. The observables and their critical inverse couplings: $\Delta\langle u_p\rangle_{\beta_{CV}}$, $\hat{I}$, and $\beta_{CV}(f)$, for $Sp(4)$ gauge theory on a lattice of size 4×24^3, against the square of the interval size, $(\Delta_{u_p})^2$. The error on each point with finite interval size is the error on the mean found by bootstrapping over the repeats. We carry out a linear extrapolation, orange dashed line, on each observable in $(\Delta_{u_p})^2$, using the points $\Delta_{u_p} = 0.00064$ and 0.00048, and take the limit of vanishing interval size, orange triangle.

We also compute the critical inverse coupling, $\beta_{CV}(f)$, the plaquette jump, $\Delta\langle u_p\rangle_{\beta_{CV}}$, and the interface term, $\hat{I}$, for each interval size. These results are given in Tab. 5.2 and Tab. 5.3, and presented in Fig. B.8, against the interval size square, $\Delta^2_{u_p}$. The error on each point with finite interval size is the error on the mean found by bootstrapping over the repeats. We carry out a linear extrapolation in $\Delta^2_{u_p}$ of the results for $\Delta_{u_p} = 0.00064$, 0.00048, as shown by the dashed line. For all observables we extrapolate to the limit of $\Delta_{u_p} \to 0$, as shown by the triangle. The critical inverse coupling gives an extrapolation of $\beta_{CV}(f) = 7.340036(43)$. The plaquette jump has an extrapolation of $\Delta\langle u_p\rangle_{\beta_{CV}} = 0.002403(30)$. The quantity $\hat{I}$ has an extrapolated value of $\hat{I} = 0.02616(25)$.

B.3 4×28^3

For $Sp(4)$ gauge theory on a lattice of size 4×28^3, we choose two interval sizes, Δ_{u_p} =0.00048 and 0.00025. For Δ_{u_p} =0.00048, we have a plaquette ranges, with $(u_p)_{min} = 0.565$ and $(u_p)_{max} = 0.580$, with N_{int} =64. For Δ_{u_p} =0.00048, we have a plaquette ranges, with $(u_p)_{min} = 0.568$ and $(u_p)_{max} = 0.576$, with N_{int} =64. The final values of the coefficients a_n are shown against the plaquette value at the centre of the interval in Fig. B.9. We have focused on the critical region as this is where we expect the largest difference between interval sizes. We see that they are both in good agreement, with the larger interval sizes appearing to approximately interpolate between the results for smaller intervals size.

To verify that for all systems we can accurately reconstruct the canonical ensemble, we compute the plaquette distribution, $P_\beta(u_p)$, at the critical inverse couplings, $\beta_{CV}(f)$, $\beta_{CV}(C_V)$, $\beta_{CV}(\chi_l)$ and $\beta_{CV}(B_V)$, the results are shown in Fig. B.10, for each interval size. For

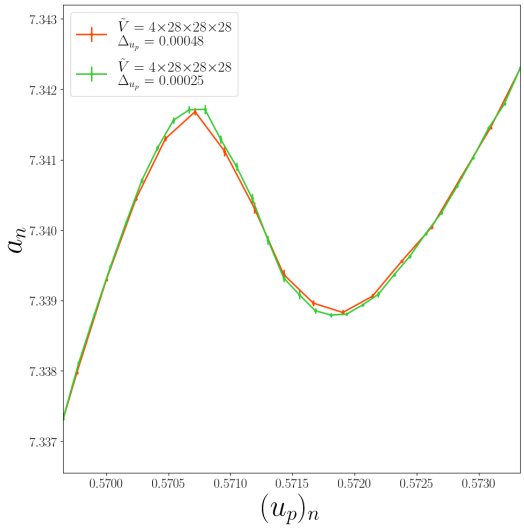

Figure B.9. The coefficients a_n, against plaquette value at the centre of the interval, $(u_p)_n$, focused on the critical region, for $Sp(4)$ on a lattice of size 4×28^3, for two interval sizes, Δ_{u_p}, shown in different colours.

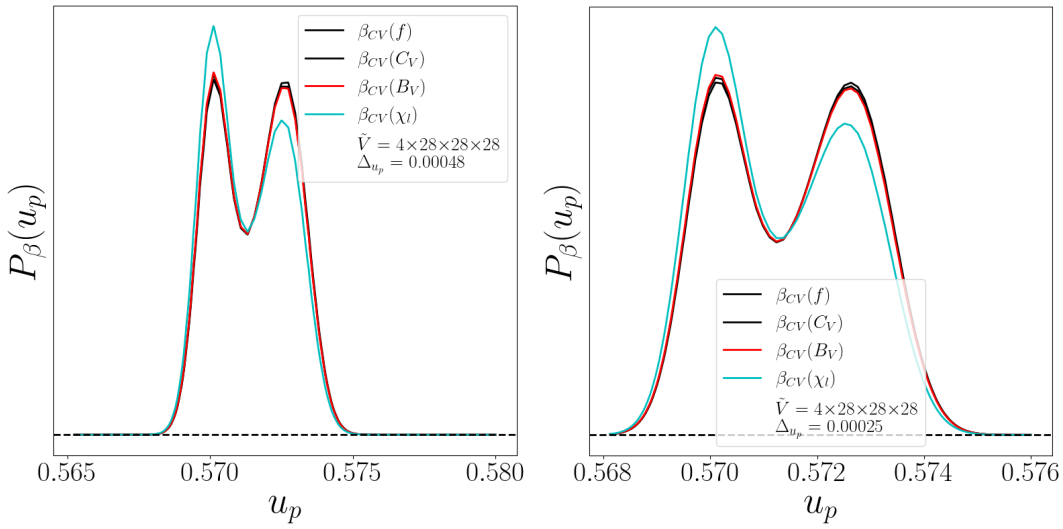

Figure B.10. The plaquette distribution for the critical inverse couplings: $\beta_{CV}(f)$, $\beta_{CV}(C_V)$, $\beta_{CV}(B_V)$ and $\beta_{CV}(\chi_l)$, for $Sp(4)$ on a lattice of size 4×28^3, for several interval widths, (left) $\Delta_{u_p} = 0.00048$ and (right) $\Delta_{u_p} = 0.00025$. The dashed line is at $P_\beta(u_p) = 0$.

both interval sizes we can see that the plaquette distribution appears to vanish on both sides of the distribution, for all inverse couplings. Therefore, the effect of the cutoff of the micro-states will be minimal and we can accurately reconstruct observables with these systems.

To find the inverse couplings at the peak of the specific heat, $\beta_{CV}(C_V)$, and the minimum

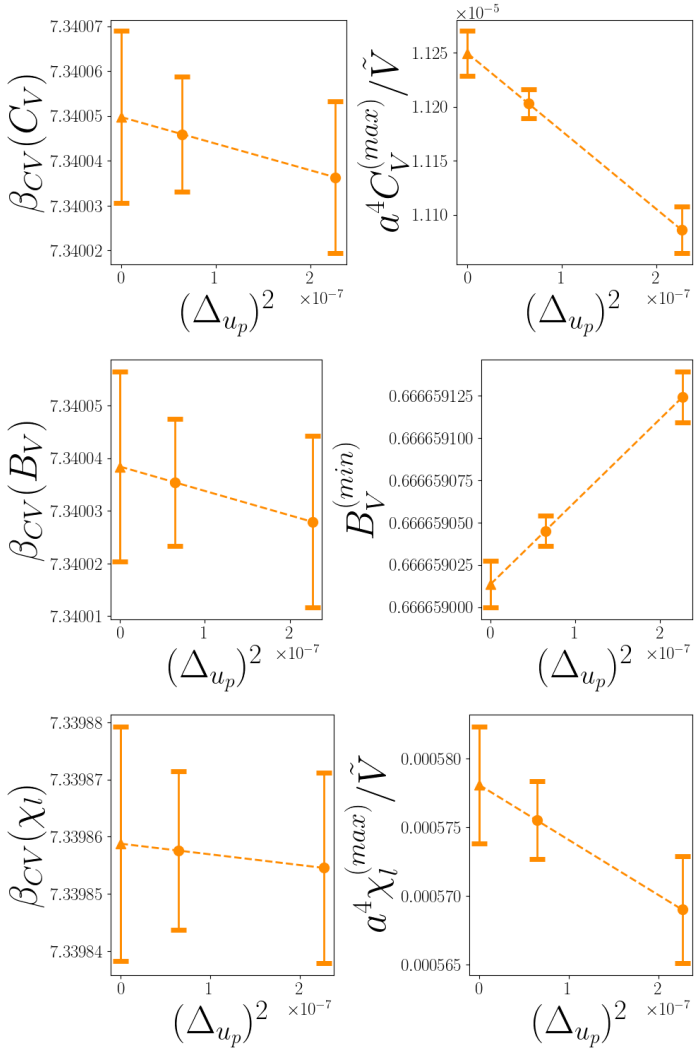

Figure B.11. The critical inverse couplings and the corresponding observables: $\beta_{CV}(C_V)$, $a^4 C_V^{(max)}/\tilde{V}$, $\beta_{CV}(B_V)$, $B_V^{(min)}$, $\beta_{CV}(\chi_l)$, $a^4 \chi_l^{(max)}/\tilde{V}$, for $Sp(4)$ gauge theory on a lattice of size 4×28^3, against the square of the interval size, $(\Delta_{u_p})^2$. The error on each point with finite interval size is the error on the mean found by bootstrapping over the repeats. We carry out a linear extrapolation, orange dashed line, on each observable in $(\Delta_{u_p})^2$, using the points $\Delta_{u_p} = 0.00048$ and 0.00025, and take the limit of vanishing interval size, orange triangle.

Binder cumulant, $\beta_{CV}(B_V)$, for each interval size we carry out a scan of 1000 inverse couplings between $\beta = 7.337$ and 7.343, and take the value that gives rise to the extremal value of the observables, $C_V^{(max)}$ and $B_V^{(min)}$. We verify that our results, and errors are not affected by our choice of β values by comparing results with a different number of inverse couplings in the scan. We find that 100 values are sufficient to get accurate results, for these observables we use 1000 values to be conservative. We also carry out a fine scan of the Polyakov loop

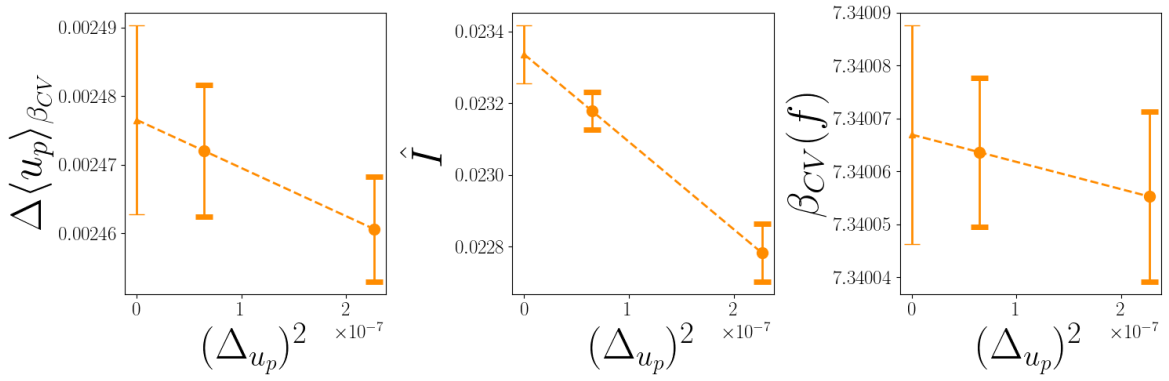

Figure B.12. The observables and their critical inverse couplings: $\Delta\langle u_p\rangle_{\beta_{CV}}$, $\hat{I}$, and $\beta_{CV}(f)$, for $Sp(4)$ gauge theory on a lattice of size 4×28^3, against the square of the interval size, $(\Delta_{u_p})^2$.The error on each point with finite interval size is the error on the mean found by bootstrapping over the repeats. We carry out a linear extrapolation, orange dashed line, on each observable in $(\Delta_{u_p})^2$, using the points $\Delta_{u_p} = 0.00048$ and 0.00025, and take the limit of vanishing interval size, orange triangle.

susceptibility, $\chi_l(\beta)$, and find the value at the peak, $\chi_l^{(max)}$, and the corresponding inverse coupling, $\beta_{CV}(\chi_l)$. However for this observable we only measure 100 inverse couplings between $\beta = 7.337$ and 7.343, as the computation of this observable is more time consuming. The results for these critical inverse couplings and observables are given in Tab. 5.2 and Tab. 5.3, and presented in Fig. B.11 against the square of the interval size, $(\Delta_{u_p})^2$. The error on each point with finite interval size is the error on the mean found by bootstrapping over the repeats. We expect a systematic error on the observables proportional to the square of the interval size, $\Delta_{u_p}^2$. We carry out a linear extrapolation on the results, dashed lines and take the limit of vanishing interval size, triangle. Based on the work presented in Chap. 4, we expect that this extrapolation is valid for sufficiently small interval sizes.

For the extrapolation of the specific heat we found $\beta_{CV}(C_V) = 7.340050(19)$ and $a^4 C_V^{(max)}/\tilde{V} = 1.1249(21) \times 10^{-5}$. For the Binder cumulant we found, $\beta_{CV}(B_V) = 7.340038(18)$ and $B_V^{(min)} = 0.66665901(1)$. For the Polyakov loop susceptibility we found, $\beta_{CV}(\chi_l) = 7.339859(21)$ and $a^4 \chi_l^{(max)}/\tilde{V} = 5.781(43) \times 10^{-4}$. Based on the work presented in Chap. 4, we expect that this extrapolation is valid for sufficiently small interval sizes.

We also compute the critical inverse coupling, $\beta_{CV}(f)$, the plaquette jump, $\Delta\langle u_p\rangle_{\beta_{CV}}$, and the interface term, $\hat{I}$, for each interval size. These results are given in Tab. 5.2 and Tab. 5.3, and presented in Fig. B.12, against the interval size square, $\Delta_{u_p}^2$. The error on each point with finite interval size is the error on the mean found by bootstrapping over the repeats. We carry out a linear extrapolation in $\Delta_{u_p}^2$ to the results, as shown by the dashed line. For all observables we take the limit of $\Delta_{u_p} \to 0$, as shown by the triangle. The critical inverse coupling gives an extrapolation of $\beta_{CV}(f) = 7.340067(21)$, the plaquette jump $\Delta\langle u_p\rangle_{\beta_{CV}} =$

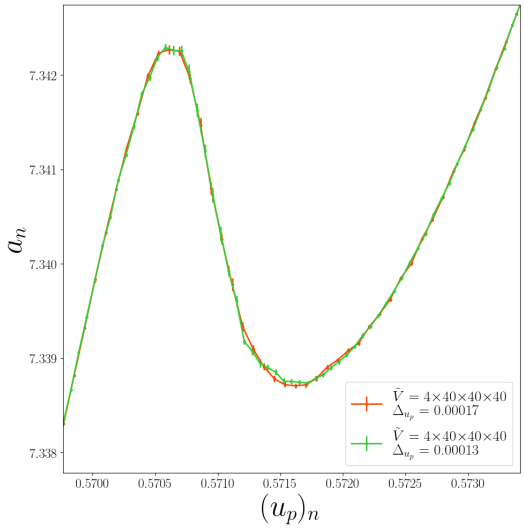

Figure B.13. The coefficients a_n, against plaquette value at the centre of the interval, $(u_p)_n$, focused on the critical region, for $Sp(4)$ on a lattice of size 4×40^3, for two interval sizes, Δ_{u_p}, shown in different colours.

0.002477(14), and $\hat{I} = 0.02334(8)$.

B.4 4×40^3

For $Sp(4)$ gauge theory on a lattice of size 4×40^3, we choose two interval sizes, $\Delta_{u_p} = 0.00017$ and 0.00013. For both interval sizes we have a plaquette range $(u_p)_{min} = 0.568$ and $(u_p)_{max} = 0.578$, with $N_{int} = 96$ and 128. The final values of the coefficients a_n are shown against the plaquette value at the centre of the interval in Fig. B.13. We have focused on the critical region as this is where we expect the largest difference. We see they have very good agreement.

To verify if our approach of reducing the plaquette to reduce the interval size will cut off relevant micro-states, we reconstruct the plaquette distribution at the critical inverse couplings, $\beta_{CV}(f)$, $\beta_{CV}(C_V)$, $\beta_{CV}(\chi_l)$ and $\beta_{CV}(B_V)$, for each interval size, these are shown in Fig. B.14. For both interval sizes we can see that the plaquette distribution appears to vanish on both sides of the distribution, for all inverse couplings. Therefore, the effect of the cutoff of the micro-states will be minimal and we can accurately reconstruct observables with these systems.

To find the inverse couplings at the peak of the specific heat, $\beta_{CV}(C_V)$, and the minimum Binder cumulant, $\beta_{CV}(B_V)$, for each interval size we carry out a scan of 1000 inverse couplings between $\beta = 7.339$ and 7.341, and take the value that gives rise to the extremal value of the observables, $C_V^{(max)}$ and $B_V^{(min)}$. We verify that our results, and errors are not affected by

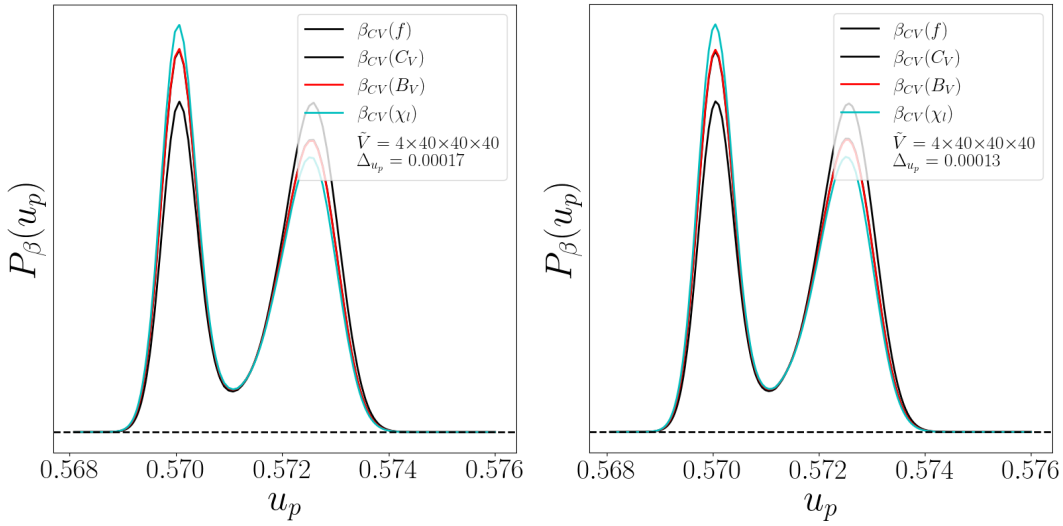

Figure B.14. The plaquette distribution for the critical inverse couplings: $\beta_{CV}(f)$, $\beta_{CV}(C_V)$, $\beta_{CV}(B_V)$ and $\beta_{CV}(\chi_l)$, for $Sp(4)$ on a lattice of size 4×40^3, for several interval widths, (left) $\Delta_{u_p} = 0.00017$ and (right) $\Delta_{u_p} = 0.00013$. The dashed line is at $P_\beta(u_p) = 0$.

our choice of β values by comparing results with a different number of inverse couplings in the scan. We find that 100 values are sufficient to get accurate results, for these observables we use 1000 values to be conservative. We also carry out a fine scan of the Polyakov loop susceptibility, $\chi_l(\beta)$, and find the value at the peak, $\chi_l^{(max)}$, and the corresponding inverse coupling, $\beta_{CV}(\chi_l)$. However for this observable we only measure 100 inverse couplings between $\beta = 7.339$ and 7.341, as the computation of this observable is more time consuming. The results for these critical inverse couplings and observables are given in Tab. 5.2 and Tab. 5.3, and presented in Fig. B.15 against the square of the interval size, $(\Delta_{u_p})^2$. The error on each point with finite interval size is the error on the mean found by bootstrapping over the repeats. We expect a systematic error on the observables proportional to the square of the interval size, $\Delta_{u_p}^2$. We carry out a linear extrapolation on the results, dashed lines and take the limit of vanishing interval size, triangle. Based on the work presented in Chap. 4, we expect that this extrapolation is valid for sufficiently small interval sizes.

For the extrapolation of the specific heat we found $\beta_{CV}(C_V) = 7.340012(24)$ and $a^4 C_V^{(max)}/\tilde{V} = 0.9433(54) \times 10^{-5}$. For the Binder cumulant we found, $\beta_{CV}(B_V) = 7.340009(24)$ and $B_V^{(min)} = 0.66666025(3)$. For the Polyakov loop susceptibility we found, $\beta_{CV}(\chi_l) = 7.339974(25)$ and $a^4 \chi_l^{(max)}/\tilde{V} = 6.311(63) \times 10^{-4}$.

We also compute the critical inverse coupling, $\beta_{CV}(f)$, the plaquette jump, $\Delta\langle u_p \rangle_{\beta_{CV}}$, and the interface term, $\hat{I}$, for each interval size. These results are given in Tab. 5.2 and Tab. 5.3, and presented in Fig. B.16, against the interval size square, $\Delta_{u_p}^2$. The error on each point with finite interval size is the error on the mean found by bootstrapping over the

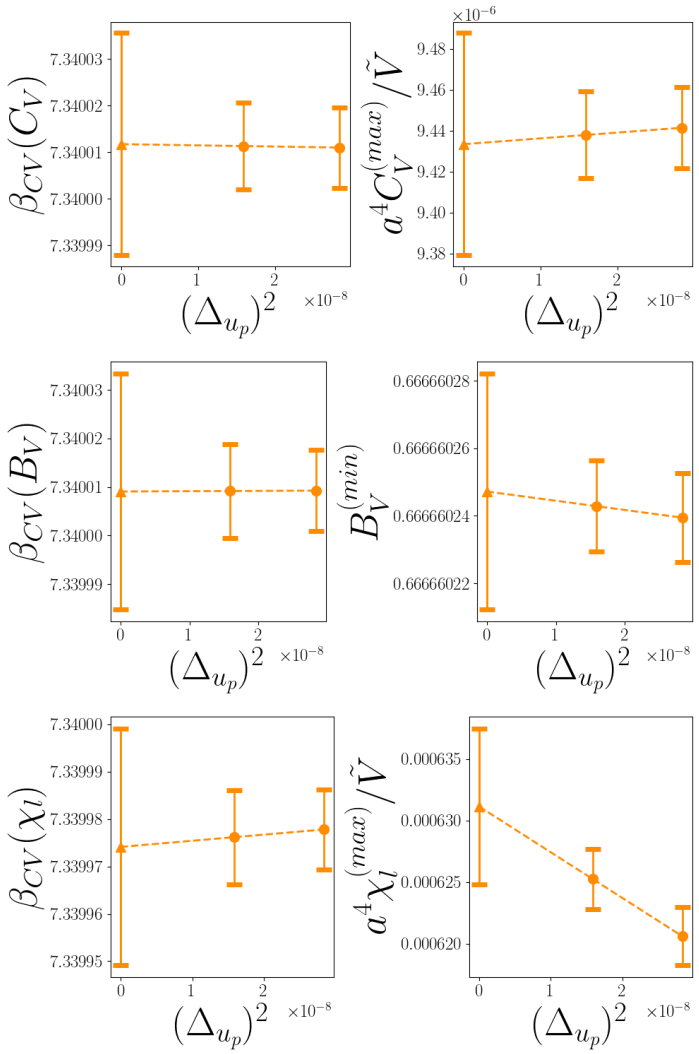

Figure B.15. The critical inverse couplings and the corresponding observables: $\beta_{CV}(C_V)$, $a^4 C_V^{(max)}/\tilde{V}$, $\beta_{CV}(B_V)$, $B_V^{(min)}$, $\beta_{CV}(\chi_l)$, $a^4 \chi_l^{(max)}/\tilde{V}$, for $Sp(4)$ gauge theory on a lattice of size 4×40^3, against the square of the interval size, $(\Delta_{u_p})^2$. The error on each point with finite interval size is the error on the mean found by bootstrapping over the repeats. We carry out a linear extrapolation, orange dashed line, on each observable in $(\Delta_{u_p})^2$, using the points $\Delta_{u_p} = 0.00017$ and 0.00013, and take the limit of vanishing interval size, orange triangle.

repeats. We carry out a linear extrapolation in $\Delta_{u_p}^2$ of the results, as shown by the dashed line. For all observables we take the limit of $\Delta_{u_p} \to 0$, as shown by the triangle. The critical inverse coupling gives an extrapolation of $\beta_{CV}(f) = 7.340074(24)$. The plaquette jump has an extrapolation of $\Delta\langle u_p \rangle_{\beta_{CV}} = 0.002481(18)$. The quantity $\hat{I}$, has an extrapolated value of $\hat{I} = 0.01965(20)$.

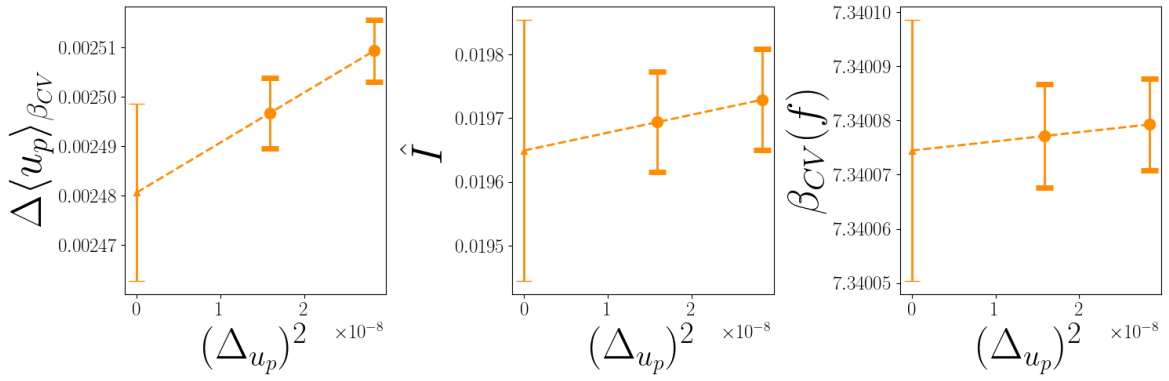

Figure B.16. The observables and their critical inverse couplings: $\Delta\langle u_p\rangle_{\beta_{CV}}$, $\hat{I}$, and $\beta_{CV}(f)$, for $Sp(4)$ gauge theory on a lattice of size 4×40^3, against the square of the interval size, $(\Delta_{u_p})^2$.The error on each point with finite interval size is the error on the mean found by bootstrapping over the repeats. We carry out a linear extrapolation, orange dashed line, on each observable in $(\Delta_{u_p})^2$, and take the limit of vanishing interval size, orange triangle.

Many of the results at finite interval size for this volume are consistent with the extrapolation, and the results for the other interval size. In these cases the main effect of the extrapolation is to increase the error. To be conservative with the error, we choose to use the extrapolated results in our analysis of the thermodynamic limit. However, it indicates that results at finite interval size are likely valid, as an estimate for the limit of vanishing interval size, for this volume.

B.5 4×48^3

For 4×48^3, due to limitations of computational resources, we only have one results for one interval size. In this case we choose to estimate the results for vanishing interval size with our only value at finite interval size.

Appendix C

Meta-stable dynamics with IS for $Sp(4)$ with $N_t = 5$

"Okay"
David Mason in a letter to Robert Mason

To take the continuum limit, we need to study the behaviour of the system as we increase N_t. As mentioned in the introduction, around first order phase transitions we can approximate the plaquette distribution of the system as a double Gaussian, with width of each Gaussian scaling inversely with the spatial volume of the system. As we decrease the lattice spacing, by increasing N_t, we must increase the spatial volume, controlled by N_s, to ensure we can resolve each peak of the plaquette distribution. In this section we discuss an initial exploration of $Sp(4)$ pure gauge theory at $N_t = 5$ using standard importance sampling methods, to find the required aspect ratio, N_t/N_s, to observe the meta-stable dynamics around the deconfinement phase transitions

We begin with a lattice of size 5×20^3. Using standard importance sampling methods, we initially carry out a parameter scan of inverse couplings, $\beta = 7.48, 7.49$ and 7.50. We chose these couplings as the infinite volume critical inverse coupling for $N_t = 5$ was determined to be $\beta_C = 7.486(4)$, in Ref. [86]. For each ensemble we measure the Polyakov loop and average plaquette on 10,000 configurations, with 5,000 thermalisation steps. For each lattice update, we carry out one heat-bath and four over-relaxation steps. The results for the VEV of the absolute value of the Polyakov loop, $\langle |l_p| \rangle_\beta$, and the susceptibility, $\chi_l(\beta)$, are presented against their inverse coupling, β, in Fig. C.1. We see that the phase transition appears to be at approximately $\beta = 7.49$, due to the slight increase in Polyakov loop susceptibility and the change in the VEV of the Polyakov loop between $\beta = 7.49$ and 7.50.

To verify if we can observe the meta-stable dynamics we carry out a more in-depth study at $\beta = 7.49$, by carrying out 100,000 new measurements, after 10,000 thermalisation steps. The Monte-Carlo trajectories of the absolute value of the Polyakov loop and the average

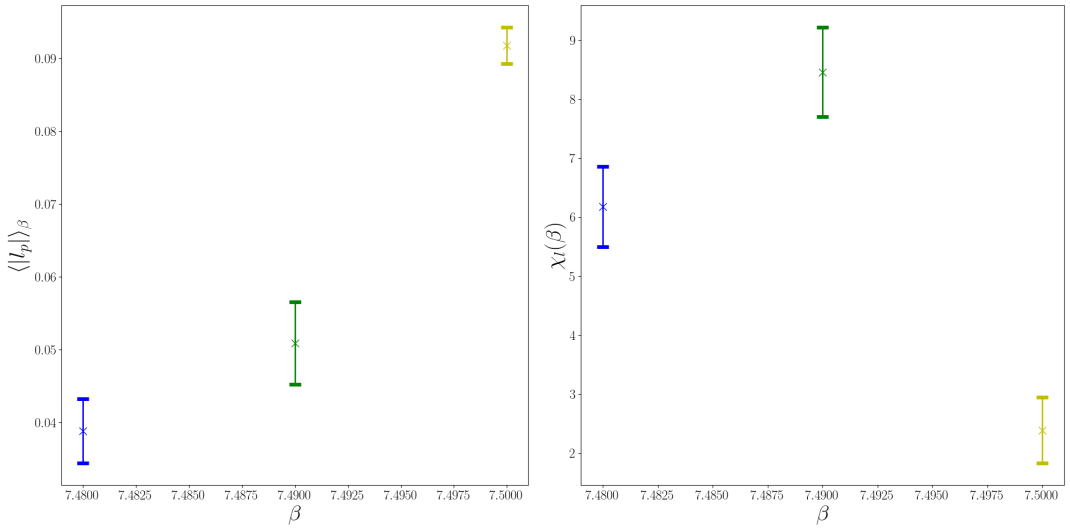

Figure C.1. Importance sampling results for the absolute value of the Polyakov loop, $\langle |l_p| \rangle_\beta$, and the susceptibility, $\chi_l(\beta)$, are presented against the inverse coupling β, for $Sp(4)$ pure gauge theory on a lattice of size 5×20^3. For these ensembles we carry out 10,000 measurements after 5,00 thermalisation steps.

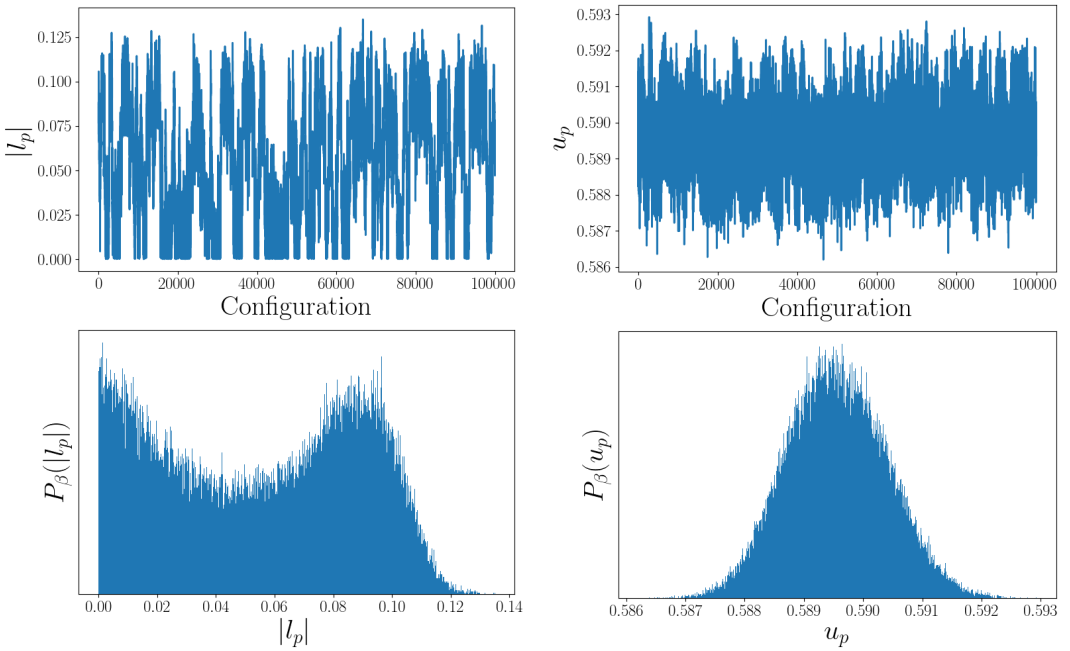

Figure C.2. The history of the measured value of the absolute value of the Polyakov loop (top left), $|l_p|$, and average plaquette (top right), u_p, for 100,000 configurations generated using importance sampling methods, for $Sp(4)$ pure gauge theory on a lattice of size 5×20^3 with $\beta = 7.49$. The corresponding histogram of the measured values, $P_\beta(u_p)$ and $P_\beta(|l_p|)$, are shown in bottom left and right.

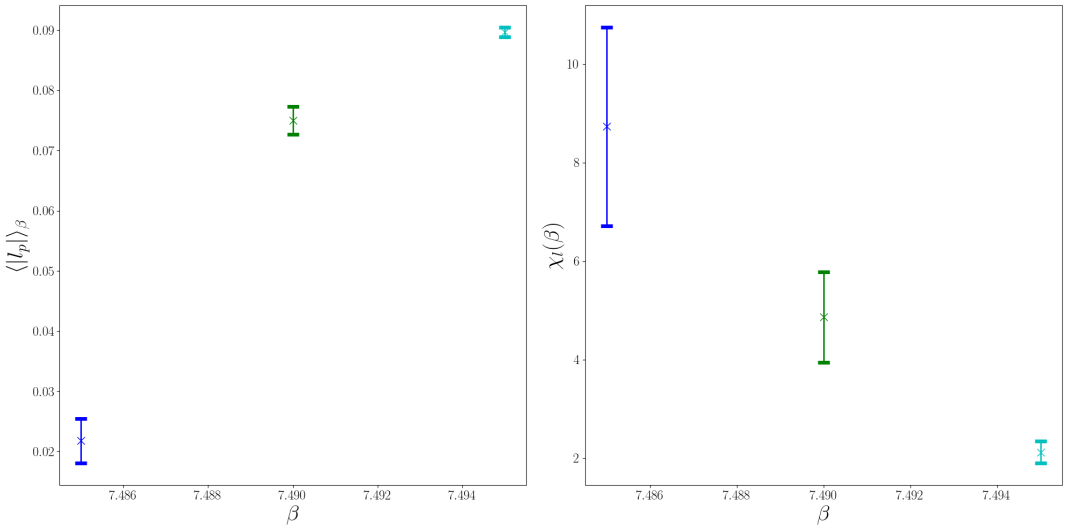

Figure C.3. Importance sampling results for the absolute value of the Polyakov loop, $\langle |l_p| \rangle_\beta$, and the susceptibility, $\chi_l(\beta)$, are presented against the inverse coupling β, for $Sp(4)$ pure gauge theory on a lattice of size 5×32^3. For each ensemble we carry out 10,000 measurements after 5,00 thermalisation steps.

plaquette for this new ensemble are shown in top two plots of Fig. C.2. The resulting histograms of measured values are shown in bottom plots. From the trajectory and histogram of Polyakov loop values, we can see that this system has moved between the phases multiple times. The Polyakov loop distribution clearly has a double peak distribution. However, we cannot resolve the separate peaks of the average plaquette, with the plaquette distribution appearing to only have a single peak. Therefore we will require a larger volume to observe the meta-stable dynamics.

Next we moved onto $\tilde{V}/a^4 = 5 \times 32^3$. Initially we studied ensembles at $\beta = 7.48$, 7.49 and 7.5, with 10,000 measurements after 5,000 thermalisation steps. The VEV of the absolute value of the Polyakov loop, and it's susceptibility are shown in Fig. C.3. We see that the phase transition is somewhere between $\beta = 7.48$ and 7.49, as the value of the Polyakov loop has changed, but there appears to be no peak in the susceptibility.

We choose to carry out a more in depth analysis on the system for an inverse coupling of $\beta = 7.488$. For this ensemble we carry out 100,000 measurements after 10,000 thermalisation steps. The Monte-Carlo trajectory of measured Polyakov loop and plaquette values are shown in the top plots of Fig. C.4. While the histogram of measured values are shown in the bottom plots. Again we see that in the Polyakov loop there is a clear separation between the phases, and it clearly tunnels between the phases multiple times. However, again we do not observe the double peak structure in the average plaquette.

We again increase the volume, increasing the aspect ratio to 8 with 5×40^3. This is well

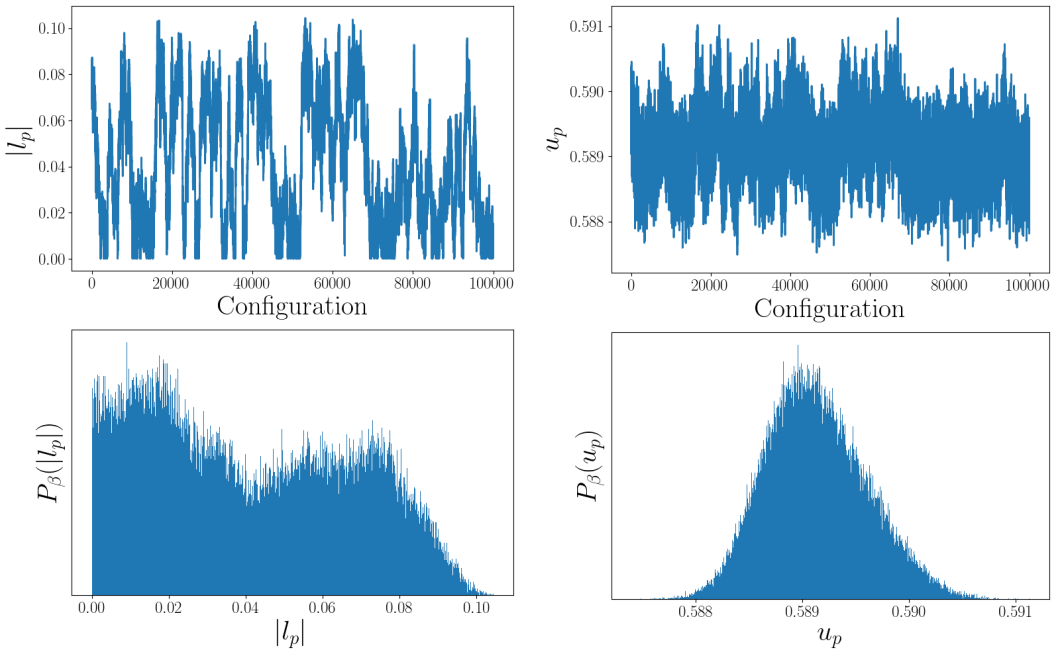

Figure C.4. The history of the measured value of the absolute value of the Polyakov loop (top left), $|l_p|$, and average plaquette (top right), u_p, for 100,000 configurations generated using importance sampling methods, for $Sp(4)$ pure gauge theory on a lattice of size 5×32^3 with $\beta = 7.488$. The corresponding histogram of the measured values, $P_\beta(u_p)$ and $P_\beta(|l_p|)$, are shown in bottom left and right.

beyond the aspect ratio of 5 in which we were able to resolve the two peaks of the plaquette distribution in $N_t = 4$. We carry out measurements on ensembles at $\beta = 7.485, 7.490, 7.491, 7.492, 7.495$. The results for the VEV of the absolute value of the Polyakov loop and it's susceptibility are shown in Fig. C.5. For $\beta = 7.485$ and 7.495, we carry out 10,000 measurements after 5,000 thermalisation steps. For $\beta = 7.490$ and 7.492, we carry out 100,000 measurements after 10,000 thermalisation steps. From these results we can see that the ensemble at $\beta = 7.490$, appears to be closest to the critical point and is therefore mostly likely to exhibit the meta-stable dynamics. The value of the Polyakov loop susceptibility is larger than the value for the other ensembles, and there is a clear difference in the value of the Polyakov loop between $\beta = 7.490$ and 7.492. In Fig. C.6, we plot the trajectories and histograms of measured Polyakov loop and plaquette values for this ensemble. Again we can clearly see a separation between the two phases in the Polyakov loop. From the average plaquette we can start to see some separation between the phases. This is particularly clear from the trajectory, as we can see the centre of the oscillation shift. The histogram has also started to show some indication of a double peak structure.

Although we have a strong indication of the separation of the peaks in the plaquette

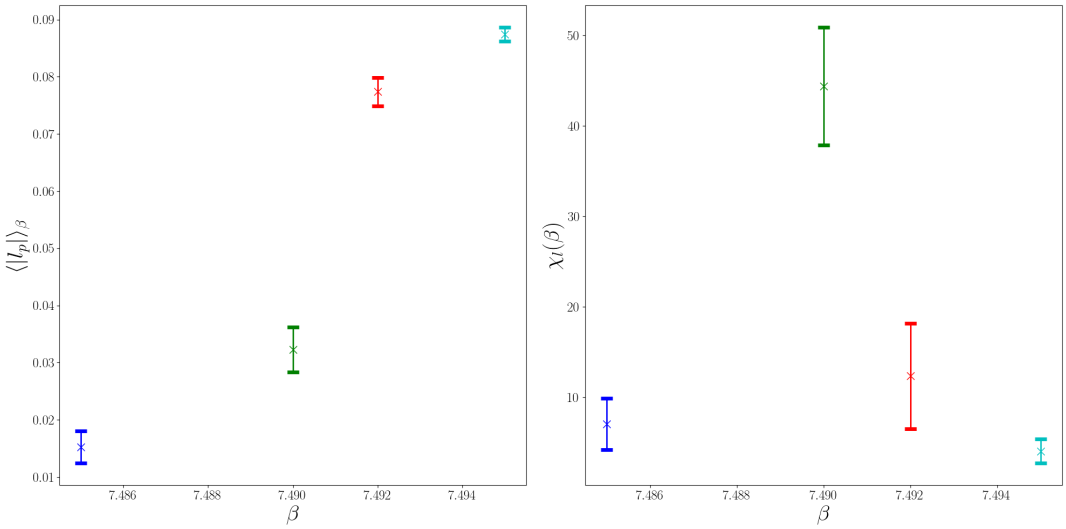

Figure C.5. Importance sampling results for the absolute value of the Polyakov loop, $\langle |l_p| \rangle_\beta$, and the susceptibility, $\chi_l(\beta)$, are presented against the inverse coupling β, for $Sp(4)$ pure gauge theory on a lattice of size 5×40^3. For these ensembles we carry out 10,000 measurements after 5,00 thermalisation steps.

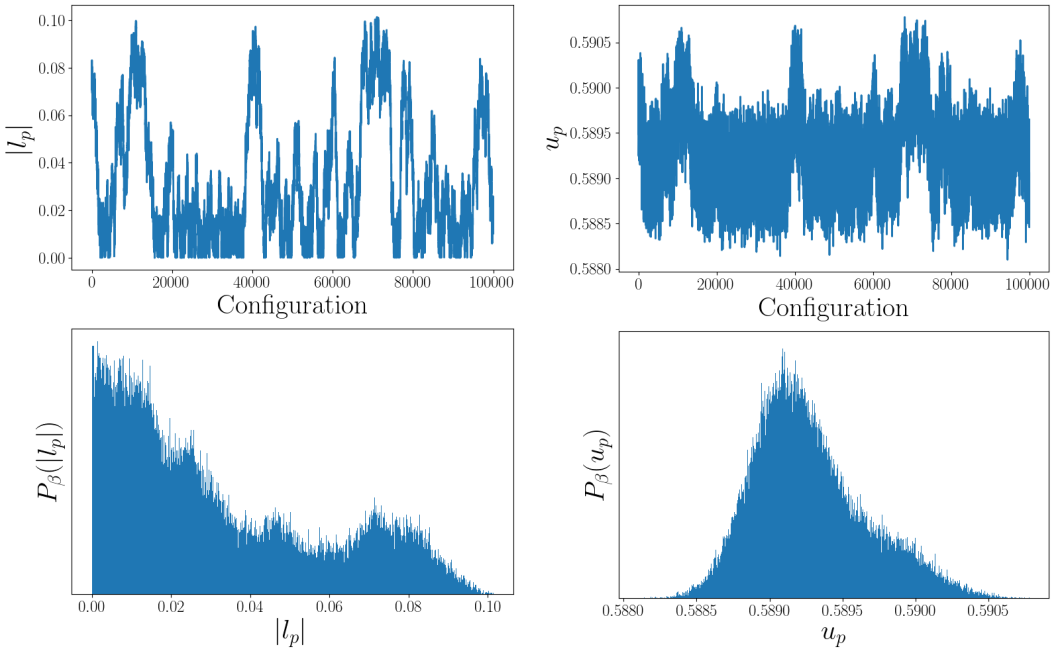

Figure C.6. The history of the measured value of the absolute value of the Polyakov loop (top left), $|l_p|$, and average plaquette (top right), u_p, for 100,000 configurations generated using importance sampling methods, for $Sp(4)$ pure gauge theory on a lattice of size 5×40^3 with $\beta = 7.49$. The corresponding histogram of the measured values, $P_\beta(u_p)$ and $P_\beta(|l_p|)$, are shown in bottom left and right.

distribution, to be safe for $N_t = 5$, we choose to study start our study with 5×48^3. From the LLR results we have a clear indication that we do indeed see the meta-stable dynamics at this volume. We also study 5×56^3, so we can begin to study the large volume limit.

Bibliography

[1] B. Lucini, D. Mason, M. Piai, E. Rinaldi, and D. Vadacchino, *First-order phase transitions in Yang-Mills theories and the density of state method*, *Phys. Rev. D* **108** (2023), no. 7 074517, [arXiv:2305.07463].

[2] Bennett, B. Lucini, D. Mason, M. Piai, E. Rinaldi, and D. Vadacchino, *The density of states method for symplectic gauge theories at finite temperature*, arXiv:2409.19426.

[3] E. Bennet, B. Lucini, D. Mason, M. Piai, E. Rinaldi, and D. Vadacchino, *The density of states method for Symplectic gauge theories at finite temperature—data and analysis code release*, 2024.

[4] B. Lucini, D. Mason, M. Piai, E. Rinaldi, and D. Vadacchino, *First-order phase transitions in Yang-Mills theories and the density of state method—data and analysis code release*, 2023.

[5] B. Lucini, D. Mason, M. Piai, E. Rinaldi, and D. Vadacchino, *First-order phase transitions in Yang-Mills theories and the density of state method — HiRep LLR Code v1.0.0*, 2023.

[6] E. Bennet, B. Lucini, D. Mason, M. Piai, E. Rinaldi, and D. Vadacchino, *The density of states method for Symplectic gauge theories at finite temperature — HiRep LLR Code v1.0.0*, 2024.

[7] G. M. Fuller, G. J. Mathews, and C. R. Alcock, *The Quark - Hadron Phase Transition in the Early Universe: Isothermal Baryon Number Fluctuations and Primordial Nucleosynthesis*, *Phys. Rev. D* **37** (1988) 1380.

[8] M. Maggiore, *Gravitational Waves. Vol. 2: Astrophysics and Cosmology*. Oxford University Press, 3, 2018.

[9] A. D. Sakharov, *Violation of CP Invariance, C asymmetry, and baryon asymmetry of the universe*, *Pisma Zh. Eksp. Teor. Fiz.* **5** (1967) 32–35.

[10] D. E. Morrissey and M. J. Ramsey-Musolf, *Electroweak baryogenesis*, *New J. Phys.* **14** (2012) 125003, [arXiv:1206.2942].

[11] J. Shelton and K. M. Zurek, *Darkogenesis: A baryon asymmetry from the dark matter sector*, *Phys. Rev. D* **82** (2010) 123512, [arXiv:1008.1997].

[12] G. Elor et al., *New Ideas in Baryogenesis: A Snowmass White Paper*, in *Snowmass 2021*, 3, 2022. arXiv:2203.05010.

[13] **LIGO Scientific, Virgo** Collaboration, B. P. Abbott et al., *Observation of Gravitational Waves from a Binary Black Hole Merger*, *Phys. Rev. Lett.* **116** (2016), no. 6 061102, [arXiv:1602.03837].

[14] **NANOGrav** Collaboration, A. Afzal et al., *The NANOGrav 15 yr Data Set: Search for Signals from New Physics*, *Astrophys. J. Lett.* **951** (2023), no. 1 L11, [arXiv:2306.16219].

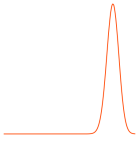

[15] C. Caprini et al., *Detecting gravitational waves from cosmological phase transitions with LISA: an update*, *JCAP* **03** (2020) 024, [arXiv:1910.13125].

[16] W.-C. Huang, M. Reichert, F. Sannino, and Z.-W. Wang, *Testing the dark SU(N) Yang-Mills theory confined landscape: From the lattice to gravitational waves*, *Phys. Rev. D* **104** (2021), no. 3 035005, [arXiv:2012.11614].

[17] E. Witten, *Cosmic Separation of Phases*, *Phys. Rev. D* **30** (1984) 272–285.

[18] M. Kamionkowski, A. Kosowsky, and M. S. Turner, *Gravitational radiation from first order phase transitions*, *Phys. Rev. D* **49** (1994) 2837–2851, [astro-ph/9310044].

[19] B. Allen, *The Stochastic gravity wave background: Sources and detection*, in *Les Houches School of Physics: Astrophysical Sources of Gravitational Radiation*, pp. 373–417, 4, 1996. gr-qc/9604033.

[20] P. Schwaller, *Gravitational Waves from a Dark Phase Transition*, *Phys. Rev. Lett.* **115** (2015), no. 18 181101, [arXiv:1504.07263].

[21] D. Croon, V. Sanz, and G. White, *Model Discrimination in Gravitational Wave spectra from Dark Phase Transitions*, *JHEP* **08** (2018) 203, [arXiv:1806.02332].

[22] N. Christensen, *Stochastic Gravitational Wave Backgrounds*, *Rept. Prog. Phys.* **82** (2019), no. 1 016903, [arXiv:1811.08797].

[23] M. Hindmarsh, S. J. Huber, K. Rummukainen, and D. J. Weir, *Gravitational waves from the sound of a first order phase transition*, *Phys. Rev. Lett.* **112** (2014) 041301, [arXiv:1304.2433].

[24] J. Dahl, M. Hindmarsh, K. Rummukainen, and D. Weir, *Primordial acoustic turbulence: three-dimensional simulations and gravitational wave predictions*, arXiv:2407.05826.

[25] M. D'Onofrio and K. Rummukainen, *Standard model cross-over on the lattice*, *Phys. Rev. D* **93** (2016), no. 2 025003, [arXiv:1508.07161].

[26] K. Kajantie, M. Laine, K. Rummukainen, and M. E. Shaposhnikov, *Is there a hot electroweak phase transition at $m_H \gtrsim m_W$?*, *Phys. Rev. Lett.* **77** (1996) 2887–2890, [hep-ph/9605288].

[27] F. Karsch, T. Neuhaus, A. Patkos, and J. Rank, *Critical Higgs mass and temperature dependence of gauge boson masses in the SU(2) gauge Higgs model*, *Nucl. Phys. B Proc. Suppl.* **53** (1997) 623–625, [hep-lat/9608087].

[28] M. Gurtler, E.-M. Ilgenfritz, and A. Schiller, *Where the electroweak phase transition ends*, *Phys. Rev. D* **56** (1997) 3888–3895, [hep-lat/9704013].

[29] K. Rummukainen, M. Tsypin, K. Kajantie, M. Laine, and M. E. Shaposhnikov, *The Universality class of the electroweak theory*, *Nucl. Phys. B* **532** (1998) 283–314, [hep-lat/9805013].

[30] F. Csikor, Z. Fodor, and J. Heitger, *Endpoint of the hot electroweak phase transition*, *Phys. Rev. Lett.* **82** (1999) 21–24, [hep-ph/9809291].

[31] Y. Aoki, F. Csikor, Z. Fodor, and A. Ukawa, *The Endpoint of the first order phase transition of the SU(2) gauge Higgs model on a four-dimensional isotropic lattice*, *Phys. Rev. D* **60** (1999) 013001, [hep-lat/9901021].

[32] **CMS** Collaboration, S. Chatrchyan et al., *Observation of a New Boson at a Mass of 125 GeV with the CMS Experiment at the LHC*, *Phys. Lett. B* **716** (2012) 30–61, [arXiv:1207.7235].

[33] **ATLAS, CMS** Collaboration, G. Aad et al., *Combined Measurement of the Higgs Boson Mass in pp Collisions at $\sqrt{s} = 7$ and 8 TeV with the ATLAS and CMS Experiments*, *Phys. Rev. Lett.* **114** (2015) 191803, [arXiv:1503.07589].

[34] O. Gould, S. Güyer, and K. Rummukainen, *First-order electroweak phase transitions: A nonperturbative update*, *Phys. Rev. D* **106** (2022), no. 11 114507, [arXiv:2205.07238].

[35] A. Y. Kotov, M. P. Lombardo, and A. Trunin, *QCD transition at the physical point, and its scaling window from twisted mass Wilson fermions*, *Phys. Lett. B* **823** (2021) 136749, [arXiv:2105.09842].

[36] J. Greensite, *An introduction to the confinement problem*, vol. 821. 2011.

[37] Y. Aoki, G. Endrodi, Z. Fodor, S. D. Katz, and K. K. Szabo, *The Order of the quantum chromodynamics transition predicted by the standard model of particle physics*, *Nature* **443** (2006) 675–678, [hep-lat/0611014].

[38] F. R. Brown, F. P. Butler, H. Chen, N. H. Christ, Z.-h. Dong, W. Schaffer, L. I. Unger, and A. Vaccarino, *On the existence of a phase transition for QCD with three light quarks*, *Phys. Rev. Lett.* **65** (1990) 2491–2494.

[39] O. Philipsen, *Lattice Constraints on the QCD Chiral Phase Transition at Finite Temperature and Baryon Density*, *Symmetry* **13** (2021), no. 11 2079, [arXiv:2111.03590].

[40] **ATLAS, CMS** Collaboration, D. Perez Adan, *Dark Matter searches at CMS and ATLAS*, in *56th Rencontres de Moriond on Electroweak Interactions and Unified Theories*, 1, 2023. arXiv:2301.10141.

[41] M. Cirelli, A. Strumia, and J. Zupan, *Dark Matter*, arXiv:2406.01705.

[42] E. Del Nobile, C. Kouvaris, and F. Sannino, *Interfering Composite Asymmetric Dark Matter for DAMA and CoGeNT*, *Phys. Rev. D* **84** (2011) 027301, [arXiv:1105.5431].

[43] A. Hietanen, R. Lewis, C. Pica, and F. Sannino, *Composite Goldstone Dark Matter: Experimental Predictions from the Lattice*, *JHEP* **12** (2014) 130, [arXiv:1308.4130].

[44] J. M. Cline, W. Huang, and G. D. Moore, *Challenges for models with composite states*, *Phys. Rev. D* **94** (2016), no. 5 055029, [arXiv:1607.07865].

[45] N. A. Dondi, F. Sannino, and J. Smirnov, *Thermal history of composite dark matter*, *Phys. Rev. D* **101** (2020), no. 10 103010, [arXiv:1905.08810].

[46] V. Beylin, M. Y. Khlopov, V. Kuksa, and N. Volchanskiy, *Hadronic and Hadron-Like Physics of Dark Matter*, *Symmetry* **11** (2019), no. 4 587, [arXiv:1904.12013].

[47] N. Yamanaka, H. Iida, A. Nakamura, and M. Wakayama, *Dark matter scattering cross section and dynamics in dark Yang-Mills theory*, *Phys. Lett. B* **813** (2021) 136056, [arXiv:1910.01440].

[48] N. Yamanaka, H. Iida, A. Nakamura, and M. Wakayama, *Glueball scattering cross section in lattice SU(2) Yang-Mills theory*, *Phys. Rev. D* **102** (2020), no. 5 054507, [arXiv:1910.07756].

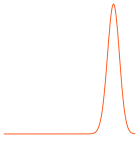

[49] T. Appelquist et al., *Stealth Dark Matter: Dark scalar baryons through the Higgs portal*, *Phys. Rev. D* **92** (2015), no. 7 075030, [arXiv:1503.04203].

[50] N. Bernal, X. Chu, S. Kulkarni, and J. Pradler, *Self-interacting dark matter without prejudice*, *Phys. Rev. D* **101** (2020), no. 5 055044, [arXiv:1912.06681].

[51] Y. Hochberg, E. Kuflik, T. Volansky, and J. G. Wacker, *Mechanism for Thermal Relic Dark Matter of Strongly Interacting Massive Particles*, *Phys. Rev. Lett.* **113** (2014) 171301, [arXiv:1402.5143].

[52] Y. Hochberg, E. Kuflik, H. Murayama, T. Volansky, and J. G. Wacker, *Model for Thermal Relic Dark Matter of Strongly Interacting Massive Particles*, *Phys. Rev. Lett.* **115** (2015), no. 2 021301, [arXiv:1411.3727].

[53] Y. Hochberg, E. Kuflik, and H. Murayama, *SIMP Spectroscopy*, *JHEP* **05** (2016) 090, [arXiv:1512.07917].

[54] N. Bernal, X. Chu, and J. Pradler, *Simply split strongly interacting massive particles*, *Phys. Rev. D* **95** (2017), no. 11 115023, [arXiv:1702.04906].

[55] A. Berlin, N. Blinov, S. Gori, P. Schuster, and N. Toro, *Cosmology and Accelerator Tests of Strongly Interacting Dark Matter*, *Phys. Rev. D* **97** (2018), no. 5 055033, [arXiv:1801.05805].

[56] Y.-D. Tsai, R. McGehee, and H. Murayama, *Resonant Self-Interacting Dark Matter from Dark QCD*, *Phys. Rev. Lett.* **128** (2022), no. 17 172001, [arXiv:2008.08608].

[57] D. Kondo, R. McGehee, T. Melia, and H. Murayama, *Linear sigma dark matter*, *JHEP* **09** (2022) 041, [arXiv:2205.08088].

[58] A. Maas and F. Zierler, *Strong isospin breaking in $\boldsymbol{Sp}(4)$ gauge theory*, *PoS* **LATTICE2021** (2022) 130, [arXiv:2109.14377].

[59] F. Zierler and A. Maas, *$Sp(4)$ SIMP Dark Matter on the Lattice*, *PoS* **LHCP2021** (2021) 162.

[60] S. Kulkarni, A. Maas, S. Mee, M. Nikolic, J. Pradler, and F. Zierler, *Low-energy effective description of dark $Sp(4)$ theories*, *SciPost Phys.* **14** (2023) 044, [arXiv:2202.05191].

[61] F. Zierler, J.-W. Lee, A. Maas, and F. Pressler, *Singlet Mesons in Dark $Sp(4)$ Theories*, *PoS* **LATTICE2022** (2023) 225, [arXiv:2210.11187].

[62] F. Zierler, S. Kulkarni, A. Maas, S. Mee, M. Nikolic, and J. Pradler, *Strongly Interacting Dark Matter from Sp(4) Gauge Theory*, *EPJ Web Conf.* **274** (2022) 08014, [arXiv:2211.11272].

[63] Y. Dengler, A. Maas, and F. Zierler, *Scattering of dark pions in an Sp(4)-gauge theory*, *PoS* **LATTICE2023** (2024) 103, [arXiv:2311.18549].

[64] Y. Dengler, A. Maas, and F. Zierler, *Scattering of dark pions in Sp(4) gauge theory*, arXiv:2405.06506.

[65] O. Witzel, *Review on Composite Higgs Models*, *PoS* **LATTICE2018** (2019) 006, [arXiv:1901.08216].

[66] K. G. Wilson, *Confinement of Quarks*, *Phys. Rev. D* **10** (1974) 2445–2459.

[67] E. Bennett, D. K. Hong, J.-W. Lee, C. J. D. Lin, B. Lucini, M. Piai, and D. Vadacchino, *Sp(4) gauge theory on the lattice: towards SU(4)/Sp(4) composite Higgs (and beyond)*, *JHEP* **03** (2018) 185, [arXiv:1712.04220].

[68] J.-W. Lee, E. Bennett, D. K. Hong, C. J. D. Lin, B. Lucini, M. Piai, and D. Vadacchino, *Progress in the lattice simulations of Sp(2N) gauge theories*, *PoS* **LATTICE2018** (2018) 192, [arXiv:1811.00276].

[69] E. Bennett, D. K. Hong, J.-W. Lee, C. J. D. Lin, B. Lucini, M. Piai, and D. Vadacchino, *Sp(4) gauge theories on the lattice: $N_f = 2$ dynamical fundamental fermions*, *JHEP* **12** (2019) 053, [arXiv:1909.12662].

[70] E. Bennett, D. K. Hong, J.-W. Lee, C.-J. D. Lin, B. Lucini, M. Mesiti, M. Piai, J. Rantaharju, and D. Vadacchino, *$Sp(4)$ gauge theories on the lattice: quenched fundamental and antisymmetric fermions*, *Phys. Rev. D* **101** (2020), no. 7 074516, [arXiv:1912.06505].

[71] E. Bennett, J. Holligan, D. K. Hong, J.-W. Lee, C. J. D. Lin, B. Lucini, M. Piai, and D. Vadacchino, *Color dependence of tensor and scalar glueball masses in Yang-Mills theories*, *Phys. Rev. D* **102** (2020), no. 1 011501, [arXiv:2004.11063].

[72] E. Bennett, J. Holligan, D. K. Hong, J.-W. Lee, C. J. D. Lin, B. Lucini, M. Piai, and D. Vadacchino, *Glueballs and strings in $Sp(2N)$ Yang-Mills theories*, *Phys. Rev. D* **103** (2021), no. 5 054509, [arXiv:2010.15781].

[73] B. Lucini, E. Bennett, J. Holligan, D. K. Hong, H. Hsiao, J.-W. Lee, C. J. D. Lin, M. Mesiti, M. Piai, and D. Vadacchino, *Sp(4) gauge theories and beyond the standard model physics*, *EPJ Web Conf.* **258** (2022) 08003, [arXiv:2111.12125].

[74] E. Bennett, J. Holligan, D. K. Hong, H. Hsiao, J.-W. Lee, C. J. D. Lin, B. Lucini, M. Mesiti, M. Piai, and D. Vadacchino, *Progress in $Sp(2N)$ lattice gauge theories*, *PoS* **LATTICE2021** (2022) 308, [arXiv:2111.14544].

[75] E. Bennett, D. K. Hong, H. Hsiao, J.-W. Lee, C. J. D. Lin, B. Lucini, M. Mesiti, M. Piai, and D. Vadacchino, *Lattice studies of the Sp(4) gauge theory with two fundamental and three antisymmetric Dirac fermions*, *Phys. Rev. D* **106** (2022), no. 1 014501, [arXiv:2202.05516].

[76] E. Bennett, D. K. Hong, J.-W. Lee, C. J. D. Lin, B. Lucini, M. Piai, and D. Vadacchino, *Color dependence of the topological susceptibility in Yang-Mills theories*, *Phys. Lett. B* **835** (2022) 137504, [arXiv:2205.09254].

[77] E. Bennett, D. K. Hong, J.-W. Lee, C. J. D. Lin, B. Lucini, M. Piai, and D. Vadacchino, *Sp(2N) Yang-Mills theories on the lattice: Scale setting and topology*, *Phys. Rev. D* **106** (2022), no. 9 094503, [arXiv:2205.09364].

[78] H. Hsiao, E. Bennett, D. K. Hong, J.-W. Lee, C. J. D. Lin, B. Lucini, M. Piai, and D. Vadacchino, *Spectroscopy of $Sp(4)$ lattice gauge theory with $n_f = 3$ antisymmetric fermions*, *PoS* **LATTICE2022** (2023) 211, [arXiv:2210.08154].

[79] H. Hsiao, E. Bennett, D. K. Hong, J.-W. Lee, C. J. D. Lin, B. Lucini, M. Piai, and D. Vadacchino, *Spectroscopy of chimera baryons in a $Sp(4)$ lattice gauge theory*, arXiv:2211.03955.

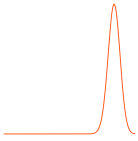

[80] E. Bennett et al., *Symplectic lattice gauge theories in the grid framework: Approaching the conformal window*, *Phys. Rev. D* **108** (2023), no. 9 094508, [arXiv:2306.11649].

[81] E. Bennett, D. K. Hong, H. Hsiao, J.-W. Lee, C. J. D. Lin, B. Lucini, M. Piai, and D. Vadacchino, *Lattice investigations of the chimera baryon spectrum in the Sp(4) gauge theory*, *Phys. Rev. D* **109** (2024), no. 9 094512, [arXiv:2311.14663].

[82] E. Bennett, J. Holligan, D. K. Hong, J.-W. Lee, C. J. D. Lin, B. Lucini, M. Piai, and D. Vadacchino, *Spectrum of mesons in quenched Sp(2N) gauge theories*, *Phys. Rev. D* **109** (2024), no. 9 094517, [arXiv:2312.08465].

[83] E. Bennett et al., *Meson spectroscopy from spectral densities in lattice gauge theories*, arXiv:2405.01388.

[84] E. Bennett, N. Forzano, D. K. Hong, H. Hsiao, J.-W. Lee, C. J. D. Lin, B. Lucini, M. Piai, D. Vadacchino, and F. Zierler, *On the mixing between flavor singlets in lattice gauge theories coupled to matter fields in multiple representations*, arXiv:2405.05765.

[85] E. Bennett, J. Holligan, D. K. Hong, H. Hsiao, J.-W. Lee, C. J. D. Lin, B. Lucini, M. Mesiti, M. Piai, and D. Vadacchino, *Sp(2N) Lattice Gauge Theories and Extensions of the Standard Model of Particle Physics*, *Universe* **9** (2023), no. 5 236, [arXiv:2304.01070].

[86] K. Holland, M. Pepe, and U. J. Wiese, *The Deconfinement phase transition of Sp(2) and Sp(3) Yang-Mills theories in (2+1)-dimensions and (3+1)-dimensions*, *Nucl. Phys. B* **694** (2004) 35–58, [hep-lat/0312022].

[87] K. Holland, P. Minkowski, M. Pepe, and U. J. Wiese, *Exceptional confinement in G(2) gauge theory*, *Nucl. Phys. B* **668** (2003) 207–236, [hep-lat/0302023].

[88] M. Pepe, *Confinement and the center of the gauge group*, *PoS* **LAT2005** (2006) 017, [hep-lat/0510013].

[89] M. Pepe and U. J. Wiese, *Exceptional Deconfinement in G(2) Gauge Theory*, *Nucl. Phys. B* **768** (2007) 21–37, [hep-lat/0610076].

[90] G. Cossu, M. D'Elia, A. Di Giacomo, B. Lucini, and C. Pica, *G(2) gauge theory at finite temperature*, *JHEP* **10** (2007) 100, [arXiv:0709.0669].

[91] M. Bruno, M. Caselle, M. Panero, and R. Pellegrini, *Exceptional thermodynamics: the equation of state of G_2 gauge theory*, *JHEP* **03** (2015) 057, [arXiv:1409.8305].

[92] L. Kynaston, *Studying the critical temperature for the deconfinement transition in lattice gauge sp(2n) theories*, master of philosophy, Swansea University, 2020.

[93] M. Bruno, N. Forzano, M. Panero, and A. Smecca, *Thermal evolution of dark matter in the early universe from a symplectic glueball model*, *in preparation* (2024).

[94] D. Mason, B. Lucini, M. Piai, E. Rinaldi, and D. Vadacchino, *The deconfinement phase transition in $Sp(2N)$ gauge theories and the density of states method*, in *40th International Symposium on Lattice Field Theory*, 10, 2023. arXiv:2310.02145.

[95] E. Bennet, B. Lucini, D. Mason, M. Piai, E. Rinaldi, D. Vadacchino, and F. Zierler, *Updates on the density of states method in finite temperature Symplectic gauge theories*, *in preparation* (2024).

[96] K. Kajantie, C. Montonen, and E. Pietarinen, *Phase Transition of SU(3) Gauge Theory at Finite Temperature*, *Z. Phys. C* **9** (1981) 253.

[97] S. A. Gottlieb, J. Kuti, D. Toussaint, A. D. Kennedy, S. Meyer, B. J. Pendleton, and R. L. Sugar, *The Deconfining Phase Transition and the Continuum Limit of Lattice Quantum Chromodynamics*, *Phys. Rev. Lett.* **55** (1985) 1958.

[98] F. R. Brown, N. H. Christ, Y. F. Deng, M. S. Gao, and T. J. Woch, *Nature of the Deconfining Phase Transition in SU(3) Lattice Gauge Theory*, *Phys. Rev. Lett.* **61** (1988) 2058.

[99] M. Fukugita, M. Okawa, and A. Ukawa, *Order of the Deconfining Phase Transition in SU(3) Lattice Gauge Theory*, *Phys. Rev. Lett.* **63** (1989) 1768.

[100] G. Boyd, J. Engels, F. Karsch, E. Laermann, C. Legeland, M. Lutgemeier, and B. Petersson, *Equation of state for the SU(3) gauge theory*, *Phys. Rev. Lett.* **75** (1995) 4169–4172, [hep-lat/9506025].

[101] G. Boyd, J. Engels, F. Karsch, E. Laermann, C. Legeland, M. Lutgemeier, and B. Petersson, *Thermodynamics of SU(3) lattice gauge theory*, *Nucl. Phys. B* **469** (1996) 419–444, [hep-lat/9602007].

[102] S. Borsanyi, G. Endrodi, Z. Fodor, S. D. Katz, and K. K. Szabo, *Precision SU(3) lattice thermodynamics for a large temperature range*, *JHEP* **07** (2012) 056, [arXiv:1204.6184].

[103] M. Shirogane, S. Ejiri, R. Iwami, K. Kanaya, and M. Kitazawa, *Latent heat at the first order phase transition point of SU(3) gauge theory*, *Phys. Rev. D* **94** (2016), no. 1 014506, [arXiv:1605.02997].

[104] S. Borsanyi, K. R., Z. Fodor, D. A. Godzieba, P. Parotto, and D. Sexty, *Precision study of the continuum SU(3) Yang-Mills theory: How to use parallel tempering to improve on supercritical slowing down for first order phase transitions*, *Phys. Rev. D* **105** (2022), no. 7 074513, [arXiv:2202.05234].

[105] B. Lucini, M. Teper, and U. Wenger, *Properties of the deconfining phase transition in SU(N) gauge theories*, *JHEP* **02** (2005) 033, [hep-lat/0502003].

[106] B. Lucini, M. Teper, and U. Wenger, *The Deconfinement transition in SU(N) gauge theories*, *Phys. Lett. B* **545** (2002) 197–206, [hep-lat/0206029].

[107] B. Lucini, M. Teper, and U. Wenger, *The High temperature phase transition in SU(N) gauge theories*, *JHEP* **01** (2004) 061, [hep-lat/0307017].

[108] M. Panero, *Thermodynamics of the QCD plasma and the large-N limit*, *Phys. Rev. Lett.* **103** (2009) 232001, [arXiv:0907.3719].

[109] S. Datta and S. Gupta, *Scaling and the continuum limit of the finite temperature deconfinement transition in SU(N_c) pure gauge theory*, *Phys. Rev. D* **80** (2009) 114504, [arXiv:0909.5591].

[110] B. Lucini, A. Rago, and E. Rinaldi, *SU(N_c) gauge theories at deconfinement*, *Phys. Lett. B* **712** (2012) 279–283, [arXiv:1202.6684].

[111] C. A. Ballon Bayona, H. Boschi-Filho, N. R. F. Braga, and L. A. Pando Zayas, *On a Holographic Model for Confinement/Deconfinement*, *Phys. Rev. D* **77** (2008) 046002, [arXiv:0705.1529].

[112] **Lattice Strong Dynamics** Collaboration, R. C. Brower et al., *Stealth dark matter confinement transition and gravitational waves*, *Phys. Rev. D* **103** (2021), no. 1 014505, [arXiv:2006.16429].

[113] R. Pasechnik, M. Reichert, F. Sannino, and Z.-W. Wang, *Gravitational Waves from Composite Dark Sectors*, arXiv:2309.16755.

[114] K. Fujikura, Y. Nakai, R. Sato, and Y. Wang, *Cosmological Phase Transitions in Composite Higgs Models*, arXiv:2306.01305.

[115] R. H. Swendsen and J.-S. Wang, *Replica Monte Carlo Simulation of Spin-Glasses*, *Phys. Rev. Lett.* **57** (1986), no. 21 2607.

[116] B. Baumann, *Noncanonical Path and Surface Simulation*, *Nucl. Phys. B* **285** (1987) 391–409.

[117] B. A. Berg and T. Neuhaus, *Multicanonical algorithms for first order phase transitions*, *Phys. Lett. B* **267** (1991) 249–253.

[118] B. A. Berg and T. Neuhaus, *Multicanonical ensemble: A New approach to simulate first order phase transitions*, *Phys. Rev. Lett.* **68** (1992) 9–12, [hep-lat/9202004].

[119] F. Wang and D. P. Landau, *Efficient, Multiple-Range Random Walk Algorithm to Calculate the Density of States*, *Phys. Rev. Lett.* **86** (2001), no. 10 2050, [cond-mat/0011174].

[120] K. Langfeld, B. Lucini, and A. Rago, *The density of states in gauge theories*, *Phys. Rev. Lett.* **109** (2012) 111601, [arXiv:1204.3243].

[121] M. Giuliani and C. Gattringer, *Density of States FFA analysis of SU(3) lattice gauge theory at a finite density of color sources*, *Phys. Lett. B* **773** (2017) 166–171, [arXiv:1703.03614].

[122] K. Langfeld, B. Lucini, R. Pellegrini, and A. Rago, *An efficient algorithm for numerical computations of continuous densities of states*, *Eur. Phys. J. C* **76** (2016), no. 6 306, [arXiv:1509.08391].

[123] F. Springer and D. Schaich, *Density of states for gravitational waves*, *PoS* **LATTICE2021** (2022) 043, [arXiv:2112.11868].

[124] F. Springer and D. Schaich, *Progress applying density of states for gravitational waves*, *EPJ Web Conf.* **274** (2022) 08008, [arXiv:2212.09199].

[125] **Lattice Strong Dynamics (LSD)** Collaboration, F. Springer and D. Schaich, *Advances in using density of states for large-N Yang–Mills*, *PoS* **LATTICE2022** (2023) 223, [arXiv:2303.01149].

[126] O. Francesconi, M. Holzmann, B. Lucini, and A. Rago, *Free energy of the self-interacting relativistic lattice Bose gas at finite density*, *Phys. Rev. D* **101** (2020), no. 1 014504, [arXiv:1910.11026].

[127] O. Francesconi, *The sign problem in particle systems*. PhD thesis, Swansea U., 2021.

[128] G. Cossu, D. Lancaster, B. Lucini, R. Pellegrini, and A. Rago, *Ergodic sampling of the topological charge using the density of states*, *Eur. Phys. J. C* **81** (2021), no. 4 375, [arXiv:2102.03630].

[129] K. Langfeld and J. M. Pawlowski, *Two-color QCD with heavy quarks at finite densities*, *Phys. Rev. D* **88** (2013), no. 7 071502, [arXiv:1307.0455].

[130] D. Mason, B. Lucini, M. Piai, E. Rinaldi, and D. Vadacchino, *The density of state method for first-order phase transitions in Yang-Mills theories*, *PoS* **LATTICE2022** (2023) 216, [arXiv:2212.01074].

[131] D. Mason, B. Lucini, M. Piai, E. Rinaldi, and D. Vadacchino, *The density of states method in Yang-Mills theories and first order phase transitions*, *EPJ Web Conf.* **274** (2022) 08007, [arXiv:2211.10373].

[132] D. J. Gross and F. Wilczek, *Asymptotically Free Gauge Theories - I*, *Phys. Rev. D* **8** (1973) 3633–3652.

[133] **QCDSF** Collaboration, R. Horsley, H. Perlt, P. E. L. Rakow, G. Schierholz, and A. Schiller, *One-loop renormalisation of quark bilinears for overlap fermions with improved gauge actions*, *Nucl. Phys. B* **693** (2004) 3–35, [hep-lat/0404007]. [Erratum: Nucl.Phys.B 713, 601–606 (2005)].

[134] L. D. McLerran and B. Svetitsky, *Quark Liberation at High Temperature: A Monte Carlo Study of SU(2) Gauge Theory*, *Phys. Rev. D* **24** (1981) 450.

[135] G. V. Bhanot and S. Sanielevici, *The Bcl Cumulant and Lattice Gauge Theories: The Order of the Deconfinement Transition*, *Phys. Rev. D* **40** (1989) 3454.

[136] M. S. S. Challa, D. P. Landau, and K. Binder, *Finite size effects at temperature driven first order transitions*, *Phys. Rev. B* **34** (1986) 1841–1852.

[137] F. Karsch, *SU(N) Gauge Theory Couplings on Asymmetric Lattices*, *Nucl. Phys. B* **205** (1982) 285–300.

[138] M. Creutz, *Monte Carlo Study of Quantized SU(2) Gauge Theory*, *Phys. Rev. D* **21** (1980) 2308–2315.

[139] M. Creutz, *Overrelaxation and Monte Carlo Simulation*, *Phys. Rev. D* **36** (1987) 515.

[140] N. Cabibbo and E. Marinari, *A New Method for Updating SU(N) Matrices in Computer Simulations of Gauge Theories*, *Phys. Lett. B* **119** (1982) 387–390.

[141] R. Belardinelli and V. Pereyra, *Wang-landau algorithm: A theoretical analysis of the saturation of the error*, *The Journal of chemical physics* **127** (2007), no. 18.

[142] H. Robbins and S. Monro, *A stochastic approximation method*, *The annals of mathematical statistics* (1951) 400–407.

[143] T. Vogel, Y. W. Li, T. Wüst, and D. P. Landau, *Scalable replica-exchange framework for wang-landau sampling*, *Phys. Rev. E* **90** (Aug, 2014) 023302.

[144] C. Gattringer and O. Orasch, *Density of states approach for lattice gauge theory with a θ-term*, *Nucl. Phys. B* **957** (2020) 115097, [arXiv:2004.03837].

[145] B. Lucini, W. Fall, and K. Langfeld, *Overcoming strong metastabilities with the LLR method*, *PoS* **LATTICE2016** (2016) 275, [arXiv:1611.00019].

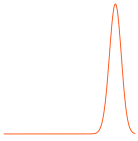

[146] C. Pica et al., "HiRep." https://github.com/claudiopica/HiRep/.

[147] L. Del Debbio, A. Patella, and C. Pica, *Higher representations on the lattice: Numerical simulations. SU(2) with adjoint fermions*, *Phys. Rev. D* **81** (2010) 094503, [arXiv:0805.2058].